Subgrid Models for Electron-Scale Tokamak Turbulence

by

Stefan Tirkas

B.S., University of California Davis, 2015

M.S., University of Colorado Boulder, 2023

A thesis submitted to the

Faculty of the Graduate School of the

University of Colorado in partial fulfillment

of the requirements for the degree of

Doctor of Philosophy

Department of Physics

2025

Committee Members:

Scott Parker, Chair

Yang Chen

Tobin Munsat

Michael Litos

James Meiss

Tirkas, Stefan (Ph.D., Physics)

Subgrid Models for Electron-Scale Tokamak Turbulence

Thesis directed by Professor Scott Parker

Tokamaks are currently the leading concept for thermonuclear fusion reactors, using magnetic fields to toroidally confine a hot plasma and achieve the conditions necessary for sustained fusion. However, experiments reveal anomalous heat and particle losses which far exceed collisional transport predictions and significantly degrade confinement. The anomalous radial transport is now known to result from drift-wave microturbulence, driven unstable in the plasma by the intense pressure gradients involved. Understanding these turbulent transport mechanisms is critical for predicting and maintaining steady-state energy production. After extensive development efforts, gyrokinetic theory and numerical modeling have emerged as essential tools for studying the complex nonlinear dynamics of tokamak microturbulence.

Gyrokinetic simulations at ion gyroradius scales have successfully reproduced transport characteristics in agreement with experiment, but often underestimate electron thermal transport levels. The electron-temperature-gradient (ETG) mode, arising at electron gyroradius scales, is a key candidate to explain excess electron heat losses. ETG transport is expected to be particularly important in reactor-relevant plasmas like ITER, where ETG turbulence can interact with ion-scale turbulence through complex multiscale processes which are sensitive to small variations in equilibrium parameters. Direct simulation of these interactions remains computationally prohibitive, even on exascale computing platforms, thereby motivating the development of the subgrid model presented here. The subgrid model captures electron-scale effects in a reduced form suitable for whole-device modeling of future burning plasmas.

Quasilinear modeling offers an efficient method for predicting turbulent transport spectra by leveraging linear gyrokinetic simulation results. Quaslinear theory is introduced here for modeling ion-scale turbulence in DIII-D shot #162940 using linear gyrokinetic simulation. The quasilinear

predictions show good agreement with nonlinear flux spectra, and analysis is successfully extended to negative triangularity shaping - a plasma configuration which has reported reduced turbulent transport levels. Quasilinear models are further compared against nonlinear gyrokinetic ETG simulations and considered for reduced modeling of local electron-scale turbulence effects in global ion-scale simulation.

A key mechanism of instability regulation is by perpendicular shearing from zonal flows (ZFs), which break up radially-elongated drift wave eddies. These are self-generated shear flows which are driven by growing primary instabilities as nonlinear effects become significant. Intermediate-scale gyrokinetic theory, encompassing wavelengths much shorter than the ion gyroradius but much longer than the electron gyroradius, predicts strong ETG-ZF coupling which is expected to drive significant ZF generation and ETG mode regulation. Zonal flow generation due to a single ETG mode is investigated in local single-mode gyrokinetic simulations and intermediate-scale results are found to be in agreement with the gyrokinetic theory. Full-spectrum results are then presented and explained qualitatively in terms of the single-mode results. The resulting intermediate-scale zonal flows have been reported to help regulate ion-scale turbulence levels in multiscale gyrokinetic simulation.

A subgrid ETG model is then demonstrated which averages local electron-scale turbulence over intermediate scales in space and time to include in global ion-temperature-gradient (ITG) simulations. This approach results in ion-scale equations which incorporate the electron heat transport from ETG turbulence and effects of electron-scale turbulence on the ion scale. Local ETG simulations are performed at different radial locations and a kinetic form of the flux is added to global ion-scale simulations as a source term. Analytic radial profiles of ETG heat flux are constructed and compared to flux-tube results at multiple radial locations. Different ratios of ITG to ETG heat flux levels are considered and the results of capturing ETG heat transport in global ion-scale simulations are discussed. Potential coupling of the ETG streamer potential and intermediate-scale zonal flows to the ion scale is further addressed.

Dedication

To my daughter Nova.

May this convince you never to go to graduate school, though it will probably do the opposite.

Acknowledgements

I would first like to thank my advisor, Prof. Scott Parker, for all the professional and academic support over the years. And especially for giving me a chance to work in such a fascinating field when I had zero knowledge of plasma physics, fusion, or computational physics. It has also been undeniably helpful to have funding and travel opportunites available and encouraged with very little effort on my part - I think I've been very lucky with the projects I've worked on and the connections I've made. Thanks also for always giving me the time when your door was open, regardless of the issue. I would also like to thank Dr. Yang Chen very much for all his help and patience any time we met regarding my research or for any question about gyrokinetic theory which is always confusing me. Thanks as well to Prof. Dmitri Uzdensky who taught my plasma physics courses and gave me a very strong foundation to work with, as well as to Prof. Mike Litos for establishing the plasma retreat which I have had the chance to enjoy many times.

A big thanks to all of the graduate students I have worked with in our group - Wes Johnson, John Zaris, Alex Engel, Calder Haubrich - for any and all times we got coffee, had some beers, played disc golf, went to trivia, went skiing, or played music together. Especially thankful to Wes Johnson for all the wonderful (horrible) conversations over the years; you're going to do big things someday I'm sure. I also want to thank my group members, Hoatian Chen, Junyi Cheng, Qiheng Cai, and Zhichen Feng for all their helpful discussions of all things fusion and supercomputing. A big thanks to Haotian Chen and Gabriele Merlo for always helping me regarding tokamak theory and GENE simulation early on in my studies, I owe you a beer or something if I ever see you again. And much thanks to Neeraj Kumar for all his help and advice and for the many opportunities and coffee breaks

to get out of the office as much as possible, it was much appreciated. I also want to give my thanks to everyone who joined our group as an undergraduate student and gave me many chances to kill time and procrastinate on their coding project when I didn't feel like doing my own work - Sophie Redd, Calder Haubrich, Olivia Chandler, and Dominic Amwoza - I hope all your future endeavors go well!

Lastly, I am endlessly thankful to my friends, family, and loved ones. To my parents, for all their helpful support and advice during my life and in graduate school, and for making me practice my talks to them. To my brother, for pretty much anything and everything always. And to Angelica, my love, (and our cats) for going on this journey with me over the last ten odd years. It is hard to imagine I would end up here without any of you in my life.

Contents

Chapter

1 Introduction **1**

1.1 Energy Production 1

1.2 Thermonuclear Fusion 4

1.3 Fusion Ignition 7

1.4 Magnetic Confinement and the Tokamak 11

1.4.1 Plasma Confinement 14

1.4.2 Tokamak Operation 28

1.5 Thesis Overview 32

2 Turbulent Transport **34**

2.1 Plasma Theory 34

2.2 Electron Drift Waves 39

2.3 Gyrokinetic Theory 44

2.3.1 Gyroaveraging 47

2.3.2 Derivation of Gyrokinetic Equations 49

2.4 Tokamak Microturbulence 55

2.4.1 ITG Mode 57

2.4.2 ETG Mode 58

2.4.3 Other Modes (TEM/KBM/MTM/TAE) 60

2.4.4 Mode Regulation and Zonal Flows . . . 61
2.5 Gyrokinetic Codes . . . 62
2.5.1 GENE . . . 64
2.5.2 GEM . . . 69
2.6 Summary . . . 74

3 Quasilinear Theory **76**
3.1 Basics of Quasilinear Theory . . . 76
3.1.1 Mixing Length Models for Turbulent Transport . . . 79
3.1.2 Quasilinear Codes . . . 84
3.2 Quasilinear Modeling of DIII-D Shot #162940 . . . 85
3.2.1 Linear Analysis . . . 87
3.2.2 Saturation Levels and Quasilinear Fluxes . . . 88
3.2.3 Comparison with Nonlinear Gyrokinetic Simulations . . . 90
3.2.4 Extension to Negative Triangularity . . . 93
3.2.5 Discussion and Future Work . . . 96

4 ETG-Driven Zonal Flows **98**
4.1 ETG Mode Regulation . . . 98
4.1.1 Hasegawa-Mima Equation . . . 100
4.1.2 Kelvin-Helmholtz Instabilities . . . 103
4.1.3 Intermediate-Scale Gyrokinetic Theory . . . 104
4.2 Gyrokinetic Simulations of ETG-Driven Zonal Flows . . . 109
4.2.1 Simulation Model and Parameters . . . 109
4.2.2 Single-Mode Simulation Results . . . 113
4.2.3 Full-spectrum Simulation Results . . . 118
4.2.4 Nonlinear Convergence Tests . . . 122
4.3 Conclusions . . . 123

5 Subgrid ETG Model **125**

5.1 Introduction . . . 125

5.2 Subgrid ETG Model . . . 128

5.3 Local Simulations . . . 132

5.4 Global Ion-Scale Simulations . . . 137

5.5 Normalizations . . . 146

5.6 Discussion . . . 149

6 Conclusions and Outlook **151**

References **155**

Appendix

A Complex Notation **172**

A.1 Drift Wave Flux . . . 172

B Gyrokinetic Theory Derivations **174**

B.1 Guiding-Center Transformation . . . 174

B.2 Gyrokinetic Ordering . . . 178

B.3 Gyroaveraging Terms . . . 181

C Derivation of ITG Dispersion Relation **186**

D Ballooning Mode Representation **190**

E Hasegawa-Mima Toy Model Derivation **195**

Tables

Table

3.1 Local tokamak plasma parameters at $\rho = 0.80$, 0.85, and 0.90. 87

4.1 Relevant GENE normalizations and definitions [148]. 111

4.2 GENE simulation parameters. 111

5.1 Time-averaged heat fluxes for all simulations, in gyroBohm units. 135

Figures

Figure

1.1 Global energy use trends by year [1, 2]. 2

1.2 Relationship between the nuclear binding energy of an isotope and its atomic mass [7]. 5

1.3 (a) Cross-sections versus center-of-mass energy for key fusion reactions [8]. (b) Comparison of $\langle \sigma v \rangle$ versus temperature for common fusion reactions [6]. 6

1.4 Various experimental peak fusion triple products attained versus (a) ion temperature and (b) time in years. More information about experimental scenarios and specifics of the plotted data can be found in Ref. [10]. 10

1.5 Basic schematic of a tokamak. The plasma is indicated in purple with helical field lines in black wrapping around the device. The total field is a combination of toroidal (blue) and poloidal (green) components. Image courtesy of EUROfusion [21]. 12

1.6 Motion of a charged particle in: (a) a static, uniform magnetic field, (b) perpendicular electric and magnetic fields, and (c) a magnetic field with a spatial gradient ∇B [25]. 16

1.7 Diagram illustrating drift surfaces for passing and trapped particles. The tokamak central axis is on the left [6]. 19

1.8 (a) Cylindrical tokamak coordinates (R, Z, ϕ) or (r, θ, ϕ) used to describe tokamak flux surfaces with circular cross-sections [22]. (b) Sketch of tokamak cross-section given a divertor configuration [29]. 20

1.9 (a) Ballooning stability diagram for large aspect-ratio circular equilibrium. Stability in the darker shaded region requires Shafranov shifted surfaces. (b) Envelope of data points for various tokamaks indicating the validity of the Troyon limit. Both figures taken from Ref. [22]. 23

1.10 (a) Comparison of different Miller-parametrized flux surfaces. (b) Diagram of a sample "D"-shaped tokamak plasma [23]. 25

1.11 Typical (a) temperature and (b) safety factor profiles of different tokamak operational scenarios [22]. 29

2.1 (a) Motion of the electron drift wave due to the **E**x**B** motion from the wave [6]. (b) Depiction of a drift wave in toroidal geometry [23]. The rectangular outline corresponds to (a) if the density gradient were flipped. 40

2.2 Portion of drift wave contours showing phase-shifted density and electrostatic potential perturbations. A net radial flux results from **E**x**B**-drift convection around contours of constant potential [36]. 43

2.3 Depiction of guiding-center coordinates used in the gyrokinetic framework. 44

2.4 (a) Comparison of spatial and temporal scales for various waves and instabilities, including ITG, ETG, and TEM. (b) Summary of electrostatic microturbulence by poloidal wavenumber, with associated transport channels and stabilizing mechanisms. Both figures from Ref. [38]. 55

2.5 (a) Instability growth rates as a function of minor radius and k_y from linear GENE simulation results of JET discharge #70084 [84]. (b) ITG/TEM stability diagram [85]. (c) TEM/ETG stability diagram calculated from linear gyrokinetic GS2 simulations given $\nabla T_i = 0$ [86]. R/L_n and R/L_T are normalized equilibrium density and temperature gradients. 56

2.6 Standard depiction of the ETG instability mechanism at the outer side of the tokamak, inspired by Ref. [100]. The magnetic drift is the sum of grad-B and curvature contributions, and depends on the kinetic energy of the particle. This can lead to charge separation across a perturbation and a corresponding resonance and instability due to the resulting **ExB** motion. 59

2.7 Global GEM simulation results depicting TAE mode turbulence [156]. 70

3.1 Depiction of the background electron distribution function relaxing due to quasilinear diffusion in the case of the "bump-on-tail" instability [25]. 79

3.2 Profiles for DIII-D 162940 ELMy H-mode just prior to ELM onset. (**a**) Electron and main ion density profiles. (**b**) Impurity density profiles. (**c**) Electron temperature profile. (**d**) Main ion temperature profile. 86

3.3 (a) Growth rate and real frequency plots for radial locations $\rho = 0.80$, 0.85, and 0.90 from linear initial-value GENE simulations. (b) Comparison of linear frequencies and growth rates given by GENE and TGLF at $\rho = 0.85$. 88

3.4 The three saturation rules obtained from linear GENE results along with TGLF SAT1 in the GENE gyroBohm units described in the text. 89

3.5 Quasilinear fluxes from GENE and TGLF SAT1 versus $k_y\rho_i$ at $\rho = 0.85$ for the three saturation rules in GENE gyroBohm units. (**a**) Deuterium heat flux. (**b**) Electron heat flux. (**c**) Carbon heat flux. (**d**) Deuterium particle flux. (**e**) Electron particle flux. (**f**) Carbon particle flux. Fluxes are normalized such that the total ion heat flux matches SAT1. 90

3.6 Lapillonne QL flux model, NL from GENE, and GEM results versus $k_y\rho_i$ at $\rho = 0.85$ in GENE gyroBohm units. GEM fluxes scaled by 3.49. (a) Deuterium heat flux. (b) Electron heat flux. (c) Carbon heat flux. (d) Deuterium particle flux. (e) Electron particle flux. (f) Carbon particle flux. 91

3.7 (a) Global GEM ion heat flux versus time in GENE gyroBohm units at multiple radial locations. (b) GEM ion heat flux versus $k_y\rho_i$ and the corresponding smooth polynomial fit. 92

3.8 Comparison of equilibrium flux surfaces from $\rho = 0.10$ to 0.90 at intervals of 0.10 for DIII-D shot #162940. (a) Original magnetic equilibrium data. (b) Miller parametrization with positive triangularity. (c) Miller parametrization with negative triangularity. 93

3.9 Growth rates and real frequencies at radial locations $\rho = 0.80$, 0.85, and 0.90 from linear electrostatic GENE simulations with $\beta = 1e^{-4}$ and negative triangularity. . . . 94

3.10 Lapillonne QL flux model and NL flux-tube results from GENE in PT and NT at $\rho = 0.90$ in GENE gyroBohm units. (a) Deuterium heat flux. (b) Electron heat flux. (c) Carbon heat flux. (d) Deuterium particle flux. (e) Electron particle flux. (f) Carbon particle flux. 95

4.1 Initial ETG streamer potential from the nonlinear GENE simulations of Section 4.2.1 plotted in (a) real space and (b) Fourier space. Late-time electrostatic potential after evolution by HM Equation (4.2), plotted in (c) real space and (d) Fourier space. . . . 102

4.2 GENE linear simulation results showing growth rates and real mode frequencies for (a) CBC ITG benchmark case, (b) electron-scale ETG case, and (c) ion-scale ETG case showing CTEM modes as well. Positive (negative) frequencies indicate propagation in the ion(electron)-diamagnetic direction. 110

4.3 Original (small-box, no collisions) nonlinear simulation results showing (a) time-marked electrostatic electron heat flux and electrostatic potential contours for the (b) early nonlinear phase (green marker), and (c) late zonal phase (red marker). 112

4.4 Original (small-box, no collisions) nonlinear simulation results showing Fourier-space electrostatic potential contours for the (a) initial time (blue marker), (b) early nonlinear phase (green marker), and (c) late zonal phase (red marker). The markers correspond to the times marked in Figure 4.3(a). 112

4.5 Plots of collisionless single ETG mode evolution for (a) $k_y\rho_i = 6.36$ and (b) $k_y\rho_i = 30$ with respective growth rates $\gamma \approx 7.037$ and 7.015. The strongest four ZF modes in the late time are plotted for (c) the $k_y\rho_i = 6.36$ case, while (d) shows the excitation of a larger range of ZF modes in the $k_y\rho_i = 30$ case. 114

4.6 Plot of the sum of zonal potential amplitudes at final times, $\sum |\phi_z| = \sum_{k_x} |\phi_{k_x,0}|$, as driven by a single ETG mode. The fourth and seventh points correspond to the ETG modes from Figure 4.5. 115

4.7 Plot of total (a) ETG and (b) ZF mode potential as an integral over k_x in the collisional, Gaussian-k_x ETG case for $k_y\rho_i = 6.36$. Markers have been added to match the spectral snapshots of Figure 4.8. 116

4.8 Radial-spectrum snapshots of (a) the single ETG mode and (b) ZF as a function of tilting angle for the $k_y\rho_i = 6.36$ case. Snapshot times match the markers in Figure 4.7. 116

4.9 Plot in time of the average dimensionless radial wavenumber for the total ETG and ZF spectra in the quasi-saturated stage. 117

4.10 Ratio of total absolute amplitudes of ZF to ETG modes with varying collisionality. Results are taken at the final timestep. The reference value corresponds to the fourth point, $\gamma_z = 0.014$. 117

4.11 Full-spectrum collisional nonlinear simulation results showing (a) the electron heat flux time-evolution and (b) the time evolution of the four strongest final ZF modes. Data is averaged over z. 118

4.12 Time trace of full-spectrum ETG modes ranging from the longest mode to the most unstable mode. Data is averaged over z. 119

4.13 Comparison of quasilinear and nonlinear heat flux spectra for the $24\rho_i \times 3\rho_i$ full-spectrum electron-scale case. NL and QL stand for nonlinear and quasilinear respectively. 120

4.14 Convergence of the electrostatic electron heat flux for the various box size cases compared to the original $6\rho_i \times 3\rho_i$ case. 123

4.15 (a) ETG and (b) four strongest final ZF mode time traces for the $12\rho_i \times 6\rho_i$, large-y box size. All data is averaged over z. 123

5.1 (a) Outboard midplane potential showing ETG streamers present for run 2 from (b) comparison of multiscale to ion-scale ion heat fluxes from Ref. [218]. (c) Outboard midplane potential for highest shear flow run showing intermediate-scale ZFs present, and (d) comparison of multiscale to ion-scale ion heat fluxes from Ref. [61]. Note, Fig. (c) was originally Fig. 7(e) in Ref. [61]. 126

5.2 (a) Density and temperature profiles and (b) the respective normalized gradient profiles as functions of r/a defined by Equation (5.9) and Equation (5.10). (c) ITG and ETG growth rates from linear electrostatic GENE simulations at $r/a = 0.50$. 133

5.3 Comparison of electron heat fluxes at $r/a = 0.50$ for the many cases considered for convergence. The values of nx0, nz0, nv0, and nw0 are the number of x, z, $v_{\|}$ and μ gridpoints respectively and nky is the number of toroidal modes. All dimensions are in reference to those of Run #1, i.e. the case nx0/2 is the case used for multiple radial locations. The spurious drop in the red line is due to an issue continuing from a checkpoint file. 134

5.4 Flux spectra for GENE IS and ES flux-tube scenarios. (a) Electron heat flux and (b) electrostatic potential spectra as functions of k_y, averaged over k_x and z. (c) Electrostatic potential spectra as a function of k_x, averaged over k_y and z. Labels 'es' and 'em+$\gamma_{E'}$' correspond to electrostatic runs and electromagnetic runs with shear flow respectively. 137

5.5 Comparison of surface-averaged heat fluxes over time for local GENE ES and global GEM IS cases (Runs #1 and #5). The final times, $t_{\max}$, are $27.50R/c_s$ for the ES run and $147.85R/c_s$ for the IS run. 138

5.6 Mesoscale and z average of kinetic flux density taken from GENE ES run #1 at $r/a = 0.50$. 141

5.7 Comparison of the electron temperature perturbations generated by ITG (IS) and ETG (ES) turbulence in GEM. 142

5.8 Comparison of (a) electron heat flux evolution averaged over a toroidal annulus from $r/a = 0.35$ to 0.65 and (b) electron temperature profile flattening for three different GEM scenarios at $t = 129.75R/c_s$. 'GEM', 'SM', and 'SMx3' correspond to standard GEM, GEM with subgrid model, and GEM with enhanced (3x factor) subgrid model runs. The dashed red line corresponds to the initial electron temperature profile. . . 143

5.9 Kinetic flux density averaged in time over (a) the linear phase, $t/t_{\max} = 0.007 - 0.072$, and (b) the nonlinear saturated phase, $t/t_{\max} = 0.182 - 0.982$, of run #1 shown in Figure 5.5. (c) Quasilinear model of kinetic flux density using linear GENE simulations. All plots at $r/a = 0.50$. 144

5.10 (a) Comparison of quasilinear and nonlinear electron heat flux spectra at $r/a = 0.50$ averaged over k_x and z. (b) Comparison of three radial ETG heat flux models with increasing fidelity. 'QL' and 'NL' stand for quasilinear and nonlinear respectively. A red x corresponds to points assumed to go to zero for nonlinear simulations. 146

5.11 (a) Comparison of source terms when integrating GENE data directly in velocity-space and when integrating by interpolating over particles in GEM. (b) Electron flux profiles when $\hat{\Gamma}_{0,\mathrm{ETG}}$ is integrated assuming only radial changes in geometry $(B(r,z), J(r,z))$. 149

D.1 (a) Ballooning mode structure in the tokamak cross section given by the radial eigenmodes shown in (b). 192

D.2 Real value of the electrostatic potential plotted along the field line for the ballooning mode from Figure D.1(a). 193

Chapter 1

Introduction

This chapter introduces thermonuclear fusion as a potential energy source and provides an overview of the basic concepts and operation of a tokamak regarding its viability as a fusion power plant.

1.1 Energy Production

Global population and energy consumption levels have exploded in the last century with the advent of the industrial age. The majority of energy used today comes from fossil fuels such as coal, oil, and natural gas. These constitute non-renewable energy resources extracted from the remains of prehistoric plants and animals buried naturally in the Earth's crust over millions of years. Not only are these resources finite and expected to be quickly depleted at current usage rates, they also release significant amounts of carbon into the atmosphere which contribute to issues of climate change and air pollution. As a result, countries are more recently pivoting to renewable energy sources, such as wind, solar, geothermal, and hydroelectric power. While more environmentally friendly, renewable energy sources have their own limitations. Renewables are significantly less efficient and more intermittent than their counterparts, leading to the need for more robust energy storage technologies and improved grid integration measures for large-scale adoption. A comparison of various energy options and their current global use is shown in Figure 1.1.

A number of these issues can be circumvented by considering nuclear energy options as well. Two possibile avenues for nuclear power exist: fission, where nuclei are split into several parts, and fusion, where nuclei are fused together. Currently, only fission reactors have been developed as

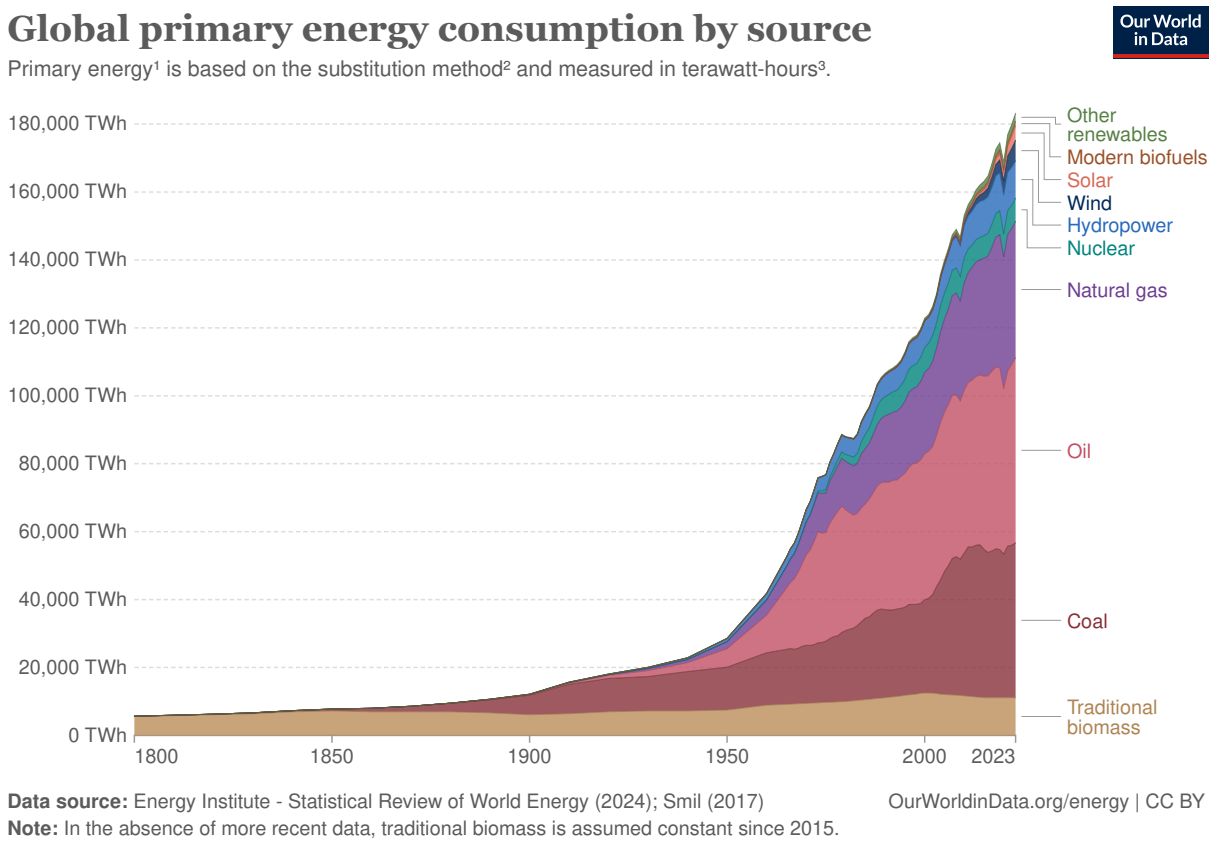

1.Primary energy: Primary energy is the energy available as resources – such as the fuels burnt in power plants – before it has been transformed. This relates to the coal before it has been burned, the uranium, or the barrels of oil. Primary energy includes energy that the end user needs, in the form of electricity, transport and heating, plus inefficiencies and energy that is lost when raw resources are transformed into a usable form. You can read more on the different ways of measuring energy in our article.

2.Substitution method: The 'substitution method' is used by researchers to correct primary energy consumption for efficiency losses experienced by fossil fuels. It tries to adjust non-fossil energy sources to the inputs that would be needed if it was generated from fossil fuels. It assumes that wind and solar electricity is as inefficient as coal or gas. To do this, energy generation from non-fossil sources are divided by a standard 'thermal efficiency factor' – typically around 0.4 Nuclear power is also adjusted despite it also experiencing thermal losses in a power plant. Since it's reported in terms of electricity output, we need to do this adjustment to calculate its equivalent input value. You can read more about this adjustment in our article.

3.Watt-hour: A watt-hour is the energy delivered by one watt of power for one hour. Since one watt is equivalent to one joule per second, a watt-hour is equivalent to 3600 joules of energy. Metric prefixes are used for multiples of the unit, usually: - kilowatt-hours (kWh), or a thousand watt-hours. - Megawatt-hours (MWh), or a million watt-hours. - Gigawatt-hours (GWh), or a billion watt-hours. - Terawatt-hours (TWh), or a trillion watt-hours.

Figure 1.1: Global energy use trends by year [1, 2].

successful and practical sources of energy production. Such fission power plants are the most reliable form of continuous energy, with a current capacity factor of around 93% in the United States [3]. The capacity factor indicates the percentage of total annual time during which nuclear plants are producing maximum power, and for fission plants is about double that of natural gas and coal, and even triple that of some renewable energy sources such as wind and solar. While fission reactions are not renewable, as they generally require uranium fuel to be extracted from the earth, the energy density of nuclear fuels is approximately one million times that of other traditional energy sources. For instance, the energy extractable from a single uranium pellet is equivalent to that of one ton of coal or 120 gallons of oil [4]. Fission reactors suffer significant drawbacks though. Namely, the generation and storage of hazardous nuclear waste with half-lives varying from 30 to millions of years, concerns about nuclear proliferation of fuels, and negative public perception due to production of harmful ionizing radiation, which has previously led to catastrophic environmental and human disasters in cases of extreme failure.

Fusion reactors, on the other hand, can potentially solve many of the challenges faced by current energy sources, thereby offering safe, clean, and abundant energy [5]. Compared to fission reactions, fusion reactions release approximately four times more energy per mass and produce no high-activity, long-lived nuclear waste. Current fusion reactors primarily use a 50/50 mixture of deuterium and tritium fuel. Deuterium can be abundantly extracted from all types of water, but tritium is not as readily available on Earth, though it might be bred artificially during the fusion reaction using naturally abundant lithium. Moreover, fusion power plants pose no catastrophic risk, as the conditions necessary for fusion are difficult to maintain; fuel must be continuously supplied in small amounts, and the reaction will stop if the plasma is sufficiently disturbed. Furthermore, by harnessing the same processes that power stars - which are among nature's most effective energy sources - achieving fusion on Earth comes with the possibility of fusion ignition, the generation of more energy than is necessary to sustain the reaction.

Altogether, these properties make fusion a "holy grail" of energy production capable of revolutionizing future energy consumption. However, fusion reactors must overcome the Coulomb

barrier so that ions are fused via the strong force. This requires creating extreme temperatures on the order of 100 million Kelvin, and sustaining such reactions on Earth presents significant challenges. Despite more than 50 years of active research, steady-state operation of a viable fusion power plant remains elusive though substantial progress has been made. Much of the current effort in the field is focused on addressing the numerous technical obstacles.

1.2 Thermonuclear Fusion

The discussion here introduces the basics of thermonuclear fusion and the concept of ignition - the point at which fusion reactions become self-sustaining - and largely follows from the introductory sections in Ref. [6]. The energy released in nuclear reactions is due to the difference in masses of the nuclei involved and their constituent particles. This energy is given by the famous formula

$$E = \Delta m c^2, \tag{1.1}$$

where E is the nuclear binding energy released, Δm is the total mass difference of the reaction, and c is the speed of light. The binding energy can be understood as the amount of energy required to separate an atomic nucleus into its constituent protons and neutrons. The average binding energy per nucleon is shown in Figure 1.2 below, where increasing binding energy per nucleon means the release of energy during the reaction. A maximum value is clearly seen near iron, which delineates a general transition point where fusion reactions no longer yield energy, but fission reactions become viable. As fusion is the viable reaction when elements are light, this means most of the isotopes involved are stable. The challenge with fusion though, is overcoming the electrostatic Coulomb repulsion to allow ions to fuse, whereas fission can be more easily forced due to the unstable nuclei involved and the often spontaneous nature of fission.

A 50/50 mixture of hydrogen isotopes, deuterium (D) and tritium (T), is primarily used as a

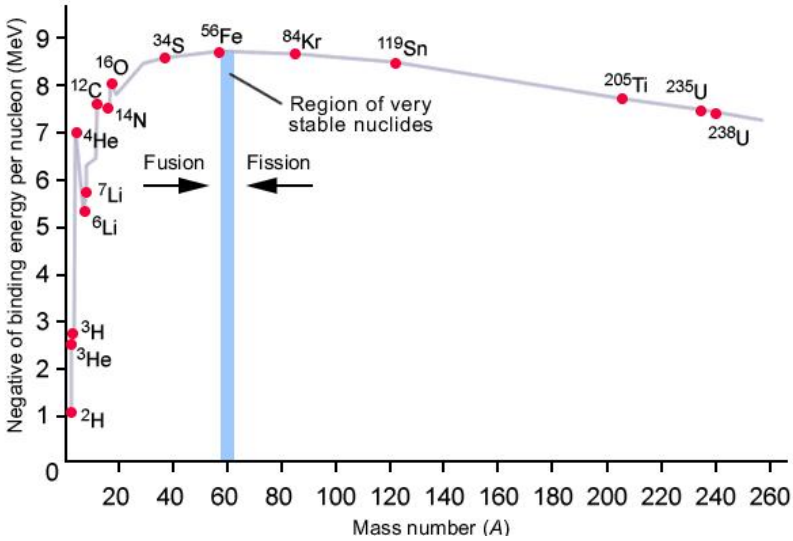

Figure 1.2: Relationship between the nuclear binding energy of an isotope and its atomic mass [7].

fuel in current fusion reactors. The D-T fusion reaction produces an alpha particle and a neutron

$$ {}_{1}^{2}\mathrm{D}^{+} + {}_{1}^{3}\mathrm{T}^{+} \rightarrow {}_{2}^{4}\mathrm{He}^{2+} + {}_{0}^{1}\mathrm{n}. \tag{1.2} $$

The numbers on the top left of each element represent the mass number of the element, $A = Z + N$, with N the number of neutrons and Z the number of protons, where Z is represented at the bottom left of each element. The total reaction energy is 17.6 MeV, with 4/5 of the energy, or 14.1 MeV, going to the kinetic energy of the neutron which is around 1/5 of the total mass. The remaining 3.5 MeV goes to the kinetic energy of He-4, otherwise known as an α-particle. This reaction is largely preferred due to the lower temperatures required to reach the peak collisional cross-section for collisions. Figure 1.3(a) shows a comparison of common fusion reaction cross-sections as a function of center-of-mass energy in keV, and clearly indicates D-T reactions to have the highest cross-section at the lowest energies, peaking near 60 keV.

Calculating the overall reaction rate per volume requires integration over velocity space of the

cross-section, σ, and distribution functions, f, of both species

$$\mathcal{R} = \int \int \sigma(v')v' f_1(v_1) f_2(v_2) d^3v_1 d^3v_2, \tag{1.3}$$

with $v' = v_1 - v_2$. The distribution function describes the phase-space density of particles. For a Maxwellian distribution - indicating thermal equilibrium - it is defined as

$$f_j(v_j) = n_j \left(\frac{m_j}{2\pi T_j} \right)^{3/2} e^{-\frac{m_j v_j^2}{2T_j}}, \tag{1.4}$$

for a species j with mass m_j, temperature T_j, density n_j, and velocity v_j. Assuming Maxwellian distributions, the total reaction rate per volume can be calculated as

$$\mathcal{R} = n_1 n_2 \langle \sigma v \rangle, \tag{1.5}$$

which is maximized when $n_1 = n_2$. The quantity $\langle \sigma v \rangle$ is plotted below in Figure 1.3(b) for three common fusion reactions, again showing the D-T reaction to be the most viable, in practice requiring temperatures of approximately 10 keV or around 10^8 K.

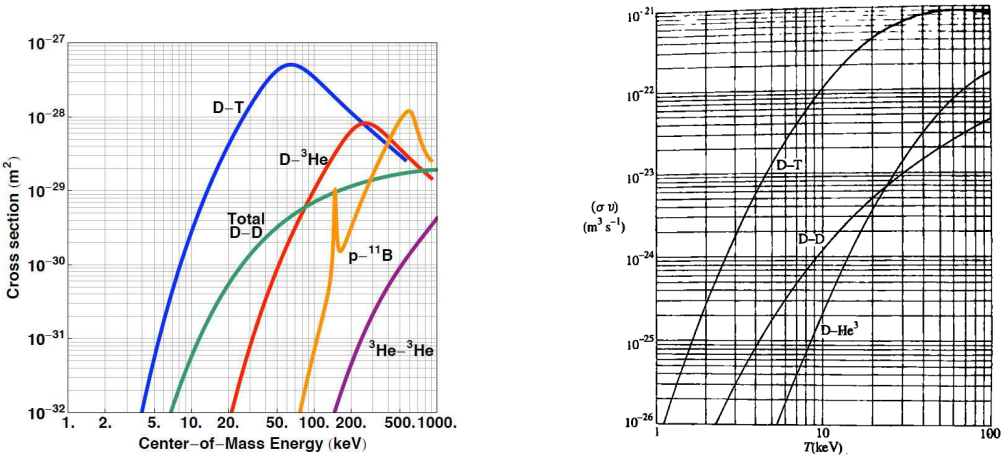

(a) (b)

Figure 1.3: (a) Cross-sections versus center-of-mass energy for key fusion reactions [8]. (b) Comparison of $\langle \sigma v \rangle$ versus temperature for common fusion reactions [6].

1.3 Fusion Ignition

Maintaining sufficient densities and temperatures for long enough times is critical for achieving a self-sustaining fusion reaction, a condition known as fusion "ignition". These constraints can be formally understood by considering power balance equations for a fusion plasma [6]. In a magnetically confined fusion reaction, the neutrons, being neutral, will not be confined to the magnetic fields and therefore will escape, hitting the walls of the device, where their energy can be captured and converted to more practical forms of energy. The α-particles however will remain in the core and their energy will go to heating the plasma. The total α-particle heating can then be found by integrating the reaction rate, (1.5), and the α-particle energy over the total volume V to find

$$P_\alpha = \int_V \frac{1}{4} n^2 \langle \sigma v \rangle \mathcal{E}_\alpha d^3x = \frac{1}{4} \overline{n^2 \langle \sigma v \rangle} \mathcal{E}_\alpha V, \tag{1.6}$$

where $\mathcal{E}_\alpha$ is the 3.5 MeV of energy carried by the α-particles which goes to heating the plasma via collisions. The bar here denotes a volume-averaged quantity.

In magnetic confinement fusion plasmas there exist strong equilibrium gradients which are necessary for fusion to occur in the core of a reactor. These gradients ultimately lead to continuous power losses, P_L, which must be balanced by external heating, P_H, as well as α-particle heating, P_α, in order to maintain the fustion reaction:

$$P_L = P_H + P_\alpha. \tag{1.7}$$

The total energy density of the plasma particles is $\frac{3}{2}nT$ given 3 degrees of freedom. Considering both electrons and ions, the total energy in the plasma, W, can be found by integrating the total energy density of all species over the volume V,

$$W = \int_V 3nT d^3x = 3\overline{nT}V. \tag{1.8}$$

The overall losses can then be characterized assuming some energy confinement time, τ_E, such that

$$P_L = \frac{W}{\tau_E}, \tag{1.9}$$

and (1.7) can be rewritten, assuming a constant density and temperature for simplicity, as

$$P_H + \frac{1}{4}n^2\langle\sigma v\rangle\mathcal{E}_\alpha V = \frac{3nT}{\tau_E}V. \tag{1.10}$$

Conditions for achieving ignition are then found by assuming no externally applied heating, that is $P_H = 0$, so that

$$n\tau_E > \frac{12T}{\langle\sigma v\rangle\mathcal{E}_\alpha}. \tag{1.11}$$

However, disruptive instabilities in the plasma generally limit the total thermal pressure, $p = nT$, that can be attained, and a better figure of merit requires mutiplying by an extra factor of temperature to get [6]

$$nT\tau_E > \frac{12T^2}{\langle\sigma v\rangle\mathcal{E}_\alpha}. \tag{1.12}$$

With the above assumptions of constant temperature and density throughout the plasma, $T^2/\langle\sigma v\rangle$ is minimized around $T = 14$ keV, where the reaction rate parameter is approximately $\langle\sigma v\rangle = 1.1 \times 10^{-24}T^2\mathrm{m}^3\mathrm{s}^{-1}$, with $T = 14$. Using $\mathcal{E}_\alpha = 3.5$ MeV gives the final ignition condition [6]

$$nT\tau_E > 3 \times 10^{21}\frac{\mathrm{keV}\cdot\mathrm{s}}{\mathrm{m}^3}. \tag{1.13}$$

This parameter, $nT\tau_E$, is famously known as the "fusion triple product", and (1.13) is similar to the Lawson criterion, originally derived as the Lawson parameter, $n\tau_E$, in the case of no external heating, but balancing the losses from Brehmstrallung radiation [9]. The triple product is one of the primary figures of merit for realizing viable fusion reactors, and can be understood in very simple physical terms. Sufficient temperature is required to reach a high probability for the reaction to occur, and the density then sets the total number of reactions which will occur. The time over which

this energy is lost in the system needs to be long enough in addition with the other two factors to reach a minimum threshold for maintaining a self-sustaining reaction. For instance, this condition can be satisified by the values $n = 10^{20}\mathrm{m}^{-3}$, $T = 10\mathrm{keV}$, and $\tau_E = 3\mathrm{s}$.

One more common figure of merit for a fusion reaction is Q, the energy gain factor,

$$Q = \frac{P_T}{P_H}, \tag{1.14}$$

or the ratio of total thermonuclear power to external heating power. Similary to the α-particle heating, the total fusion power can be calculated by considering (1.5), to find

$$P_T = \int_V \frac{1}{4} n^2 \langle \sigma v \rangle \mathcal{E} d^3x = \frac{1}{4} \overline{n^2 \langle \sigma v \rangle} \mathcal{E} V, \tag{1.15}$$

with $\mathcal{E}$ the total energy released in each reaction. The current state of fusion power plants is $Q < 1$ operation, with $Q = 1$ defining the "breakeven" point, while ignition would mean $P_H \to 0$ and so $Q \to \infty$.

The progress of fusion experiments in achieving both a satisfactory triple product and energy gain has been compiled together recently in Ref. [10]. The results are shown in Figure 1.4(a) as a function of ion temperature and in Figure 1.4(b) as records set for a given fusion concept over time. Likewise, contours of Q are provided to demonstrate progress towards the points of breakeven operation and ignition. Figure 1.4(b) illustrates that growth over time was approximately linear for tokamaks, indicative of a Moore's law type scaling characteristic of transistor number in integrated circuits, which suggests the eventual realization of fusion ignition. However, a gap exists when extrapolating to current tokamak reactors. This gap is partly due to limitations in technology, for instance in the case of SPARC which employs novel superconducting ribbon cables [11]. Additionally, the complexity involved in the design and realization of an international mega-project reactor contributes to the case of ITER [12]. Furthermore, currently active reactors play essential supporting roles in advancing understanding and capabilities for future burning plasma experiments. Some of

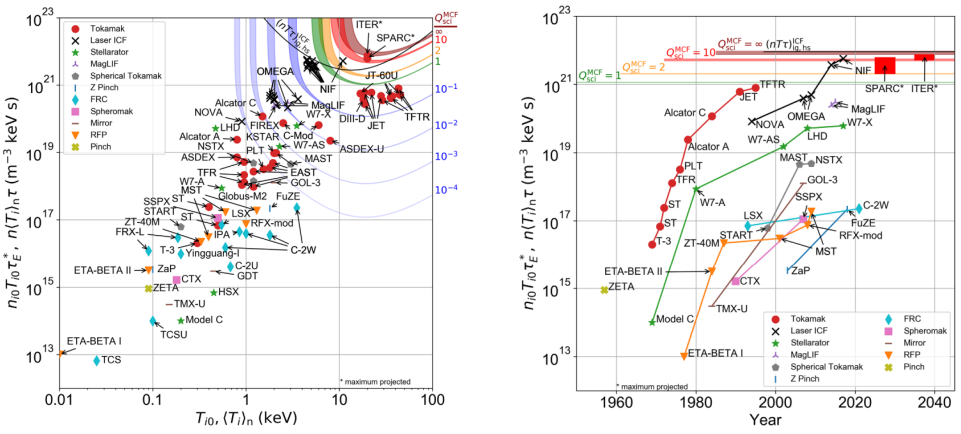

(a) (b)

Figure 1.4: Various experimental peak fusion triple products attained versus (a) ion temperature and (b) time in years. More information about experimental scenarios and specifics of the plotted data can be found in Ref. [10].

the relevant experimental campaigns are described further in Section 1.4.2.

The experiments considered span a range of different fusion reactor concepts. These can be simply categorized as follows:

(1) Magnetic Confinement Fusion (MCF): Magnetic fields are used to confine hot plasma particles long enough so that fusion can occur. This involves low densities and long confinement times.

- Linear Confinement: The plasma is confined along straight paths in a cylindrical geometry using straight open field lines or closed poloidal (around the linear axis) field lines. Examples include Z-pinch, mirror, and field-reversed configuration (FRC) devices.
- Toroidal Confinement: The plasma is contained in a toroidal (donut-shaped) vessel, with field lines winding around repeatedly. Examples include tokamaks, spherical tokamaks, spheromaks, and stellarators.

(2) Inertial Confinement Fusion (ICF): Fuel pellets are compressed to extremely high densities and rapidly heated by the use of strong lasers or particle beams, creating fusion reactions

over very short times. The National Ignition Facility (NIF) experiment is an example.

(3) Magneto-Intertial Fusion: A hybrid concept combining magnetic and inertial confinement methods, such as with the MagLIF experiment.

Clearly, tokamaks and laser ICF constitute the experiments capable of highest triple products and energy gains, with a recent NIF shot achieving breakeven gain [13]. However, as discussed further in Ref. [10], many other factors play a role in evaluating the approach to fusion [14]. Some extra factors include total yields, economics [15, 16], and government regulation [17]. For instance, laser ICF is generally inefficient for steady-state power generation due to its short pulsed operation, limited fuel and pulse repetition rates, and high energy cost to power the lasers. Furthermore, in the case of NIF, the primary goal is to simulate and study the conditions of nuclear detonations and nuclear weapons physics in a controlled manner in accordance with the National Nuclear Security Administration's (NNSA) Stockpile Stewardship Program [18].

Further analysis which considers the cost and efficiency of magnetic confinement systems can be attained by integrating the plasma beta factor, $\beta = 2\mu_0 p/B_0^2$, into the conventional triple product framework [19, 20]. The plasma beta factor is defined as the ratio of thermal to magnetic pressure and describes the effectiveness of the magnetic field in confining the plasma. This therefore represents another key performance metric which can be used to evaluate and optimize reactor stability, confinement, and efficacy. For many of the various reasons mentioned above, many private companies have chosen to focus on alternative approches of commercial fusion systems [10]. The technical hurdles facing steady-state operation of tokamak reactors are discussed in more detail in Section 1.4.2.

1.4 Magnetic Confinement and the Tokamak

The current leading candidate for fusion power plants is the tokamak. The tokamak was invented in the Soviet Union during the 1950s, and its name comes from the Russian words **to**roidalnaya **ka**mera s **ma**gnitnymi **k**atushkami, meaning "toroidal chamber with magnetic coils"

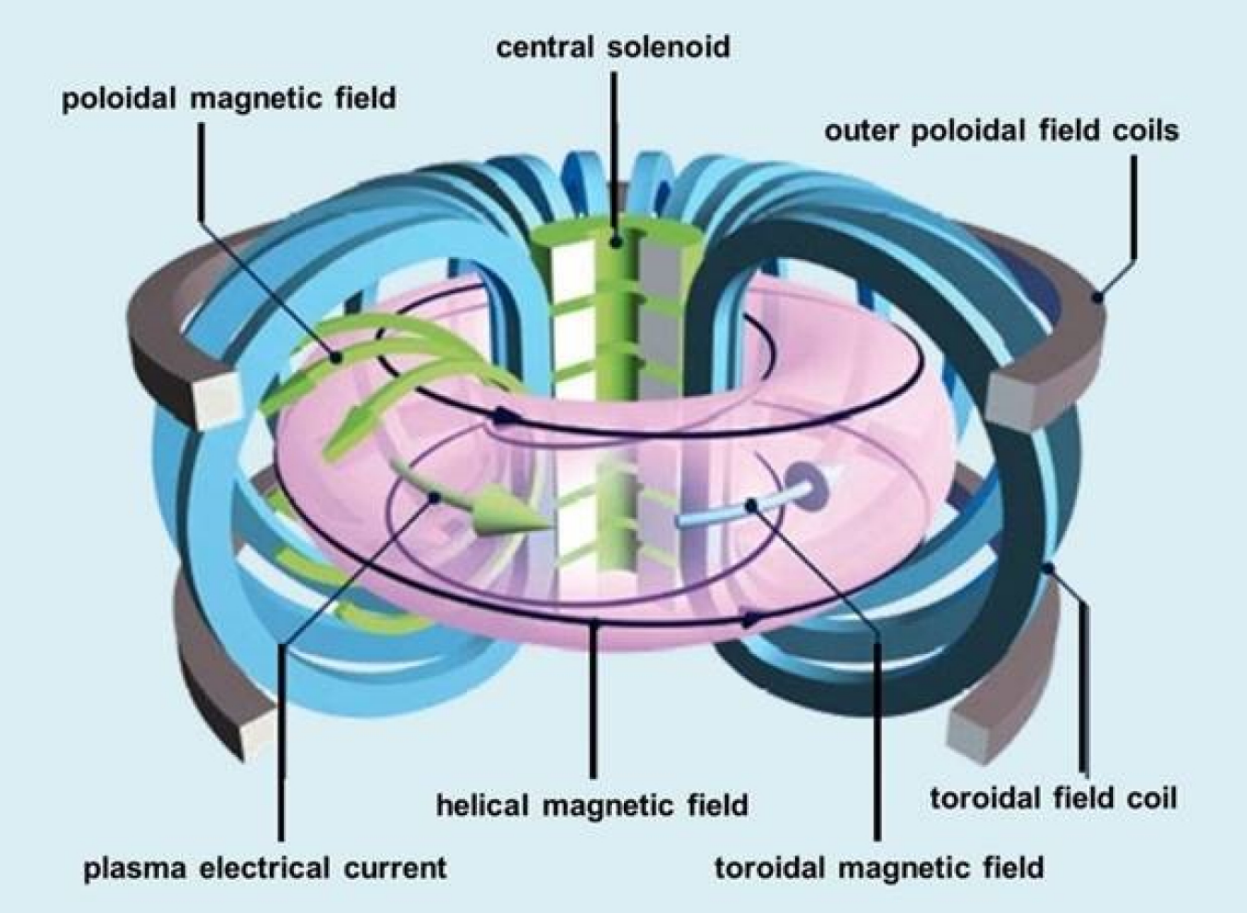

Figure 1.5: Basic schematic of a tokamak. The plasma is indicated in purple with helical field lines in black wrapping around the device. The total field is a combination of toroidal (blue) and poloidal (green) components. Image courtesy of EUROfusion [21].

[22]. Tokamaks are magnetic confinement devices designed to produce controlled fusion power. They consist of a toroidal vacuum chamber enveloped by electromagnetic coils which generate strong magnetic fields in the torus to confine a plasma consisting of hot, ionized particles along field lines. The purpose of the magnetic fields is to prevent diffusion of hot, dense particles radially outward such that core conditions required to sustain fusion reactions can be maintained. A general schematic for a tokamak is shown in Figure 1.5 above. The primary magnetic field is driven in the toroidal direction - around the central axis - by the toroidal field coils. Furthermore, a central solenoid and poloidal field coils are used to generate a smaller poloidal magnetic field. The poloidal direction is the shorter angular direction in the cross-section of the torus, and the poloidal fields help to shape

the plasma in the cross-sectional plane.

The overall field results in charged particles moving along helical trajectories through the torus. The central solenoid induces a toroidal electric field, driving a toroidal current and ohmically heating the plasma to a temperature of a few keV. As the plasma is heated charged particles move faster along field lines and spend less time interacting with each other. As a result, Coulomb collisions become less frequent with increasing temperature and the plasma resistivity varies as $\eta \sim T_e^{-3/2}$ [6]. To further heat the plasma one must inject energetic particle beams or electromagnetic waves in order to reach desired temperatures of ~ 10 keV as specified previously. Typically the magnetic fields reach values around 10 T, with the central current on the order of a few MA. As heating losses in standard coils are unacceptable, superconducting coils are in use today.

The motion of charged particles in electromagnetic fields is governed by the Lorentz force,

$$\mathbf{F}_L = q(\mathbf{E} + \mathbf{v} \times \mathbf{B}). \tag{1.16}$$

Here q is the charge of a particle, $\mathbf{v}$ is its velocity, and $\mathbf{E}$ and $\mathbf{B}$ represent the electric and magnetic fields in the tokamak. Particles are accelerated along field lines by the induced electric field, while their thermal velocity perpendicular to the field leads to tight orbits around magnetic field lines. The orbital radius is called the gyroradius and is defined as $\rho = mv_\perp/qB$ for a particle with mass m and velocity $v_\perp$ perpendicular to the field. The orbital frequency is called the cyclotron frequency, defined by $\Omega = qB/m$. The overall motion then inhibits radial diffusion and allows for maintaining the intense temperature gradients required for a successful fusion power plant - from approximately 10^8 K in the core where fusion must occur to $1,000$ K near the edge of the device so that the outer walls are not damaged. The following section outlines the fundamental plasma dynamics underlying confinement in tokamaks using material covered in many introductory plasma physics textbooks [23–26].

1.4.1 Plasma Confinement

Plasma is the most abundant state of observable matter in the universe, making up around 99% of the total in the form of stars as well as much of the space between them. Reference [23] defines a plasma as "a quasineutral gas of charged and neutral particles which exhibits collective behavior." Collective behavior refers to the fact that the motions of charged particles can lead to the generation of macroscopic electric and magnetic fields. These fields affect the motions of charged particles not just locally but at large distances, leading to complex and rich phenomena. Quasineutrality refers to the existence of Debye shielding, an effect which results in the effective shielding of any applied or localized potentials in the plasma. One can consider adding a negative test charge, Q, to a homogeneous plasma of density n_0 to find that the potential around the test charge will be

$$\Phi = \frac{Q}{4\pi\epsilon_0 r} e^{-r/\lambda_D} = \Phi_0 e^{-r/\lambda_D}. \tag{1.17}$$

Here, Φ_0 is the standard Coulomb potential, ϵ_0 the permittivity of free space, r the distance from the charged particle, and λ_D the Debye length which is defined as

$$\lambda_D^2 = \frac{\epsilon_0 T_e}{n_0 e^2}, \tag{1.18}$$

for electron temperature T_e and charge e.

The Debye length defines a characteristic length scale in plasmas over which external or local charge concentrations are effectively shielded out by the motion of ions and electrons which can respond to the potential. For a plasma with a system size L, if $\lambda_D/L \ll 1$ then the plasma can be considered quasineutral to leading order and described by a single background density. However, the plasma will generally not be neutral to all orders so that small-amplitude electromagnetic phenomena such as plasma waves can still exist, whereas macroscopic fields can be generated by collective plasma behavior. While analysis of plasma dynamics is often complex and requires self-consistent determination of particle and field interactions, the basics of tokamak confinement can be understood

conceptually by considering the motion of charged particles in electromagnetic fields.

The simplest dynamics possible are those of a charged particle in a uniform and static magnetic field. The equation of motion is given by

$$m\frac{d\mathbf{v}}{dt} = q(\mathbf{v}\times\mathbf{B}). \tag{1.19}$$

The right-hand-side has no component parallel to the field and so the velocity along the field is constant. The perpendicular part of Equation (1.19) can be decomposed into x and y components and solved to find

$$\begin{aligned} \dot{v}_x &= \frac{qB}{m}v_y, \quad \dot{v}_y = \frac{qB}{m}v_x; \\ \ddot{v}_x &= -\left(\frac{qB}{m}\right)^2 v_x, \quad \ddot{v}_y = -\left(\frac{qB}{m}\right)^2 v_y; \end{aligned} \tag{1.20}$$

which describe a simple harmonic oscillator with the cyclotron frequency. These equations can further be solved to find the particle motion

$$x - x_0 = \rho\sin(\Omega t), \quad y - y_0 = \pm\rho\cos(\Omega t), \tag{1.21}$$

which describe circular motion around a guiding-center (x_0, y_0) with fixed gyroradius $\rho = v_\perp/\Omega$ (also known as the Larmor radius). The result is helical motion along field lines as pictured in Figure 1.6(a). Parallel and perpendicular motion are defined specifically in relation to the magnetic field direction from hereon.

The next simplest configuration considers adding an electric field. Any electric field component parallel to the magnetic field simply accelerates particles in the parallel direction. The perpendicular equation of motion becomes

$$m\frac{d\mathbf{v}_\perp}{dt} = q(\mathbf{E}_\perp + \mathbf{v}_\perp\times\mathbf{B}). \tag{1.22}$$

To simplify the problem, one can consider transforming to a frame perpendicular to $\mathbf{B}$ moving with velocity $\mathbf{v}_E$ for which the fields are transformed as $\mathbf{B}' = \mathbf{B}$ and $\mathbf{E}'_\perp = \mathbf{E}_\perp + \mathbf{v}_E\times\mathbf{B}$. Choosing

$\mathbf{E}'_\perp = 0$ leads to the same equation of motion as Equation (1.19) but for $\mathbf{v}'_\perp = -\mathbf{v}_E + \mathbf{v}_\perp$:

$$m\frac{d\mathbf{v}'_\perp}{dt} = q(\mathbf{v}'_\perp \times \mathbf{B}). \tag{1.23}$$

Therefore, in the frame moving with velocity $\mathbf{v}_E$, the particle is again undergoing the same motion as for a static and uniform magnetic field.

The velocity $\mathbf{v}_E$ can be found by taking the cross product of $\mathbf{E}'_\perp = 0$ to find

$$\mathbf{E}_\perp \times \mathbf{B} + (\mathbf{v}_E \times \mathbf{B}) \times \mathbf{B} = 0 \Rightarrow \mathbf{E}_\perp \times \mathbf{B} - B^2\mathbf{v}_E = 0 \Rightarrow \mathbf{v}_E = \frac{\mathbf{E} \times \mathbf{B}}{B^2}. \tag{1.24}$$

This velocity is known as the **E**x**B** drift and is the same for all particles in the plasma. The basic physical mechanism is depicted in Figure 1.6(b), where the perpendicular acceleration (deceleration) of the particle due to the electric field leads to an increase (decrease) in the gyroradius and an overall drift of the guiding center. This effect can be generalized to any force, $\mathbf{F}$, perpendicular to the field as

$$\mathbf{v}_F = \frac{1}{q}\frac{\mathbf{F} \times \mathbf{B}}{B^2}. \tag{1.25}$$

By considering fields which vary in space and time many various drifts can be found. Detailed attention is given to the derivation and description of these drifts in the many introductory plasma

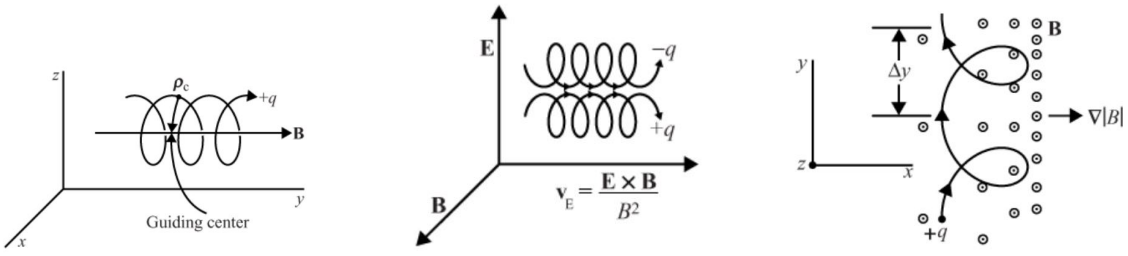

(a) (b) (c)

Figure 1.6: Motion of a charged particle in: (a) a static, uniform magnetic field, (b) perpendicular electric and magnetic fields, and (c) a magnetic field with a spatial gradient ∇B [25].

physics textbooks mentioned previously [23–26]. The various guiding-center drifts are listed here for convenience:

$$\textbf{ExB Drift:} \qquad \mathbf{v}_E = \frac{\mathbf{E}\times\mathbf{B}}{B^2}, \tag{1.26}$$

$$\text{Grad-B Drift:} \qquad \mathbf{v}_{\nabla B} = \pm\frac{v_\perp \rho}{2}\frac{\mathbf{B}\times\nabla B}{B^2}, \tag{1.27}$$

$$\text{Curvature Drift:} \qquad \mathbf{v}_c = \frac{m v_\parallel^2}{q}\frac{\mathbf{R}_c\times\mathbf{B}}{R_c^2 B^2}, \tag{1.28}$$

$$\text{Polarization Drift:} \qquad \mathbf{v}_p = \pm\frac{1}{\Omega B}\frac{d\mathbf{E}}{dt}, \tag{1.29}$$

$$\text{Nonuniform } \mathbf{E} \text{ Drift:} \qquad \mathbf{v}_{\nabla E} = \frac{\rho^2\nabla^2}{4}\frac{\mathbf{E}\times\mathbf{B}}{B^2} \tag{1.30}$$

One might notice there is no drift related to the magnetic field changing in time. Analysing this situation leads to the fact that the magnetic moment, $\mu = m v_\perp^2/(2B)$, is adiabatically invariant in a magnetic field which changes slowly compared to the cyclotron frequency. That is, as $\mathbf{B}$ changes, particles can lose or gain perpendicular energy and the gyroradius will also change. Given total energy conservation, the parallel velocity of a particle will change correspondingly as well. This is known as the magnetic mirror effect, where particles can be reflected when moving into a stronger magnetic field as all their parallel energy is converted to faster Larmor motion. The force associated with this motion is called the magnetic mirror force

$$\mathbf{F}_M = -\mu\nabla_\parallel B \tag{1.31}$$

and serves as the primary method of confinement in magnetic mirror devices.

A version of the magnetic mirror force, but perpendicular to the field, results in the "grad-B" drift defined by Equation (1.27) and depicted in Figure 1.6(c). The grad-B drift and the curvature drift, Equation (1.28), are important drifts in the context of tokamak confinement. This is because the tokamak field is primarily toroidal and the field strength generated by toroidal coils varies as $\nabla B \sim B/R_0$ according to Ampere's law of electromagnetism. R_0 here is the tokamak major radius,

the distance from the central axis, which is depicted later in Figure 1.8(a). The grad-B and curvature drifts arise from this inhomogeneity of the magnetic field. The force associated with the curvature drift is the centrifugal force from toroidal rotation, where $\mathbf{R}_c$ is the radius of curvature vector which is related to B by

$$-\frac{\mathbf{R}_c}{R_c^2} = \frac{\nabla B}{B}. \tag{1.32}$$

The grad-B and curvature drifts combine to drive vertical particle motion in the cross-sectional plane of the torus, and, most importantly, opposite charges drift in opposite directions. If only a toroidal field is considered this would lead to vertical charge displacement and loss of confinement due to the resulting radial **E**x**B** drift. For this reason the central solenoid and poloidal field coils are necessary for successful tokamak operation. The poloidal rotation driven in the cross-sectional plane cancels out these drift motions over one full poloidal orbit. The overall result is a shifted circular orbit in the cross-sectional plane, depicted for passing particles in Figure 1.7. The equation describing the shifted circular surface is [6]

$$(R - R_0 - \frac{v_d}{\omega})^2 + Z^2 = \text{constant}. \tag{1.33}$$

Here, R and Z are the major radius and elevation - the horizontal and vertical coordinates of the toroidal surface in the cross-sectional plane. R_0 is the initial center which is shifted by v_d/ω, where ω is the poloidal rotation frequency and v_d is the combined grad-B and curvature drift. Furthermore, particles with insufficient parallel velocity are reflected back by the mirror force when entering the high-field side of the tokamak. These are called trapped particles and the resulting "banana orbit" motion is depicted in Figure 1.7.

The resulting drift from a nonuniform electric field, Equation (1.30), is a correction to the standard **E**x**B** drift known as a finite-Larmor-radius (FLR) effect [23]. The primary significance of this correction is that the drift due to the electric field will no longer be independent of species as ρ is different for ions and electrons. Given a sinusoidal wave in the plasma, $\mathbf{E} \sim \mathbf{E}_0 e^{i\mathbf{k}\cdot\mathbf{x} - i\omega t}$, the ions and electrons can be driven apart, leading to a second electric field. If this second field enhances the first,

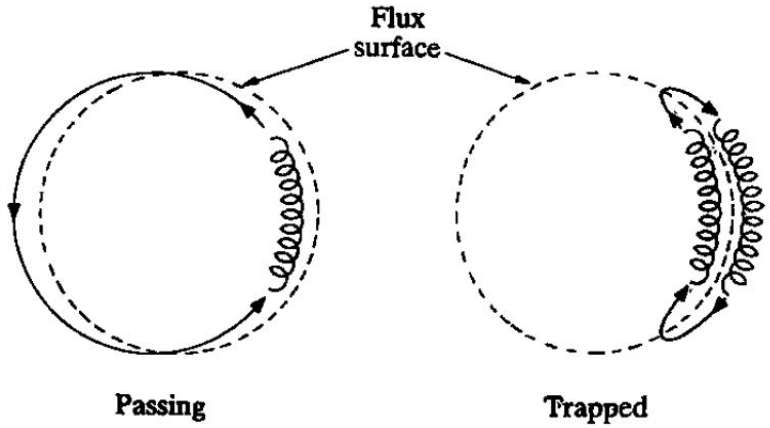

Figure 1.7: Diagram illustrating drift surfaces for passing and trapped particles. The tokamak central axis is on the left [6].

the wave can grow indefinitely and the plasma becomes unstable. Such instabilities are known as "drift instabilities" and are often the primary drivers of turbulent losses in the tokamak steady-state. Note that for the correction term to be important one must have $k\rho \sim 1$, meaning that instability wavelengths must be on the order of the species gyroradius driving the instability. For this reason drift instabilities belong to a more general class called "microinstabilities" [23]. The polarization drift can also result in instability due to the different inertial response of ions and electrons to an oscillating electric field. Drift instabilities drive radial turbulent transport of particles and heat out from the core of a tokamak, degrading plasma confinement. A detailed theoretical description of temperature-gradient-driven modes and discussion of the numerical simulation techniques employed to capture resulting turbulent transport losses are more thoroughly described in Chapter 2.

The physics and the mathematical equations governing tokamak equilibrium and stability have been extensively researched and are now comprehensively documented in many textbooks regarding the subject [6, 22, 27, 28]. Tokamak equilibria can be described by Maxwell's equations in combination with the ideal single-fluid magnetohydrodynamic (MHD) force-balance equation for a static magnetic field:

$$\nabla \cdot \mathbf{B}_0 = 0, \tag{1.34}$$

$$\nabla \times \mathbf{B}_0 = \mu_0 \mathbf{j}, \tag{1.35}$$

$$\mathbf{j} \times \mathbf{B}_0 = \nabla p. \tag{1.36}$$

Here $\mathbf{B}_0$ is the equilibrium magnetic field, $\mathbf{j}$ is the plasma current density, and μ_0 is the permeability of free space. For an axisymmetric equilibrium, that is, one independent of toroidal angle, the magnetic field lines wrap helically around nested toroidal surfaces of the tokamak. These toroidal surfaces then consist of constant magnetic flux and are called flux surfaces. Cylindrical coordinate systems, (R, Z, ϕ) or (r, θ, ϕ), can be used to describe the nested flux surfaces as depicted in Figure 1.8(a), where θ and ϕ are the poloidal and toroidal angles respectively. The radial coordinate r is the flux surface minor radius and extends to the tokamak minor radius a. Equation (1.36) describes magnetic field lines and current lines which lie on surfaces of constant pressure, meaning that density and temperature are constant on flux surfaces and only vary radially.

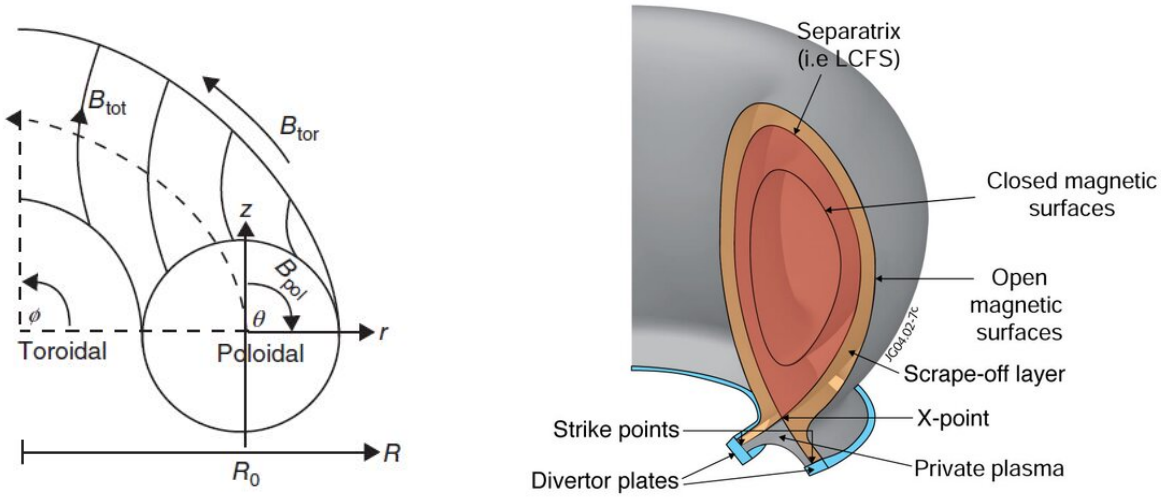

(a) (b)

Figure 1.8: (a) Cylindrical tokamak coordinates (R, Z, ϕ) or $(r,\ \theta,\ \phi)$ used to describe tokamak flux surfaces with circular cross-sections [22]. (b) Sketch of tokamak cross-section given a divertor configuration [29].

The helical divergence-free magnetic field is most often described by the equation

$$\mathbf{B}_0 = \mathbf{B}_\phi + \mathbf{B}_\theta = f(\psi)\nabla\phi + \nabla\phi \times \nabla\psi, \tag{1.37}$$

where $f(\psi) = RB_\phi = \mu_0 I_{\text{pol}}/2\pi$ is related to the poloidal current in the coils through Ampere's law, and ψ is the poloidal magnetic flux normalized by 2π

$$\psi(R, Z) = \int_0^R B_Z(R', Z)R'dR'. \tag{1.38}$$

From Equation (1.37) one can see that $\mathbf{B}_0 \cdot \nabla\psi = 0$, and so ψ can be used to uniquely label flux surfaces. The flux surface label can then be used as a generalized radial coordinate for nested toroidal surfaces of arbitrary shape. Flux surfaces range from $\psi = 0$ at the central magnetic axis to $\psi = 1$ at the separatrix, which defines the boundary between closed and open magnetic field lines. The open field line region is known as the scrape-off layer (SOL) and governs transport towards the vessel wall as well as divertors which manage the heat load. A basic depiction of the tokamak cross-sectional plane is shown in Figure 1.8(b). One can combine Equations (1.35), (1.36), and (1.37) to find [30]

$$\left[R\frac{\partial}{\partial R}(\frac{1}{R}\frac{\partial}{\partial R}) + \frac{\partial^2}{\partial Z^2}\right]\psi = -\mu_0 R^2 p'(\psi) - \mu_0^2 f f'. \tag{1.39}$$

Equation (1.39) is known as the Grad-Shafranov equation and can be used to solve for the magnetic equilibrium flux surfaces in the cross-sectional plane, $\psi(R, Z)$, given equilibrium pressure and current profiles in the plasma.

One key factor in tokamak plasma confinement is the safety factor $q(\psi)$. This parameter represents the ratio of toroidal to poloidal turns when following a field line around the torus for a given flux surface. The safety factor is defined as

$$q(\psi) = \frac{1}{2\pi}\oint_0^{2\pi} \frac{\mathbf{B}_0 \cdot \nabla\phi}{\mathbf{B}_0 \cdot \nabla\theta} = \frac{1}{2\pi}\oint_0^{2\pi} \frac{ds}{R}\frac{B_\phi}{B_\theta}, \tag{1.40}$$

where ds is an infinitesimal length along the field line. The normalized derivative of the safety factor, called the magnetic shear, is defined as

$$\hat{s} = \frac{r}{q}\frac{dq}{dr} \tag{1.41}$$

and describes the rate of change of field line bending. The safety factor is so-called because of the role it plays in the MHD stability of the plasma. Specifically, $q > 1$ is a rigorous limit required to stabilize kink modes, and in conventional tokamaks q generally varies from 1 in the core to 3-4 in the edge [22]. At rational or resonant surfaces, where $q = m/n$ for two integers m and n, field lines will close back on themselves. Such surfaces are more prone to instability. Resistive MHD theory demonstrates that resonant surfaces lead to magnetic reconnection and the formation of magnetic islands. These islands degrade magnetic confinement and can drive the formation of resistive tearing instabilities and sawtooth instabilities [22]. As the safety factor directly reflects the current profile in the plasma ($B_\theta = \mu_0 I(r)/2\pi r$), these instabilities largely fall into the category of current-driven instabilities. These modes are driven unstable by the parallel component of the current density, $\mathbf{j}_\parallel$.

As mentioned previously, another primary parameter which characterises tokamak stability is the plasma beta factor

$$\beta = \frac{2\mu_0 p}{B_0^2}, \tag{1.42}$$

which is the ratio of thermal to magnetic pressure in the plasma. Plasma beta measures the ability of the magnetic field to confine the plasma and for a tokamak often ranges from around 1-2%. The maximum achievable β is partly constrained by the fact that large thermal energy in the plasma can lead to magnetic field line distortion and poorer confinement. It is further constrained by technological factors as well, such as managing magnetic stresses from the plasma on the vessel walls and coils [6]. Instabilities which are driven unstable by the pressure gradient are known as pressure-driven instabilities. In toroidal geometry, mode stability can depend on whether the pressure gradient and curvature vector, $\kappa = \hat{\mathbf{b}} \cdot \nabla \hat{\mathbf{b}}$, are parallel or anti-parallel. This defines the high-field side of the tokamak as a "good" curvature region and the low-field side as a "bad" curvature region. Modes whose stability arise from this curvature dependence are known as interchange instabilities.

Ballooning mode instabilities are a related type of instability which are localized to resonant flux surfaces where they are driven most unstable. These modes stretch along field lines due to the fast parallel streaming of particles, which helps to quickly equilibrate perturbations along field lines. Because of this, ballooning modes extend from the inner "good" curvature region of the tokamak where they are stable to the outer "bad" curvature region where they are unstable and so "balloon" outward. Many of the drift wave microinstabilities discussed further in Chapter 2 are ballooning mode instabilities, primarily driven by density and temperature gradients in the plasma. In steady-state tokamak operation, these drift waves are usually responsible for the largest contributions to the loss of heat and particles from the core. Understanding these losses is crucial for predicting and maintaining steady-state energy production. While categorizing instabilities as current or pressure driven can be helpful, in principle most instabilities are often affected in some way by both factors. Ballooning modes, for instance, are stabilized by magnetic shear effects, and

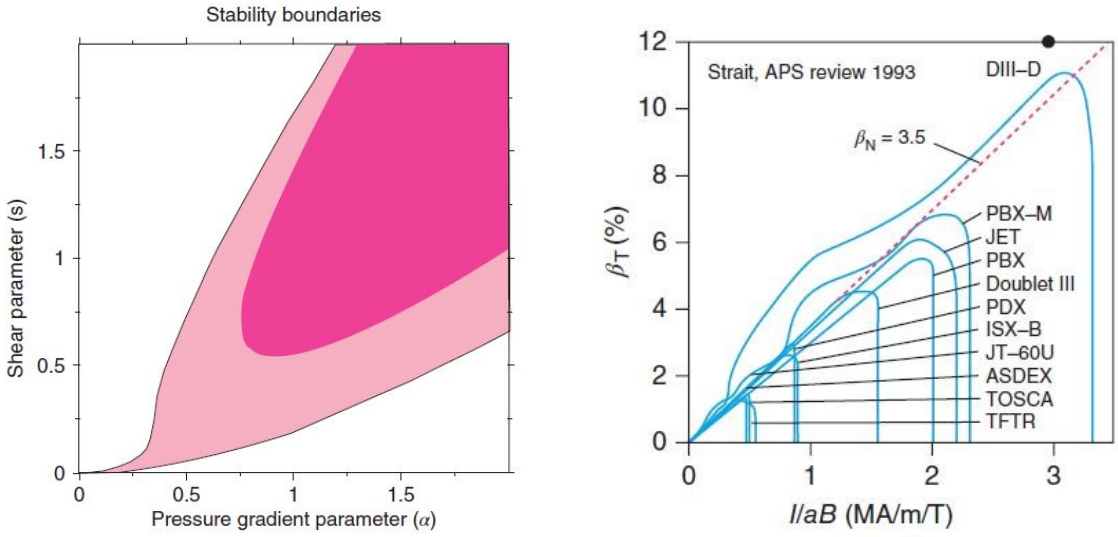

(a) (b)

Figure 1.9: (a) Ballooning stability diagram for large aspect-ratio circular equilibrium. Stability in the darker shaded region requires Shafranov shifted surfaces. (b) Envelope of data points for various tokamaks indicating the validity of the Troyon limit. Both figures taken from Ref. [22].

stability can be characterized by $\hat{s}$-α diagrams, where α is the normalized pressure gradient

$$\alpha = -\frac{2\mu_0 R_0}{B^2} q^2 \frac{dp}{dr}, \tag{1.43}$$

as shown in Figure 1.9(a). Furthermore, the Troyon limit [31]

$$\beta_{T,\max}[\%] = 2.8 \frac{I_{\text{pol}}}{aB} \tag{1.44}$$

provides a robust empirical upper bound for β based on stability considerations of both kink and ballooning mode instabilities. Curves indicating the validity of the Troyon limit for various tokamak experiments are shown in Figure 1.9(b).

Flux-surface shaping is an important method of controlling and stabilizing the plasma. Poloidal field coils are primarily responsible for controlling the shape and position of the plasma in the cross-sectional plane, and this shaping is essential for achieving favorable equilibrium configurations that help enhance MHD stability and reduce turbulent transport. One simple solution to Equation (1.39) is that of concentric circular flux surfaces in the large aspect-ratio limit, $\epsilon = r/R \ll 1$. The resulting equilibrium magnetic field is given by

$$\mathbf{B} = B_\theta \hat{\mathbf{e}}_\theta + B_\phi \hat{\mathbf{e}}_\phi \approx B_0 [\frac{\epsilon}{q} \hat{\mathbf{e}}_\theta + (1 - \epsilon \cos\theta) \hat{\mathbf{e}}_\phi], \tag{1.45}$$

$$B \equiv \sqrt{\boldsymbol{B} \cdot \boldsymbol{B}} = \sqrt{B_0^2 [(1 - \epsilon \cos\theta)^2 + (\frac{\epsilon}{q})^2]} = B_0 \sqrt{1 - 2\epsilon \cos\theta} \simeq B_0 (1 - \epsilon \cos\theta), \tag{1.46}$$

where $B_\phi = B_0 R_0 / R$ for $R = R_0 + r\cos\theta$ and $q = r B_\phi / R_0 B_\theta$. To lowest order the magnetic field is toroidal and, as mentioned previously, varies as $1/R$. The magnetic field direction and gradient operator can be calculated to lowest order as

$$\hat{\boldsymbol{b}} \equiv \frac{\boldsymbol{B}}{B} = \frac{\frac{\epsilon}{q} \hat{\boldsymbol{e}}_\theta + (1 - \epsilon \cos\theta) \hat{\boldsymbol{e}}_\phi}{1 - \epsilon \cos\theta} \simeq \frac{\epsilon}{q} (1 + \epsilon \cos\theta) \hat{\boldsymbol{e}}_\theta + \hat{\boldsymbol{e}}_\phi \simeq \frac{\epsilon}{q} \hat{\boldsymbol{e}}_\theta + \hat{\boldsymbol{e}}_\phi, \tag{1.47}$$

$$\nabla = \partial_r \hat{\boldsymbol{e}}_r + \frac{1}{r}\partial_\theta \hat{\boldsymbol{e}}_\theta + \frac{1}{R}\partial_\phi \hat{\boldsymbol{e}}_\phi = \partial_r \hat{\boldsymbol{e}}_r + \frac{1}{r}\partial_\theta \hat{\boldsymbol{e}}_\theta + \frac{1}{R_0 + r\cos\theta}\partial_\phi \hat{\boldsymbol{e}}_\phi \, . \tag{1.48}$$

The minor radius for flux surfaces of arbitrary shape is defined as

$$r = \frac{R_{\max} - R_{\min}}{2}, \tag{1.49}$$

though for modeling experimental scenarios the generalized toroidal coordinate is usually preferred

$$\rho_{\text{tor}} = \sqrt{\frac{\psi - \psi_{\min}}{\psi_{\max} - \psi_{\min}}}. \tag{1.50}$$

$R_{\min}$ and $R_{\max}$ are the minimum and maximum major radii of a flux surface, while $\psi_{\min}$ and $\psi_{\max}$ are the enclosed toroidal flux at the magnetic axis and the last closed flux surface respectively.

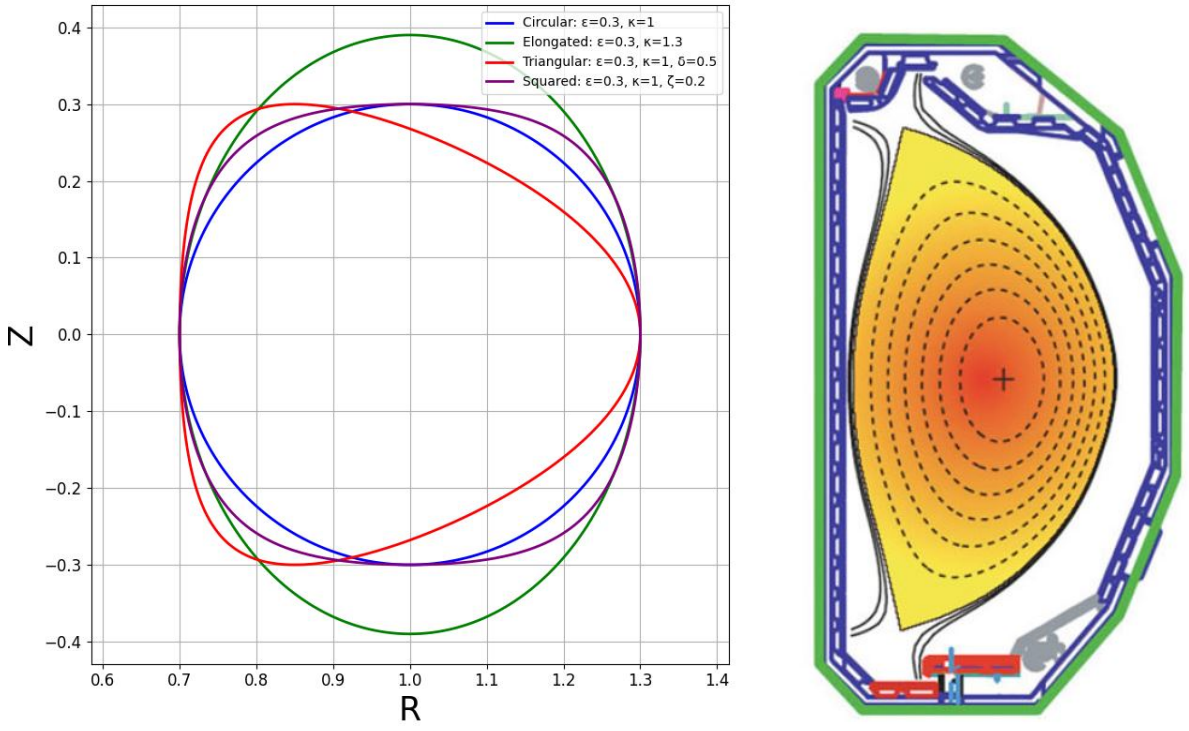

(a) (b)

Figure 1.10: (a) Comparison of different Miller-parametrized flux surfaces. (b) Diagram of a sample "D"-shaped tokamak plasma [23].

General flux surface shapes can be described by a simple analytic form using the Miller parametrization [32]

$$R = R_0 + r\cos(\theta + \sin^{-1}\delta\sin\theta), \tag{1.51}$$

$$Z = Z_0 + \kappa r\sin(\theta + \zeta\sin 2\theta). \tag{1.52}$$

R_0 and Z_0 are the central major radius and elevation respectively. The major radius, R_0, is often shifted outward by a factor $\Delta(r)$, known as the Shafranov shift, due to the hoop force. This occurs because pressure remains constant on a flux surface, while the larger surface area on the tokamak's outer side creates a pressure differential. Miller surfaces are parametrized using the elongation κ, triangularity δ, and squareness ζ. Surfaces with $\epsilon = r/R = 0.30$ and $R = 1.0$, with various Miller parameters individually varied, are shown in Figure 1.10(a). These surfaces illustrate how different Miller parameters can be combined to more accurately represent the now standard "D"-shaped configuration shown in Figure 1.10(b). Flux surfaces can further be parameterized by a Fourier mode decomposition, where amplitudes for the second, third, and fourth harmonics correspond directly to the elongation, triangularity, and squareness [33].

As evidenced by the triple product condition, Equation (1.13), achieving fusion ignition in a tokamak requires confining the plasma for sufficient time. The energy confinement time τ_E is defined as [6]

$$\tau_E = \frac{\int \frac{3}{2}n(T_i + T_e)d^3x}{P}, \tag{1.53}$$

where P is the total power input to the plasma. If MHD instabilities are stabilized, the plasma confinement time can still be largely affected by steady-state radial transport of particles and energy. Given the strong pressure gradients in the plasma, thermal conduction and convection are important limiting processes, though radiative losses such as Brehmstrallung radiation can often be significant as well. Ignoring the many instabilities present in the plasma, confinement of a tokamak plasma is largely determined by Coulomb collisions. Classical transport theory describes a standard random

walk diffusive process in cylindrical geometry. Diffusion across magnetic field lines occurs because of particle collisions and can be expressed as

$$D = \frac{\rho^2}{\tau_c}, \tag{1.54}$$

for a collision time τ_c and spatial step corresponding to the species gyroradius. In toroidal geometries this collision rate is enhanced due to the existence of magnetic drifts and trapped particle orbits. The theory of collisional transport in toroidal geometries is known as neoclassical theory. Neoclassical theory has been rigorously well-established and is covered in various references on the subject [34, 35].

In tokamak plasmas, experimentally measured transport rates often exceed those predicted by neoclassical theory. For core conditions, temperatures are usually high enough that collisional transport effects are negligible, though collisions become substantial closer to the edge. The extra, unexpected transport is referred to as anomalous and is now established to be due to nonlinear turbulent processes in the plasma [36–39], where microinstabilities are often driven by the free energy stored in the background density and temperature gradients. Understanding and explaining anomalous transport remains one of the primary challenges of theoretical tokamak physics, as multiple turbulence drives and suppression mechanisms exist which often occur at multiple scales simultaneously. In recent decades, substantial progress has been made, with strong alignment between theory, simulation, and experimental observations. Notably, modern supercomputing technology and the development of large-scale simulations have significantly advanced fundamental understanding of tokamak plasmas, enabling better interpretation of experimental results, while guiding the design and optimization of operational regimes [40].

The particle and heat fluxes, Γ and Q, induced by microinstabilities can be effectively described

using diffusive models which relate them to the underlying driving gradients

$$\begin{aligned} \Gamma &= -D\nabla n_0 \\ Q &= -n_0\chi\nabla T_0 \end{aligned} \tag{1.55}$$

at each flux surface. Here, D is the particle diffusivity and χ is the thermal diffusivity. The physical mechanisms governing turbulent transport losses are described further in Chapter 2. The overall result of radial transport is the relaxation of equilibrium gradients in the plasma, which degrades confinement and ultimately suppresses the drive of the instabilities. This process can be described by fluid transport equations at a single flux surface. Simple transport equations which describe the loss of particles and energy due to the respective fluxes are defined here as [34, 36]

$$\frac{\partial n}{\partial t} + \nabla \cdot \Gamma = 0, \tag{1.56}$$

$$\frac{\partial W}{\partial t} + \nabla \cdot Q = 0. \tag{1.57}$$

In general, fluxes can depend on both gradients as well as an additional inward convective pinch term which is non-diffusive. Turbulent diffusivity associated with macroscopic instabilities typically adheres to so-called Bohm scaling, $D_\perp \sim T/eB$, while transport from microinstabilities largely follows gyroBohm scaling, $D_\perp \sim (\rho/L_T)T/eB$, where L_T is the temperature gradient length scale [38]. Currently, tokamak transport modeling typically involves conducting separate neoclassical and turbulence simulations, with the latter focusing on individual instabilities. The results are then combined by simply superimposing flux contributions from each simulation.

1.4.2 Tokamak Operation

Keeping the plasma sufficiently separated from the vessel walls is a major concern for tokamak operation. Damaging of wall components can lead to impurities entering the plasma which dilute the fuel and significantly degrade confinement because of line radiation losses. The "D"-shaped

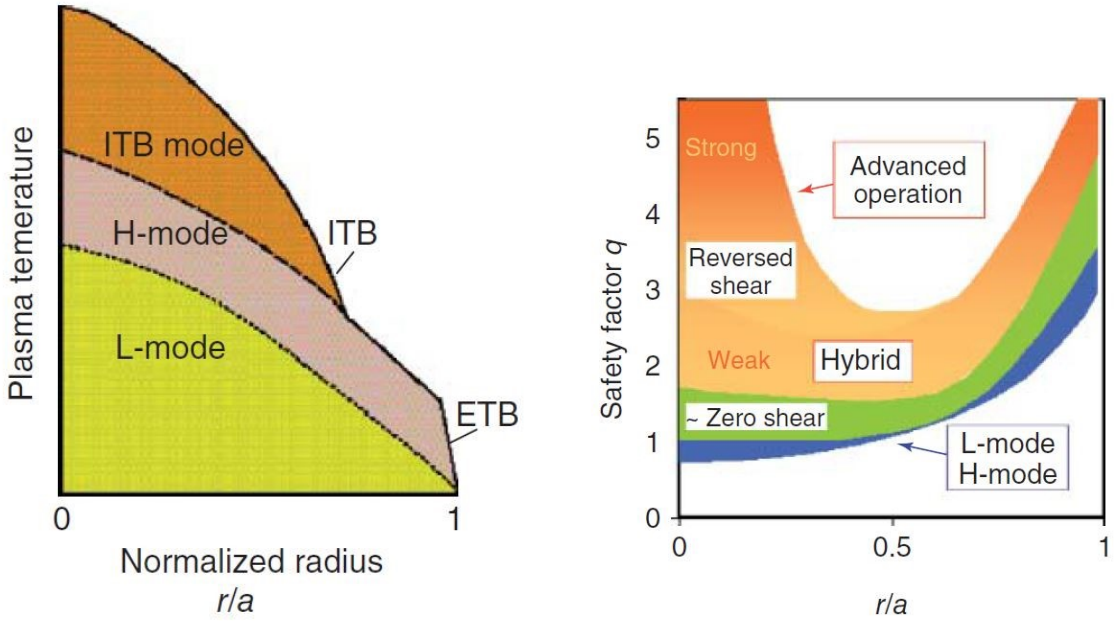

(a) (b)

Figure 1.11: Typical (a) temperature and (b) safety factor profiles of different tokamak operational scenarios [22].

plasma helps to alleviate this concern by channeling open field lines, and therefore radial transport losses, around the X-point towards the divertors, as shown in Figure 1.8(b). Transport losses in the plasma must be managed to ensure reasonable heat and particle loads on the divertors. Various techniques exist for mitigating divertor heat loads, such as using detached divertor configurations as well as utilizing gas puffing [41]. Recently, tungsten has become the material of choice for divertor components due to its exceptionally high melting point and low erosion rate. However, as a high-Z impurity, tungsten accumulation in the core becomes a major problem. Tungsten atoms will only be partially ionized even in extreme core temperatures, and they can cool the plasma due to line radiation and electron recombination effects.

As mentioned previously, external heating methods must be employed to reach necessary core plasma temperatures. These methods include neutral beam injection (NBI), ion cyclotron resonance heating (ICRH), and electron cyclotron resonance heating (ECRH) [6]. The combination

of a divertor configuration and sufficiently high auxiliary heating levels in the ASDEX-U tokamak led to the discovery of a mode of plasma operation with significantly longer confinement times [42]. This new mode of operation, known as H-mode (high confinement mode), contrasts with L-mode (low confinement mode) operation which was the standard at the time. The transition to H-mode operation is abrupt and associated with a strong reduction of turbulent transport in the plasma edge. This results in a narrow region of steep density and temperature gradients known as the pedestal, as illustrated by the edge transport barrier (ETB) in Figure 1.11(a). The precise reasons for the formation of the transport barrier remain unknown, but the suppression of turbulence is due to the generation of sheared rotational flows which break apart the turbulent eddies. While H-mode operation improves confinement, it also gives rise to edge localized modes (ELMs) [43]. ELMs are disruptive MHD instabilities that expel significant amounts of heat and particles from the plasma edge in large bursts. However, they can also be controlled and driven at faster rates and lower amplitudes to help flush out impurities from the core.

The use of a central solenoid in tokamaks necessitates pulsed operation, posing a challenge for long-term steady-state operation. Tokamaks cannot be run indefinitely because the current drive must be constantly varied over time, usually spanning the solenoid's maximum range. Pulsed operation is further constrained by thermal stresses imposed on the field coils which limit repetition rates. Conventional operational scenarios are largely ohmically heated and have monotonically increasing current profiles, as depicted in Figure 1.11(b) for L-mode and H-mode operation. Non-inductive current can be achieved through particle and electromagnetic wave injection; however, maximizing the fraction of bootstrap current, which arises naturally from pressure gradients of trapped particles in the plasma, is more common. Advanced tokamak scenarios focus on this, and are typically characterized by flat or reversed shear profiles in the inner core, as shown in Figure 1.11(b). Furthermore, stellarators are preferred for steady-state operation as they do not rely on the plasma current. While stellarator performance has not reached the same levels as tokamaks, they avoid the problems associated with pulsed operation and lessen the impact of current-driven instabilities.

Various other concerns exist which must be addressed for a viable fusion power plant, including

fusion energy capture, tritium breeding, and helium ash removal. Neutron energy capture is primarily achieved through breeding blankets and neutron multipliers, while neutron shields help to otherwise protect critical reactor components from harmful radiation [44]. In ITER, the blanket covers approximately 85% of the plasma surface area and plays a role in tritium production, heat removal, and structural protection [45]. Breeding blankets are vital due to the scarcity of tritium. They are typically made of lithium which reacts with neutrons to generate tritium through reactions such as ${}^{6}_{3}\mathrm{Li}^{3+} + {}^{1}_{0}\mathrm{n} \rightarrow {}^{3}_{1}\mathrm{T}^{+} + {}^{4}_{2}\mathrm{He}^{2+} + 4.8\mathrm{MeV}$ [6]. Additionally, using liquid lithium walls is a more contemporary approach, where lithium is circulated to facilitate electricity production and tritium extraction. Finally, dilution of the core plasma by alpha particles from the fusion reaction leads to degradation of confinement given long-pulse or steady-state operation. Impurity density control by way of ELMs can be sufficient in flushing out helium ash impurities within acceptable times [37].

Various tokamaks which currently operate have provided critical insights to help guide the design and operation of future burning plasmas such as ITER [46, 47]. DIII-D, which is known for its extensive diagnostic suite [48] and flexibility in plasma shaping, has led to successful negative triangularity campaigns which demonstrate improved confinement and stability [49, 50]. JET has played a pivotal role in carrying out tritium campaigns concurrently with the use of ITER-like wall materials such as beryllium and tungsten [51, 52]. EAST and KSTAR have pushed the boundaries of long-pulse operations, achieving record durations and temperatures while exploring advanced scenarios like fully non-inductive current drive [53, 54]. Research on the high-field, compact Alcator C-Mod tokamak has served as an essential stepping stone to the planned SPARC and ARC reactors, which leverage novel high-temperature superconducting ribbon cable technology to achieve significantly stronger magnetic fields, enabling compact designs and more efficient fusion performance [11, 55].

Finally, some contemporary updates in fusion research are discussed. Regarding computational advancements, the US Department of Energy launched the Exascale Computing Project, which aimed to take advantage of exascale supercomputing resources to provide high-fidelity modeling capabilities for scientific research purposes. In fusion research, this initiative facilitated whole device

modeling (WDM) efforts [56]. WDM seeks to encompass coupled simulations of distinct tokamak regions such as the core, edge and walls, as well as coupling of physical proccesses which exist at disparate spatial and temporal scales. Concurrently, the advent of machine learning and artificial intelligence has introduced novel numerical methodologies in fusion research. These techniques have been applied to enhance magnetic shaping and plasma control and predict the onset of instabilities, thereby offering proactive solutions for real-time disruption prevention [57, 58]. Privately funded fusion ventures have recently experienced significant growth as well, now approaching the scale of public government funding programs [59]. Although public and private sectors may have differing views on the most promising research areas, the increasing private investment reflects a broader recognition of fusion power plants as sufficiently developed to become commercially viable.

1.5 Thesis Overview

The focus of this thesis is to advance the understanding and prediction of turbulent transport in fusion devices through gyrokinetic simulations, with particular emphasis on the role of electron gyroradius scales. As described in Section 1.4, microinstabilities are responsible for anomalous transport levels well above the expectations of collisional transport theory. While gyrokinetic simulation methods have been extensively developed to accurately predict transport by ion-gyroradius-scale turbulence in experimental tokamak plasmas, electron thermal transport levels are often underestimated. Addressing this excess anomalous electron heat loss remains an unsolved problem in tokamak physics and an area of active research. The electron-temperature-gradient (ETG) instability is a leading candidate to explain these excess electron heat losses. Additionally, electron-scale turbulence can affect ion-scale turbulence in reactor-relevant plasmas, as demonstrated recently in local multiscale gyrokinetic simulations [60, 61]. Multiscale simulations require resolving electron gyroradius scales, and so domain sizes become limited. Consequently, the development of reduced models - such as quasilinear models - of electron-scale turbulence is particularly valuable for global ion-scale simulations in future whole device modeling efforts.

Initial gyrokinetic simulations of ETG turbulence reported the existence of radially-extended

"streamers" [62, 63]. These eddies have long radial correlation lengths and drive significant radial **E**x**B** heat transport, exceeding electron gyroBohm estimates. The early ETG simulations showed weak regulation of long-wavelength ETG turbulence in accordance with fluid theories which predict inverse cascades to longer wavelengths and Kelvin-Helmholtz type shearing that more strongly regulates shorter wavelength modes. However, the transition to longer wavelengths raises the question of whether fluid theories of ETG mode regulation are sufficient. A more recent gyrokinetic theory of ETG modes at intermediate scales, between that of ion and electron gyroradii, predicts more significant generation of "zonal" shear flows, which may help to further regulate ETG transport levels over longer simulation times [64]. In multiscale simulations, streamer-dominated electron-scale turbulence has been seen to increase ion-scale turbulent transport levels [60, 61], while intermediate-scale zonal flows can also emerge to help regulate ion-scale turbulence [61].

The primary aim of this thesis is to validate the theory of intermediate-scale zonal flow generation by ETG modes and to explore whether reduced models can be used to capture the cross-scale effects of ETG turbulence on ion scales. The remainder of this thesis is outlined as follows: Chapter 2 introduces the gyrokinetic framework and common instabilities responsible for turbulent transport, such as the ion-temperature-gradient (ITG) and ETG modes. Two gyrokinetic codes, GENE and GEM, which are used extensively in this work to study ETG turbulence, are described therein. Chapter 3 introduces heuristic quasilinear models for turbulent flux spectra and compares their predictive capabilities in estimating ion-scale transport levels for DIII-D shot #162940. Quasilinear modeling of ETG turbulence is further considered in chapters Chapter 4 and Chapter 5. Chapter 4 introduces the various models of ETG mode regulation and validates the intermediate-scale theory of zonal flow generation using GENE gyrokinetic simulations. Finally, Chapter 5 considers averaging ETG turbulence effects from local GENE simulations over intermediate scales to include in global ion-scale GEM simulations. Appendices A to E include various derivations that complement the main body of work, and the interested reader is encouraged to refer to them for more detail.

Chapter 2

Turbulent Transport

This chapter introduces the basics of plasma theory and drift wave microturbulence, and derives the gyrokinetic equations used to model turbulent tokamak transport effectively. Key instabilities relevant to turbulent transport are discussed here, and the primary gyrokinetic codes, GENE and GEM, employed to study the ETG instability in this thesis are described.

Tokamak confinement, as considered in Chapter 1, can theoretically achieve the necessary confinement times required for a sustainable fusion reactor when considering only neoclassical transport of particles and heat across magnetic field lines. However, experimental observations from tokamaks reveal anomalously high radial losses that significantly reduce confinement times. It is now widely recognized that low-frequency drift wave microturbulence is primarily responsible for these anomalous losses. The spatial and temporal characteristics of these instabilities allow for gyrokinetic models tailored to capturing drift wave dynamics and transport. An overview of theoretical plasma models is given here along with a description of the basic drift wave mechanism. The gyrokinetic framework is then explained and derived, followed by discussion of common microturbulence instabilities in tokamaks. Gyrokinetic simulation methods and codes used to study turbulent transport in this thesis are discussed in the last section.

2.1 Plasma Theory

In principle, a plasma can be modeled by tracking particle motion under the Lorentz force, with self-consistent coupling to electromagnetic fields via Maxwell's equations. This would require

solving for the trajectories of every particle in the plasma, where $n \sim 10^{20}\mathrm{m}^{-3}$ in a tokamak, which is completely intractable for any practical purpose. Instead, fluid or kinetic models are employed in practice. The theoretical description of these models is the subject of many introductory textbooks on plasma physics [23–26]. Kinetic models are more fundamental and describe the plasma statistically using the distribution function $f_j(\mathbf{x}, \mathbf{v}, t)$, with j the particle index. The distribution function represents the 6-D phase-space density of particles and depends on position, velocity, and time. The probability to find a particle of species j at position $\mathbf{x}$ with velocity $\mathbf{v}$ at time t is

$$f_j(\mathbf{x}, \mathbf{v}, t) d^3x d^3v. \tag{2.1}$$

Evolution of the distribution function in time is governed by Hamiltonian dynamics and can be described by the Boltzmann equation

$$\frac{df_j(\mathbf{x}, \mathbf{v}, t)}{dt} = \partial_t f_j + \frac{d\mathbf{x}}{dt} \cdot \frac{\partial f_j}{\partial \mathbf{x}} + \frac{d\mathbf{v}}{dt} \cdot \frac{\partial f_j}{\partial \mathbf{v}} = \left[\partial_t + \mathbf{v} \cdot \frac{\partial}{\partial \mathbf{x}} + \frac{\mathbf{F}_L}{m} \cdot \frac{\partial}{\partial \mathbf{v}} \right] f_j(\mathbf{x}, \mathbf{v}, t) = C_j[f_j] + S_j. \tag{2.2}$$

$\mathbf{F}_L$ is the Lorentz force, Equation (1.16), which depends on the electric and magnetic fields, and C_j represents a collision operator. S_j is an arbitrary source term which contains all unnaccounted for physical processes - atomic physics, fusion reactions, brehmstrallung radiation, and heating and current drive [65]. The Boltzmann equation describes local changes in the distribution function over time which are due to advection of gradients of the distribution function in real space and in velocity space, as well as changes due to collisions and sources. In general, the core plasma temperature is high enough that the collision frequency is very small compared to the frequency of drift waves in the plasma. For this reason, the effect of collisions will often be ignoreed from this point on. Equation (2.2) without collisions and sources is known as the Vlasov equation, for which the total time derivative describes motion along constant trajectories in phase-space.

A self-consistent description of the plasma requires coupling the Vlasov equation to Maxwell's

equations of electrodynamics

$$\nabla \cdot \mathbf{E} = \rho_e/\epsilon_0, \tag{2.3}$$

$$\nabla \cdot \mathbf{B} = 0, \tag{2.4}$$

$$\nabla \times \mathbf{E} = -\frac{\partial \mathbf{B}}{\partial t} \tag{2.5}$$

$$\nabla \times \mathbf{B} = \mu_0 \mathbf{j} + \mu_0 \epsilon_0 \frac{\partial \mathbf{E}}{\partial t}. \tag{2.6}$$

The charge density, ρ_e, and current density, $\mathbf{j}$, are calculated from moments of the distribution function as

$$\rho_e = \sum_j q_j n_j = \sum_j q_j \int f_j d^3v, \tag{2.7}$$

$$\mathbf{j} = \sum_j q_j n_j \mathbf{u}_j = \sum_j q_j \int \mathbf{v} f_j d^3v. \tag{2.8}$$

These can then be used to calculate the electric and magnetic fields which evolve the distribution function per the Vlasov or Boltzmann equations.

Kinetic models can further be simplified by averaging over velocity space to obtain fluid equations for hydrodynamic quantities such as density, bulk velocity, energy, and temperature. Different quantities are calculated by taking different moments of f_j in velocity space, where the kth moment is given by [22]

$$\int \mathbf{v}^k f_j d^3v = n_j \langle \mathbf{v}^k \rangle. \tag{2.9}$$

Some of the most common values are [25]

$$n_j = \int f_j d^3v, \tag{2.10}$$

$$\mathbf{u}_j = \frac{1}{n_j} \int \mathbf{v} f_j d^3v, \tag{2.11}$$

$$W_j = \frac{3}{2} p_j = \int \frac{1}{2} m_j v^2 f_j d^3v, \tag{2.12}$$

where $\mathbf{u}_j$ is the bulk velocity, W_j is the species kinetic energy, and an isotropic ideal gas law has been assumed for the pressure ($p = nT$). Moments of the Vlasov equation can be taken to get dynamical fluid equations, for instance zeroth and first moments reuslt in the continuity and momentum equations:

$$\frac{\partial n_j}{\partial t} + \nabla \cdot (n_j \mathbf{u}_j) = 0, \tag{2.13}$$

$$m_j n_j \left[\frac{\partial \mathbf{u}_j}{\partial t} + (\mathbf{u}_j \cdot \nabla)\mathbf{u}_j \right] = n_j q_j (\mathbf{E} + \mathbf{u}_j \times \mathbf{B}) - \nabla p_j. \tag{2.14}$$

However, this approach introduces a closure problem: each moment equation depends on the next higher-order moment. Closing the equations is often done by relying on some standard assumption of thermodynamics such as the adiabatic equation of state,

$$\frac{d}{dt}(P_j/n_j^\gamma) = 0, \tag{2.15}$$

for an ideal gas, where $\gamma = (f+2)/f$ is related to the internal degrees of freedom. Another option is closing the third moment, the change in time of the heat flux, with a thermal conduction equation.

In these cases, closure often assumes that the plasma is in local thermal equilibrium and close to a Maxwellian distribution. This in turn relies on high collision rates and short mean free paths, and so validity depends on timescales being significantly longer than collisional timescales, $\tau_{\text{coll}}/\tau \ll 1$. While this condition holds for motion perpendicular to the magnetic field, where particles undergo tight gyromotion and frequent collisions, it breaks down along magnetic field lines in tokamaks, where mean free paths can extend to kilometers. A kinetic description which retains the velocity-space distribution of particles is necessary to accurately capture parallel dynamics. Accounting for this anisotropy can also lead to fluid properties like pressure and temperature being distinguished into parallel and perpendicular components in tokamaks. Furthermore, fluid models lose critical information about wave-particle interactions that depend on velocity-space resonances, leading to the omission of various stabilizing or destabilizing effects on waves. Similarly, the dependence of gyroradii on particle thermal velocity limits fluid models in capturing various drift motions. For

instance, while a two-fluid model can adequately describe simple phenomena like the electron drift wave by separating electron and ion dynamics, more complex drift wave mechanisms often demand a kinetic treatment.

A further single-fluid approximation can be derived by assuming a center-of-mass representation given the small electron-to-ion mass ratio. As outlined in Chapter 1, single-fluid MHD models of tokamak plasmas are useful for describing the plasma equilibrium and various global instabilities or disruptions. However, these models have inherent limitations and are unable to account for the physics of microinstabilities or the steady-state losses they drive [22]. Single-fluid MHD theory requires a continuum fluid description, treating the plasma as a collection of infinitesimally small, indistinguishable particles. This framework therefore neglects the differing gyroradii of distinct particles and loses FLR effects. Consequently, single-fluid MHD theory is only valid on spatial scales L where $\rho/L \ll 1$, and it fails to describe drift phenomena such as drift wave instabilities which can involve distinct ion and electron drift motions. In the limit of infinite conductivity, one finds the ideal MHD equations which are described by charge conservation, current conservation, ideal Ohm's law,

$$\mathbf{E} + \mathbf{v} \times \mathbf{B} = 0, \tag{2.16}$$

and the momentum equation

$$\rho_m \left(\frac{\partial \mathbf{v}}{\partial t} + \mathbf{v} \cdot \nabla \mathbf{v} \right) = -\nabla p + \mathbf{j} \times \mathbf{B}, \tag{2.17}$$

where ρ_m and $\mathbf{v} \approx \mathbf{u}_i$ are the center-of-mass mass density and fluid velocity respectively.

The system of equations governing any of the models described above can be linearized and solved to find wave dispersion relations, $\omega(\mathbf{k})$, for wave frequency ω and wavenumber $\mathbf{k}$. The eigenvalues of the system give the real and complex frequencies for different types of waves that can be excited. The subject of waves in plasmas is inherently complex as plasma dynamics span a wide range of spatial and temporal scales and involve the self-consistent interaction of charged particles with the intrinsic electric and magnetic fields. This complexity gives rise to a large array of waves

and instabilities in the plasma, which are discussed in detail in Ref. [66]. Plasma waves are often divided into two categories - electrostatic and electromagnetic waves. Electrostatic waves only have an electric field component and are longitudinal in nature, while electromagnetic waves are made up of both electric and magnetic field fluctuations which oscillate transverse to the direction of wave propagation, but can also have some longitudinal component.

2.2 Electron Drift Waves

To gain insight into the primary drift waves responsible for turbulent transport in tokamaks, it is instructive to examine the basic mechanism of the electron drift wave [6, 23]. This is most easily done by ignoring toroidal effects and considering a plasma with a uniform magnetic field and no magnetic shear, known as a "slab" geometry. The drift wave scenario is illustrated in Figure 2.1(a) with a small-amplitude ion density wave in the $\hat{\mathbf{y}}$ and $\hat{\mathbf{z}}$ directions,

$$\delta n_i(\mathbf{x}, t) = \delta n_i e^{ik_y y + ik_z z - i\omega t}, \tag{2.18}$$

where $\delta n_i / n_0 \ll 1$. A density gradient exists in $\hat{\mathbf{x}}$ and the magnetic field is into the plane in the $\hat{\mathbf{z}}$ direction. Fourier analysis is possible in y and z, but not in x because of the spatial gradient in the plasma. Due to their low mass, electrons move rapidly along field lines compared to the ion wave motion and respond to the fluctuating pressure, forming an electric field. A parallel force balance is established by the electrons, described by the steady-state momentum fluid equation,

$$n_e e \nabla_\parallel \delta\phi = \nabla_\parallel p_e, \tag{2.19}$$

where e is the magnitude of the electron charge, and $\delta\phi$ is the perturbed electrostatic potential. Linearizing 2.19 and solving for δn_e gives

$$\frac{\delta n_e}{n_{0e}} = \frac{e\delta\phi}{T_e}. \tag{2.20}$$

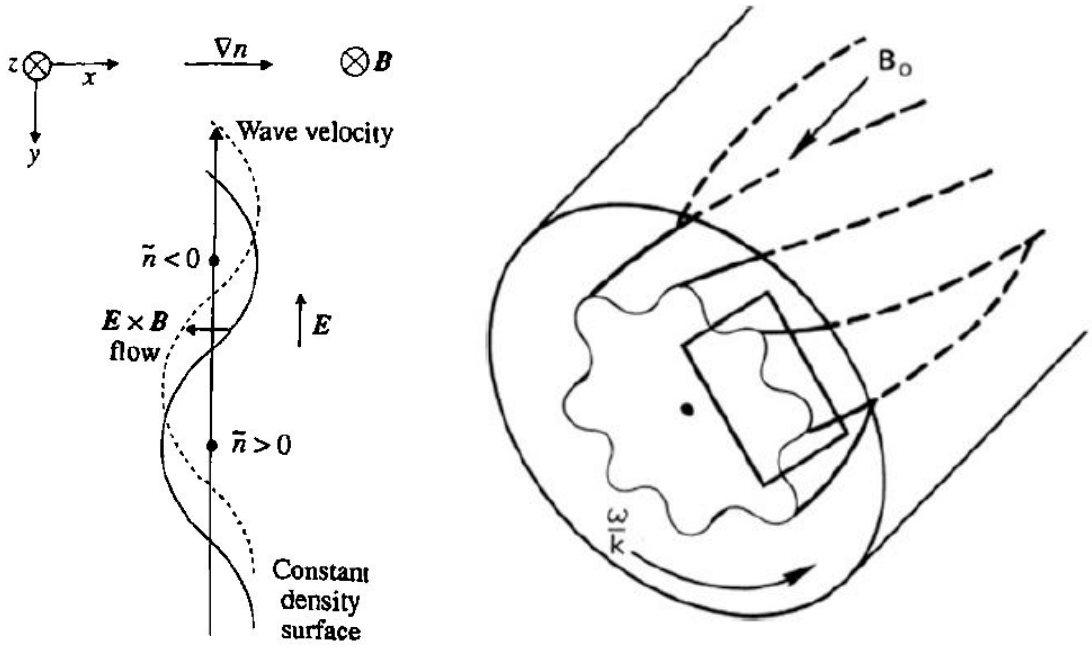

(a) (b)

Figure 2.1: (a) Motion of the electron drift wave due to the **E**x**B** motion from the wave [6]. (b) Depiction of a drift wave in toroidal geometry [23]. The rectangular outline corresponds to (a) if the density gradient were flipped.

Equation (2.20) is known as the Boltzmann relation. The ion density evolution, and therefore the wave motion, is given by the ion continuity equation,

$$\frac{\partial n_i}{\partial t} + \nabla \cdot (n_i \mathbf{u}_i) = 0. \tag{2.21}$$

Linearizing this equation and ignoring any parallel ion motion, ($\omega/k_{\|} \gg v_{th,i}$), the **E**x**B** drift velocity in the perpendicular plane leads to

$$i\omega \delta n_i = -\frac{ik_y}{B} \delta\phi \nabla n_0, \tag{2.22}$$

giving the drift wave frequency,

$$\omega = \omega_{*,e} = -\frac{k_y T_e}{eB}\frac{\nabla n_0}{n_0} = k_y v_{De}. \tag{2.23}$$

The drift wave propagates in $\hat{\mathbf{y}}$ due to the **E**x**B** drift induced by the wave's electric field, as shown in Figure 2.1(a). The phase velocity of the wave, v_{De}, is known as the electron diamagnetic drift velocity. The diamagnetic drift is formally defined as

$$v_D = -\frac{\nabla p \times \mathbf{B}}{qnB^2}, \tag{2.24}$$

and it is a drift which is not associated with any net guiding center motion. The diamagnetic drift results from the pressure gradient in the plasma, where a net current arises because of the changing number (density) or velocity (temperature) of gyrating particles across a spatial gradient. If one considers two side-by-side gyration locations separated by a gradient, the total downward and upward current between the guiding centers don't cancel perfectly in the middle if there is a pressure gradient. Note that this drift gives zero contribution to Equation (2.21) and so could be ignored. In this case, because the potential and density perturbations are in phase, the wave frequency is real and one simply has wave propagation in $\hat{\mathbf{y}}$. However, one can also consider various other drifts such as the polarization drift, Equation (1.29), or the correction to the **E**x**B** drift due to FLR effects, Equation (1.30). These drifts lead to the potential distribution lagging behind the density perturbation, such that the **E**x**B** drift will be shifted along the wave contour, acting to stabilize or destabilize the wave [23]. A complex component of the frequency, γ, arises in Equation (2.22), and thus leads to exponential growth or decay through a factor $\delta n_i \sim e^{\pm|\gamma|t}$.

Figure 2.1(b) depicts a drift wave in toroidal geometry. Comparing to the slab geometry, the $\hat{\mathbf{x}}$ and $\hat{\mathbf{y}}$ directions are local approximations of the radial and poloidal directions. Given periodicity in the poloidal and toroidal directions on a single flux surface, perturbed quantities such as the

electrostatic potential can be decomposed into toroidal (n) and poloidal (m) Fourier harmonics [36]

$$\delta\phi = \sum_{m,n} \delta\widetilde{\phi}_{m,n}(r) e^{im\theta - in\zeta - i\omega t} + \text{c.c.} \tag{2.25}$$

The toroidal angle is now represented using ζ so as not to conflict with the electrostatic potential ϕ. Note, ζ is defined in the opposite direction as the toroidal angle of Chapter 1. Equations 1.47 and 1.48 can be used to calculate the parallel wavenumber in the large aspect-ratio, circular limit

$$k_\parallel = -i\hat{\mathbf{b}} \cdot \nabla = \frac{\epsilon}{q}\frac{m}{r} - \frac{n}{R} = \frac{m - nq}{qR}. \tag{2.26}$$

Because particles are confined to tight perpendicular orbits, the gradients related to drift waves have the orderings $\nabla_\perp \sim 1/\rho$ and $\nabla_\parallel \sim 1/R$. Wavelengths are then much longer along field lines, such that $k_\parallel/k_\perp \ll 1$. Note that $m - nq \to 0$ on resonant flux surfaces.

The phase shift between the potential and density perturbations which drives instability is also important for driving average fluxes. Considering electrostatic waves at a given flux surface, averaging over the surface ψ gives radial fluxes $\langle \Gamma_r \rangle_\psi = \langle \delta n \delta v_{Er} \rangle_\psi$. From a kinetic perspective one has

$$\begin{aligned}
\Gamma_r &= \langle \int \delta f \frac{\delta \boldsymbol{E} \times \hat{\boldsymbol{B}}}{B^2} d^3v \rangle_\psi = \frac{1}{4\pi^2}\int_0^{2\pi}\int_0^{2\pi}\int \delta f \frac{\delta E_\theta}{B} d\theta d\zeta d^3v \\
&= \frac{1}{4\pi^2}\int_0^{2\pi}\int_0^{2\pi}\int \delta\widetilde{f}\frac{(-\nabla_\theta(\delta\widetilde{\Phi}))}{B_0} d\theta d\zeta d^3v \\
&= \frac{ik_\theta}{4\pi^2 B_0}\int_0^{2\pi}\int_0^{2\pi}\int (\delta\widetilde{f}\delta\widetilde{\Phi}^* - \delta\widetilde{f}^*\delta\widetilde{\Phi}) d\theta d\zeta d^3v,
\end{aligned} \tag{2.27}$$

where the flux-surface-average is defined as a poloidal and toroidal angular average. The perturbations in Equation (2.27) have been Fourier decomposed into complex form as in Equation (2.25) and the total real contribution to the flux evaluated using the results of Appendix A.1. One can see that a complex flux will be driven if the perturbations are in phase, however, as they shift the flux will gain a real component. The physical reason for the phase shift driving a flux is depicted in Figure 2.2. Particles **E**x**B** drift around contours of constant potential, and when contours of the density perturbation do not align a net flux will arise from the difference in outward and inward flux

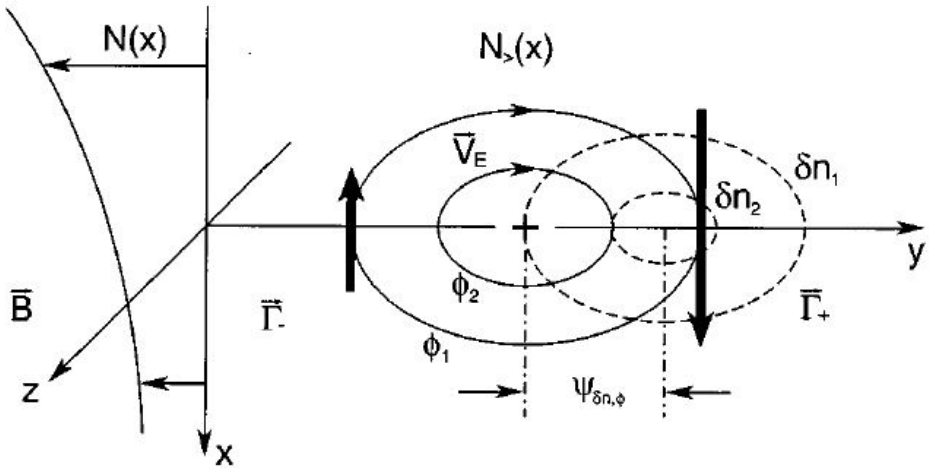

Figure 2.2: Portion of drift wave contours showing phase-shifted density and electrostatic potential perturbations. A net radial flux results from **E**x**B**-drift convection around contours of constant potential [36].

around the potential contour. Note, in the kinetic framework the phase shift is in relation to the distribution function and various moments can be taken to capture the different fluxes. For instance, a heat flux, $\langle Q_r \rangle_\psi = \langle \delta T \delta v_{Er} \rangle_\psi$, will also be driven given a phase-shift between temperature and electrostatic potential perturbations.

As mentioned above, perpendicular wavelengths for drift waves are on the order of the particle gyroradius, $k_\perp \rho \sim 1$. One can show from this that quasineutrality is satisfied to first order, i.e. true for perturbations as well as the background [36, 67]. Consider the potential determined by Poisson's equation

$$\nabla^2 \delta\phi = -\frac{e(\delta n_i - \delta n_e)}{\epsilon_0}. \tag{2.28}$$

Dividing by δn_e, and assuming a Boltzmann electron response, one finds

$$\frac{\delta\phi}{\frac{n_0 e \delta\phi}{T_e}\rho_i^2} = -\frac{e\delta n_i - \delta n_e}{\epsilon_0 \delta n_e} \Rightarrow \frac{\delta n_i - \delta n_e}{\delta n_e} = \frac{\left(\frac{\epsilon_0 T_e}{n_0 e^2}\right)}{\rho_i^2} = \frac{\lambda_{\mathrm{De}}^2}{\rho_i^2} \ll 1. \tag{2.29}$$

Given this ordering, the right-hand-side of Equation (2.28) is small to first order, so that one can assume $\nabla^2 \delta\phi \approx 0$, and the plasma is approximately quasineutral in the case of perturbations.

Furthermore, drift wave frequencies are much smaller than the cyclotron frequencies, $\omega_{*j}/\Omega_j \ll 1$. These spatial and temporal properties of drift waves, combined with their small amplitudes, form the basis of the gyrokinetic ordering which is described more formally in Section 2.3. One can use the gyrokinetic ordering to asymptotically expand the Vlasov-Maxwell system and then average equations over the fast particle gyromotion. This process results in the gyrokinetic framework which has been instrumental in modeling drift wave turbulence dynamics and the associated transport losses in tokamak plasmas.

2.3 Gyrokinetic Theory

Initial development of gyrokinetic theory and simulation [68–71] was motivated by the need to describe the dynamics of low-frequency drift wave microturbulence in tokamak plasmas. The mathematical methods established were specifically informed by experimental measurements of core tokamak microturbulence expected to be responsible for anomalous experimental transport levels [72, 73]. The validation of gyrokinetic theory continues to be an active area of research [74], especially in regions where standard assumptions break down, such as in the tokamak pedestal where gradients are much steeper [75, 76]. The gyrokinetic framework first introduces a transformation to guiding-center

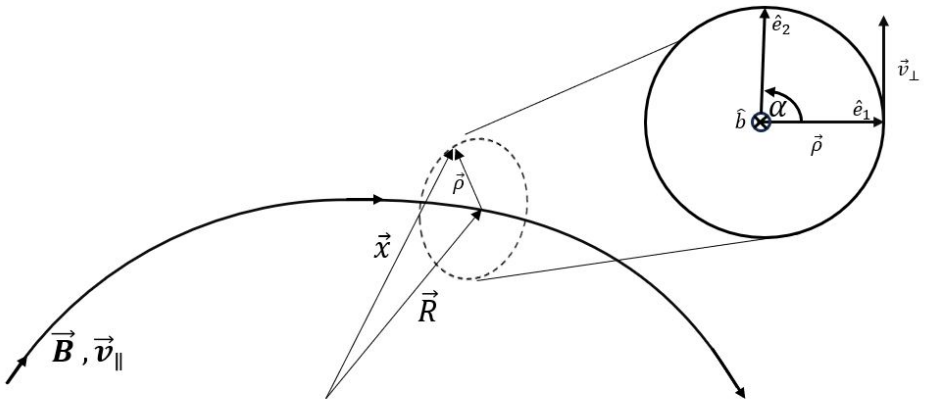

Figure 2.3: Depiction of guiding-center coordinates used in the gyrokinetic framework.

coordinates

$$f_j(\mathbf{x},\mathbf{v},t) \rightarrow f_j(\mathbf{R}_j,\epsilon_j,\mu_j,\alpha,t), \tag{2.30}$$

where the original coordinates and the guiding-center coordinate variables are related by the Catto transformation [77]

$$\mathbf{R}_j = \mathbf{x} - \boldsymbol{\rho}_j \tag{2.31}$$

$$\mathbf{v} = v_\parallel \hat{\mathbf{b}} + v_\perp \cos\alpha \hat{\mathbf{e}}_2 - v_\perp \sin\alpha \hat{\mathbf{e}}_1. \tag{2.32}$$

Here $\mathbf{R}_j$ is the guiding-center position vector and $\boldsymbol{\rho}_j = (\hat{\mathbf{b}} \times \mathbf{v})/\Omega_j$ is the gyroradius vector for a single species j. A right-handed field-line-following coordinate system is defined by the vectors $\hat{\mathbf{b}}(\mathbf{x}), \hat{\mathbf{e}}_1(\mathbf{x})$, and $\hat{\mathbf{e}}_2(\mathbf{x})$, where $\hat{\mathbf{b}} = \hat{\mathbf{e}}_2 \times \hat{\mathbf{e}}_1$. The lowest order energy is defined as $\epsilon_j = m_j v^2/2 + q_j \Phi_0$, and α represents the gyrophase angle. The coordinate system is illustrated in Figure 2.3. Once the Vlasov-Maxwell system of equations is converted to guiding-center coordinates, one can average over the fast particle gyromotion. This results in a simpler 5-D phase space description which considers the distribution function of guiding-center charged rings and their interaction with low-frequency drift waves. These charged rings stream along field lines and drift across them due to the average Lorentz force they feel.

Two primary methods are usually employed to convert the Vlasov equation to guiding-center coordinates. The original involves a full chain-rule expansion of partial derivatives [68]

$$\begin{aligned}\frac{df_j}{dt} = \frac{\partial f_j}{\partial t} + \mathbf{v}\cdot\left[\frac{\partial \mathbf{R}_j}{\partial \mathbf{x}}\frac{\partial f_j}{\partial \mathbf{R}_j} + \frac{\partial \epsilon_j}{\partial \mathbf{x}}\frac{\partial f_j}{\partial \epsilon_j} + \frac{\partial \mu_j}{\partial \mathbf{x}}\frac{\partial f_j}{\partial \mu_j} + \frac{\partial \alpha}{\partial \mathbf{x}}\frac{\partial f_j}{\partial \alpha}\right] \\ + \frac{\mathbf{F}_L}{m}\cdot\left[\frac{\partial \mathbf{R}_j}{\partial \mathbf{v}}\frac{\partial f_j}{\partial \mathbf{R}_j} + \frac{\partial \epsilon_j}{\partial \mathbf{v}}\frac{\partial f_j}{\partial \epsilon_j} + \frac{\partial \mu_j}{\partial \mathbf{v}}\frac{\partial f_j}{\partial \mu_j} + \frac{\partial \alpha}{\partial \mathbf{v}}\frac{\partial f_j}{\partial \alpha}\right] = C_j[f_j] + S_j,\end{aligned} \tag{2.33}$$

while a second option focuses on calculating total time derivatives of the guiding-center quantities [65]

$$\frac{df_j}{dt} = \frac{\partial f_j}{\partial t} + \dot{\mathbf{R}}_j\frac{\partial f_j}{\partial \mathbf{R}_j} + \dot{\epsilon}\frac{\partial f_j}{\partial \epsilon_j} + \dot{\mu}\frac{\partial f_j}{\partial \mu_j} + \dot{\alpha}\frac{\partial f_j}{\partial \alpha} = C_j[f_j] + S_j. \tag{2.34}$$

The two methods are equivalent, however the second method is more convenient given that conser-

vation of energy and the adiabatic invariance of μ usually hold to lowest order ($\dot{\mu} \approx 0$ and $\dot{\epsilon} \approx 0$). These methods then follow with an asymptotic expansion of the Vlasov-Maxwell system using the gyrokinetic ordering [65]

$$\frac{\delta f_j}{f_{0j}} \sim \frac{q\delta\phi_1}{T} \sim \frac{\delta B}{B} \sim \frac{\delta E}{E} \sim \frac{k_\parallel}{k_\perp} \sim \frac{\omega}{\Omega_j} \sim \frac{\nu}{\Omega_j} \sim \frac{\rho_j}{L} \sim \epsilon, \tag{2.35}$$

$$k_\perp \rho_j \sim 1, \tag{2.36}$$

$$\frac{E}{v_{th} B} \sim \epsilon. \tag{2.37}$$

Here ν represents a collision frequency, and Equation (2.37) implies **E**x**B** flows are not relativistic. L represents a macroscopic length scale which is often the tokamak minor or major radius, a or R_0.

Furthermore, spatial and temporal scales must be defined for macroscopic quantities

$$\nabla f_{0j} \sim \frac{f_{0j}}{L}, \tag{2.38}$$

$$\partial_t f_{0j} \sim \frac{f_{0j}}{\tau_E} \sim \frac{\chi_{gB}}{L^2} f_{0j} \sim \frac{\frac{T}{Z_j e B}\frac{\rho_j}{L}}{L^2} f_{0j} \sim \frac{\frac{m_j v_{th,j}^2}{Z_j e B}\frac{\rho_j}{L}}{L^2} f_{0j} \sim \frac{v_{th,j}^2}{\Omega_j}\frac{\rho_j}{L}\frac{1}{L^2} f_{0j} \sim \frac{\rho_j^3}{L^3}\Omega_j f_{0j} \sim \epsilon^3 \Omega_j f_{0j}, \tag{2.39}$$

where a gyroBohm diffusive random walk process has been assumed to give the energy transport timescale. The overall ordering depends crucially on experimentally measured characteristics of tokamak transport and drift wave turbulence as mentioned previously, and allows for separating and tailoring equations to specific scales of interest. From here, the distribution function (and fields) can be separated into different orders for non-fluctuating and fluctuating components [65]

$$f_j = f_{0j} + f_{1j} + f_{2j} + \ldots, \tag{2.40}$$

$$\delta f_j = \delta f_{1j} + \delta f_{2j} + \ldots, \tag{2.41}$$

where $f_{0j} \sim f_j$, $f_{1j} \sim \delta f_{1j} \sim \epsilon f_j$, and so on. Finally, the different order equations must be

gyroaveraged, a step which reduces the phase space to five dimensions by utilizing the slow drift wave frequency compared to the fast particle gyromotion. The gyroaveraging technique is described mathematically in the next section. Moments of the gyrokinetic equation can also be taken to derive equations for so-called gyrofluid theory [78].

Taking advantage of the separation of temporal and spatial scales allows for capturing the dynamics of the background equilibrium and small-scale turbulence separately, as well as how they influence each other. Examples of the different length and time scales in select fusion plasmas are given in Table 1 of Ref. [65]. Reference [65] gives a comprehensive derivation of equations up to the third order transport equations which govern slow changes in the macroscopic equilibrium profiles. The gyrokinetic and neoclassical equations are found at second order and give the faster evolution of the small-scale fluctuating and non-fluctuating components of the distribution function respectively. Additionally, a third, more modern, mathematical prescription exists for deriving the gyrokinetic equation. This method exploits noncanonical Hamiltonian techniques and Lie algebra transformations which simplify the form and manipulation of the perturbed equations [69, 70]. A comprehensive review of modern techniques for gyrokinetic theory is the subject of Ref. [79]. Much of the following information on the gyrokinetic formalism and derivation incorporates work from a combination of Refs. [65, 68, 77]. The species subscript j is dropped for the derivation from hereon to keep notation simpler.

2.3.1 Gyroaveraging

A mathematical definition of the gyroaverage is given here, as well as various useful gyroaveraged values which will be required for the gyrokinetic derivation that follows. The gyroaverage is defined for a general quantity A as

$$\langle A \rangle_\alpha = \oint d\alpha A(\mathbf{R}, \epsilon, \mu, \alpha), \tag{2.42}$$

where $\mathbf{R}$, ϵ, and μ must be held fixed during integration.

For small-scale fluctuating quantities with $k_\perp \rho \sim 1$ the gyroaverage can be calculated as

$$\langle A(\mathbf{r},\mathbf{v})\rangle_\alpha = \frac{1}{2\pi}\oint d\alpha A(\mathbf{R},\epsilon,\mu)e^{i\mathbf{k}_\perp\cdot\boldsymbol{\rho}-i\omega t} = J_0(k_\perp\rho)A(\mathbf{R},\epsilon,\mu)e^{-i\omega t}. \tag{2.43}$$

Here J_0 is the zeroth order Bessel function of the first kind. For long wavelengths compared to the gyroradius, $k_\perp\rho \ll 1$, one finds $J_0(k_\perp\rho) \to 1$, meaning the fluctuating quantity is approximately constant over the small orbit. When wavelengths become very short compared to the gyroradius, $k_\perp\rho \gg 1$, one finds $J_0(k_\perp\rho) \to 0$, and the fine scale fluctuating quantity averages out over a large gyroradius. For macroscopic quantities one must Taylor expand in terms of the small gyroradius to take a gyroaverage,

$$A(\mathbf{R}+\boldsymbol{\rho},\epsilon,\mu) = A(\mathbf{R},\epsilon,\mu) + \boldsymbol{\rho}\cdot\nabla A(\mathbf{R},\epsilon,\mu) + \boldsymbol{\rho}\boldsymbol{\rho}:\nabla\nabla A(\mathbf{R},\epsilon,\mu) + \mathcal{O}(\epsilon^3). \tag{2.44}$$

Recalling the definition of the gyroradius, $\boldsymbol{\rho} = (\hat{\mathbf{b}}\times\mathbf{v})/\Omega = (\hat{\mathbf{b}}\times\mathbf{v}_\perp)/\Omega$, and that the components of $\mathbf{v}_\perp$ are $v_\perp\cos\alpha\hat{\mathbf{e}}_2 - v_\perp\sin\alpha\hat{\mathbf{e}}_2$, it is clear that the first order term will vanish after gyroaveraging, giving

$$\langle A(\mathbf{r},\epsilon,\mu)\rangle_\alpha = \langle A(\mathbf{R},\epsilon,\mu) + \frac{\hat{\mathbf{b}}\times\mathbf{v}_\perp}{\boldsymbol{\Omega}}\cdot\nabla A(\mathbf{R},\epsilon,\mu) + \mathcal{O}(\epsilon^2)\rangle_\alpha = A(\mathbf{R},\epsilon,\mu) + \mathcal{O}(\epsilon^2). \tag{2.45}$$

That is, $A(\mathbf{x}) \approx A(\mathbf{R})$ to lowest order since the expansion terms for macroscopic quantities scale as $\rho/L \ll 1$, rather than $k_\perp\rho \sim 1$ for the small-scale fluctuating quantities. Because of this, macroscopic quantities are simply functions of $\mathbf{R}$ to lowest order, and so these terms can be considered constant and taken out of the gyroaverage integral.

Some useful gyroaverages are now defined that will help in deriving the gyrokinetic Vlasov equation. The first considers the gyroaverage of the quantity $\mathbf{v}_\perp\cdot\delta\mathbf{E}_1$. First note that this term is related to the derivative of $\delta\phi_1$ with respect to α

$$\Omega\frac{\partial\delta\phi_1}{\partial\alpha} = \Omega\left[\frac{\partial\mathbf{x}}{\partial\alpha}\frac{\partial\delta\phi_1}{\partial\mathbf{x}} + \frac{\partial\mathbf{v}}{\partial\alpha}\cancel{\frac{\partial\delta\phi_1}{\partial\mathbf{v}}}\right] = \Omega\frac{\partial\boldsymbol{\rho}}{\partial\alpha}\cdot\nabla\delta\phi_1 = \cancel{\Omega}\frac{\mathbf{v}_\perp}{\cancel{\Omega}}\cdot\nabla\delta\phi_1 = -\mathbf{v}_\perp\cdot\delta\mathbf{E}_1. \tag{2.46}$$

Using Equation (2.46) one necessarily has

$$\langle \mathbf{v}_\perp \cdot \delta\mathbf{E}_1 \rangle_\alpha = -\Omega \langle \frac{\partial \delta\phi_1}{\partial \alpha} \rangle_\alpha = -\frac{\Omega}{2\pi} \delta\phi|_{\alpha=0}^{2\pi} = 0. \tag{2.47}$$

Furthermore, the gyroaverage of the electric field can be simplified a little. One can show that $\nabla\delta\phi \approx \nabla_{\mathbf{R}}\delta\phi$ and the gradient can then be taken out of the gyroaverage to find

$$\langle \delta\mathbf{E}_1 \rangle_\alpha = -\langle \nabla\delta\phi_1 \rangle_\alpha \approx -\nabla_{\mathbf{R}} \langle \delta\phi_1 \rangle_\alpha. \tag{2.48}$$

Lastly, one useful tensor gyroaverage is defined here:

$$\begin{aligned} \langle \mathbf{vv} \rangle_\alpha &= \frac{1}{2\pi} \oint_0^{2\pi} d\alpha \begin{pmatrix} v_\parallel^2 \hat{\mathbf{b}}\hat{\mathbf{b}} & v_\parallel v_\perp \cos\alpha \hat{\mathbf{b}}\hat{\mathbf{e}}_1 & v_\parallel v_\perp \cos\alpha \hat{\mathbf{b}}\hat{\mathbf{e}}_2 \\ v_\parallel v_\perp \cos\alpha \hat{\mathbf{e}}_1\hat{\mathbf{b}} & v_\perp^2 \cos^2\alpha \hat{\mathbf{e}}_1\hat{\mathbf{e}}_1 & v_\perp^2 \cos\alpha \sin\alpha \hat{\mathbf{e}}_1\hat{\mathbf{e}}_2 \\ v_\parallel v_\perp \sin\alpha \hat{\mathbf{e}}_2\hat{\mathbf{b}} & v_\perp^2 \cos\alpha \sin\alpha \hat{\mathbf{e}}_2\hat{\mathbf{e}}_1 & v_\perp^2 \sin^2\alpha \hat{\mathbf{e}}_2\hat{\mathbf{e}}_2 \end{pmatrix} = \begin{pmatrix} v_\parallel^2 \hat{\mathbf{b}}\hat{\mathbf{b}} & 0 & 0 \\ 0 & \frac{v_\perp^2}{2} \hat{\mathbf{e}}_1\hat{\mathbf{e}}_1 & 0 \\ 0 & 0 & \frac{v_\perp^2}{2} \hat{\mathbf{e}}_2\hat{\mathbf{e}}_2 \end{pmatrix} \\ &= v_\parallel^2 \hat{\mathbf{b}}\hat{\mathbf{b}} + \frac{v_\perp^2}{2} (\overleftrightarrow{\mathrm{I}} - \hat{\mathbf{b}}\hat{\mathbf{b}}). \end{aligned} \tag{2.49}$$

Note, the outer product tensor notation has been dropped here for simplicity - i.e. $\hat{\mathbf{b}} \otimes \hat{\mathbf{b}} \rightarrow \hat{\mathbf{b}}\hat{\mathbf{b}}$.

2.3.2 Derivation of Gyrokinetic Equations

The derivation of the gyrokinetic Vlasov equation is given here and follows from Equation (2.33), assuming electrostatic turbulence in the collisionless limit with no bulk flow, no sources, and no background electric field in the tokamak. For the general case - which considers electromagnetic turbulence, collisions, bulk flow, a background electric field, sources, and the derivation of the neoclassical equation and higher-order transport equations - the reader is referred to Ref. [65]. Note that this derivation here focuses on turbulent transport, and so only higher-order fluctuating components of the distribution function and fields are kept, i.e. δf_1, δf_2, and so on.

The real-space and velocity-space gradients of the guiding-center variables in Equation (2.33) are derived in Appendix B. Substituting the values from Equations (B.1) to (B.8) into Equation (2.33)

gives

$$\begin{aligned}\partial_t f + \mathbf{v}\cdot\Big[(\overleftrightarrow{\mathrm{I}} - \nabla\rho)\cdot\nabla_{\mathbf{R}} f - (\frac{\mu}{B}\nabla B + \frac{m v_\parallel}{B}\mathbf{v}_\perp\cdot\nabla\hat{\mathbf{b}})\frac{\partial f}{\partial\mu} + (\frac{v_\parallel}{v_\perp^2}\hat{\mathbf{b}}\cdot(\mathbf{v}_\perp\times\hat{\mathbf{b}}) + \hat{\mathbf{e}}_1\cdot\nabla\hat{\mathbf{e}}_2)\frac{\partial f}{\partial\alpha}\Big] \\ + \frac{q}{m}(\delta\mathbf{E} + \mathbf{v}\times\mathbf{B})\cdot\Big[(\frac{1}{\Omega}\overleftrightarrow{\mathrm{I}}\times\hat{\mathbf{b}})\cdot\nabla_{\mathbf{R}} f + m\mathbf{v}\frac{\partial f}{\partial\epsilon} + \frac{m\mathbf{v}_\perp}{B}\frac{\partial f}{\partial\mu} - \frac{1}{v_\perp^2}(\hat{\mathbf{b}}\times\mathbf{v}_\perp)\frac{\partial f}{\partial\alpha}\Big].\end{aligned} \tag{2.50}$$

Various terms in Equation (2.50) can then be simplified using Equations (B.23) to (B.29) to get

$$\begin{aligned}\partial_t f + (v_\parallel\hat{\mathbf{b}} + \mathbf{v}_E)\cdot\nabla_{\mathbf{R}} f + \Omega\frac{\partial f}{\partial\alpha} \\ + \mathbf{v}\cdot\Big[-(\nabla\rho)\cdot\nabla_{\mathbf{R}} f - (\frac{\mu}{B}\nabla B + \frac{m v_\parallel}{B}\mathbf{v}_\perp\cdot\nabla\hat{\mathbf{b}})\frac{\partial f}{\partial\mu} + (\frac{v_\parallel}{v_\perp^2}\hat{\mathbf{b}}\cdot(\mathbf{v}_\perp\times\hat{\mathbf{b}}) + \hat{\mathbf{e}}_1\cdot\nabla\hat{\mathbf{e}}_2)\frac{\partial f}{\partial\alpha}\Big] \\ + \frac{q}{m}\delta\mathbf{E}\cdot\Big[m\mathbf{v}\frac{\partial f}{\partial\epsilon} + \frac{m\mathbf{v}_\perp}{B}\frac{\partial f}{\partial\mu} - \frac{1}{v_\perp^2}(\hat{\mathbf{b}}\times\mathbf{v}_\perp)\frac{\partial f}{\partial\alpha}\Big].\end{aligned} \tag{2.51}$$

Next, the terms in Equation (2.51) must be split up by order. The ordering of each term is given in Appendix B, specifically by equations (B.34) - (B.61). To lowest order one finds

$$\Omega\frac{\partial f_0}{\partial\alpha} = 0. \tag{2.52}$$

This simply states that the background distribution is independent of α, such as for a Maxwellian distribution which depends on v^2 only. To first order one finds

$$\begin{aligned}v_\parallel\hat{\mathbf{b}}\cdot\nabla_{\mathbf{R}} f_0 + \Omega\frac{\partial\delta f_1}{\partial\alpha} + \frac{q}{m}\delta\mathbf{E}_1\cdot\Big[m\mathbf{v}_\perp\frac{\partial f_0}{\partial\epsilon} + \frac{m\mathbf{v}_\perp}{B}\frac{\partial f_0}{\partial\mu} - \frac{1}{v_\perp^2}(\hat{\mathbf{b}}\times\mathbf{v}_\perp)\cancel{\frac{\partial f_0}{\partial\alpha}}\Big] \\ - \mathbf{v}\cdot\Big[\frac{\mu}{B}\nabla B\frac{\partial f_0}{\partial\mu} + \frac{m v_\parallel}{B}(\mathbf{v}_\perp\cdot\nabla\hat{\mathbf{b}})\frac{\partial f_0}{\partial\mu} + (\frac{v_\parallel}{v_\perp^2}\hat{\mathbf{b}}\cdot(\mathbf{v}_\perp\times\hat{\mathbf{b}}) + \hat{\mathbf{e}}_1\cdot\nabla\hat{\mathbf{e}}_2)\cancel{\frac{\partial f_0}{\partial\alpha}}\Big] = 0,\end{aligned} \tag{2.53}$$

where two terms can be dropped because f_0 does not depend on α per the zeroth order Equation (2.52).

Furthermore, to second order one finds

$$\begin{aligned}
&\partial_t \delta f_1 + \mathbf{v}_E \cdot \nabla_{\mathbf{R}} f_0 + (v_\parallel \hat{\mathbf{b}} + \mathbf{v}_E) \cdot \nabla_{\mathbf{R}} \delta f_1 + \Omega \frac{\partial \delta f_2}{\partial \alpha} \\
&\quad + \frac{q}{m} \delta \mathbf{E}_1 \cdot \left[m v_\parallel \hat{\mathbf{b}} \frac{\partial f_0}{\partial \epsilon} + m \mathbf{v}_\perp \frac{\partial \delta f_1}{\partial \epsilon} + \frac{m \mathbf{v}_\perp}{B} \frac{\partial \delta f_1}{\partial \mu} - \frac{1}{v_\perp^2} (\hat{\mathbf{b}} \times \mathbf{v}_\perp) \frac{\partial \delta f_1}{\partial \alpha} \right] \\
&\quad - \mathbf{v} \cdot \left[\nabla \rho \cdot \nabla_{\mathbf{R}} (f_0 + \delta f_1) + \frac{\mu}{B} \nabla B \frac{\partial \delta f_1}{\partial \mu} + \frac{m v_\parallel}{B} (\mathbf{v}_\perp \cdot \nabla \hat{\mathbf{b}}) \frac{\partial \delta f_1}{\partial \mu} \right. \\
&\qquad \left. + \left(\frac{v_\parallel}{v_\perp^2} \hat{\mathbf{b}} \cdot (\mathbf{v}_\perp \times \hat{\mathbf{b}}) + \hat{\mathbf{e}}_1 \cdot \nabla \hat{\mathbf{e}}_2 \right) \frac{\partial \delta f_1}{\partial \alpha} \right] = 0.
\end{aligned} \tag{2.54}$$

The gyroaverage of the first order equation is considered here first. Removing the terms dropped in Equation (2.53), one has

$$v_\parallel \hat{\mathbf{b}} \cdot \nabla_{\mathbf{R}} f_0 + \Omega \frac{\partial \delta f_1}{\partial \alpha} + \frac{q}{m} \delta \mathbf{E}_1 \cdot \left[m \mathbf{v}_\perp \frac{\partial f_0}{\partial \epsilon} + \frac{m \mathbf{v}_\perp}{B} \frac{\partial f_0}{\partial \mu} \right] - \mathbf{v} \cdot \left[\frac{\mu}{B} \nabla B \frac{\partial f_0}{\partial \mu} + \frac{m v_\parallel}{B} (\mathbf{v}_\perp \cdot \nabla \hat{\mathbf{b}}) \frac{\partial f_0}{\partial \mu} \right] = 0. \tag{2.55}$$

Term two gyroaverages to zero as with $\delta \phi_1$ in Equation (2.47), while terms three and four gyroaverage to zero according to Equation (2.47). Terms five and six gyroaverage to zero according to Equation (B.62), and one is simply left with

$$\mathbf{v}_\parallel \cdot \nabla_{\mathbf{R}} f_0 = 0, \tag{2.56}$$

which states that there is no spatial gradient of f_0 along field lines. Equation (2.52) and Equation (2.56) together imply that f_0 can be considered Maxwellian to lowest order, as the density and temperature only vary radially across field lines and the energy is not a function of α. In the more rigorous derivation, Equation (2.56) would also retain the effect of collisions, from which one can show that Boltzmann's H-theorem is satisfied and that f_0 truly is Maxwellian [65]. This only holds given the collisional ordering of Ref. [65], and f_0 can more generally be anisotropic if collision rates are considered much lower along the field line.

From here it is assumed f_0 is a Maxwellian distribution, giving $\partial_\epsilon f_0 = -1/T$ and $\partial_\mu f_0 = 0$. Combining these derivatives with Equation (2.46) and Equation (2.56) and substituting into

Equation (2.55) gives

$$\cancel{\Omega}\frac{\partial \delta f_1}{\partial \alpha} = -\cancel{\Omega}\frac{q}{T}\frac{\partial \delta \phi_1}{\partial \alpha} f_0. \tag{2.57}$$

Finally, Equation (2.57) can be integrated over α to find

$$\delta f_1(\mathbf{x}, \mathbf{v}) = -\frac{q\delta\phi_1(\mathbf{x})}{T} f_0(\mathbf{x}, \mathbf{v}) + \delta h(\mathbf{R}, \epsilon, \mu), \tag{2.58}$$

where δh is a constant of integration which does not depend on α. The first term is just the Boltzmann response, Equation (2.20), and represents a statistical equilibrium response to the electrostatic potential of the wave. One can see this by including the potential energy from the electrostatic wave in the Maxwellian distribution and Taylor expanding for $q\delta\phi_1/T \ll 1$. This term is also known as the adiabatic response. The second term is the gyrokinetic response, which represents the distribution function of guiding-center charged rings. The gyrokinetic response drives much of the interesting dynamical behavior, such as wave-particle resonances and therefore wave instability.

The evolution of the gyrokinetic response is given by the gyrokinetic Vlasov equation which can found by substituting Equation (2.58) into the second order Vlasov equation, Equation (2.54), gyroaveraging, and solving for δh. Substituting Equation (2.58) into Equation (2.54) gives

$$\begin{aligned}
&\partial_t \delta h + \mathbf{v}_E \cdot \nabla_{\mathbf{R}} f_0 + (v_\parallel \hat{\mathbf{b}} + \mathbf{v}_E) \cdot \nabla_{\mathbf{R}} \delta h + \Omega \frac{\partial \delta f_2}{\partial \alpha} \\
&\quad + \frac{q}{m}\delta \mathbf{E}_1 \cdot \left[m v_\parallel \hat{\mathbf{b}} \frac{\partial f_0}{\partial \epsilon} + m\mathbf{v}_\perp \frac{\partial \delta h}{\partial \epsilon} + \frac{m\mathbf{v}_\perp}{B}\frac{\partial \delta h}{\partial \mu} - \frac{1}{v_\perp^2}(\hat{\mathbf{b}} \times \mathbf{v}_\perp)\cancel{\frac{\partial \delta h}{\partial \alpha}} \right] \\
&\quad - \mathbf{v} \cdot \left[\nabla \rho \cdot \nabla_{\mathbf{R}}(f_0 + \delta h) + \frac{\mu}{B}\nabla B \frac{\partial \delta h}{\partial \mu} + \frac{m v_\parallel}{B}(\mathbf{v}_\perp \cdot \nabla \hat{\mathbf{b}})\frac{\partial \delta h}{\partial \mu} \right. \\
&\qquad \left. + \left(\frac{v_\parallel}{v_\perp^2}\hat{\mathbf{b}} \cdot (\mathbf{v}_\perp \times \hat{\mathbf{b}}) + \hat{\mathbf{e}}_1 \cdot \nabla \hat{\mathbf{e}}_2\right)\cancel{\frac{\partial \delta h}{\partial \alpha}} \right] = \frac{d}{dt}\left(\frac{q\delta\phi_1}{T} f_0\right).
\end{aligned} \tag{2.59}$$

Note that all terms related to the adiabatic response have been combined into a total time derivative term, and remaining terms with derivatives of α can again be dropped because δh does not depend on the gyroangle. The combination of all adiabatic terms into a total time derivative is not entirely possible at this point because the $\Omega\partial_\alpha(q\delta\phi_1 f_0/T)$ term is actually first order, but gyroaveraging will

remove this term and the equation will then be consistent to second order. Again, as with the first order equation, term five gyroaverages to zero similar to $\delta\phi_1$ in Equation (2.47), while terms seven, eight, eleven, and twelve gyroaverage to zero according to Equation (2.47) and Equation (B.62), giving

$$\begin{aligned}&\partial_t \delta h + \langle \mathbf{v}_E \rangle_\alpha \cdot \nabla_{\mathbf{R}} f_0 + (v_\parallel \hat{\mathbf{b}} + \langle \mathbf{v}_E \rangle_\alpha) \cdot \nabla_{\mathbf{R}} \delta h \\ &\quad - \frac{q}{T} v_\parallel \hat{\mathbf{b}} \cdot \langle \delta \mathbf{E}_1 \rangle_\alpha - \langle \mathbf{v} \cdot \nabla \rho \rangle_\alpha \cdot \nabla_{\mathbf{R}} (f_0 + \delta h) = \langle \frac{d}{dt} (\frac{q \delta \phi_1}{T} f_0) \rangle_\alpha.\end{aligned} \tag{2.60}$$

The gyroaverage of the last two terms to second order are substituted from Equation (B.69) and Equation (B.80), giving

$$\begin{aligned}&\partial_t \delta h + \langle \mathbf{v}_E \rangle_\alpha \cdot \nabla_{\mathbf{R}} f_0 + (v_\parallel \hat{\mathbf{b}} + \langle \mathbf{v}_E \rangle_\alpha) \cdot \nabla_{\mathbf{R}} \delta h \\ &\quad \cancel{- \frac{q}{T} f_0 v_\parallel \hat{\mathbf{b}} \cdot \langle \delta \mathbf{E}_1 \rangle_\alpha} + \mathbf{v}_d \cdot \nabla_{\mathbf{R}} (f_0 + \delta h) = \frac{q}{T} f_0 \partial_t \langle \delta \phi_1 \rangle_\alpha - \cancel{\frac{q}{T} f_0 v_\parallel \hat{\mathbf{b}} \cdot \langle \delta \mathbf{E}_1 \rangle_\alpha},\end{aligned} \tag{2.61}$$

where v_d is the combined grad-B and curvature drift velocity. Equation (2.61) can be averaged over fluctuations to find

$$\mathbf{v}_d \cdot \nabla_{\mathbf{R}} f_0 = 0. \tag{2.62}$$

Note, this is not strictly true and in general this step should be done earlier with Equation (2.59) to find the neoclassical equation as in Ref. [65], but only fluctuating first order quantities were retained in the analysis here for clarity. Finally, rearranging terms and substituting in Equation (2.62), one finds the gyrokinetic Vlasov equation

$$\partial_t \delta h + (v_\parallel \hat{\mathbf{b}} + \langle \mathbf{v}_E \rangle_\alpha + \mathbf{v}_d) \cdot \nabla_{\mathbf{R}} \delta h = \frac{q}{T} f_0 \partial_t \langle \delta \phi_1 \rangle_\alpha - \langle \mathbf{v}_E \rangle_\alpha \cdot \nabla_{\mathbf{R}} f_0, \tag{2.63}$$

where the gyroaveraged **ExB** velocity is defined as

$$\langle \mathbf{v}_E \rangle_\alpha = \frac{\hat{\mathbf{b}} \times \nabla \langle \delta \phi_1 \rangle_\alpha}{B}. \tag{2.64}$$

The gyrokinetic Vlasov equation describes the evolution of the distribution function of guiding-

center rings, where gradients are advected along field lines by parallel streaming and across field lines by various drift motions. The first term on the right-hand-side describes the polarization response to the fluctuating field, while the last term allows for the **E**x**B** drift to pull in energy from the background gradients and drive waves unstable. As unstable waves grow they form radially-elongated 'streamers' due to the **E**x**B** drift motion. The **E**x**B** nonlinearity is responsible for turbulent transport as illustrated in Figure 2.2. Furthermore, the nonlinear term leads to Navier-Stokes type shearing in the perpendicular plane which breaks up the streamers and results in steady-state transport levels.

To complete the gyrokinetic framework, Equation (2.63) must also be coupled to gyroaveraged versions of Maxwell's equations. The total first order perturbations, Equation (2.58), can be substituted into the quasineutrality condition to find

$$\sum_j \frac{Z_j^2 e^2 n_j \delta\phi_1}{T_j} = \sum_j Z_j e \int d^3\mathbf{v} \langle \delta h_j \rangle_\alpha. \tag{2.65}$$

If electromagnetic perturbations are retained one must also gyroaverage Ampere's law [65],

$$\nabla \times \delta\mathbf{B} = -\nabla^2 \delta\mathbf{A} = \mu_0 \sum_j Z_j e \int d^3\mathbf{v}\mathbf{v} \langle \delta h_j \rangle_\alpha, \tag{2.66}$$

where the displacement current can be ignored when plasma particles are not relativistic. Note that Maxwell's equations must be solved in the original particle space and the gyroaverages of δh here are taken at constant $\mathbf{r}$, $\mathbf{v}_\parallel$, $\mathbf{v}_\perp$. Considering the inverse coordinate transform from Equation (2.43), one has

$$A(\mathbf{R}) \sim e^{-i\mathbf{k}_\perp \cdot \boldsymbol{\rho}} A(\mathbf{x}) \quad \Rightarrow \quad \langle A(\mathbf{R}) \rangle_\alpha = J_0(k_\perp \rho) A(\mathbf{x}), \tag{2.67}$$

and the gyroaverage of the inverse transform also results in the Bessel function factor $J_0(k_\perp \rho)$. Together Equation (2.63) and Equation (2.65) constitute the gyrokinetic Vlasov-Maxwell system of equations for electrostatic microturbulence. Gyrokinetic codes generally solve equations for the total fluctuating distribution function, δf_1, rather than δh. In these cases the polarization response is included in the distribution function, resulting in a polarization density and current.

2.4 Tokamak Microturbulence

The primary steady-state losses in a tokamak occur due to the formation of drift wave instabilities at gyroradius length scales which are caused by the strong gradients and drift motions present in the plasma. The nonlinear dynamics of these microinstabilities can be modeled using the gyrokinetic system of equations. Drift waves exist over a wide range of spatial and temporal scales, as depicted in Figure 2.4(a), and obtaining analytical solutions is often highly complex, requiring numerous assumptions to derive individual dispersion relations and stability conditions. As a result, numerical solutions are crucial for understanding nonlinear drift wave dynamics and tokamak transport. However, many modes can often coexist in tokamak plasmas, and while numerical simulations provide the most practical approach, it can often be challenging to distinguish and isolate the contributions of individual modes [80].

Waves are typically classified by several characteristics: spatial scales associated with species gyroradii, whether waves are electrostatic or electromagnetic, and if wave-particle interactions involve trapped or passing particles. Additionally, modes are categorized as either "slab" or "toroidal",

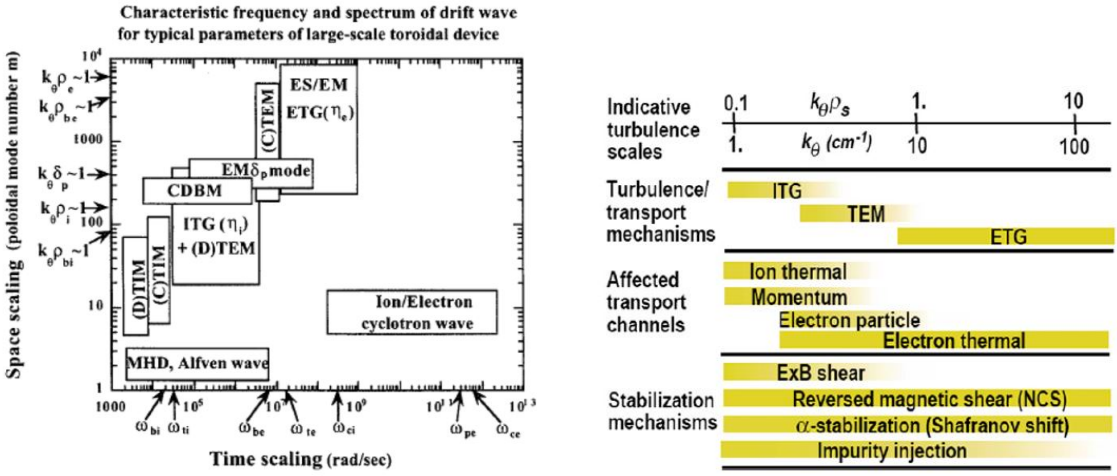

(a) (b)

Figure 2.4: (a) Comparison of spatial and temporal scales for various waves and instabilities, including ITG, ETG, and TEM. (b) Summary of electrostatic microturbulence by poloidal wavenumber, with associated transport channels and stabilizing mechanisms. Both figures from Ref. [38].

depending on whether toroidal geometry introduces significant destabilizing effects. Common electrostatic modes include ion-temperature-gradient (ITG) and electron-temperature-gradient (ETG) modes, which are destabilized at ion and electron gyroradius scales respectively, mainly by the corresponding temperature gradients. Furthermore, trapped ion and trapped electron modes (TIM/TEM) arise from wave-particle resonance due to trapped particle bounce motion. These modes are all driven unstable on the low-field side of the tokamak by the primary species' density and temperature gradients. Their physical characteristics can be mathematically described using the ballooning mode representation for high-n modes detailed in Appendix D [81–83]. A brief summary of the spatial scales of these electrostatic drift waves is given in Figure 2.4(b), along with associated transport channels and stabilization mechanisms. Sample plots of growth rates and stability contours are depicted in Figures 2.5(a) to 2.5(c).

While the aforementioned modes are electrostatic in nature, they can also be influenced by electromagnetic effects in tokamaks, where β is usually on the order of a few percent. Moreover, electromagnetic fluctuations involving magnetic field and vector potential components can also be driven unstable in a tokamak. Notable examples include the microtearing mode (MTM) and kinetic ballooning mode (KBM). A brief overview of electromagnetic effects in gyrokinetic simulation is

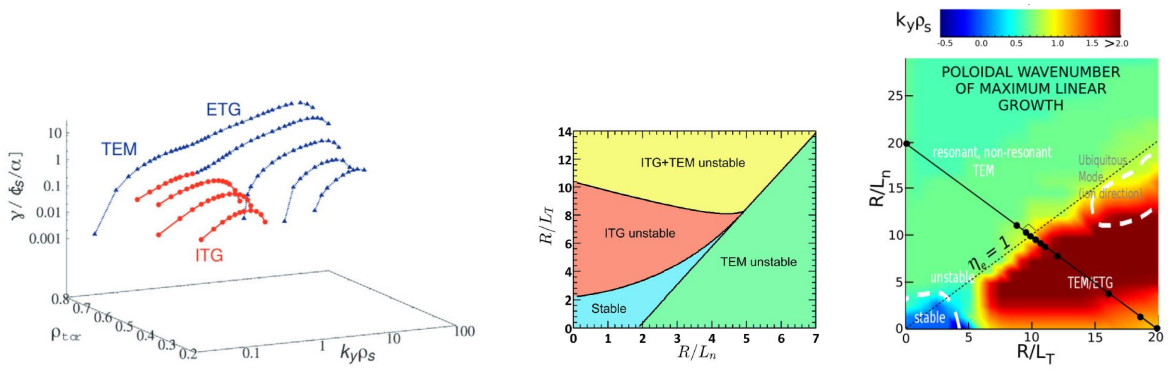

(a) (b) (c)

Figure 2.5: (a) Instability growth rates as a function of minor radius and k_y from linear GENE simulation results of JET discharge #70084 [84]. (b) ITG/TEM stability diagram [85]. (c) TEM/ETG stability diagram calculated from linear gyrokinetic GS2 simulations given $\nabla T_i = 0$ [86]. R/L_n and R/L_T are normalized equilibrium density and temperature gradients.

given in Ref. [87]. Another common instability is the Toroidal Alfvén Eigenmode (TAE), a high-n toroidal MHD-like Alfvénic mode, which is destabilized by interactions with high-energy particles. The following sections describe the ITG and ETG modes which are central to this thesis, while other modes which appear are mentioned briefly afterwards.

2.4.1 ITG Mode

The ion-temperature-gradient (ITG) instability or "η_i mode" is the typical ion-scale microinstability in the tokamak core, characterized by ion density and temperature fluctuations which drive ion heat and particle losses [88]. The electron response can be assumed to be drift-kinetic, $J_0(k_{\perp,i}\rho_e) \to 1$, given their much smaller cyclotron orbits, and equal electron particle transport is driven as the plasma must remain quasineutral. This equal flux effect is known as ambipolar diffusion. Extensive research has been conducted in investigating ITG transport utilizing gyrokinetic theory and simulation to the point of accurate prediction of experimental transport levels and flux spectra in local and global scenarios [89–95]. While simulation is often required for a full nonlinear dynamical description, linearization of the gyrokinetic equations is useful in understanding instability conditions and the physical drives of unstable modes.

The ITG dispersion relation is derived in Appendix C from the gyrokinetic equation and quasineutrality condition under simplifying assumptions which allow for analytic calculation. The final result is given to lowest order by Equation (C.13)

$$(1+\frac{1}{\tau}) = 1 - \frac{\omega_{*i}}{\omega} + 2\frac{\omega_{di}}{\omega}\cos\theta + \left(\frac{k_\parallel v_{th,i}}{\omega}\right)^2 - 2\frac{\omega_{di}\omega_{*i}}{\omega^2}(1+\eta_i)\cos\theta, \tag{2.68}$$

where $\tau = T_e/T_i$ and $v_{th,i} = \sqrt{T_i/m_i}$. Equation (2.68) admits two solutions of interest. For a homogeneous plasma and uniform magnetic field (∇n, ∇T, $\nabla B \to 0$) one finds

$$\omega^2 = k_\parallel^2 c_s^2, \tag{2.69}$$

which describes an acoustic wave along the field line with sound speed $c_s = \sqrt{T_e/m_i}$. Retaining the ion equilibrium and magnetic field gradients and assuming $k_\parallel \to 0$, the resulting dispersion relation is

$$\omega^2 - 2\tau\omega(\omega_{di} - \omega_{*i})\cos\theta + 2\tau\omega_{di}\omega_{*i}(1+\eta_i)\cos\theta, \tag{2.70}$$

where $\eta_i = n_0\nabla T_{0i}/T_{0i}\nabla n_{0i}$.

A simple formula for the ITG growth rate can be found by considering one last assumption of a flat density profile so that $\nabla n \to 0$ and one necessarily has $\eta_i \to \infty \gg 1$ and $\omega_{*i} \ll \omega_{di}$. The roots of Equation (2.70) then yield

$$\omega = \tau\omega_{di}\cos\theta \pm \sqrt{\cancel{\omega_{di}^2\cos^2\theta} - 2\tau\omega_{di}\omega_{*i}\eta_i\cos\theta}, \tag{2.71}$$

and the ITG growth rate is given by

$$\gamma = \sqrt{-2\frac{T_e}{T_i}\omega_{di}\omega_{*i}\eta_i\cos\theta} = \sqrt{-2\frac{T_e}{T_i}\nabla\ln T_i\cdot\nabla\ln B}. \tag{2.72}$$

Equation (2.72) indicates ITG modes are destabilized on the low-field side of the tokamak where the temperature and magnetic field gradient are both inward. The real frequency is on the order of the ion diamagnetic drift frequency ($\omega_{di} \sim \omega_{*i}/\nabla n$) and is usually taken to be the positive frequency/direction in gyrokinetic codes. The ITG mode can be stabilized by electromagnetic effects when β reaches around $1-2\%$ [96], as well as by background **ExB** flows which shear apart the radial turbulent eddies [97–99] (for spatial scales shown in Figure 2.4(b)). More detailed information regarding the ITG mode, including stability constraints and a more thorough kinetic derivation, can be found in Ref. [36].

2.4.2 ETG Mode

The ETG mode is a counterpart to the ITG mode which results in radially-elongated "streamers" at electron gyroradius scales [62, 63, 101, 102]. The basic mechanism that drives temperature-gradient

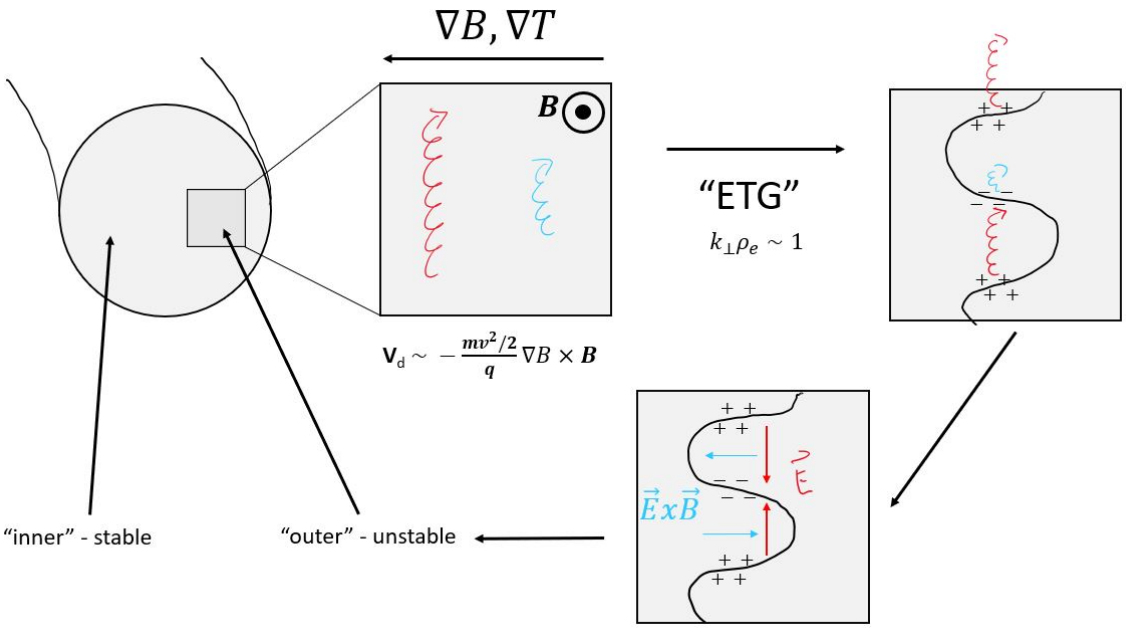

Figure 2.6: Standard depiction of the ETG instability mechanism at the outer side of the tokamak, inspired by Ref. [100]. The magnetic drift is the sum of grad-B and curvature contributions, and depends on the kinetic energy of the particle. This can lead to charge separation across a perturbation and a corresponding resonance and instability due to the resulting **E**x**B** motion.

instabilities is illustrated for the ETG mode in Figure 2.6, where a wave is driven unstable by electron drift motion at electron gyroradius scales. The magnetic drift of particles depends on the kinetic energy, and when there is a temperature perturbation the drifts on different sides of the wave will lead to charge separation. The resulting **E**x**B** drift can then act to destabilize or suppress the wave. In the linear, electrostatic, adiabatic-ion case the ETG mode is isomorphic to the counterpart ITG case considered in the previous section, and all the same results hold with the species indices swapped. While adiabatic electrons is often not a good approximation for ITG turbulence as electron gyroradii are much smaller than ITG wavelengths ($J_0(k_{\perp,i}\rho_e) \to 1$), the ion response to ETG turbulence is near adiabatic given the much shorter wavelengths ($J_0(k_{\perp,e}\rho_i) \to 0$).

However, the ETG mode differs in many ways. The ETG drift motion is in the opposite direction of the ITG mode, and ETG wavelengths are on the order of the electron gyroradius so quasineutrality is not always ensured as in the case of ITG modes. Furthermore, gyroBohm estimates

of ETG transport lead to much lower expected levels of heat flux than from ITG transport, but often ETG modes can produce relevant levels of electron thermal transport. As a result, the ETG mode is a leading candidate to explain excess electron thermal losses in tokamaks - a topic which remains an area of active research [37–39, 93, 103]. Experimental validation of ETG modes is complicated by the difficulty of direct measurement given the fine scale of the fluctuations [104]. Due to the much shorter wavelengths and higher linear growth rate, ETG modes are not generally affected by background **E**x**B** shear flows [38, 105]. Additionally, ETG modes are destabilized by electromagnetic effects [106]. These two facts are contrary to finite-beta and background shear flow effects on ITG modes, and this often results in ETG modes becoming important when ITG modes are suppressed, particularly in spherical tokamaks [107, 108] or the edge pedestal [109, 110]. A recent overview of ETG turbulent transport is given in Ref. [111].

2.4.3 Other Modes (TEM/KBM/MTM/TAE)

While not central to the work in this thesis, additional modes which are encountered are briefly discussed here. TEMs are one such mode which exist in the scale $k_y\rho_i \sim 0.50 - 2.0$ intermediate to ITG and ETG modes. They are driven by the resonant wave-particle interaction due to the toroidal precessional drift of trapped electrons [112–114]. TEMs are another possible candidate for explaining excess electron thermal losses, but can also drive electron particle transport as well. Like ETG modes, TEM stability depends on the electron temperature and density gradients, but they can usually be differentiated by their ion-scale wavelengths and further dependence on the aspect ratio $\epsilon = r/R$.

In addition to electrostatic modes, various electromagnetic modes are present in tokamak plasmas. Kinetic ballooning modes are ion-scale electromagnetic modes which involve resonances due to magnetic drifts [115]. KBMs can be viewed as a type of interchange mode, where their instability is driven by a combination of the pressure gradient and magnetic curvature effects. KBMs are destabilized by electromagnetic effects, particularly in the tokamak core. Similar to ITG modes, they propagate in the ion diamagnetic and exhibit even (odd) parity of electrostatic (magnetic)

fluctuations along field lines.

Micro-tearing modes are electromagnetic instabilities analogous to the MHD tearing instabilities which exist at larger scales, and often drive significant electron thermal transport losses due to the electron temperature gradient and electron-ion collisions [116]. These are typically the dominant ion-scale modes in the tokamak pedestal, coexisting with the ETG turbulence present there [117]. MTMs can be identified by motion in the electron diamagnetic direction and even (odd) parity of magnetic (electrostatic) fluctuations along the field line.

The last mode considered here is the TAE mode [118]. These are high-n MHD modes which are driven unstable in the presence of energetic particles, such as from NBI or fusion α-particle heating. TAE modes are electromagnetic, with frequencies on the order of the Alfvén frequency $\omega = k_{\|} v_A$, where $v_A = B/\sqrt{\mu_0 \rho}$ is the Alfvén speed. TAEs enhance transport of energetic particles, leading to reduced confinement and potential damage of the vessel walls [119].

2.4.4 Mode Regulation and Zonal Flows

Nonlinear dynamics in the perpendicular plane play a crucial role in regulating drift wave instabilities and determining steady-state turbulent transport levels. As instabilities grow exponentially, the **E**x**B** nonlinearity in the gyrokinetic equation becomes significant, leading to the generation of zonal flows (ZFs) through turbulent stresses. Zonal flows are poloidal **E**x**B** flows which do not directly drive transport. Instead, they act as a self-regulating mechanism, distorting and breaking apart turbulent eddies, thereby reducing radial correlation lengths and reducing transport levels. Physically, ZFs correspond to $n = 0$ elecrostatic potential fluctuations with zero frequency, characterized solely by an electric field component in k_r. The poloidal shearing rate is commonly defined as $\gamma_{E'} = d\mathbf{v}_E/dr \sim \nabla_r E_r$, and shear effects become significant as this rate approaches or exceeds the mode growth rate, $\gamma_{E'} > \gamma$ [6]. Zonal flows are now recognized to be an important loss mediator for many cases of drift-wave turbulence [120].

Heuristic models of mode regulation via zonal flow shearing often rely on the standard mixing-length estimate, $D \sim \gamma/k_\perp^2$ [6, 121, 122], which describes a balance between instability growth and

turbulent diffusion in the perpendicular plane. Mixing-length models for turbulent transport and their role in quasilinear modeling are discussed further in Chapter 3. Zonal flow amplitudes are themselves regulated by collisional damping [120], and the system ultimately reaches a fluctuating quasi steady-state, alternating between instability growth and self-regulated shearing. As dynamics in the perpendicular plane are highly nonlinear and turbulent, gyrokinetic simulations provide an important tool in accurately predicting steady-state transport levels for experimental tokamak scenarios. Additionally, background shear flows generated by equilibrium electric fields provide an effective mechanism for suppressing long-wavelength microturbulence such as ITG modes [99, 123]. The emergence of mean **ExB** shear flows is critical in the formation of transport barriers and the transition from L-mode to H-mode operation.

2.5 Gyrokinetic Codes

Numerical codes which solve the gyrokinetic Vlasov-Maxwell system of equations have been extensively developed over the previous decades, where simulation efforts have largely been made possible by significant increases in available computing power [40]. Gyrokinetic simulations have since become a crucial link in simulating tokamak turbulence and connecting turbulent transport theory to experimental measurements [124–138]. Multiple techniques can be employed for plasma simulation, which can be broadly categorized as follows

(1) Eulerian: Such codes solve the gyrokinetic Vlasov-Maxwell equations by direct discretization on a 5-D phase-space grid using standard discretization methods like finite difference, element, or volume. These are often highly accurate in phase-space, but computationally expensive given high order schemes and high dimensionality. Eulerian codes are limited in time-step by the Courant-Friedrichs-Lewy (CFL) condition. Examples include GENE [62] and CGYRO [139].

(2) Particle-in-Cell (PIC): PIC codes simulate a plasma as a reduced collection of discrete macro-particles which interact with fields on a coarse grid in real-space. While these can be

more efficient due to the lower grid dimensionality, statistical noise presents a problem if the number of particles is too low. Examples of PIC codes include GEM [140] and XGC [141].

(3) Semi-Lagrangian: This represents a hybrid approach in which the distribution function is tracked along particle trajectories and moments are evaluated after interpolating onto a phase-space grid. GYSELA is one such code [142].

Given the availability of various simulation methods and their different strengths and limitations, code benchmarking has become an essential tool for reliable validation of gyrokinetic simulation results [143–147]. By comparing results across different codes, benchmarking helps identify numerical errors and builds confidence in predictive capabalities for direct experimental comparison.

Two different gyrokinetic codes are employed to study turbulent transport in this thesis - the continuum code GENE and the PIC code GEM. GENE is primarily used to study ETG turbulence and zonal flow generation in the local flux-tube limit in Chapter 4. In this approach, the system is confined to a single flux surface, assuming $\rho_j/L \to 0$, which retains only first order effects through spatial gradients in equilibrium quantities ($\nabla n, \nabla T, \hat{s}$, etc.). This simplification enables a Fourier representation in the radial direction with perpendicular box sizes on the order of hundreds of gyroradiii of the species of interest, while parallel box sizes extend along field lines to capture the full parallel ballooning mode structure from unstable to stable regions. GEM is largely run using a global model in Chapter 5 to incorporate local ETG effects from GENE into global ITG simulations, which range over a large radial domain of the tokamak. As a PIC code, GEM is efficient and robust for carrying out ITG simulations over global radial scales; however, it suffers more from particle noise issues at electron gyroradius scales and GENE is instead used for local ETG simulations to capture phase-space dynamics more accurately. GENE and GEM are described briefly in the following sections.

2.5.1 GENE

GENE (Gyrokinetic Electromagnetic Numerical Experiment) is a gyrokinetic Eulerian code which solves the nonlinear gyrokinetic equations for multiple particle species on a 5-D grid in phase space to carry out nonlinear simulations of tokamak microturbulence. It can also be run linearly to calculate the various eigenmodes (real and complex frequencies) of the drift wave instabilities, where GENE defines the ion diamgnetic frequency to be positive. Furthermore, GENE is parallelized for use on CPU and GPU supercomputing clusters using the Message Passing Interface (MPI) protocol. The information presented here is compiled directly from the GENE reference manual and various theses which directly utilize or advance GENE; readers are encouraged to consult these works for more detailed explanation [148–151].

The gyrokinetic equation for the gyrocenter distribution function of each species, $F_s(\mathbf{X}, v_\parallel, \mu)$, solved by GENE is given here in CGS units with electromagnetic and collisions

$$\frac{\partial F_s}{\partial t}+\left(v_\parallel\hat{\mathbf{b}}+\frac{B_0}{B_{0\parallel}^*}(\frac{c}{B_0}\hat{\mathbf{b}}_0\times\nabla\chi_s+\mathbf{v}_d)\right)\cdot\left(\nabla F_s+\frac{1}{mv_\parallel}(q_s\langle\mathbf{E}_1\rangle-\mu\nabla(\mathbf{B}_0+\langle\mathbf{B}_{1\parallel}\rangle)\frac{\partial F_s}{\partial v_\parallel})\right)=\langle C_s(F)\rangle, \tag{2.73}$$

where $\chi_s=\langle\phi\rangle-\frac{v_\parallel}{c}\langle A_{1\parallel}\rangle$ and $B_{0\parallel}^*=\hat{\mathbf{b}}\cdot(\nabla(\mathbf{A}+\frac{m_sc}{q_s}v_\parallel\hat{\mathbf{b}}))$. Angled brackets denote a gyroaverage above. GENE uses a δf-splitting method where Equation (2.73) is split up by order for F_{0j} and the small-scale perturbation f_j. The field equations are given by

$$\nabla_\perp^2\phi_1=-4\pi\sum_s q_sn_{1s}, \tag{2.74}$$

$$\nabla_\perp^2A_{1\parallel}=-\frac{4\pi}{c}\sum_s j_{1\parallel s}, \tag{2.75}$$

$$\nabla_\perp^2B_{1\parallel}=-4\pi\sum_s\frac{p_{1\perp s}}{B_0}, \tag{2.76}$$

where the charge density, current density, and perpendicular pressure are calculated by taking

moments of the total distribution function

$$n_{1s} = \frac{2\pi B_0}{m_s} \int dv_\parallel d\mu \left[J_0 h_{1s} - \frac{q_s \phi_1}{T_{0s}} F_{0s} \right], \tag{2.77}$$

$$j_{1\parallel s} = q_s \frac{2\pi B_0}{m_s} \int dv_\parallel d\mu v_\parallel \left[J_0 h_{1s} - \frac{q_s \phi_1}{T_{0s}} F_{0s} \right], \tag{2.78}$$

$$p_{1\perp s} = \frac{2\pi B_0}{m_s} \int dv_\parallel d\mu \mu B_0 I_1 h_{1s}. \tag{2.79}$$

Here h_{1s} is the non-adiabatic part of f_1, defined by

$$h_{1s} = f_{1s} + [q_s J_0 \phi_1 + \mu I_1 B_{1\parallel}] \frac{F_{0s}}{T_{0s}}, \tag{2.80}$$

with $J_0 = J_0(k_\perp \rho)$ and $I_1 = 2J_1(k_\perp \rho)/(k_\perp \rho)$ involving Bessel functions of the first kind. Note that Maxwell's equations are calculated in particle space and the guiding-center distribution function must be transformed using a pull-back operator.

The magnetic geometry and spatial dynamics are described by a field-aligned coordinate system which takes advantage of the anisotropic motion in a strongly magnetized plasma. The coordinates, labeled x, y, and z, represent the radial, binormal, and parallel directions

$$\begin{aligned} x &= \rho, \\ y &= C_y[q(\rho)\theta - \zeta], \\ z &= \theta. \end{aligned} \tag{2.81}$$

Here, ρ is the flux-surface label, θ is the straight-field-line poloidal angle, ζ is the toroidal angle, and $C_y = \rho_0/q_0$, with ρ_0 and q_0 taken at a reference position generally at the center of the simulation domain. Periodicity in the toroidal angle can be expressed using Equation (2.81) in the field-line-following coordinates as

$$f(x, y, z) = f(x, y - C_y 2\pi, z). \tag{2.82}$$

Therefore, to capture a full toroidal turn requires $L_y = 2\pi C_y$, and k_y is related to the toroidal mode number n as

$$k_y = nk_{y,\min} = n\frac{2\pi}{L_y} = \frac{n}{C_y}. \tag{2.83}$$

The poloidal periodicity constraint becomes

$$f(x,y,z) = f(x, y + 2\pi q C_y, z + 2\pi) = f(x, y + 2\pi q/k_{y,\min}, z + 2\pi). \tag{2.84}$$

Represented in Fourier space, Equation (2.84) can be rewritten as

$$f(x,k_y,z) = f(x,k_y,z+2\pi)e^{i2\pi jq(x)}. \tag{2.85}$$

In the global version of the code this is how the parallel boundary condition is enforced, however in the local flux-tube approximation $q(x)$ must be Taylor expanded to first order resulting in $q(x) \approx q_0 + (x - x_0)\hat{s}/x_0$. Expanding into Fourier modes in x and y, Equation (2.85) becomes

$$f(x,y,z) = \sum_{k_x,k_y} f(k_x,k_y,z)e^{ik_x x} = \sum_{k_x,j} f(k_x,k_y,z+2\pi)e^{ik_x x}e^{i2\pi jq_0}e^{i2\pi j\hat{s}(x-x_0)/C_y}, \tag{2.86}$$

which requires $k_x' = k_x + 2\pi\hat{s}k_y$ and the perpendicular box-size quantization $\mathcal{N} = 2\pi\hat{s}L_x/L_y$. Note that due to the finite shear and radial extent of the domain the perpendicular domain will be sheared as one moves along field lines.

Time-stepping of the gyrokinetic Vlasov equation is handled by a fourth-order explicit Runge-Kutta method. The initial time step is chosen close to a minimum based on linear mode stability, generally set by the parallel streaming of electrons in multi-species runs. However, an adaptive time step is used as fluctuations grow and the CFL condition must be accounted for given nonlinear terms. Rather than timestepping, a linearized version of the gyrokinetic equation can also be solved by eigenvalue computation using the PETSc/SLEPc numerical packages. Discretization along the field in z and $v_\parallel$ is handled by a fourth-order Arakawa scheme [152] which conserves free energy,

while perpendicular dimensions are handled pseudo-spectrally in the local flux-tube limit. The pseudo-spectral method considers calculation of linear terms in Fourier space, but evaluation of nonlinear terms as products in real space. Nonlinear products result in modenumbers too high to be resolved by the initial grid, and unresolved modes are removed by a three-halves dealiasing scheme [153] or by a more efficient phase-space dealiasing scheme [154]. In the global version of the code radial variation is maintained and Dirichlet or Neumann boundary conditions must be utilized which allow the equilibrium profiles to relax over time due to transport losses. Radial discretization is handled globally with a mixed Fourier-space/real-space version of the fourth order Arakawa scheme.

Integration in velocity space employs trapezoidal and Gauss-Laguerre quadrature rules for $v_\parallel$ and μ directly. Velocity distributions are assumed to be Maxwellian, and default box sizes in $v_\parallel$ and μ range within $\pm 3 v_{th,s} = \pm 3\sqrt{2T_s/m_s}$ and $0 - 9\ T_s/B_0$ respectively. Collisions are modeled using a linearized Landau-Boltzmann operator [149] and finite volume discretization, or more recently with a Sugama-type collision operator [155]. All quantities in GENE are normalized such that dimensionless values are of order unity. Gradients of equilibrium quantities are given by a macroscopic length scale L_{ref}, which GENE allows users to specify along with reference magnetic field, density, temperature, mass, charge, and toroidal angular velocity - $B_{\text{ref}}, n_{\text{ref}}, T_{\text{ref}}, m_{\text{ref}}, \Omega_{\text{tor,ref}}$. Various other reference quantities are derived from these, including

$$\begin{gathered} p_{\text{ref}} = n_{\text{ref}} T_{\text{ref}}, \quad c_{\text{ref}} = \sqrt{T_{\text{ref}}/m_{\text{ref}}}, \quad \Omega_{\text{ref}} = \frac{q_{\text{ref}} B_{\text{ref}}}{m_{\text{ref}} c}, \\ \rho_{\text{ref}} = c_{\text{ref}}/\Omega_{\text{ref}}, \quad \rho^* = \rho_{\text{ref}}/L_{\text{ref}}, \quad \beta_{\text{ref}} = 8\pi p_{\text{ref}}/B_{\text{ref}}^2. \end{gathered} \tag{2.87}$$

Normalized quantities for each phase-space dimension and time are given with hats as

$$\begin{gathered} t = \hat{t}\frac{L_{\text{ref}}}{c_{\text{ref}}}, \quad x = \hat{x}\rho_{\text{ref}}, \quad y = \hat{y}\rho_{\text{ref}}, \quad z = \hat{z}, \\ v_{\parallel,s} = \hat{v}_\parallel \hat{v}_{th,s} c_{\text{ref}}, \quad \mu_s = \hat{\mu}\hat{T}_s \frac{T_{\text{ref}}}{B_{\text{ref}}}, \end{gathered} \tag{2.88}$$

where quantities with subscript s represent specific species quantities and $v_{th,s} = \sqrt{2\hat{T}_s/\hat{m}_s}$. The

distribution functions are normalized as

$$F_{0s} = \hat{F}_{0s}\frac{n_{\rm ref}}{c_{\rm ref}^3}\frac{\hat{n}_{0s}}{\hat{v}_{th,s}^3}, \quad f_s = \hat{F}_{0s}\frac{n_{\rm ref}}{c_{\rm ref}^3}\frac{\hat{n}_{0s}}{\hat{v}_{th,s}^3}\rho^*, \tag{2.89}$$

and the field fluctuations as

$$\phi = \hat{\phi}\frac{T_{\rm ref}}{e}\rho^*, \quad A_\parallel = \hat{A}_\parallel \rho_{\rm ref} B_{\rm ref}\rho^*, \quad B_\parallel = \hat{B}_\parallel B_{\rm ref}\rho^*. \tag{2.90}$$

Lastly, the gyroBohm normalized fluxes are defined for electrostatic turbulence in GENE as ITG and ETG transport will largely be reported in this thesis. The normalized flux-surface-averaged particle and heat fluxes driven by radial **ExB** transport are defined by

$$\frac{\Gamma_s}{\Gamma_{gB}} = \frac{\Gamma_s}{n_{\rm ref}c_{\rm ref}(\rho^*)^2} = -\frac{\hat{n}_{0s}}{\int_{-\pi}^{\pi}\hat{J}d\hat{z}}\int_{-\pi}^{\pi}d\hat{z}\sum_{\mathbf{k}}\hat{J}i\hat{k}_y\bar{\hat{\phi}}(\mathbf{k})\left(\pi\hat{B}_0\int d\hat{v}_\parallel d\hat{\mu}\hat{f}_s(\mathbf{k})\right)^*, \tag{2.91}$$

$$\frac{Q_s}{Q_{gB}} = \frac{Q_s}{n_{\rm ref}T_{\rm ref}c_{\rm ref}(\rho^*)^2} = -\frac{\hat{n}_{0s}\hat{T}_{0s}}{\int_{-\pi}^{\pi}\hat{J}d\hat{z}}\int_{-\pi}^{\pi}d\hat{z}\sum_{\mathbf{k}}\hat{J}i\hat{k}_y\bar{\hat{\phi}}(\mathbf{k})\left(\pi\hat{B}_0\int d\hat{v}_\parallel d\hat{\mu}\hat{v}^2\hat{f}_s(\mathbf{k})\right)^*. \tag{2.92}$$

Here, $\bar{\phi}$ is the gyroaveraged electrostatic potential, and the normalized radial **ExB** velocity which has been used is defined as

$$\mathbf{v}_E\cdot\mathbf{e}_x = -\frac{\rho_{\rm ref}c_{\rm ref}}{L_{\rm ref}}i\hat{k}_y\bar{\hat{\phi}}. \tag{2.93}$$

The spatial average of the product $(\phi * f_s)$ in Fourier space simplified using

$$\langle A(\mathbf{X})B(\mathbf{X})\rangle = \frac{\int_{-\pi}^{\pi}\sum_{\mathbf{k}}dzJA(\mathbf{k},z)B^*(\mathbf{k},z)}{\int_{-\pi}^{\pi}Jdz}, \tag{2.94}$$

with $\mathbf{X}$ the guiding-center coordinate. Often times the particle and heat diffusivities D and χ are reported, which are related to the normalized fluxes by

$$\frac{\Gamma_s}{\Gamma_{gB}} = \hat{D}_s\hat{\omega}_{ns}, \quad \frac{Q_s}{Q_{gB}} = \hat{n}_{0s}\hat{\chi}_s\hat{\omega}_{Ts}, \tag{2.95}$$

for normalized gradients $\hat{\omega}_{ns} = -L_{\text{ref}}\frac{\nabla n_{0s}}{n_{0s}}$ and $\hat{\omega}_{Ts} = -L_{\text{ref}}\frac{\nabla T_{0s}}{T_{0s}}$.

2.5.2 GEM

GEM (Gyrokinetic ElectroMagnetic) is a numerical code which solves the gyrokinetic equations using a PIC approach - the earliest method applied to gyrokinetic simulation [71]. Much of the information here can be found in more detail in the GEM manual [156] and various papers describing GEM [140, 157–161]. GEM supports electromagnetic effects [140], a pitch-angle scattering collision operator, drift-kinetic electrons [158], general magnetic equilibria [159], flux-tube and radially global simulation, subsonic equilibrium flows, and energetic particle species. In traditional PIC simulations the distribution function is sampled by a large number of particles which are averaged onto a coarser grid on which moments are calculated. GEM employs the δf PIC method, where particle weights are defined as $w = \delta f/f$, an approach originally developed to efficiently reduce particle noise [162, 163]. Particle weights are advanced by the gyrokinetic Vlasov equation

$$\frac{dw}{dt} = -\frac{1}{f_M}\left((\mathbf{v}_E + v_\parallel\frac{\delta\mathbf{B}_\perp}{B_0})\cdot\nabla f_M + \dot{\epsilon}_k\frac{\partial f_M}{\partial\epsilon_k}\right), \tag{2.96}$$

where $f_M = f_M(\mathbf{R}, \epsilon_k)$ is the Maxwellian distribution, which is a function of guiding-center and the lowest order particle energy $\epsilon_k = mv_\parallel^2/2 + \mu B$, and $\delta f = \delta f(\mathbf{R}, \mu, v_\parallel, t)$ is the fluctuating first-order distribution function. As a PIC code, GEM consists of two parts: a particle push and a field solve. Particles are evolved by interpolating field values from nearby grid locations, known as the "gather" process. Charge density and current are accumulated on grid points by a process known as "deposition". Time advancement of Equation (2.96) is handled using an explicit second order Runge-Kutta scheme. GEM is parallelized on CPU and GPU, with particle loops parallelized using either the Open Multi-Processing (OpenMP) or Open Accelerators (OpenACC) software packages, while the toroidal geometry is parallelized along field lines using MPI. Figure 2.7 depicts TAE turbulence in a global GEM simulation.

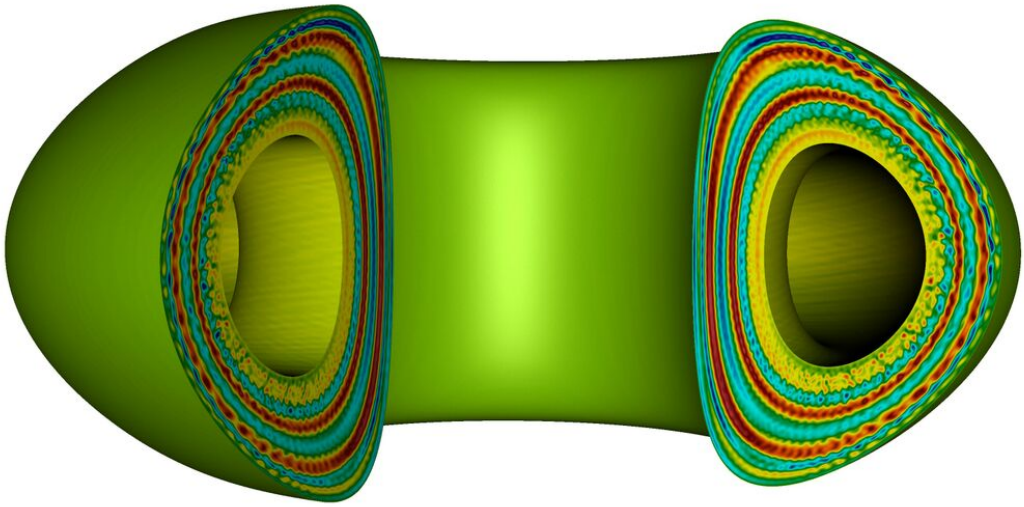

Figure 2.7: Global GEM simulation results depicting TAE mode turbulence [156].

The total time derivative of the energy quantity is defined as

$$\dot{\epsilon_k} = q\mathbf{v}_G \cdot (-\nabla\phi - \frac{\partial A}{\partial t}\hat{\mathbf{b}}), \tag{2.97}$$

with $\mathbf{v}_G$ the overall guiding-center drift. In explicit finite difference schemes the appearance of the $\partial A_\parallel/\partial t$ term leads to numerical instability. Implementation of an implicit method is more complicated in PIC codes and is handled by switching coordinates from parallel velocity ($v_\parallel$) to parallel momentum ($p_\parallel$) [164]. The rate of change of the energy variable then becomes

$$\dot{\epsilon}_p = -q\mathbf{v}_G \cdot \nabla\langle\phi\rangle - \frac{q}{m}\langle A_\parallel\rangle\hat{\mathbf{b}} \cdot \mu\nabla B + qp_\parallel \mathbf{v}_G \cdot \nabla\langle A_\parallel\rangle, \tag{2.98}$$

and the distribution function is redefined here for loaded particles, giving the new weight equation

$$\frac{dw}{dt} = -\frac{1}{g_0}\left((\mathbf{v}_E + v_\parallel\frac{\delta\mathbf{B}_\perp}{B_0}) \cdot \nabla f_M + \dot{\epsilon}\frac{\partial f_M}{\partial \epsilon_p}\right). \tag{2.99}$$

The term $g_0 = (1/(2\pi T)^{3/2})e^{-(\mu B + mp_\parallel^2/2)/T}$ represents the loaded marker particle distirbution function. The numerical representation of g_0 (given by a "$\sim$") is

$$\begin{aligned}\tilde{g} &= \frac{V}{N_p}\sum_j \delta(\mathbf{x}-\mathbf{x}_j)\delta(\mathbf{v}-\mathbf{v}_j) \\ &= \frac{V}{N_p}\sum_{j,l}\frac{1}{N}\frac{1}{\mathcal{J}}\delta(\mathbf{R}-\mathbf{R}_j)\delta(\mu-\mu_j)\delta(v_\parallel - v_{\parallel j})\delta(\gamma-\gamma_{jl}),\end{aligned} \tag{2.100}$$

for j the particle index, N_p the total particle number, V the total volume, $\mathcal{J}$ the Jacobian of the guiding-center coordinate transformation, and the subscript l denoting an N-point gyroaverage. Generally a four-point gyroaveraging is sufficient [71] and is used in GEM. For ion-scale turbulence, electrons are handled in the drift-kinetic limit ($k_\perp \rho_e \to 0$), and fluctuating quantities are unchanged by gyroaveraging. The distribution function and moments giving the density and current are calculated as

$$\delta\tilde{f} = w_j\tilde{g}, \tag{2.101}$$

$$\delta\tilde{n} = \frac{V}{N_p}\sum_{j,l}\frac{1}{N}w_j\delta(\mathbf{x}-\mathbf{R}-\boldsymbol{\rho}_{jl}), \tag{2.102}$$

$$\delta\widetilde{j}_\parallel = \frac{V}{N_p}\sum_{j,l}\frac{1}{N}v_\parallel w_j\delta(\mathbf{x}-\mathbf{R}-\boldsymbol{\rho}_{jl}), \tag{2.103}$$

and the particle shape in real space is given by

$$\begin{aligned}\delta(\mathbf{x}-\mathbf{x}_j) &\approx \frac{1}{J(x,z)}\frac{1}{\Delta x\Delta y\Delta z}S_{1D}(\frac{x-x_j}{\Delta x})S_{1D}(\frac{y-y_j}{\Delta y})S_{1D}(\frac{z-z_j}{\Delta z}), \\ S_{1D}(x) &= \begin{cases} 1-|x| & |x|\ll 1 \\ 0 & |x|>1 \end{cases}.\end{aligned} \tag{2.104}$$

The ion weight equation in GEM is defined as

$$\dot{w}_i = -\left[(\mathbf{v}_E + v_\parallel\frac{\delta\mathbf{B}_\perp}{B_0})\cdot\frac{f_M}{f} + \frac{q}{T}(\mathbf{v}_G\cdot\nabla\langle\phi\rangle - \dot{v}_\parallel\langle A_\parallel\rangle + v_\parallel\mathbf{v}_G\cdot\nabla\langle A_\parallel\rangle)\right]\frac{f_M}{g_0}. \tag{2.105}$$

Furthermore, GEM uses a split-weight scheme to model kinetic electrons [157, 165]. The updated electron weight is defined as

$$w_e = w - \epsilon_g \frac{e\phi}{T_e}\frac{f_M}{g_0}, \tag{2.106}$$

where ϵ_g represents a free parameter which is 1 for adiabatic electrons. The electron weight equation then becomes

$$\begin{aligned}\frac{dw_e}{dt} = -\Bigg[(\mathbf{v}_E + v_\parallel \frac{\delta \mathbf{B}_\perp}{B_0})\cdot\nabla f_M + \frac{e}{T}\left(-\mathbf{v}_G\cdot\nabla\phi + \dot{v}_{\parallel 0}A_\parallel - \frac{\mu}{m}(\hat{\mathbf{b}}\cdot\nabla B_0)\mathbf{v}_G\cdot\nabla A_\parallel\right) \\ + \epsilon_g\frac{e}{T_e}(\dot{\phi}(\mathbf{x}_j) + \mathbf{v}_G\cdot\nabla\phi|_{\mathbf{x}_j})\Bigg]\frac{f_M}{g_0}.\end{aligned} \tag{2.107}$$

The solution for $\dot{\phi}$ above is given by the vorticity equation, which is the partial time derivative of the quasi-neutrality equation

$$-q\dot{n}_p = q\partial_t\overline{\delta n_i} - e\partial_t\delta n_e, \tag{2.108}$$

where n_p is the polarization density

$$n_p = -\int \frac{q}{T}(\phi(\mathbf{x}) - \langle\phi\rangle)f_M d\mathbf{v} = -\sum_{k_\perp}\frac{qn_0}{T}(1-\Gamma_0(b))\phi_{k_\perp}e^{ik_x x + ik_y y}, \tag{2.109}$$

with $b = k_\perp^2\rho^2$ and $\Gamma_0(b) = I_0(b)e^{-b}$ given a local Fourier representation. Using an analytic form of Ampere's law results in a cancellation problem and a properly discretized numerical form must be used [158]. The solution to the ion and electron parallel currents become

$$\frac{1}{q}\delta j_{\parallel i} = \frac{V}{N_p}\sum_j\frac{1}{N}\sum_l\left(w_i - qv_\parallel\frac{\langle A\rangle_\parallel}{T_i}\frac{f_M}{g_0}\right)_j v_{\parallel j}\delta(\mathbf{x} - \delta R_j - \boldsymbol{\rho}_{jl}), \tag{2.110}$$

$$-\frac{1}{e}\delta j_{\parallel e} = \frac{V}{N_p}\sum_j\left(w_e + \epsilon_g\frac{e\phi}{T_e}\frac{f_M}{g_0} + ev_\parallel\frac{A_\parallel}{T_e}\frac{f_M}{g_0}\right)_j v_{\parallel j}\delta(\mathbf{x} - \delta R_j). \tag{2.111}$$

Collisions are modeled with a Lorentzian operator, where random changes to particle pitch angles are calculated using a Monte-Carlo method.

GEM defines the field-line-following coordinate system

$$\begin{aligned} x &= r - r_0 \\ y &= (\int_0^\theta \hat{q}(r,\theta')d\theta' - \zeta) = \frac{r_0}{q_0}(q\theta_f - \zeta) \\ z &= q_0 R_0 \theta, \end{aligned} \tag{2.112}$$

in the large aspect-ratio limit, where R_0 and q_0 are arbitrary, usually taken to be on the magnetic axis and at the center of the domain respectively. The Jacobian of the coordinate system is given by

$$\frac{1}{\mathcal{J}} = \nabla z \cdot \nabla x \times \nabla y = \frac{r_0 R_0}{R} |\nabla r \times \nabla \theta|. \tag{2.113}$$

The simulation domain is a rectangle of dimensions $L_x \times L_y \times L_z$ with $L_x = r_{\rm out} - r_{\rm in}$ and $L_z = 2\pi|q_0|R_0$. The domain size in y is generally chosen to be a wedge of the tokamak, $L_y = 2\pi r_0/|q_0|/lymult$, for the fundamental toroidal mode number $n = lymult$. The endpoints of the z domain are the high-field sides $\pm\pi$. The domain conditions $r_{\rm in} \le r \le r_{\rm out}$, $-\pi \le \theta < \pi$, and $\zeta \in [0, 2\pi)$, can be mapped onto a rectangle to find new coordinate definitions

$$\begin{aligned} x &= r - r_0 + L_x/2, \\ y &= \mod \left((\frac{r_0}{q_0})(\int_0^\theta \hat{q}(r,\theta')d\theta' - \zeta), L_y \right), \\ z &= q_0 R_0 (\theta + \pi q_0/|q_0|), \end{aligned} \tag{2.114}$$

where $\mod(x, 2\pi)$ means modulus of x by 2π. Quantities are periodic in θ and ζ, but not y and z. A shift occurs in y as one moves from $(\theta = -\pi, \zeta)$ to $(\theta = \pi, \zeta)$, where

$$y(r, \theta = \pi, \zeta) = \mod \left[y(r, \theta = -\pi, \zeta) + 2\pi \frac{r_0}{q_0} q(r), L_y \right]. \tag{2.115}$$

That is, if particles move outside the simulation box in z they continue at the other end, but with their value in y shifted by $2\pi r_0 q(r)/q_0$. In local simulations, the boundary condition in x is also

periodic. Global simulations use Dirichlet boundary conditions, and particles which move beyond the radial boundaries are relocated according to their equilibrium trajectories. To ensure numerical steady-state turbulence and transport a numerical heat source is applied to all particles in global simulations [160].

Units for temperature, density, and the magnetic field can be arbitrarily chosen, with B usually taken at the magnetic axis, while other normalization values are accordingly calculated. These units are denoted by a subscript u as

$$\begin{gathered} m_u = m_p, \quad q_u = e, \quad v_u = \sqrt{T_u/m_u}, \quad x_u = m_u v_u/q_u B_u, \quad \omega_u = eB_u/m_u, \\ t_u = 1/\omega_u, \quad j_u = en_u v_u, \quad A_u = T_u/ev_u, \quad \phi_u = T_u/e, \quad E_u = \phi_u/x_u. \end{gathered} \tag{2.116}$$

Particle and heat fluxes, or their associated diffusivities, are among the most commonly used quantities for comparison with experimental transport losses. The fluxes normalized to gyroBohm units are given by

$$\begin{aligned} \Gamma_{gB} &= n_e c_s \left(\frac{\rho_s}{a}\right)^2 \\ Q_{gB} &= n_e T_e c_s \left(\frac{\rho_s}{a}\right)^2, \end{aligned} \tag{2.117}$$

for $c_s = \sqrt{T_e/m_i}$ and $\rho_s = c_s/\Omega_i$. Flux values are calculated by averaging over a volume V_s in GEM according to

$$\Gamma = \frac{1}{V_s}\int \delta f \left(\frac{\mathbf{E}\times\hat{\mathbf{b}}}{B_0} + v_\parallel \frac{\delta \mathbf{B}_\perp}{B_0}\right)\cdot\frac{\nabla r}{|\nabla r|} d\mathbf{x}d\mathbf{v} = \frac{1}{V_s}\sum_{j\in V_s} w_j \left(v_{Er} + v_\parallel \frac{\delta B_r}{B_0}\right), \tag{2.118}$$

$$Q = \frac{1}{V_s}\int \frac{1}{2}mv^2\delta f \left(\frac{\mathbf{E}\times\hat{\mathbf{b}}}{B_0} + v_\parallel \frac{\delta \mathbf{B}_\perp}{B_0}\right)\cdot\frac{\nabla r}{|\nabla r|} d\mathbf{x}d\mathbf{v} = \frac{1}{V_s}\sum_{j\in V_s} w_j \frac{1}{2}mv^2 \left(v_{Er} + v_\parallel \frac{\delta B_r}{B_0}\right). \tag{2.119}$$

2.6 Summary

Drift wave turbulence represents an important loss mechanism which can significantly reduce confinement times in tokamak reactors. Drift waves are typically driven unstable by the intense equilibrium pressure gradients necessary for sustaining fusion reactions in the core. A brief introduction

to fluid and kinetic plasma descriptions was given here initially. This was followed by an outline of a basic two-fluid model of the electron drift wave, which provides a practical conceptual understanding of the underlying drift wave physics. However, a kinetic representation which retains particle velocity information is generally required to account for wave-particle resonances and finite Larmor radius effects. One limitation of kinetic theory is its computational expense. This led to the development of the gyrokinetic framework, which provides an efficient approach to modeling drift-wave transport by leveraging experimentally verified characteristics of core plasma turbulence. Gyrokinetic theory has become an essential tool in simulating and understanding turbulent transport in tokamak plasmas. A minimal, instructive derivation of the gyrokinetic equations was presented, along with an overview of the most common microinstabilities in magnetized plasmas. Particular emphasis was placed on the ion(electron)-temperature-gradient instabilities, which are central to this thesis, and a simple dispersion relation was derived from gyrokinetic theory. Additionally, the gyrokinetic codes GENE and GEM, which are employed in this thesis to investigate nonlinear turbulent transport dynamics, were described.

Chapter 3

Quasilinear Theory

This chapter introduces quasilinear theory for plasmas and demonstrates its effectiveness in modeling turbulent transport flux spectra in tokamaks. The main focus of this chapter is on comparing various quasilinear saturation rules for transport spectra in regards to DIII-D experimental shot #162940. As a co-author of the primary work discussed here, results are presented in this chapter which are taken directly from Ref. [166]. This includes the discussion of the three saturation rules used as well linear gyrokinetic simulation results and comparison of quasilinear and nonlinear flux spectra. Extension of analysis to negative triangularity scenarios is taken from the related Ref. [167]. The CUGK python library, available on the official CU Boulder GitHub, was developed as part of this work and used to perform all post-run analysis and calculate quasilinear flux models as described herein.

3.1 Basics of Quasilinear Theory

The discussion of quasilinear theory given here follows along the introductory plasma texts Ref. [24] and [25]. Previously, it has been assumed that fluctuations are small and nonlinear terms can be ignored in order to linearize the governing equations of interest for a tokamak plasma. While this can provide one with dispersion relations for unstable waves in the system, these instabilities will eventually grow large enough that nonlinear effects must be taken into account. Quasilinear theory provides a method of nonlinear analysis in which instabilities are weak and nonlinear interactions can lead to slow changes in the background plasma profiles. Consider for simplicity a 1-D Vlasov-Poisson system of equations,

$$\partial_t f_s + v_z \partial_z f_s + \frac{q_s}{m_s} \partial_z \phi \frac{\partial f_s}{\partial v_z} = 0, \tag{3.1}$$

$$\frac{\partial^2 \phi}{\partial z^2} = \sum_s \frac{q}{\epsilon_0} \int_{-\infty}^{\infty} f_s dv_z, \tag{3.2}$$

where s denotes the particle species. Initially the plasma is assumed to be homogeneous with no equilibrium potential, and the distribution function is decomposed into an initial background and fluctuating term

$$f_s(z, v_z, t = 0) = f_{0s}(v_z) + f_{1s}(z, v_z, t = 0). \tag{3.3}$$

Fluctuations are assumed to be spatially periodic and spatially averaging Equation (3.3) gives $\langle f_s \rangle_z(v_z, t = 0) = f_{0s}(v_z)$, where f_s is allowed to deviate from the initial equilibrium configuration over time. The focus of quasilinear theory here is to describe the time evolution of the spatially averaged distribution function. Equation (3.1) is spatially averaged to find

$$\partial_t \langle f_{0s} \rangle_z = -\frac{q_s}{m_s} \langle \partial_z \phi_1 \frac{\partial f_s}{\partial v_z} \rangle_z = -\frac{q_s}{m_s} \frac{\partial}{\partial v_z} \langle \partial_z \phi_1 f_{1s} \rangle_z, \tag{3.4}$$

where it has been assumed f_s decays to zero at large values of z so that the $\langle v_z \partial_z f_s \rangle$ term integrates to zero. The time evolution of f_{1s} can be solved for by subtracting Equation (3.4) from Equation (3.1), giving

$$(\partial_t + v_z \partial_z) f_{1s} = -\frac{q_s}{m_s} \partial_z \phi_1 \frac{\langle f_s \rangle_z}{\partial v_z} - \frac{q_s}{m_s} \left[\partial_z \phi_1 f_{1s} - \langle \partial_z f_{1s} \rangle_z \right]. \tag{3.5}$$

It is clear from here that the time rate of change of f_{1s} depends on second order fluctuating quantities and a closure problem exists. However, these terms are simply assumed to be small and neglected.

Dropping the second term on the right hand side, and linearizing Equation (3.5) and the first order Poisson equation results in

$$\widetilde{f}_{1s} = \frac{q_s}{m_s} \frac{k \phi_1}{\omega - k v_z} \frac{\partial \langle f_s \rangle_z}{\partial v_z}, \tag{3.6}$$

$$k^2 \widetilde{\phi}_1 = -\sum_s \frac{q_s}{m_s} \int_{-\infty}^{\infty} \widetilde{f}_{1s} dv_z, \tag{3.7}$$

where a "$\sim$" represents a Fourier mode. Note that for real quantities such as the electrostatic

potential one has

$$\phi_1(z,t) = \phi_1^*(z,t) \Rightarrow \widetilde{\phi}_1(k) = \widetilde{\phi}_1^*(-k). \tag{3.8}$$

The nonlinear term in Equation (3.4) can be simplified using Equation (3.8) and by assuming an infinitely large box size and the Dirac delta function identity

$$\lim_{L\to\infty} \int_{-L}^{L} e^{i(k+k')z} dz = 2\pi\delta(k+k'), \tag{3.9}$$

to find

$$\begin{aligned} \frac{\partial}{\partial v_z}\langle \partial_z \phi_1 f_{1s}\rangle_z &= \frac{\partial}{\partial v_z}\frac{1}{2L}\int_{-L}^{L} \partial_z \phi_1 f_{1s} dz = \frac{\partial}{\partial v_z}\frac{1}{2L}\int_{-L}^{L}\left[\partial_z \int_{-\infty}^{\infty} \widetilde{\phi}_1 e^{ikz} dk \int_{-\infty}^{\infty} \widetilde{f}_{1s} e^{ik'z} dk'\right] dz \\ &= -\frac{\pi}{L}\frac{\partial}{\partial v_z}\int_{-\infty}^{\infty} ik\widetilde{\phi}_1(-k,t)\widetilde{f}_{1s}(k,t)dk = -\frac{\pi}{L}\frac{\partial}{\partial v_z}\int_{-\infty}^{\infty} ik\widetilde{\phi}_1(k)\widetilde{f}_{1s}(k)e^{2\gamma t}dk. \end{aligned} \tag{3.10}$$

Substituting Equation (3.6) into Equation (3.10) gives

$$\frac{\partial}{\partial v_z}\langle \partial_z \phi_1 f_{1s}\rangle_z = -\frac{\pi}{L}\frac{q_s}{m_s}\frac{\partial}{\partial v_z}\int_{-\infty}^{\infty} ik^2 \frac{\widetilde{\phi}_1(k)\widetilde{\phi}_1(-k)}{\omega - kv_z}\frac{\partial}{\partial v_z}\langle f_{0s}\rangle_z e^{2\gamma t} dk. \tag{3.11}$$

Rewriting the field fluctuations in terms of the spectral energy density,

$$\mathcal{E}(k,t) = \frac{\pi\epsilon_0}{2L}|\widetilde{E}_1(k)|^2 e^{2\gamma t}, \tag{3.12}$$

and substituting Equation (3.11) into Equation (3.4) yields a final velocity-space diffusion equation

$$\partial_t \langle f_{0s}\rangle_z = \frac{\partial}{\partial v_z}\left[D(v_z,t)\frac{\partial\langle f_{0s}\rangle_z}{\partial v_z}\right], \tag{3.13}$$

with diffusion coefficient

$$D(v_z,t) = \frac{2}{\epsilon_0}\left(\frac{q_s}{m_s}\right)^2 \int_{-\infty}^{\infty} \frac{i\mathcal{E}(k,t)}{\omega - kv_z} dk = \frac{2}{\epsilon_0}\left(\frac{q_s}{m_s}\right)^2 \int_{-\infty}^{\infty} \frac{\gamma\mathcal{E}}{[\omega_r - kv_z]^2 + \gamma^2} dk. \tag{3.14}$$

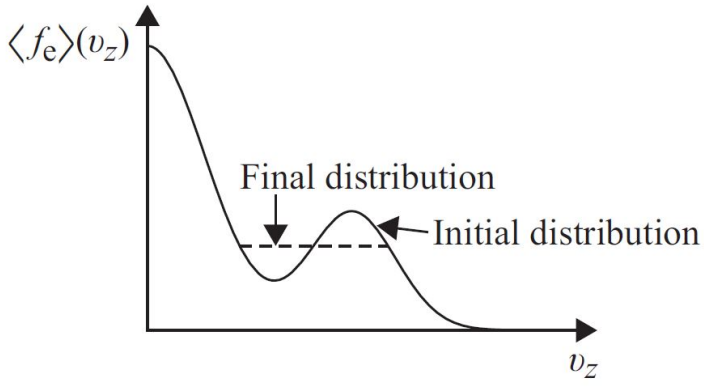

Figure 3.1: Depiction of the background electron distribution function relaxing due to quasilinear diffusion in the case of the "bump-on-tail" instability [25].

The last step in calculating Equation (3.14) is possible as $\mathcal{E}$ is even in k and ω_r is odd, so that the complex part integrates to zero. This indicates the diffusion coefficient is required to be real. One simple application of this result is to the electron "bump-on-tail" instability illustrated in Figure 3.1. Such a situation might occur if a small amount of high-energy particles are injected into the system. The parallel wave-particle resonance drives unstable growth when $\partial f_0/\partial v_z > 0$, an effect known as inverse Landau damping [25]. The instability here leads to quasilinear diffusion and a subsequent flattening of the equilibrium distribution function. As the equilibrium profile relaxes, instabilities no longer grow, and the system ultimately becomes stable.

3.1.1 Mixing Length Models for Turbulent Transport

The drift wave fluctuations involved in tokamak turbulence are small in amplitude and quasilinear analysis provides a reasonable approximation to model nonlinear properties of the turbulent system. The quasilinear picture of turbulent transport is analogous to that of the bump-on-tail instability described in Section 3.1, though diffusion occurs in real space. Gradients in the equilibrium profiles drive instabilities, leading to turbulent transport losses and subsequent flattening of the background profiles. As the equilibrium profiles are relaxed, the critical gradients required to drive instabilities in the plasma are no longer sustained and the turbulent system is stabilized.

Many standard quasilinear models of turbulent diffusion depend on the so-called mixing length estimate [6, 121, 122]. The mixing-length estimate defines a maximum bound on perturbation amplitudes when perturbed gradients and equilibrium gradients become equal. That is, the linear and nonlinear **E**x**B** advection terms are balanced and one has

$$\mathbf{v}_E \cdot \nabla \delta n = \mathbf{v}_E \cdot \nabla n_0 \Rightarrow \frac{\delta n}{n_0} = \frac{1}{k_\perp L_n}, \tag{3.15}$$

given a density gradient length scale L_n. The displacement of perturbations by the **E**x**B** velocity is defined by $d\boldsymbol{\xi}/dt = \mathbf{v}_E$, and perturbations are stretched by this flow (as depicted in Figure 2.6) such that

$$\delta n = \boldsymbol{\xi} \cdot \nabla n_0. \tag{3.16}$$

Combining Equation (3.15) and Equation (3.16) one finds the maximum radial displacement, i.e. streamer length, is set by

$$\frac{\boldsymbol{\xi} \cdot \nabla n_0}{n_0} = \frac{1}{k_\perp L_n} \Rightarrow \xi_r = \frac{1}{k_\perp}. \tag{3.17}$$

Linearizing the **E**x**B** velocity to lowest order in terms of $\boldsymbol{\xi}$ gives

$$i(-\omega_r + i\gamma)\boldsymbol{\xi} = \mathbf{v}_E, \tag{3.18}$$

where ω_r is the real frequency of the mode. An expression for the radial particle flux can then be derived by ignoring any complex contribution from Equation (3.18) to find

$$\Gamma_r = v_{Er}\delta n = \gamma \xi_r \delta n = \gamma \frac{1}{k_\perp} \frac{n_0}{k_\perp L_n} = \frac{\gamma}{k_\perp^2} \frac{n_0}{L_n} = \frac{\gamma}{k_\perp^2} \nabla n_0. \tag{3.19}$$

It is clear now that Equation (3.19) describes a diffusive model for the particle flux with

$$D \sim \frac{\gamma}{k_\perp^2}. \tag{3.20}$$

Likewise, the same value can be derived for the heat flux and the thermal diffusivity. This is the standard mixing-length diffusion estimate, which can be interpreted as a balance between the unstable growth of a mode and the stabilizing effect of turbulent diffusion in the perpendicular plane.

As linear calculations with gyrokinetic codes are routine and computationally fast, linear simulations provide a practical method for estimating nonlinear flux characteristics by employing quasilinear models. Using linear gyrokinetic simulation, one can straightforwardly obtain linear fluxes as well as the various parameters such as mode growth rates and wavenumbers which are typically required for quasilinear estimates, as evidenced by the case of the mixing length estimate. However, linear calculations provide no information about the nonlinear saturation level of the turbulence, while nonlinear simulations are significantly more compute-intensive. For this reason, heuristic "saturation rules" are generally invoked which provide saturation levels given linear characteristics of the instabilities. In this sense, saturation rules are not rigorous values, and sophisticated quasilinear models typically scale results to match a database of nonlinear simulation results [168]. There is also some approximation possible regarding the choice of a quasilinear expression for the flux.

Typically, one combines the quasilinear expression for the flux and a heuristic saturation rule to obtain mode amplitudes for the nonlinear fluxes. The overall level of the fluxes may not be so accurate using this approach, but often characteristic dependences on mode and plasma parameters are insightful. Here, three plausible saturation rules are discussed, following along Ref. [166]. The quasilinear expression of the flux is taken from the prescription in Ref. [169], where it is used for GENE gyrokinetic simulation results. The quasilinear fluxes are calculated given the GENE field-line-following coordinate system described previously in Section 2.5.1. Linear fluxes, represented generally by F, are decomposed for each toroidal mode (k_y) and defined proportional to the mode amplitude squared as

$$F_{k_y}^{\mathrm{lin}} = \hat{G}_{k_y} \left| \hat{\Phi}_{0,k_y}(z=0) \right|^2, \tag{3.21}$$

where it is assumed that the mode amplitude can be parametrized by the k_y component at $z = 0$ ($\theta = 0$), the ballooning mode peak.

The quasilinear amplitude for the flux can then be straightforwardly calculated from the amplitude-normalized linear flux, $\hat{G}_{k_y}$, as

$$F^{\mathrm{QL}} = \sum_{k_y} A^2(k_y) \hat{G}_{k_y} \Delta k_y, \tag{3.22}$$

where Δk_y is the spacing in k_y and $A^2(k_y)$ represents the choice of saturation rule. In the case of Ref. [169], the saturation amplitude is given by a mixing-length type rule [170]

$$A^2(k_y) = A_0^2 \left(\frac{\gamma_{k_y}}{\langle k_\perp^2 \rangle} \right)^2, \tag{3.23}$$

where γ_{k_y} is the linear growth rate and $k_\perp$ is the perpendicular wavenumber. The denominator, $\langle k_\perp^2 \rangle$, is calculated by averaging $k_\perp$ over the ballooning mode envelope, $\hat{\Phi}_{k_x,k_y}(z)$, and is given by

$$\langle k_\perp^2 \rangle = \frac{\sum_{k_x} \int (g^{xx} k_x^2 + 2 g^{xy} k_x k_y + g^{yy} k_y^2) \left| \hat{\Phi}_{k_x k_y}(z) \right|^2 J dz}{\sum_{k_x} \int \left| \hat{\Phi}_{k_x k_y}(z) \right|^2 J dz}. \tag{3.24}$$

Here, J is the Jacobian and g^{xx}, g^{xy}, g^{yy} are geometric coefficients $g^{\mu\nu} = \nabla\mu \cdot \nabla\nu$ in the field-line following coordinates.

While linear parameters do play a role in determining the quasilinear flux, parametric dependence of the fluctuation amplitude is more complex and demands running nonlinear gyrokinetic simulations many times over a range of parameters [171]. However, some insight can be gained regarding transport properties by comparing various saturation rules and the sensitivity of the observed trends. The goal in this work was not to develop a transport model that accurately reproduces nonlinear gyrokinetic simulation results, but rather to present results which scan the sensitivity of fluxes to the saturation rule. Three common saturation rules are considered here, and simple scaling arguments from which they can be derived are given. First, the saturation rule defined by Equation (3.23) can be found by balancing the linear growth of the instability with the advection

from the **ExB** nonlinearity [166],

$$\gamma \delta n_k \sim \frac{k_\perp^2}{B} |\delta\phi_k| |\delta n_k| \Rightarrow \frac{e|\delta\phi_k|}{T} \sim \frac{eB}{T}\frac{\gamma_k}{k_\perp^2}. \tag{3.25}$$

It has been assumed that the regulated turbulence is isotropic in the perpendicular plane and $k_x \sim k_y \sim k_\perp$. This saturation rule can also be obtained by considering wave-particle trapping of resonant particles which gives the correct saturation level in slab geometry [172].

The second saturation rule invokes a dimensional argument where the diffusion coefficient is simply set to the mixing length estimate, Equation (3.20). The expression for the flux, $D\nabla n_0 = \langle v_{Ex}\delta n\rangle$, then gives [166]

$$\begin{aligned} & \frac{\gamma}{k_\perp^2}\frac{n_0}{L_n} \sim \frac{k_y}{B}\delta\phi_k\delta n_k \\ \Rightarrow\quad & \frac{\gamma}{k_\perp^2}\frac{n_0}{L_n} \sim \frac{k_y}{B}\delta\phi_k\frac{e\delta\phi_k}{T}n_0 \\ \Rightarrow\quad & \frac{\gamma}{k_\perp^2} \sim L_n k_y \frac{T}{eB}\left|\frac{e\delta\phi_k}{T}\right|^2 \\ \Rightarrow\quad & \frac{e|\delta\phi_k|^2}{T} \sim \frac{eB}{T}\frac{1}{Lk_y}\frac{\gamma_k}{k_\perp^2}. \end{aligned} \tag{3.26}$$

A similar calculation could be made for the thermal diffusivity, so L is used in Equation (3.26) more generally. Equation (3.26) is similar to the saturation rule used in the quasilinear code QuaLiKiz [173]. Finally, the third saturation rule used for comparison is the following [166]

$$\frac{e|\delta\phi_k|^2}{T} \sim \frac{eB}{T}\frac{\gamma_k}{k_\perp^2}, \tag{3.27}$$

which has a similar $\frac{\gamma}{k_\perp^2}$ scaling for the flux as Equation (3.26), but does not diverge as k_y approaches zero. The saturation rule given in Equation (3.27) has been used previously for comparison to nonlinear gyrokinetic simulation and experiment in the case of KBM transport in the tokamak core [174]. Note that in Ref. [174] the flux normalization described by Equation (3.21) instead involves integrating the mode potential along the field line and considering a sum over all k_x modes.

3.1.2 Quasilinear Codes

Prediction of turbulent transport of particles and energy is critical to improving fusion reactor performance, and much progress has been made towards reduced modeling in the core region of tokamaks. Quasilinear models are often employed to compare to transport in nonlinear gyrokinetic simulation and experiment, and they have shown success in predicting core transport profiles over a range of tokamak plasma operating conditions [169, 170, 175]. Sophisticated quasilinear codes include the Trapped Gyro-Landau Fluid (TGLF) model [168, 171, 176, 177], the multi-mode model (MMM) [178–181], and the gyrokinetic transport model QuaLiKiz [173, 182–184]. Though quasilinear modeling of transport has been largely successful, better understanding is still required in many cases. For instance, particle transport regarding density build-up is not well understood [185, 186], and controlling core concentrations of high-Z impurities, such as tungsten in ITER, would help in significantly reducing radiative power losses [187, 188].

The TGLF code is employed in this chapter for comparison with the three heuristic saturation rules described previously. TGLF solves a system of gyrofluid moment equations for both trapped and passing particles to find linear eigenmodes for various instabilities of interest. Linear eigenmodes can be computed for ITG modes, ETG modes, trapped ion and electron modes, and electromagnetic KBMs. TGLF contains multiple saturation models, which consider different saturation effects for the nonlinear mode amplitudes. The nonlinear scaling coefficient in the TGLF model is specifically fit to a database of 83 nonlinear gyrokinetic simulation conducted using the GYRO code [189]. The SAT1 model which is used here considers both the effects of so-called zonal flow mixing as well as zonal flow shearing in the regulation of ion and electron scale turbulence [177]. Inclusion of zonal-flow mixing effects allows for reproduction of multiscale simulation fluxes when ion-scale ZFs mitigate electron-scale turbulence levels.

3.2 Quasilinear Modeling of DIII-D Shot #162940

The quasilinear transport modeling efforts of Refs. [166] and [167] are recounted here. These works study a conventional ELMy H-mode DIII-D case (#162940) just prior to the onset of an ELM. Further details and MTM analysis of this scenario can be found in Ref. [117], along with additional studies on ETG and MTM turbulence in Refs. [147, 190]. A Miller equilibrium is employed, where the Miller [32] parameters are obtained from Equilibrium Fitting (EFIT) [191] data on a 513×513 (R, Z) grid, and radial profiles of density and temperature. Local and global nonlinear gyrokinetic simulations were carried out and results compared to the three heuristic saturation rules described in Section 3.1.1 as well as the TGLF SAT1 model. The focus of these comparisons is on considering the sensitivity of the chosen saturation rules.

Results are discussed here from gyrokinetic simulation using the GENE and GEM codes. GENE is used for linear and nonlinear local simulation, including calculations of the quasilinear expression for the flux, while GEM is employed for global gyrokinetic simulations. Electrons and two ion species are included, namely, deuterium (main) and carbon (impurity). The plasma parameters are first discussed and the linear properties of the selected profiles investigated. Quasilinear models are constructed from linear GENE simulation data and compared directly against nonlinear simulation fluxes from local GENE and global GEM simulations. Equilibrium shear flow is not considered in the simple quasilinear models, and so is also ignored in the gyrokinetic simulations. This allows for a clearer comparison of the saturation rules. Realistic collisionality is included in all simulations. GENE considers all species as gyrokinetic, while GEM takes gyrokinetic ions and drift-kinetic electrons. Electromagnetic fluctuations perpendicular to B ($\delta B_\perp$) are included in both linear and nonlinear simulations, while $\delta B_\parallel$ effects are neglected. The plasma β is reduced for some nonlinear simulations presented, with further details provided in the discussion.

Figure 3.2 shows the equilibrium temperature and density profiles for all species of DIII-D shot #162940 prior to ELM buildup. The impurity temperature is assumed to be equal to the main ion temperature, and only the carbon impurity is considered in this analysis. As the carbon density

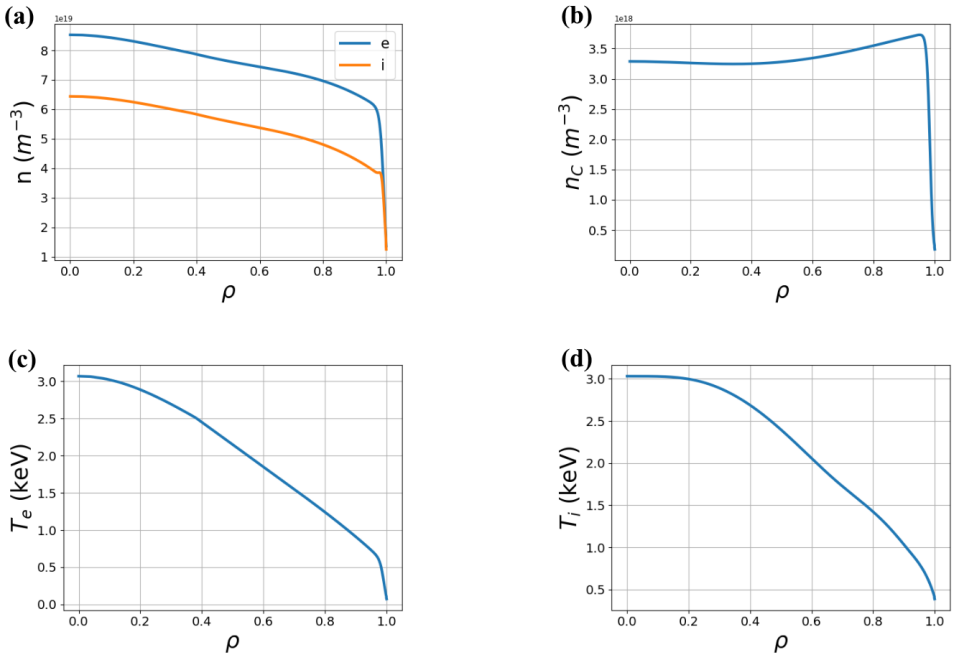

Figure 3.2: Profiles for DIII-D 162940 ELMy H-mode just prior to ELM onset. (**a**) Electron and main ion density profiles. (**b**) Impurity density profiles. (**c**) Electron temperature profile. (**d**) Main ion temperature profile.

profile is hollow, inward radial particle flux is expected. Radial locations, $\rho = r/a$, are defined by the Miller radial coordinate, Equation (1.49), and a which is the value of r at the separatrix. The major radius is defined as

$$R = \frac{R_{\max} + R_{\min}}{2}. \tag{3.28}$$

Local simulation parameters are given in Table 3.1 for the multiple radial locations considered for this analysis. Linear stability is first examined at these radial locations. As described in Section 2.5.1, various physical quantities are used to determine the collisionality and for unit conversion. The normalized density and temperature gradients for each species j are given by R/L_{nj} and R/L_{Tj} respectively. The ratio of electron to ion temperature is given by $\frac{T_e}{T_i}$ and the carbon impurity concentration is given in terms of the electron density by $\frac{n_C}{n_e}$. Note that the impurity density and density gradients have been adjusted so that quasineutrality is satisfied at each radial location. The safety factor and magnetic shear are given by q and $\hat{s} = \frac{\rho}{q}\frac{dq}{dr}$, and β_e is the electron plasma

Table 3.1: Local tokamak plasma parameters at $\rho = 0.80$, 0.85, and 0.90.

ρ	$\frac{R}{L_{T_i}}$	$\frac{R}{L_{T_e}}$	$\frac{T_e}{T_i}$	$\frac{R}{L_{ne}}$	$\frac{R}{L_{ni}}$	$\frac{R}{L_{nC}}$	$\frac{n_C}{n_e}[\%]$	q	$\hat{s}$	$\beta_e[\%]$	κ	δ	ζ
0.8	6.71	7.49	0.87	1.44	2.40	-0.71	5.16	2.28	1.75	1.00	1.47	0.21	-0.03
0.85	9.16	8.94	0.87	1.84	3.06	-0.75	5.37	2.56	2.17	0.85	1.51	0.24	-0.04
0.9	12.49	11.17	0.88	2.36	3.98	-0.79	5.65	2.97	2.94	0.67	1.55	0.28	-0.05

beta defined by $\beta_e = \mu_0 n_e T_i / B_0^2$. The Miller parameters - κ, δ, and ζ - describe the elongation, triangularity, and squareness of the parametrized flux surface as explained in Section 1.4.1 and are calculated directly by GENE.

3.2.1 Linear Analysis

The local linear properties of the tokamak plasma parameters discussed above are studied here for the radial locations $\rho = 0.80$, 0.85, and 0.90 near the pedestal top. Linear initial-value calculations are carried out with the GENE code in the local flux-tube limit. The grid resolution used in linear simulations was 20x16x32x8 in the x,z,$v_\parallel$, and μ dimensions. The linear growth rates and real frequencies of the most unstable modes are plotted in Figure 3.3(a) as functions of $k_y\rho_i$. Here ρ_i is the deuterium gyroradius and $v_{th} = \sqrt{T_i/m_i}$. The "i" subscript refers to the main ion species, deuterium, throughout this section. The results in Figure 3.3(a) show features standard to core H-mode plasmas as well as the "Cyclone Base Case" (CBC) scenario [192]. An ion mode, the ITG mode, is present for $k_y\rho_i \lesssim 1.4$, indicated by positive frequency in the ion diamagnetic direction, while an electron mode, the collisionless trapped-electron mode (CTEM), dominates when $k_y\rho_i \gtrsim 1.4$, indicated by the crossover to negative frequencies. Moving towards the pedestal region, the gradients become steeper and the most unstable longest wavelength mode switches to a negative frequency. This was identified to be a micro-tearing mode (MTM) by its even parity vector potential fluctuation along the field line. MTMs are often the most dominant mode in the pedestal region for such H-mode tokamak parameters [117], and global analysis is needed to accurately model these long wavelength modes.

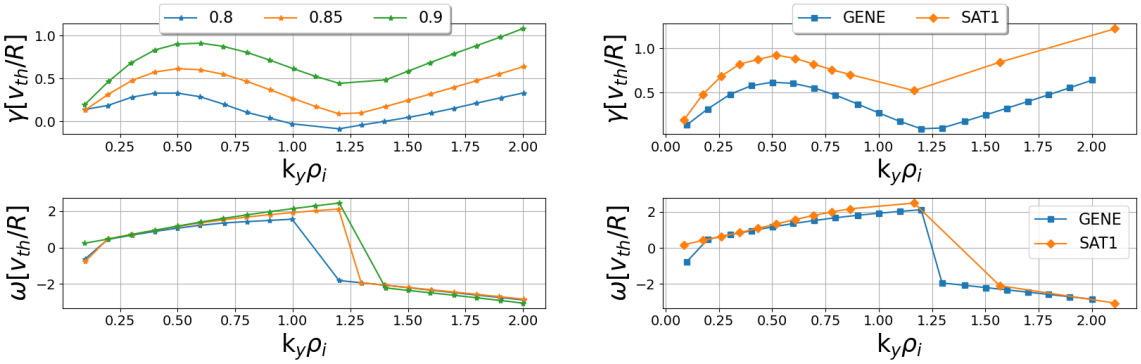

(a) (b)

Figure 3.3: (a) Growth rate and real frequency plots for radial locations $\rho = 0.80$, 0.85, and 0.90 from linear initial-value GENE simulations. (b) Comparison of linear frequencies and growth rates given by GENE and TGLF at $\rho = 0.85$.

Figure 3.3(b) gives a comparison between linear simulation results from TGLF and GENE at $\rho = 0.85$. There is good agreement in the real frequencies, however the TGLF SAT1 model predicts higher growth rates than GENE. As GENE solves the linearized gyrokinetic equation directly, the GENE results are more accurate. However, it is possible that the SAT1 model allows for higher growth rates to calculate more accurate fluxes. Global effects, which are typically stabilizing, are not accounted for in this analysis.

3.2.2 Saturation Levels and Quasilinear Fluxes

Figure 3.4 compares the three saturation rules, given $T = T_i$, with the TGLF SAT1 results. GENE gyroBohm units are used in which the electrostatic potential is normalized as $e\phi/(T_i\rho^*)$ as described in Section 2.5.1. The saturation rules, Equations (3.25) to (3.27), are respectively labeled "Lapillonne(2011)", "Bourdelle(2007)", and "Kumar(2021)", and the TGLF SAT1 model is labeled "SAT1". No consideration of the relative validity of each model is made as the rules are simply used here for comparison. Additionally, the overall levels for each saturation rule are not important given that the TGLF value is scaled using a constant coefficient to best match nonlinear simulation results. The saturation rules all peak in the range $k_y\rho_i \sim 0.20 - 0.30$, while some difference in the spectral

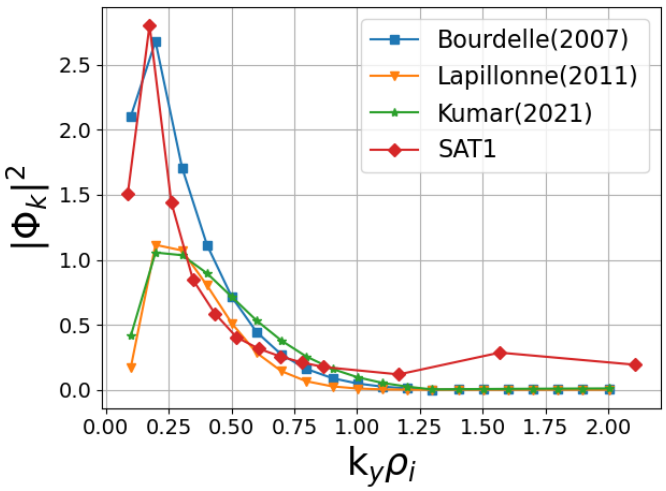

Figure 3.4: The three saturation rules obtained from linear GENE results along with TGLF SAT1 in the GENE gyroBohm units described in the text.

width is observed. The narrowest spectrum is given by the SAT1 model, while the broadest spectrum is given by Equation (3.27), which is reasonable due to the power of the $\gamma_k/k_\perp^2$ term and the lack of a $1/k_y$ factor. Interestingly, Equation (3.26) gives the closest approximation to the SAT1 model, though only the SAT1 model predicts unregulated modes at shorter wavelengths, which are likely TEM modes.

Next, the quasilinear flux spectra are calculated from the normalized GENE linear fluxes and the three saturation rules. Comparison of the various quasilinear flux spectra are given with the SAT1 model in Figure 3.5. GENE gyroBohm units for the fluxes are used, where $Q_{\mathrm{gB}} = v_{th}\rho_i^2 n_e T_i/R^2$ and $\Gamma_{\mathrm{gB}} = v_{th}\rho_i^2 n_e/R^2$. Results have been normalized to the SAT1 model by adjusting A_0 for each saturation rule to match the total ion heat flux, Q_i, predicted by SAT1. Notably, the carbon flux is directed inward as expected by the hollow density profile. The results agree qualitatively well, with some variation in the spectral widths. Note that because the total fluxes are normalized to the SAT1 model, the broader quasilinear spectra will have lower flux values for each point. Finally, the SAT1 model indicates fluxes likely driven by TEM modes at shorter wavelengths, whereas the GENE results generally do not.

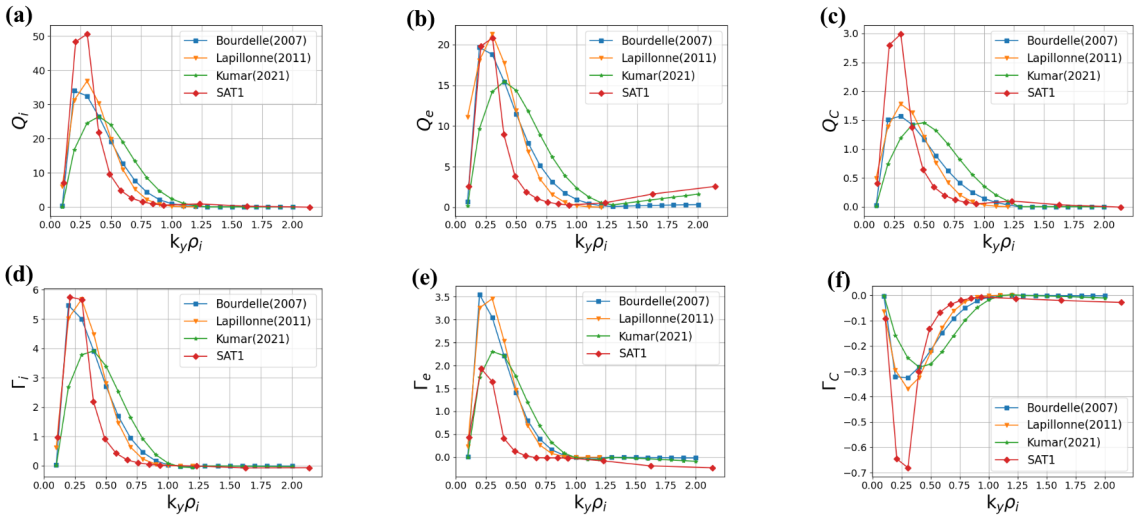

Figure 3.5: Quasilinear fluxes from GENE and TGLF SAT1 versus $k_y\rho_i$ at $\rho = 0.85$ for the three saturation rules in GENE gyroBohm units. (**a**) Deuterium heat flux. (**b**) Electron heat flux. (**c**) Carbon heat flux. (**d**) Deuterium particle flux. (**e**) Electron particle flux. (**f**) Carbon particle flux. Fluxes are normalized such that the total ion heat flux matches SAT1.

3.2.3 Comparison with Nonlinear Gyrokinetic Simulations

The quasilinear models were then validated against nonlinear flux-tube GENE simulations carried out at $\rho = 0.85$. The perpendicular flux-tube domain was $167\rho_i \times 126\rho_i$ in the radial and binormal dimensions, with 256 radial grid points and 32 toroidal modes. The values of $k_y\rho_i$ were evenly spaced, ranging from 0.05 to 1.60. Grid resolution in the $z, v_\parallel$, and μ dimensions was taken to be $32 \times 32 \times 16$ respectively, where these values were found by running linear growth rate convergence tests. Initial runs with the value of $\beta_e = 0.85\%$, as specified in Table 3.1, showed nonlinearly excited lower-k_y MTMs dominating the transport at earlier times which led to numerical instability at late times. Electromagnetic modes were not observed in the global nonlinear GEM simulations discussed further below, likely because of destabilization by nonlocal effects, and β_e was reduced by 90% to produce robust electrostatic simulation results.

Particle and heat flux spectra in $k_y\rho_i$ are compared between the Lapillonne quasilinear model, local nonlinear GENE simulation, and global nonlinear GEM simulation in Figure 3.6. The quasilinear fluxes shown in blue and labeled "QL GENE" agree well with the nonlinear GENE results shown in

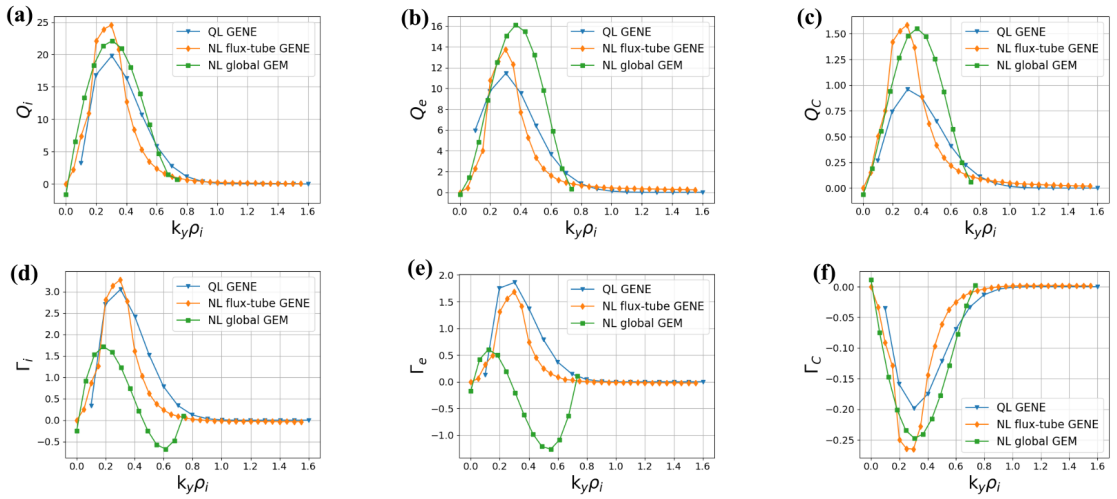

Figure 3.6: Lapillonne QL flux model, NL from GENE, and GEM results versus $k_y\rho_i$ at $\rho = 0.85$ in GENE gyroBohm units. GEM fluxes scaled by 3.49. (a) Deuterium heat flux. (b) Electron heat flux. (c) Carbon heat flux. (d) Deuterium particle flux. (e) Electron particle flux. (f) Carbon particle flux.

orange and labeled "NL flux-tube GENE", where the saturation amplitude A_0 is normalized using the nonlinear GENE ion heat flux. The global GEM results, discussed below, are scaled by a factor of 3.49 for comparison in order to match the total ion heat flux. This is necessary because nonlocal effects - variations in the equilibrium profiles - have a stabilizing effect, and global calculations typically see lower fluxes overall.

The results labeled "NL global GEM" in Figure 3.6 are from nonlocal nonlinear electromagnetic gyrokinetic GEM simulations. For the current analysis, drift-kinetic electrons are included using the split-weght scheme described in Section 2.5.2. A numerical heat source is applied to all species to prevent profile relaxation, and a numerical scheme used which evaluates the marker distribution into significantly late times [161]. The grid resolution is $(N_x, N_y, N_z) = (128, 128, 64)$, in the radial, binormal and parallel directions, respectively. The particle number is 32/cell for the ion species and 64/cell for electrons, and the time step is $\Omega_p \triangle t = 1$, with Ω_p the proton gyro-frequency. The global radial simulation domain extends from $0.65 < r/a < 0.95$. Attempts were made to extend the simulation domain to the separatrix ($r/a = 1.0$), however nonphysical modes emerged near the edge. The cause is not known, but is likely a result of the equilibrium configuration. Specifically,

poloidal variation is expected in steep gradient regions such as the pedestal, but local Maxwellian distributions are assumed here which only vary radially with the density and temperature. Density and temperature gradients were reduced within a region $\pm r/a \sim 0.05$ near the outer boundary to help stop instabilities peaking at the end of the domain.

The simulation domain is a toroidal wedge which is 1/8 of the total torus, and the electromagnetic fields were filtered to include only the toroidal mode numbers $n = 0, 8, 16, \ldots, 88$. As mentioned previously, no nonlinear excitation of low-n electromagnetic modes, e.g. MTMs, was observed in the global GEM simulations. This is contrary to the local GENE nonlinear results, and likely a result of nonlocal stabilizing effects. Ion energy fluxes are plotted in time in Figure 3.7(a) for various radial locations in the GEM simulation. In order to compare to the GENE quasilinear and nonlinear results, turbulent GEM fluxes were decomposed by toroidal mode number. Considering the formula for the radial heat flux, Equation (2.119),

$$Q(r) = \frac{1}{\triangle V} \int_{\triangle V} \frac{1}{2} m v^2 \, \delta f \left(\frac{\mathbf{E} \times \mathbf{b}}{B} + v_{\parallel} \frac{\delta \mathbf{B}_{\perp}}{B} \right) \cdot \frac{\nabla r}{|\nabla r|} \, d\mathbf{x} d\mathbf{v}, \tag{3.29}$$

one can replace the fields by specific toroidal components to calculate the contribution of each

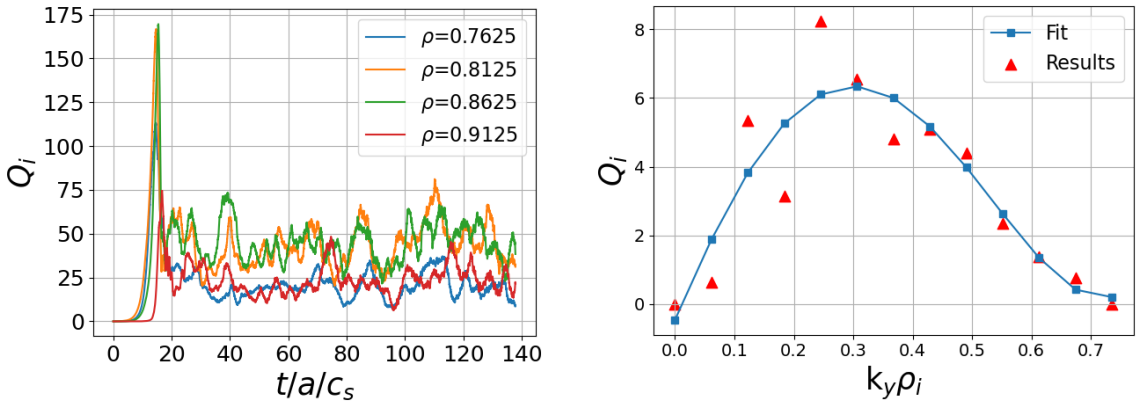

(a) (b)

Figure 3.7: (a) Global GEM ion heat flux versus time in GENE gyroBohm units at multiple radial locations. (b) GEM ion heat flux versus $k_y\rho_i$ and the corresponding smooth polynomial fit.

component to the total value. Here $\triangle V$ is a thin toroidal annulus with a radial size of $\triangle r/a = 0.025$. The ion heat flux spectra is shown in Figure 3.7(b), with values indicated by solid red triangles. The solid blue squares are calculated from a polynomial fit as GEM does not evolve the distribution function spectrally and summing over particles introduces statistical noise when calculating the total fluxes. The smoother polynomial fit was introduced for each flux value in order to more clearly compare to the quasilinear and nonlinear GENE models in Figure 3.6.

3.2.4 Extension to Negative Triangularity

The results from the preceding sections are extended here to the case of negative triangularity (NT) flux surfaces. Negative triangularity has seen renewed interest recently, with DIII-D experimental campaigns demonstrating highly favorable properties in tokamak plasmas [49, 50]. While NT configurations were previously investigated decades ago, they fell out of favor due to a lack of access to the advantageous H-mode state of operation. However, the more recent DIII-D NT experiments were able to achieve ELM-free operation in high-confinement-like regimes with reduced levels of

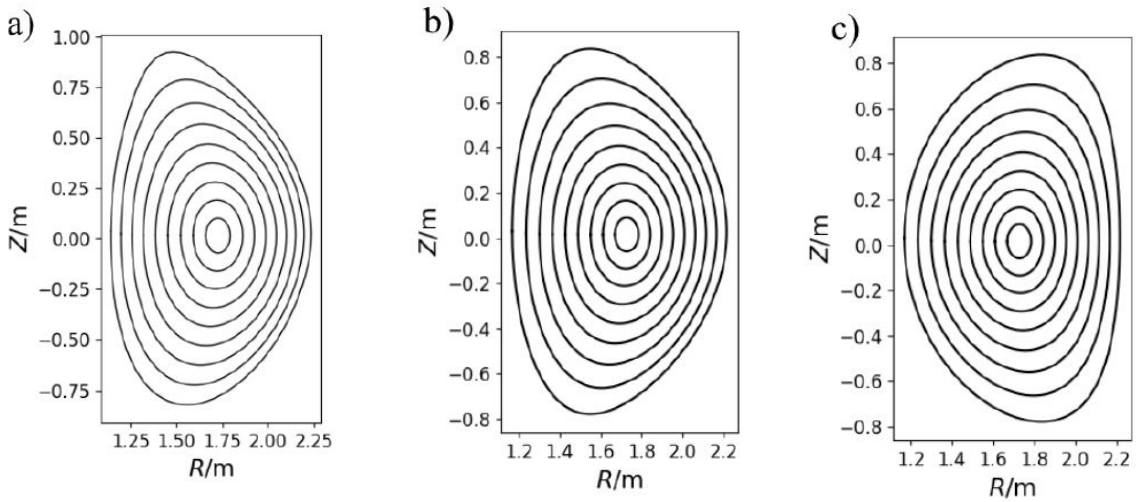

(a) (b) (c)

Figure 3.8: Comparison of equilibrium flux surfaces from $\rho = 0.10$ to 0.90 at intervals of 0.10 for DIII-D shot #162940. (a) Original magnetic equilibrium data. (b) Miller parametrization with positive triangularity. (c) Miller parametrization with negative triangularity.

core turbulent transport. Investigations into turbulent transport in NT scenarios with nonlinear gyrokinetic simulation have reported that there are stabilizing effects on ion-scale turbulence [193, 194]. This was largely attributed to modification of the precessional drift of trapped electrons and a reduction in TEM transport. The effect of negative triangularity on ITG mode stability is currently an active topic of research, and simulations have shown modest ITG stabilization [195].

The original magnetic equilibrium data is shown in Figure 3.8(a) in comparison to the positive and negative triangularity Miller parametrizations in Figure 3.8(b) and Figure 3.8(c). To calculate NT Miller parametrizations the value of the triangularity, δ, in Table 3.1 simply has its sign flipped. However, the Miller equilibrium calculations used by GENE define the squareness in terms of δ and the new values required for valid surfaces are $\zeta = 0.015$, 0.018, and 0.037 at $\rho = 0.80$, 0.85, and 0.90 respectively. Linear electromagnetic simulations were carried out at these radial locations. Conversely to the results of Section 3.2.1, it was found that the electromagnetic MTM mode dominated for all values of $k_y\rho_i$ considered. Electrostatic simulations with $\beta = 1e^{-4}$ were instead run in order to focus on the effects of NT on ITG and TEM mode stability. Nonlinear gyrokinetic simulations were again run given these updated parameters for comparison to the quasilinear saturation models.

The linear electrostatic gyrokinetic simulation results are presented in Figure 3.9. Comparing

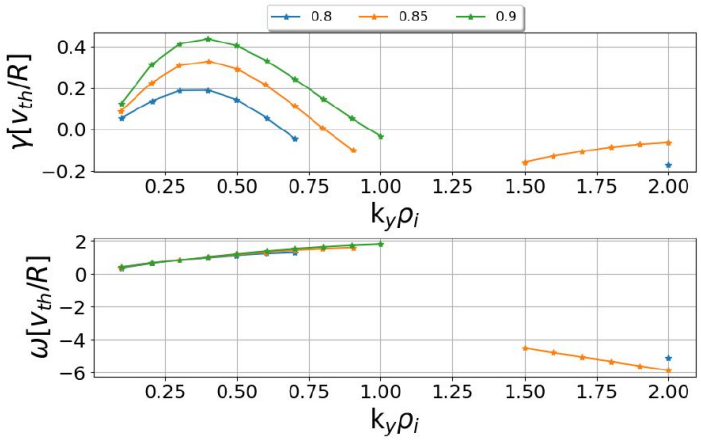

Figure 3.9: Growth rates and real frequencies at radial locations $\rho = 0.80$, 0.85, and 0.90 from linear electrostatic GENE simulations with $\beta = 1e^{-4}$ and negative triangularity.

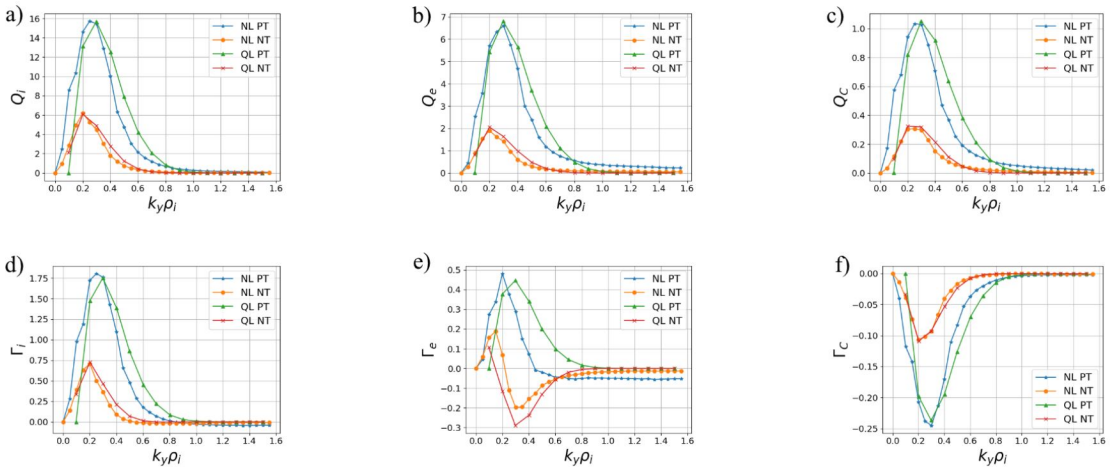

Figure 3.10: Lapillonne QL flux model and NL flux-tube results from GENE in PT and NT at $\rho = 0.90$ in GENE gyroBohm units. (a) Deuterium heat flux. (b) Electron heat flux. (c) Carbon heat flux. (d) Deuterium particle flux. (e) Electron particle flux. (f) Carbon particle flux.

to the PT results of Figure 3.3(a), it is clear that the ITG growth rates are lower, and a transition from positive to negative growth rates is evident with increasing $k_y\rho_i$ into TEM scales. Not all points were converged in the linear simulations, indicated by missing points, which is likely a result of the stabilization of higher $k_y\rho_i$ modes. The ITG results were most robust for the case of $\rho = 0.90$, and so this radial location was taken for quasilinear comparison to nonlinear results. The quasilinear and nonlinear particle and heat flux spectra for each species are plotted below in Figure 3.10. These are further compared to the PT results from the previous section. It is clear that a drop in ITG flux levels is associated with the change in triangularity from positive to negative for all fluxes considered. This qualitatively aligns with findings indicating that NT enhances ITG stability due to changes in the magnetic shear and field-line curvature [196]. Interestingly, the electron particle flux changes direction in the NT case, which is likely required to maintain ambipolar diffusion as the main ion particle flux drops more significantly compared to the carbon impurity flux between the PT and NT cases.

3.2.5 Discussion and Future Work

Quasilinear theory was introduced in this chapter as a framework for modeling nonlinear plasma dynamics, specifically when capturing the nonlinear effects of small pertubations and their gradual influence on the background equilibrium. This approach is particularly relevant to high-confinement tokamak regimes, for which mixing-length models can be used to describe turbulent transport spectra effectively. The particular experiment considered was a DIII-D ELMy H-mode shot (#162940), with analysis focused on modeling ion-scale turbulent transport. Miller parameterization was used to describe the magnetic equilibrium, and experimental density and temperature profiles were considered. Collisional and electromagnetic effects were included, with particle dynamics either gyrokinetic or drift-kinetic (as in the case of electrons in GEM). Three common saturation rules were introduced and compared, and linear gyrokinetic simulation results were used to calculate the quasilinear expressions for the flux. Comparisons were further made to the SAT1 TGLF model as well as local and global nonlinear gyrokinetic simulations. The three saturation rules were shown to exhibit similar behavior. Local nonlinear GENE simulations were extended to negative triangularity flux surfaces, and a reduction in transport was observed corresponding to stabilization of ITG and TEM modes.

Low-k_y electromagnetic MTM modes dominated local nonlinear GENE simulations, but were absent in global GEM simulations, likely due to nonlocal stabilizing effects. The value of β was reduced in GENE simulations to eliminate the MTM modes, and nonlinear GENE results then agreed well with the quasilinear models. Global GEM results gave a lower ion and electron particle flux, while nonlinear GENE and GEM showed a higher impurity flux than the quasilinear models predicted. It would be interesting to further include equilibrium shear flow effects and investigate the parametric dependence of the models for a variety of tokamak equilibria. Future work might also consider breaking up the diffusive and convective pinch contributions to the flux, as well as consider the impurity peaking factor. Furthermore, all quasilinear models described here focus on electrostatic modes, and extension to electromagnetic instabilities is a topic of interest. It has been made evident

here that quaslinear theory constitutes a powerful tool for reduced modeling of turbulent transport characteristics. This offers significant advantages for the subgrid modeling efforts of Chapter 5, which seek to capture electron-scale turbulent effects in global ion-scale simulation. However, the validity of such mixing-length models is found to be less robust for ETG modes in sections 4 and 5, likely due to the different saturation mechanisms present at different wavelengths. This indicates a need for better saturation models of ETG turbulence.

Chapter 4

ETG-Driven Zonal Flows

The focus of this chapter is on nonlinear regulation of ETG turbulence. Previous fluid theories of ETG mode regulation are briefly introduced, where the self-regulating effect of zonal flow drive is expected to be weak. More recent work regarding nonlinear gyrokinetic theory of zonal flow generation at intermediate scales is described, and gyrokinetic simulation results validating the theory are presented. The theoretical framework and simulation results discussed here are directly based on the contents of Refs. [64] and [197], and represent the primary original work of this chapter.

4.1 ETG Mode Regulation

Electron-scale turbulence is a primary candidate for the anomalous transport of electron energy well above the neoclassical values seen in a variety of tokamak plasma scenarios [36–38, 40]. Additionally, electron energy transport may become more important in future burning plasma experiments such as ITER because the electron channel is preferentially heated by Coulomb collisions with fusion alpha particles [111]. The electron-temperature-gradient (ETG) instability produces radially-elongated streamers at the electron gyroradius scale and is a primary candidate to explain electron-scale transport [37, 38, 62, 63, 101, 102, 198]. Electron heat flux due to ETG turbulence has been seen to play a role in various tokamak experiments [107, 199–201], and the inclusion of electron-scale dynamics at the ion scale has resulted in better agreement with experimental heat flux levels for both species [60, 61].

Electron-scale [108, 202] and multiscale [60, 61] long-time, large-box gyrokinetic flux-tube simulations have reported that intermediate-scale zonal flows (ZFs) help to regulate streamer turbulence in the quasi-saturated state and can eventually become dominant. These results are

inconsistent with fluid ETG turbulence models in which zonal flow generation occurs via the standard Hasegawa-Mima nonlinear mechanism [203, 204], which is significantly weaker for ETG turbulence than for ion-temperature-gradient (ITG) turbulence [205, 206]. Moreover, while shearing due to zonal flows generated by ITG turbulence can suppress ion transport levels, the finer scale ETG turbulence is unlikely to be affected by the ITG-driven zonal flows [40, 105]. These effects have led to the expectation of a streamer-dominated steady state at the electron scale.

A more recent weak-turbulence, toroidal, gyrokinetic-electron analysis [64] of nonuniform tokamak plasmas in the intermediate-scale ($k_\perp^2\rho_e^2 \ll 1 \ll k_\perp^2\rho_i^2$) results in a Navier-Stokes type nonlinearity which is typically stronger than the Hasegawa-Mima coupling of the fluid approximation. This stronger Navier-Stokes type nonlinearity is predicted to drive notable ZF generation and ETG mode regulation at intermediate scales when compared to the Hasegawa-Mima type coupling of the short-wavelength fluid regime [64]. ETG mode saturation in the short-wavelength fluid regime has been extensively studied and includes saturation mechanisms such as secondary instabilities [62, 63] and toroidal inverse-cascading [105, 205, 206] which would lead to a turbulent state characterized by intermediate-scale ETG modes. After the initial transition to the intermediate scale, the nonlinear interaction between ETG and ZF modes is expected to be enhanced such that zonal flows may grow to regulate long-term steady state transport levels as measured by experiment [64]. The intermediate-scale turbulent state might then be characterized by kinetic saturation mechanisms such as standard quasilinear estimates [173, 175, 207] and $\mathbf{E}\times\mathbf{B}$ particle trapping [172].

Collisionless Cyclone base-case (CBC) simulations of ETG turbulence initially reported the algebraic growth of zonal flows into late times [202]. Electron-scale MAST simulations [108] demonstrated that the long-time saturated electron heat flux scales roughly proportionally to the collisionality, and this was tied to the nonlinear interaction of ETG modes with zonal flows which are well-known to be damped by collisions [120]. In both cases, an initial turbulent state developed characterized by ETG mode streamers which were eventually suppressed by the slow growth of intermediate-scale zonal flows. DIII-D and Alcator C-Mod simulations [60, 61] involving multiscale ion and electron dynamics also saw significant intermediate-scale zonal flow generation which helped

to suppress ITG and ETG turbulence into the late stage.

This chapter provides results which compare the generation of zonal flow by ETG turbulence in electron-scale, gyrokinetic simulations with theoretical predictions in the intermediate-scale limit [64]. First, brief introductions are given to the Hasegawa-Mima and secondary Kelvin-Helmholtz type methods of ETG regulation as an overview of previous work on the subject. This is followed by a description of the intermediate-scale nonlinear gyrokinetic theory of Ref. [64]. Analysis of gyrokinetic ETG simulations is then given for two types of nonlinear simulations. Simulation parameters and details are described in Section 4.2.1, and the "single-mode" results which are described next in Section 4.2.2 serve to illuminate the role of a single ETG mode in generating zonal flows. As the theoretical description is limited to a single ETG mode for tractability, these results convey the primary scope of the original work described herein. The "full-spectrum" nonlinear simulations provided in Section 4.2.3 include a typical range of ETG modes and are qualitatively explained in terms of the single-mode results. In both types of simulations it is found that intermediate-scale zonal flows are primarily driven by slowly-saturating intermediate-scale ETG modes. The results are in good agreement with the gyrokinetic theory in the intermediate-scale and the fluid models of secondary instability at the short wavelength scale.

4.1.1 Hasegawa-Mima Equation

One possible governing equation for drift-wave turbulence is the Hasegawa-Mima (HM) equation, a second order nonlinear partial differential fluid equation that describes nonlinear drift-wave dynamics [203]. The intrinsic nonlinearity of the HM equation drives the isotropization of turbulence in the perpendicular plane through the advection of vorticity ($\omega = \nabla \times \mathbf{v}_E = \nabla^2 \phi$). While the total energy of the system is conserved, it spreads isotropically in k_x and k_y due to rotational dynamics in the perpendicular plane. As a result, radially extended drift-wave streamers are broken up into circular eddies in the final steady-state configuration. This process ultimately reduces radial correlation lengths, and, consequently, results in lower radial transport levels.

A simple derivation for the Hasegawa-Mima equation starts from the ion continuity equation and

further assuming adiabatic electrons, quasineutrality, no parallel dynamics, and no divergence for the **ExB** drift (which can easily be shown in slab geometry for electrostatic waves as $\nabla\cdot\mathbf{E} = \nabla\cdot\mathbf{B} = 0$). In order to retain nonlinear effects the second order polarization drift must be kept in the perpendicular divergence of the velocity and the governing ion continuity equation is [36]

$$\partial_t n_i + \mathbf{v}_E \cdot \nabla n_i + \nabla_\perp \cdot \left(\frac{c^2 n_i m_i}{q_i B^2} \frac{d\mathbf{E}_\perp}{dt} \right) = 0. \tag{4.1}$$

The time derivative of the electric field is expanded using the **ExB** drift, i.e. $d/dt = \partial_t + \mathbf{v}_E \cdot \nabla$, and Equation (4.1) reduces to the Hasegawa-Mima equation

$$(1 - \rho_s^2 \nabla_\perp^2)\partial_t \phi + v_d \partial_y \phi - \frac{c}{B}\{\phi, \nabla^2 \phi\} = 0. \tag{4.2}$$

The curly braces here correspond to Poisson brackets, where $\{A, B\} = \partial_x A \partial_y B - \partial_y A \partial_x B$. Linearizing Equation (4.2) simply results in the standard drift wave dispersion relation, Equation (2.23). The last term is nonlinear in the perturbation ϕ, and the expanded notation clearly involves a cross product which leads to rotation in the perpendicular plane and an isotropic potential in Fourier space.

A more thorough derivation is given for an ETG mode in Appendix E, which results in the electron-scale-normalized HM equation, Equation (E.15),

$$\begin{aligned} &- (1 - \frac{1+\tau}{2\tau}\nabla_\perp^2)\partial_t \Phi + \frac{1+\tau}{2\tau}\frac{r_n^2}{\rho_e^2}\partial_t^{-1}\nabla_\parallel^2 \Phi + \frac{(1+\tau)(1+\eta_e)}{4\tau}\partial_y \nabla_\perp^2 \Phi \\ &+ \frac{(1+\eta_e)}{2\tau}\partial_y \Phi + \frac{(1+\tau)^2}{\tau^2}\frac{r_n}{4\rho_e}\left[\hat{\mathbf{b}} \times \nabla_\perp \Phi \cdot \nabla_\perp\right] \nabla_\perp^2 \Phi = 0. \end{aligned} \tag{4.3}$$

Equation (4.3) is solved numerically in the perpendicular plane (assuming $k_\parallel = 0$), and the results are presented here for illustrative purposes. The time step is handled by a 4th-order Runge-Kutta scheme, and the nonlinear term is calculated pseudo-spectrally. Nonlinear products are de-aliased by a 2/3 rule, where the largest 1/3 of the initial wavenumbers must be truncated so that products of modes remain well-resolved on the simulation grid. The initial condition is taken from a steady-state

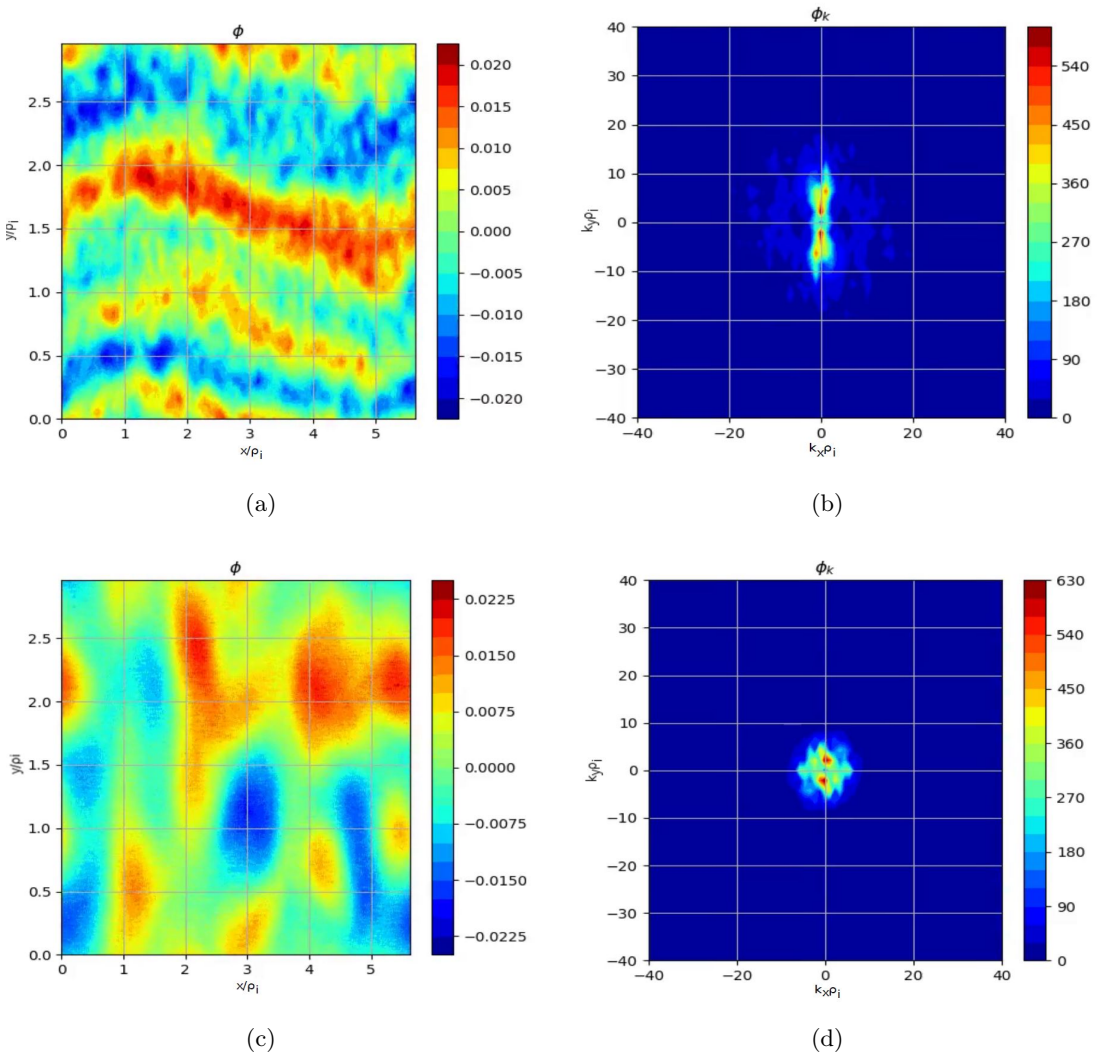

Figure 4.1: Initial ETG streamer potential from the nonlinear GENE simulations of Section 4.2.1 plotted in (a) real space and (b) Fourier space. Late-time electrostatic potential after evolution by HM Equation (4.2), plotted in (c) real space and (d) Fourier space.

snapshot of ETG turbulence from the small-box nonlinear GENE simulation described later in Section 4.2.1, and the initial and final states are shown in real and Fourier space in Figure 4.1. The transition from a streamer dominated state to one consisting of more circular eddies corresponds clearly to rotation and isotropization of the potential in Fourier space. Note, there is also a toroidal inverse cascade present, which is expected in the HM system [204].

4.1.2 Kelvin-Helmholtz Instabilities

Secondary instabilities represent another type of regulation mechanism which can lead to ETG turbulence suppression. A secondary instability refers to any instability which is itself driven by the primary instability, in this case the ETG mode. Secondary instabilities grow as the primary instability grows and so will eventually grow faster than the primary until nonlinear effects lead to primary mode saturation. Original work on gyrokinetic simulations of ETG turbulence showed Kelvin-Helmholz-type (KH) instabilities played an important role in the regulation of high-k ETG streamers [62, 63, 101]. Physically, this is because as the ETG wavenumber increases, the **E**x**B** convective layers get closer together and shearing effects become stronger. The KH instability leads to shearing flows which break up the radial streamers, and the resulting zonal flows were found to be themselves regulated by tertiary KH instabilities [63]. All analysis of ETG saturation by secondary modes described here is taken from Ref. [63]. The dynamics of the secondary mode are described by the equations

$$\frac{dn}{dt} + \frac{1}{2}[\nabla_\perp^2 \psi, T_\perp] = 0, \tag{4.4}$$

$$n = [\tau - (1+\tau)\nabla_\perp^2]\psi, \tag{4.5}$$

where $\tau = Z_{\text{eff}} T_{0e}/T_{0i}$, and n and ψ represent a normalized density and electrostatic potential. The primary mode structure is given simply by $\psi = \psi_{p0}\cos(k_p y) + \widetilde{\psi}(y)\exp(\gamma t + ik_x x)$ with k_p the poloidal wavenumber of the primary mode. Substituting the form of the primary mode into Equation (4.4) and using Equation (4.5) for the density gives

$$\left[\left(\frac{\tau}{1+\tau}\right)\gamma + k_x^2\bar{\gamma}\right]\widetilde{\psi} = \partial_y[\bar{\gamma}\partial_y(\widetilde{\psi}/\bar{\gamma})], \tag{4.6}$$

where $\bar{\gamma} = \gamma - ik_x\psi_y'(y)$. Note, the resulting ETG secondary equation differs from the conventional KH equation because of the first term on the left-hand-side which is due to the ion response in the plasma.

Balancing terms in Equation (4.6) gives a maximum growth rate

$$\gamma_{\max} \sim k_p^4 \psi_{p0}, \tag{4.7}$$

for $k_x \sim k_p$, which is $\mathcal{O}((k_\perp \rho_e)^2)$ smaller than the standard KH mechanism. Because of this, saturation by secondary instability growth is quite weak for small $k_\perp \rho_e$, and long wavelength ETG streamers saturate at much higher levels. This has led to the expectation of a streamer dominated state with large electron heat transport levels in early ETG studies. Note that this method of saturation produces a $\phi \sim \gamma / k_\perp^4$ saturation rule as opposed to what might be expected by a standard mixing-length model. In this case, the potential spectra is narrower and falls off more sharply at high-k. However, as the system transitions to longer wavelength turbulence, gyrokinetic theory would better describe the nonlinear dynamics of mode regulation. Furthermore, fluid theories of ETG turbulence also predict toroidal inverse cascading to longer wavelengths [105, 205, 206]. These considerations, along with gyrokinetic simulation results showing slow growth of zonal flows into late times [61, 108, 202], motivated the development of a gyrokinetic theory of intermediate-scale ETG turbulence [64], which is formally described in Section 4.1.3.

4.1.3 Intermediate-Scale Gyrokinetic Theory

This section focuses on a gyrokinetic model of ETG mode saturation. Fluid theories of ETG regulation described previously result in a transition to intermediate scales, where it is expected that nonlinear gyrokinetic theory becomes more important. Ref. [64] has shown theoretically that intermediate-scale zonal flow may play a significant role in the saturation of ETG turbulence in tokamak plasmas. The Navier-Stokes type **ExB** nonlinearity in the gyrokinetic equation drives more notable zonal flow growth at intermediate scales, further regulating any streamer dominated ETG steady-state predicted by fluid theories. The theory described in Ref. [64] is reviewed here, and simulation results from [197] are further presented in comparison to the theoretical model.

The theoretical model takes the standard gyrokinetic equation [65, 68, 69] for electrons and

the quasineutrality condition in the intermediate-scale limit $k_\perp^2\rho_e^2 \ll 1 \ll k_\perp^2\rho_i^2$. For long-wavelength ETG modes, one can generally assume that the growth rate is much smaller than the real frequency, $|\gamma/\omega| \ll 1$, which allows for a weak-turbulence analysis. These ETG modes also satisfy the relation $|\omega_d| \ll |\omega|, |\omega_t|$, for ω_t and ω_d the transit and magnetic drift frequencies respectively. Note a fluid approximation, which is applicable at higher frequencies and wavenumbers, would instead assume $|\omega_d|, |\omega_t| \ll |\omega|$. Local approximations [208] are assumed for ω_d and ω_t in formulating a kinetic electron model. The ETG mode is modeled using the ballooning mode representation, described in Appendix D by Equation (D.8),

$$\delta\phi_{\mathbf{k}} = \sum_m e^{i(m\theta - n\zeta)} \int\int d\eta d\theta_k e^{i[nq(\eta-\theta_k)-m\eta]} A_{\mathbf{k}} \delta\widetilde{\phi}_{\mathbf{k}}, \tag{4.8}$$

where η is the field-line-following coordinate and θ_k is the mode tilting angle.

Analysis is simplified by considering a local kinetic model, by replacing η with the parallel-mode-averaged value $\bar{\eta} = [(\int d\eta \widetilde{\Phi}^* \eta^2 \widetilde{\Phi})]^{1/2}$, where $\Phi = e\delta\phi_{\mathbf{k}}/(\rho_* T_e)$ is the normalized electrostatic potential and $\rho_* = \rho_e/r_n$ with r_n the density gradient scale length. The gyrokinetic and quasineutrality equations are combined to find a dispersion relation, which reduces to the algebraic form

$$D_{\mathbf{k}}(\omega_{\mathbf{k}}, \theta_k, r) \equiv (1+\tau) - \langle \frac{(\omega_{\mathbf{k}} + \omega_{*e}^t)\bar{J}_{\mathbf{k}}^2 F_0}{\omega_{\mathbf{k}} + \omega_t + \omega_d} \rangle_v = 0, \tag{4.9}$$

where $\omega_t = -v_{te} v_\parallel/(qR_0\bar{\eta})$, $\omega_d = -\omega_{*e}\epsilon_n(2v_\parallel^2 + v_\perp^2)[\hat{s}(\bar{\eta} - \theta_k)\sin\bar{\eta} + \cos\bar{\eta}]$, and $\omega_{*e}^t = -\omega_{*e}[1 + \eta_e(v^2 - 3/2)]$ with $\epsilon_n = r_n/R_0$ and $\langle\cdots\rangle_v = \int d\mathbf{v}(\cdots)$. The drifts in the large aspect-ratio circular limit, as calculated in Appendix C, have been converted to a field-line-following coordinate system here.

The nonlinear description of zonal flow dynamics is found by considering lowest order effects

in the gyrokinetic equation [105, 209], thereby taking neoclassical effects into account,

$$\left[\partial_t + \gamma_z(1 + d_z k_\theta^2 \rho_e^2 s^2 \theta_k^2)\right] \chi_z A_z(\theta_k) = \sqrt{\frac{\pi}{2}}(k_\theta \rho_e \hat{s})\theta_k \int d\vartheta_k \vartheta_k^2 \left[A_n(\vartheta_k) A_n^*(\vartheta_k - \theta_k) a_n^* - A_n(\vartheta_k + \theta_k) A_n^*(\vartheta_k) a_n\right]. \tag{4.10}$$

The nonlinear term under the integral in Equation (4.10) is related to the Reynolds stress of the ETG modes. The ZF damping rate is given by $\gamma_z \simeq 3\nu_{ee}/(|\omega_{*e}|\sqrt{\epsilon})$, with ν_{ee} the electron-electron collision frequency and ω_{*e} the electron diamagnetic drift frequency. The total electric susceptibility is defined as $\chi_z = \tau + (1 + 1.6q^2/\sqrt{\epsilon})k_\theta^2 \rho_e^2 s^2 \theta_k^2/2$ with $\tau = T_e/T_i$, and the d_z term in Equation (4.10) represents a gyrodiffusive correction which helps suppress short wavelength zonal flows [210]. The a_n term describes the parallel correlation of the ETG turbulence and is defined as

$$a_n(\theta_k, \vartheta_k) = \int d\eta \langle \tilde{\Phi}_n^*(\eta, \vartheta_k) v_\perp^2 \delta\tilde{H}_n(\eta, \vartheta_k + \theta_k)\rangle_v, \tag{4.11}$$

where $\delta\tilde{H}_n$ is the non-adiabatic part of the distribution function perturbation.

The parallel decoupling, a_n, results from the separation of different k_x parts of the ETG mode along the field line as $k_x = \hat{s} k_y \theta_k$. This is in contrast to the case of ITG modes for which the local value $a_n(0,0)$ can reasonably be used [211] as k_y is much lower for ITG modes. Assuming a parallel ETG mode structure centered around different θ_k one expects

$$\widetilde{\phi}_n(\eta, \theta_k) = \widetilde{\phi}_n(0, \theta_k) e^{\frac{(\eta - \theta_k)^2}{\bar{\eta}^2}}, \tag{4.12}$$

i.e. a Gaussian structure shifted along the field line by an amount θ_k. A form for a_n can be found by linearizing the gyrokinetic equation for $\delta\tilde{H}_n$ and substituting into Equation (4.11), resulting in [64]

$$a_n = a_n(0,0) \exp(-\theta_k^2/2\bar{\eta}^2). \tag{4.13}$$

Keeping a_n non-local in tilting angle in order to take into account ballooning effects leads to a

parallel decoupling of ETG modes and therefore ZFs as well. It is then clear that the Reynolds stress decreases exponentially with θ_k^2, and the decoupling effect plays an important role in suppressing shorter wavelength ZFs.

The evolution of a single ETG mode can be derived in terms of a nonlinear Schrodinger equation (NLSE) by considering the gyrokinetic equation to the next order [64]

$$[i(\partial_t - \gamma_n) - b_n k_\theta^2 \rho_e^2 \hat{s}^2 \theta_k^2 - \frac{c_n}{k_\theta^2 \rho_e^2 \hat{s}^2} \frac{\partial^2}{\partial \theta_k^2}] A_n(\theta_k) = \frac{-ik_\theta \rho_e \hat{s}}{\sqrt{2\pi}} \int d\vartheta_k \vartheta_k A_z(\vartheta_k) A_n(\theta_k - \vartheta_k), \quad (4.14)$$

with A_z and A_n the amplitudes of the ZF and ETG modes, γ_n the ETG mode growth rate, θ_k and ϑ_k the tilting angle (defined by $\theta_k = k_x/(k_y \hat{s})$ in the flux-tube limit [78] for k_y of the ETG mode), and k_θ the poloidal wavenumber. The terms including b_n and c_n relate to the frequency mismatch and plasma nonuniformity corrections respectively, where the coefficients are defined as $b_n = -(\partial_{\theta_k}^2 D_{\mathbf{k}}/\partial_{\Omega_{\mathbf{k}}} D_{\mathbf{k}})/(2k_\theta^2 \rho_e^2 \hat{s}^2)$ and $c_n = (\partial_r^2 D_{\mathbf{k}}/\partial_{\Omega_{\mathbf{k}}} D_{\mathbf{k}})/2$, for $\Omega_{\mathbf{k}} = \omega_{\mathbf{k}}/|\omega_{*e}|$ [64]. The nonlinear term under the integral in Equation (4.14) describes a Navier-Stokes type coupling due to **E**x**B** shearing effects. This coupling is $\mathcal{O}((k_\theta \rho_e)^{-2})$ stronger than the usual Hasegawa-Mima type coupling in the fluid limit [205, 206], resulting in a stronger regulation of ETG turbulence by zonal flows and also leads to a reduced threshold for ZF excitation by intermediate-scale ETG modes. The threshold condition is described further in Equation (4.15).

Eqns. (4.14) and (4.10) are taken together as the NLSE model. The numerical solution of the NLSE model with a single ETG mode and a range of ZF modes gives an evolution of ETG and ZF modes that can be described by three specific stages [64]. The initial stage involves uninhibited exponential growth of the ETG mode to a threshold point at which the radial beating of the ETG drives ZF growth at a rate $e^{2\gamma t}$, as described in Ref. [64]. As the ZF modes grow, they lead to radial dispersion of the initial ETG wave and the creation of sidebands. These sidebands then drive more zonal flows via a modulational instability in the second stage. Once the zonal flow grows to appreciable levels in comparison with the ETG mode, the nonlinear interaction in Equation (4.14) acts to saturate the ETG mode. In the final stage, the linear growth rate of the ETG mode becomes

negligible and the NLSE model then results in slow, algebraic growth for the zonal flow [64]. This slow growth has been observed in previous gyrokinetic electron-scale simulations [108, 202].

A threshold condition for the ZF excitation can be calculated analytically [64] by considering a simple four-wave model for a single zonal flow mode, an ETG pump mode, and two ETG sideband modes. Narrow-band, rectangular functions are used to describe the ZF and ETG modes, $A_z\Pi[(\theta_z)/W]$ and $A_0\Pi(\theta_k/W) + A_+\Pi[(\theta_k - \theta_z)/W] + A_-\Pi[(\theta_k + \theta_z)/W]$ respectively. Here W is the full-width of the modes, θ_z is the ZF wavenumber in terms of tilting angle, and A_z, A_0, and $A_\pm$ are the ZF, ETG pump, and ETG sideband mode amplitudes. Substituting these functions into Eqns. (4.14) and (4.10) with the assumption of no plasma nonuniformities ($c_n = 0$) and a steady state pump amplitude for simplicity, one obtains the critical threshold condition [64]

$$W^2|A_{0,c}^2| = \frac{(\Delta^2 + \gamma_s^2)\gamma_z(1 + d_z(k_\theta\rho_e\hat{s}\theta_z)^2)\chi_z}{(k_\theta\rho_e\hat{s}\theta_z)^4[\gamma_s\mathrm{Re}(a_n) + \Delta\mathrm{Im}(a_n)]}. \tag{4.15}$$

Here, $\Delta = \mathrm{Re}(b_n)(k_\theta\hat{s}\theta_z\rho_e)^2$ represents the frequency mismatch of the pump and sidebands, and $\gamma_s = \gamma_n + \mathrm{Im}(b_n)(k_\theta\hat{s}\theta_z\rho_e)^2$ is the growth rate of the sidebands. This threshold condition for ZF excitation by intermediate-scale ETG modes is $\mathcal{O}(k_\theta^2\rho_e^2)$ lower than the condition found in the fluid approximation [206], and so leads to more effective ZF generation at intermediate scales.

The ZF modes are initially excited over a range of θ_z values. As the system evolves to the quasi-saturated state and the ETG mode is suppressed, the ZF spectrum narrows towards the most easily driven mode. Comparing the exponential θ_k dependence of the a_n term to the algebraic form of the d_z term, one finds that the parallel decoupling is largely responsible for minimizing the intermediate-scale threshold condition at low θ_z. If one considers the temporal evolution of the four-wave model, a fixed-point solution can be found with constant A_z and sufficiently low ZF damping rate, where the ZF and ETG mode amplitudes are given as [64]

$$W^2|A_{z,p}|^2 = \frac{\pi(\delta^2 - \Delta\delta - \gamma_n\gamma_s)}{(k_\theta\hat{s}\theta_z\rho_e)^2}, \tag{4.16}$$

and

$$W^2|A_{0,p}|^2 = \frac{\chi_z\gamma_z(1+d_z k_\theta^2\hat{s}^2\theta_z^2\rho_e^2)[\gamma_s^2+(\delta-\Delta)^2]}{(k_\theta\hat{s}\theta_z\rho_e)^4[(\Delta-\delta)\mathrm{Im}(a_n)+\gamma_s\mathrm{Re}(a_n)]}. \tag{4.17}$$

Here, $\delta = \Delta\gamma_n/(\gamma_s+\gamma_n)$ represents the amplitude oscillation frequency of ETG modes due to the nonlinear ETG-ZF coupling. The single ETG mode spectrum then continues to fluctuate in k_x while the ZF mode reaches a constant, steady state [64]. Additionally, $|A_{0,p}|^2$ is proportional to γ_z in the saturated state, and therefore the collision frequency, while $|A_{z,p}|^2$ is not. While these saturation estimates are only valid for a single ZF mode, as the ETG turbulence saturates and the ZF spectrum narrows due to the threshold condition, θ_z of the most optimally-driven mode can be used to estimate the ETG saturation level.

4.2 Gyrokinetic Simulations of ETG-Driven Zonal Flows

4.2.1 Simulation Model and Parameters

GENE [62, 148], an Eulerian 5-d gyrokinetic continuum code, is employed here in the flux-tube limit appropriate for electron-scale turbulence. Gyrokinetic ions and electrons are taken with standard Cyclone base-case (CBC) parameters which are typical of H-mode core plasmas, but here a simplified circular geometry is used [90, 145, 192, 212]. First, the linear ion-scale benchmark in Ref. [145] was verified, then the simulation was converted to the electron scale by reducing the perpendicular box dimensions by a factor of $\sqrt{m_i/m_e} \sim 42$. Here, m_e is the electron mass, and m_i is the ion mass which is taken to be the proton mass, m_p. For the electron-scale case the ion temperature gradient was set to zero to suppress ion-scale turbulence and focus on electron-scale physics.

The mode frequencies, ω, and growth rates, γ, resulting from the linear GENE simulations are shown as functions of $k_y\rho_i$ in Figures 4.2(a) to 4.2(c) below. The frequencies are normalized to units of R/c_s, as listed with other GENE normalizations in Table 4.1. Here, k_y is the binormal wavenumber of the GENE coordinate system, R is the tokamak major radius, and $c_s = \sqrt{T_i/m_e}$ is the ion sound speed with T_i the ion temperature. The ITG benchmark case is shown in Figure 4.2(a) alongside

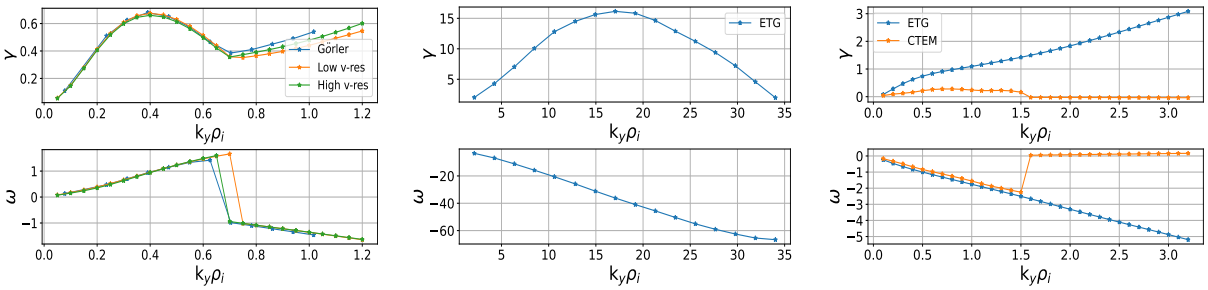

(a) (b) (c)

Figure 4.2: GENE linear simulation results showing growth rates and real mode frequencies for (a) CBC ITG benchmark case, (b) electron-scale ETG case, and (c) ion-scale ETG case showing CTEM modes as well. Positive (negative) frequencies indicate propagation in the ion(electron)-diamagnetic direction.

the electron-scale ETG case in Figure 4.2(b). Ion-scale ETG results are shown in Figure 4.2(c), where the collisionless trapped-electron mode (CTEM) [113, 213, 214] is included. One can see the ITG mode in the lower $k_y\rho_i$ range of Figure 4.2(a) characterized by propagation in the $\omega > 0$ ion diamagnetic drift direction. The ETG mode becomes unstable at higher $k_y\rho_i$ where ω crosses to the negative electron diamagnetic drift direction [36]. While the CTEM is expected to contribute to electron transport [40, 114, 175, 215], Figure 4.2(c) shows that it is stable in the intermediate-scale range.

The reference values and radial profiles are taken as specified in Ref. [145] with reduced values of m_i and $\beta = 8\pi n_e T_e/B^2$. Here n_e and T_e are the electron density and temperature, and B is the on-axis magnetic field. A value of $\beta = 10^{-4}$ was chosen to keep the simulation nearly electrostatic in order to avoid transport due to electromagnetic fluctuations. The safety factor, $q = rB_\phi/RB_\theta$, and magnetic shear, $\hat{s}$, profiles are given by $q(r) = 2.52(r/a)^2 - 0.16(r/a) + 0.86$ and $\hat{s} = \frac{r}{q}\frac{dq}{dr}$ [145]. B_ϕ and B_θ represent the toroidal and poloidal magnetic field components respectively. The radial flux-surface coordinate $r = 0.5a$ was chosen, where a is the tokamak minor radius. The normalized density and temperature gradient profiles, for a general profile $A(r)$, are defined as $R/L_A = -R\partial_r \ln(A(r))$, which can be calculated using the profile given in Eq. (2) of Ref. [145].

The values of the pertinent simulation parameters are listed in Table 4.2.

For the linear ITG case, the grid resolution was taken with 32 grid points in the radial dimension, x, and 16 grid points in the parallel spatial dimension, z. The GENE radial coordinate x corresponds to the flux-surface coordinate r for the case of a circular geometry. In Figure 4.2(a) the flux-tube GENE benchmark result from Ref. [145] is marked as “Görler" and the corresponding “low” (32×8) and “high” (64×16) velocity grid ($v_\parallel \times \mu$) resolution simulations have been plotted collectively. There is good agreement with the benchmark case in the ITG range. The intermediate scale is well resolved in the “low v-res" case, and the same grid resolution was used for the nonlinear simulation, but with the radial grid resolution increased to 192 gridpoints. The perpendicular box size was reduced from $125\rho_i \times 125\rho_i$ at the ITG turbulence scale to $6\rho_i \times 3\rho_i$ at the ETG turbulence

Table 4.1: Relevant GENE normalizations and definitions [148].

ρ^*	ρ_i/R
c_s	$\sqrt{T_i/m_e}$
t	R/c_s
ω	c_s/R
γ	c_s/R
Q_{gB}	$c_s n_e T_e (\rho^*)^2$
χ_{gB}	$\rho_i^2 c_s/R$
ϕ	$e\phi/(T_e\rho^*)$
ν_c	$\pi \ln\Lambda e^4 n_e R/(2^{3/2}T_e^2)$
Λ	$24 - \ln(\sqrt{10^{13}\cdot n_e}/(10^3 T_e))$

Table 4.2: GENE simulation parameters.

R(m)	1.67
$n_{i,e}(10^{19}\mathrm{m}^{-3})$	4.66
$T_{i,e}$(keV)	2.14
B_ϕ(T)	2.0
r/a	0.5
a/R	0.36
ρ^*	0.001413
β	1e−4
m_i/m_p	1.0
m_e/m_i	5.4462e−4
R/L_{T_i}	0
R/L_{T_e}	6.96
$R/L_{n_{i,e}}$	2.22
q	1.41
$\hat{s}$	0.837
ν_{ei}	0.106875

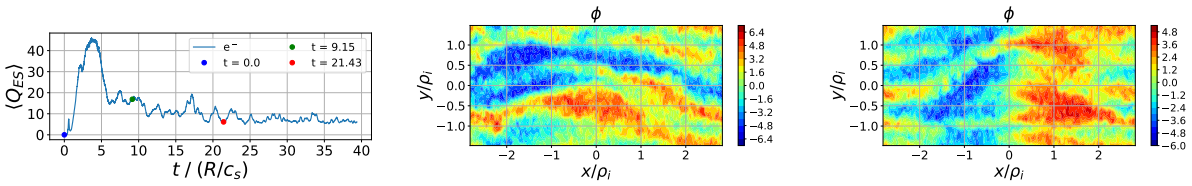

(a) (b) (c)

Figure 4.3: Original (small-box, no collisions) nonlinear simulation results showing (a) time-marked electrostatic electron heat flux and electrostatic potential contours for the (b) early nonlinear phase (green marker), and (c) late zonal phase (red marker).

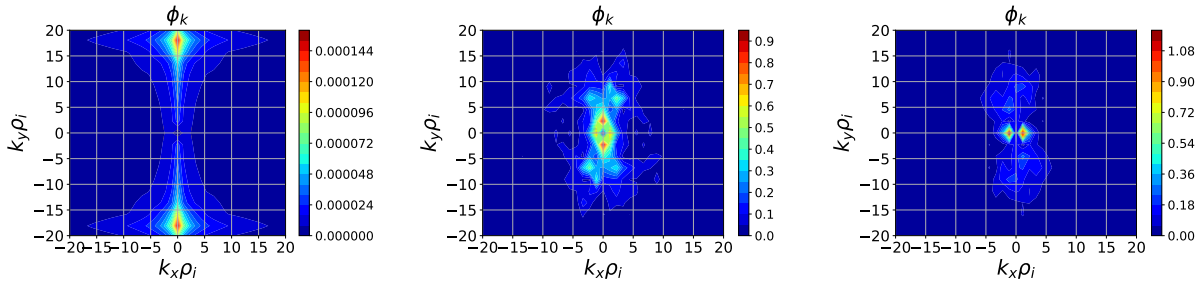

(a) (b) (c)

Figure 4.4: Original (small-box, no collisions) nonlinear simulation results showing Fourier-space electrostatic potential contours for the (a) initial time (blue marker), (b) early nonlinear phase (green marker), and (c) late zonal phase (red marker). The markers correspond to the times marked in Figure 4.3(a).

scale, where the original radial extent of the flux-tube domain was increased from $3\rho_i$ to $6\rho_i$ to allow for the full formation of the ETG mode streamers.

The electrostatic portion of the radial heat flux, $\langle Q_{ES} \rangle$, for electrons is shown approaching a statistically steady state in time in Figure 4.3(a) for the collisionless, $6\rho_i \times 3\rho_i$, nonlinear, full-spectrum, electron-scale case. The heat flux is normalized to Q_{gB}, the gyroBohm normalization given in Table 4.1, and the angled brackets, $\langle \ldots \rangle$, denote a flux-tube volume average. The heat flux is determined in GENE as [148],

$$Q_{ES} = \int d^3v \left(\frac{1}{2} m v^2 \right) \boldsymbol{v}_{E\times B} \cdot \hat{\mathbf{r}} \, \delta f \ , \tag{4.18}$$

where δf is the distribution function perturbation, $\boldsymbol{v}_{E\times B} = -(\nabla\phi \times \boldsymbol{B})/B^2$ is the $\boldsymbol{E}\times\boldsymbol{B}$ drift, ϕ is the electrostatic potential perturbation, and m and v are the particle mass and velocity. The normalization for ϕ is given in Table 4.1. One can see the shift from the early, nonlinear state characterized by radially-elongated electrostatic potential streamers in Figure 4.3(b) to the later state of Figure 4.3(c) where zonal flows have become dominant. It is during this phase that intermediate-scale zonal flows grow slowly into the final quasi-saturated state.

The initial condition for ϕ was realistically peaked about the most unstable mode as shown in Figure 4.4(a). This allowed for a transition from the high-k_y ETG turbulence regime to the intermediate scale where ZF generation is expected to be stronger [64]. Such zonal flow generation is not present in toroidal electron fluid theories [205, 206]. An inverse-cascade can clearly be seen between Figs. 4.4(a) and 4.4(b). This initial saturation is discussed further for the single-mode simulation results presented in Section 4.2.2, and for the well-converged, collisional, full-spectrum simulation results presented in Section 4.2.3. The convergence tests for finding an optimal nonlinear box size are detailed in Section 4.2.4.

4.2.2 Single-Mode Simulation Results

The expectations from the theoretical NLSE model (Eqns. 4.14 and 4.10) are tested against gyrokinetic simulation results here. Collisionless, nonlinear, ETG simulations were first carried out, where a single unstable ETG mode ($k_x = 0$) and all zonal flow modes ($k_y = 0$) are retained. This fairly accurately describes the dynamics of the NLSE model. All results presented in this section are averaged over z. The ETG growth rate spectrum with respect to $k_y\rho_i$ is utilized here to illustrate the NLSE model dynamics. As seen in Figure 4.2(b), the ETG growth rate spectrum is symmetric around the most unstable mode, so one can choose to compare the evolution of a pair of ETG modes with similar growth rates, where one mode has a $k_y\rho_i$ value in the intermediate-scale range and the other mode has a larger $k_y\rho_i$ value outside of that range. Then the ZF drive of the two modes can be compared to verify the expectations from the NLSE model.

The $k_y\rho_i = 6.36$ mode with a growth rate of $\gamma \approx 7.037$ and the $k_y\rho_i = 30$ mode with a similar

growth rate of $\gamma \approx 7.015$ are taken here for comparison. Figure 4.5(a) shows the time evolution of the $k_y\rho_i = 6.36$ mode, while Figure 4.5(b) shows the time evolution of the $k_y\rho_i = 30$ mode. Figure 4.5(c) shows the time evolution of the four strongest zonal flow modes at the final time step for the intermediate-scale case, whereas Figure 4.5(d) considers a larger range of ZF modes excited in the high-k_y case in order to illustrate a difference in the zonal flow response between the two cases. One can see that initially both ETG modes grow exponentially at similar rates until a threshold is reached, at which point zonal flows are excited. For the intermediate-scale ETG mode, this phase is followed by an algebraically-growing long wavelength ZF phase in which the ZF modes gradually reach a steady state value. The high-k_y results show no slowly-growing ZF phase at late times. This difference in ZF generation in the late stage is consistent with the threshold condition given in Equation (4.15). The intermediate-scale ETG mode continues to slowly drive zonal flows as it is suppressed to lower levels, whereas the high-k_y ETG mode does not. The zonal flows plotted were confirmed to grow linearly on a log plot, indicating exponential growth.

The peak level of the ETG mode is much lower for the high-k_y case than for the intermediate-scale case. This result is not expected from the NLSE model as the shearing of the ETG mode by the wave-wave coupling should be stronger in the intermediate scale than at higher k_y. Zonal flows are

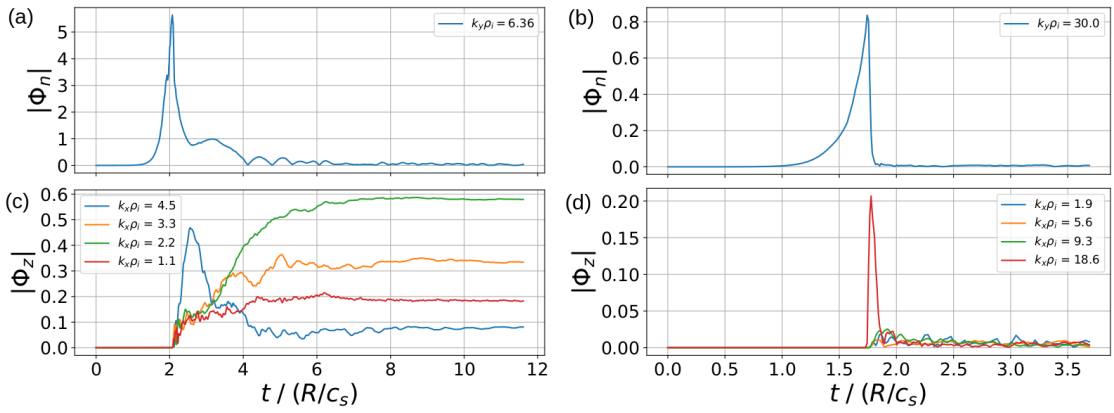

Figure 4.5: Plots of collisionless single ETG mode evolution for (a) $k_y\rho_i = 6.36$ and (b) $k_y\rho_i = 30$ with respective growth rates $\gamma \approx 7.037$ and 7.015. The strongest four ZF modes in the late time are plotted for (c) the $k_y\rho_i = 6.36$ case, while (d) shows the excitation of a larger range of ZF modes in the $k_y\rho_i = 30$ case.

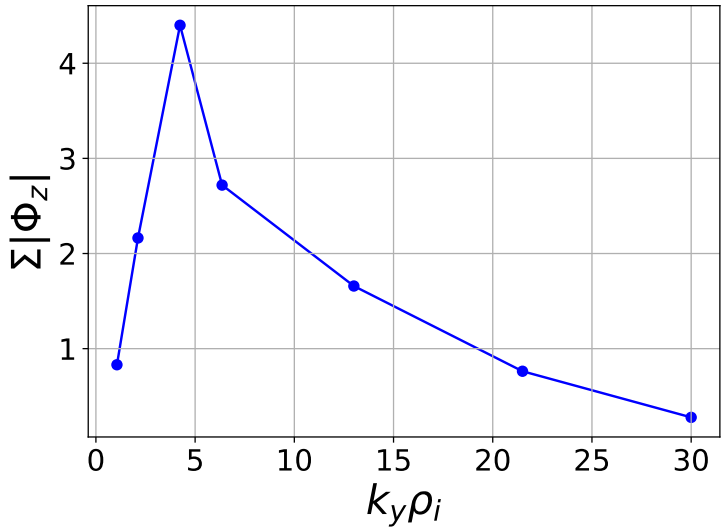

Figure 4.6: Plot of the sum of zonal potential amplitudes at final times, $\sum|\phi_z| = \sum_{k_x}|\phi_{k_x,0}|$, as driven by a single ETG mode. The fourth and seventh points correspond to the ETG modes from Figure 4.5.

also generated earlier in the high-k_y case, indicating a lower threshold initially, which is inconsistent with the NLSE model. One noticeable difference between the single-mode GENE simulations and the NLSE model is that the NLSE model only includes the ZF shearing suppression mechanism, whereas the single-mode GENE simulations include other saturation mechanisms. Comparing the zonal response between the two cases, it is found that the initial ZF excitation shown in Figure 4.5(d) is much more abrupt, growing exponentially on a log plot, possibly indicative of a secondary instability [62, 63, 216]. The change in ETG-ZF dynamics in the single-mode results is found to occur near $k_y\rho_i \sim 15$. This difference in behavior likely indicates the reason for the transition to the intermediate scale mentioned previously in Section 4.2.1, and this is further discussed in comparison to the full-spectrum simulation results presented in Section 4.2.3.

Figure 4.6 shows the sum of all ZF mode amplitudes, $\sum|\phi_z|$, as a function of $k_y\rho_i$. Each value of $k_y\rho_i$ represents initializing with a different unstable ETG mode. The sum is taken at the final simulation time, where the ZF mode amplitudes are nearing steady state levels. The notable region of ZF generation is clearly seen to be in the intermediate-scale range, as expected by the NLSE

model. Shorter ETG mode wavelengths correspond to weaker zonal flows at late times, in agreement with fluid ETG models. In addition, the drop-off at long ETG mode wavelengths is reasonable due to trapped electron effects at this wavenumber range [217]. A validation of this expectation for the full-spectrum simulations is provided in Section 4.2.4.

The unstable ETG mode is shown to be suppressed at late times in Figs. 4.5(a) and 4.5(b). The total amplitude, $\langle|\phi|\rangle = (\int d\theta_k |\phi_k|^2)^{1/2}$, of the ETG mode is small in comparison to the zonal flow amplitude. In contrast, the NLSE model simulation results given in Fig. 3 of Ref. [64] show that the total ETG and ZF mode amplitudes, $\langle|\phi|\rangle$, are of similar strength and fluctuating in the late stage. One reason to expect the strong ETG suppression in the gyrokinetic simulations is the lack of collisions which would damp the zonal flows due to the collisional dependence of the γ_z term in Equation (4.10). Another difference is that the NLSE model assumes a Gaussian radial spectrum for the ETG mode, while the single-mode flux-tube GENE simulations take $k_x = 0$ initially. The globally-Gaussian radial distribution of the ballooning modes would lead to more radial ETG mode overlap, which would then drive more ZF generation as predicted by Equation (4.10).

More physically realistic results were obtained here for the $k_y\rho_i = 6.36$ case in which the ETG and ZF modes fluctuate about similar steady state values due to their nonlinear coupling.

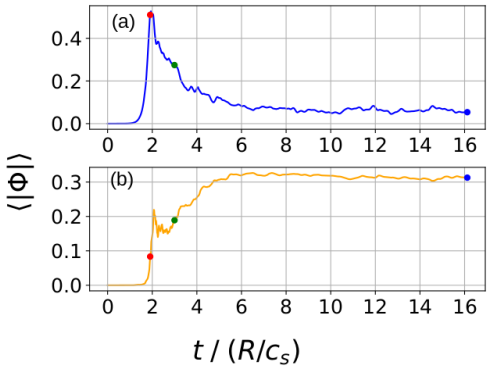

Figure 4.7: Plot of total (a) ETG and (b) ZF mode potential as an integral over k_x in the collisional, Gaussian-k_x ETG case for $k_y\rho_i = 6.36$. Markers have been added to match the spectral snapshots of Figure 4.8.

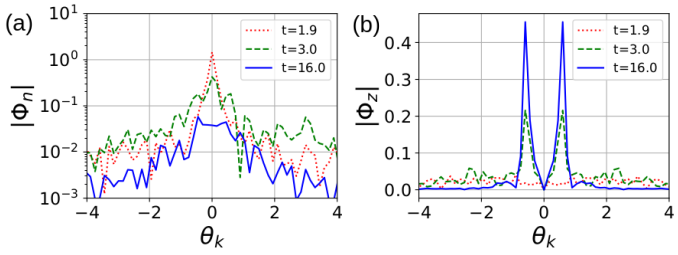

Figure 4.8: Radial-spectrum snapshots of (a) the single ETG mode and (b) ZF as a function of tilting angle for the $k_y\rho_i = 6.36$ case. Snapshot times match the markers in Figure 4.7.

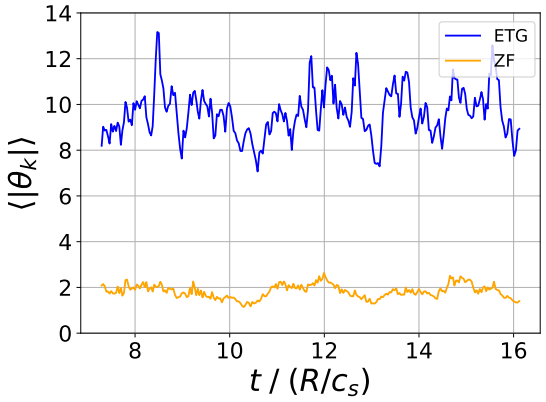

Figure 4.9: Plot in time of the average dimensionless radial wavenumber for the total ETG and ZF spectra in the quasi-saturated stage.

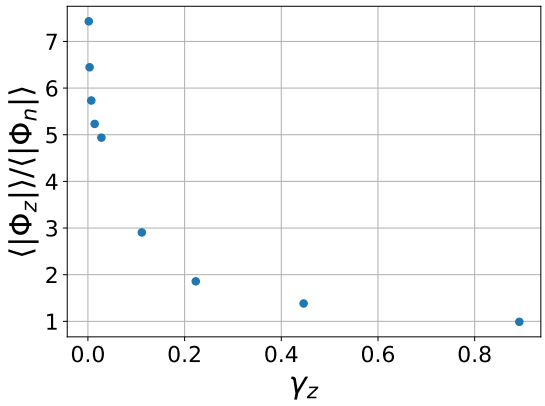

Figure 4.10: Ratio of total absolute amplitudes of ZF to ETG modes with varying collisionality. Results are taken at the final timestep. The reference value corresponds to the fourth point, $\gamma_z = 0.014$.

These results were achieved by including the physical collision rate taken in Section 4.2.3, such that $\gamma_z = 0.014$, and by initializing the ETG mode with a Gaussian k_x and z spectrum such that $\phi(k_x, z, t = 0) \sim e^{-(k_x^2+z^2)/8\pi^2}$. The corresponding $\langle|\phi|\rangle$ for the ETG and ZF modes are plotted in Figure 4.7. One can see the strong drive of the zonal flow, as well as the late-stage fluctuations of both ETG and ZF modes. Figure 4.8 shows that over time the Gaussian radial spectrum of the ETG mode is broadening into sidebands, while the radial spectrum of the zonal flow modes narrows from a broad distribution to a peak at a final, low-θ_z mode number, as predicted by the NLSE model [64]. These results suggest that one should perform global simulations to see results most consistent with the NLSE model.

The improved single-mode results for the $k_y\rho_i = 6.36$ case showed large θ_k-averaged fluctuations for the ETG mode compared to more fixed ZF fluctuations. These results agree with the expectations of Eqns. (4.16) and (4.17). The fluctuations can be seen in Figure 4.9, where the average dimenionsless radial wavenumber, $\langle|\theta_k|\rangle = \left(\int d\theta_k \theta_k^2 |\phi_k|^2\right)^{1/2} / \langle|\phi_k|\rangle$, is plotted for the ETG and ZF modes respectively. The ratio of the total absolute amplitude of ZF to ETG modes is given in Figure 4.10 as a function of γ_z and is consistent with the trend from the NLSE model. The late-stage

behavior of the ETG and ZF k_x-spectra, as shown in Figs. 4.8 and 4.9, and the collisional behavior of the mode amplitude ratio agree well with the late-time behavior reported in the electron-scale MAST simulations of Ref. [108].

4.2.3 Full-spectrum Simulation Results

The full-spectrum nonlinear simulation results are presented here and the intermediate-scale zonal flow generation mechanism is further investigated. Including multiple toroidal modes results in a final quasi-saturated heat flux characterized by richer turbulent interactions. Figure 4.11(a) shows the time history of the heat flux for the well-converged $24\rho_i \times 3\rho_i$ case with collisions. The evolution of the four strongest zonal flow modes at the final simulation time is depicted in Figure 4.11(b). The

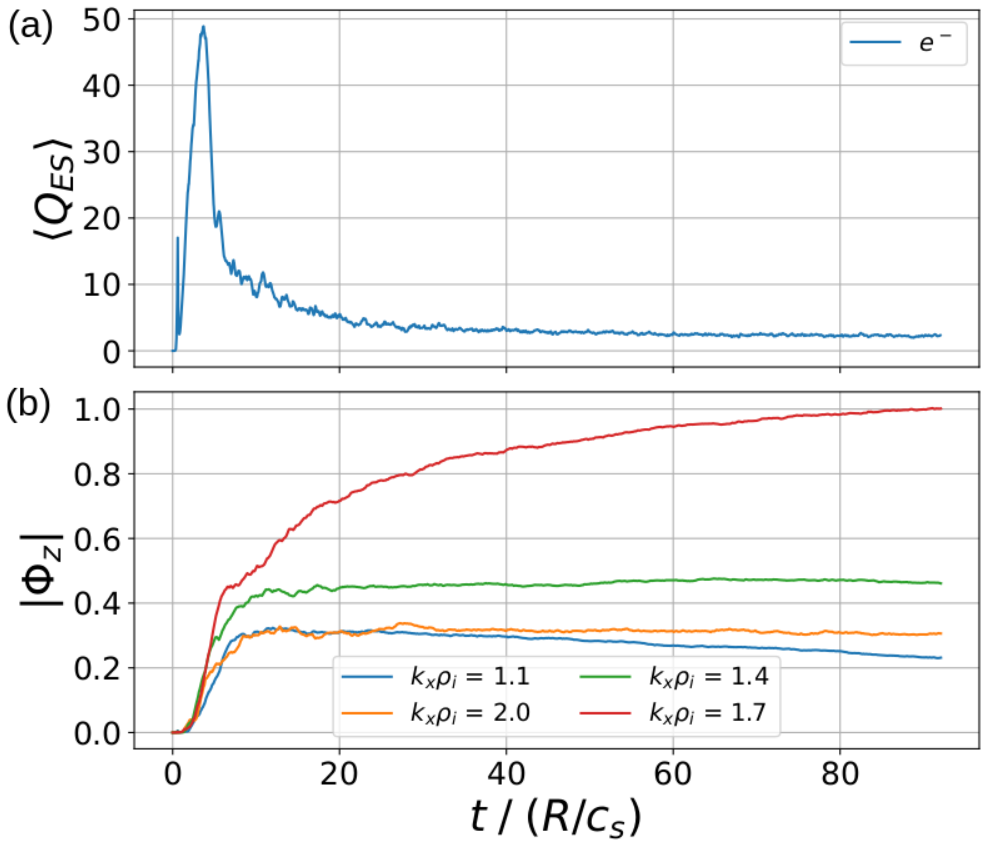

Figure 4.11: Full-spectrum collisional nonlinear simulation results showing (a) the electron heat flux time-evolution and (b) the time evolution of the four strongest final ZF modes. Data is averaged over z.

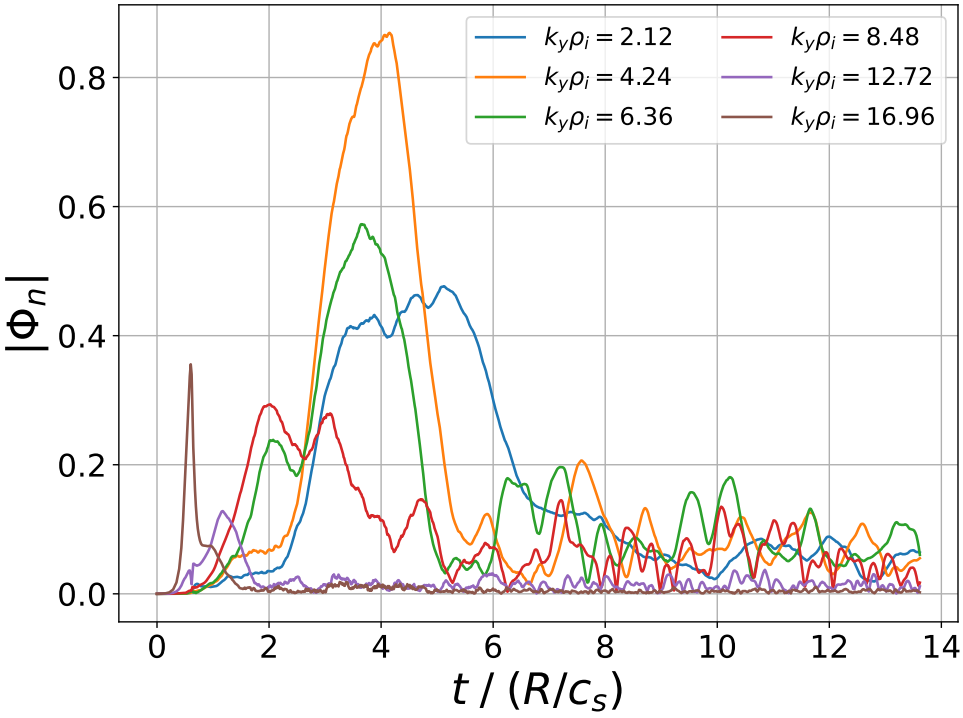

Figure 4.12: Time trace of full-spectrum ETG modes ranging from the longest mode to the most unstable mode. Data is averaged over z.

value of the normalized electron-ion collision frequency used is $\nu_{ei} = 0.106875$. This frequency is defined as $\nu_{ei} = 4v_{te}\nu_c/R$, where $v_{te} = \sqrt{T_e/m_e}$ and ν_c is the collision frequency given in Table 4.1. The self-adjoint form of the standard Landau-Boltzmann collision operator is used. Realistic collisionality allows for ZF damping when reaching a final state, and the simulation was carried out to a sufficiently long non-dimensional time, $t/(R/c_s) = 90$, to ensure that a quasi-saturated steady state in $\langle Q_{ES} \rangle$ is achieved. The convergence with respect to box size is discussed in Section 4.2.4.

Figure 4.12 shows the evolution of various ETG modes ranging from the longest wavelength to the most unstable mode. The shorter wavelength modes saturate very quickly to negligible levels, in agreement with the single-mode results, and are omitted. One can observe that the intermediate-scale modes saturate the slowest and reach the highest levels. During the period of intermediate-scale ETG mode growth, the ZF modes shown in Figure 4.11(b) are driven exponentially by the radial beating of ETG modes, leading to the modulational instability. Once the ETG modes reach a

quasi-saturated state, the ZF modes continue to grow slowly in agreement with the single-mode simulation results. Considering the findings of the NLSE model, the single-mode simulations results of Section 4.2.2, and the full-spectrum simulation results discussed here, it is the intermediate-scale ETG modes which are most responsible for driving ZF mode growth into the late stage.

The heat flux spectrum for the full-spectrum case is shown in Figure 4.13, alongside a quasilinear saturation estimate. The quasilinear estimate of the heat flux for a single k_y mode is calculated as [169, 170]

$$Q_{k_y}^{QL} = A_0 \frac{(\gamma/\langle k_\perp^2 \rangle)^2}{|\phi_{0,k_y}(0)|^2} Q_{k_y}^{\text{lin.}}, \tag{4.19}$$

with $Q_{k_y}^{\text{lin.}}$ representing the linear simulation results for the heat flux and $\phi_{0,k_y}(0)$ the linear electrostatic potential at $k_x = z = 0$. The term A_0 represents a constant of proportionality and $\langle k_\perp^2 \rangle$ is the ballooning-angle-averaged perpendicular wavenumber, described previously in Section 3.1.1 as [169]

$$\langle k_\perp^2 \rangle = \frac{\sum_{k_x} \int (g^{xx} k_x^2 + 2 g^{xy} k_x k_y + g^{yy} k_y^2) |\phi_k(z)|^2 dz}{\sum_{k_x} \int |\phi_k(z)|^2 dz}. \tag{4.20}$$

Here, ϕ_k represents a Fourier mode of the electrostatic potential perturbation. A sum over all k_x

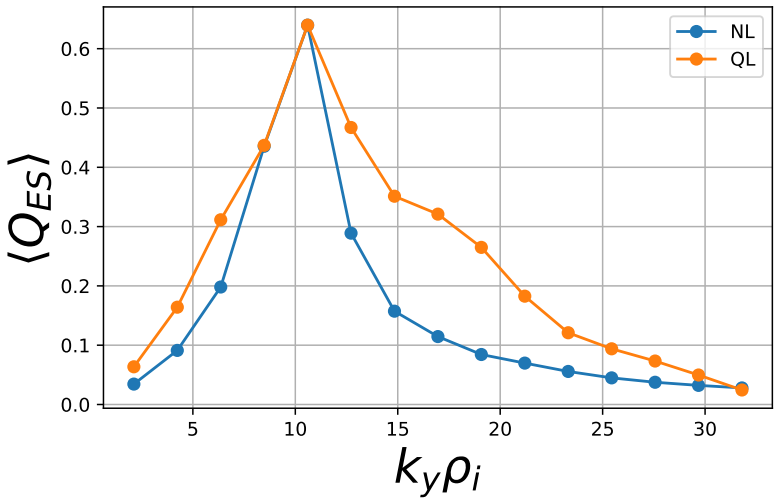

Figure 4.13: Comparison of quasilinear and nonlinear heat flux spectra for the $24\rho_i \times 3\rho_i$ full-spectrum electron-scale case. NL and QL stand for nonlinear and quasilinear respectively.

values was required for the drop-off of saturation levels at low $k_y\rho_i$.

As discussed in Chapter 3, this model of mode saturation describes a balance of the unstable growth of the instability with turbulent diffusion based on a mixing-length estimate [173, 175, 207]. Clearly there is notable agreement with the nonlinear heat flux spectrum in the intermediate scale. The disparity between the quasilinear model and the nonlinear heat flux spectrum is greatest for ETG modes with wavenumbers higher than $k_y\rho_i \approx 12$. This suggests other, stronger saturation mechanisms for these modes. While new effects, such as toroidal inverse-cascading [105, 205, 206], may play a role in the full-spectrum case, the difference in the heat flux spectra also agrees with the transition in ETG-ZF dynamics found to occur around $k_y\rho_i = 15$ for the single-mode results. The more abrupt ZF response and quicker saturation of the higher k_y modes may be consistent with secondary instability theory [62, 63], where a $|\phi_n| \sim \gamma/\langle k_\perp^4 \rangle$ saturation model for ETG mode amplitudes predicts a steeper drop-off near $k_y\rho_i \approx 12$ than that of the quasilinear mixing-length estimate.

Finally, a comparison of turbulent and neoclassical transport levels is presented for both ion and electron scales. Because the electron-scale case takes the ion temperature gradient to zero, one can compare the electron-scale thermal diffusivity to that of the ion-scale ITG case with adiabatic electrons to compare the effect of regulation by zonal flows at each scale. In units normalized to the specific species of interest, the thermal diffusion coefficients due to electrostatic turbulence are $\langle \chi_{\mathrm{ES}} \rangle_i = 0.7\rho_i^2 v_{Ti}/L_{Ti}$ for the ion-scale ITG case and $\langle \chi_{\mathrm{ES}} \rangle_e = 2.8\rho_e^2 v_{Te}/L_{Te}$ for the electron-scale ETG case, where v_{Ts} is the thermal velocity, $\sqrt{2T_s/m_s}$, for a species s. This suggests that the ETG-driven zonal flows don't regulate ETG turbulence as strongly as the isomorphic counterpart ITG turbulence is regulated by ITG-driven zonal flows. However, simulations where the zonal flow component is removed would need to be run for a proper comparison.

The neoclassical transport values were calculated using GENE for both the ion and electron scale cases. Given in units of χ_{gB} from Table 4.1, the neoclassical thermal diffusivites are $\langle \chi_{\mathrm{neo}} \rangle_i = 0.14\chi_{\mathrm{gB}}$ and $\langle \chi_{\mathrm{neo}} \rangle_e = 0.004\chi_{\mathrm{gB}}$. The neoclassical values are in close agreement with the theoretical expectation that $\chi_i = \sqrt{m_i/m_e}\chi_e$, and are negligible compared to the respective turbulent thermal

diffusivities, $\langle\chi_{\rm ES}\rangle_i = 6.95\chi_{\rm gB}$ and $\langle\chi_{\rm ES}\rangle_e = 0.328\chi_{\rm gB}$. The late-time heat flux spectrum peaks in the intermediate scale at $k_y\rho_i = 10.6$ with $\langle Q_{ES}\rangle_e = 0.66Q_{\rm gB}$ and drops off to $\langle Q_{ES}\rangle_e = 0.10Q_{gB}$ and $0.11Q_{gB}$ for $k_y\rho_i = 4.24$ and 16.96 respectively. These values are in good agreement with the theoretical expectation that $Q/Q_{gB} \sim \mathcal{O}(0.01) - \mathcal{O}(0.1)$ (in the units of Table 4.1) for the intermediate-scale ETG modes [64].

4.2.4 Nonlinear Convergence Tests

This section details a "full-spectrum" nonlinear simulation box-size convergence study. The perpendicular box size is varied in terms of the basic $6\rho_i \times 3\rho_i$ electron-scale box size shown in Section 4.2.1. The collisionality was set to the reference value discussed in Section 4.2.3. Four perpendicular domain sizes are presented: $6\rho_i \times 3\rho_i$, $12\rho_i \times 3\rho_i$, $24\rho_i \times 3\rho_i$, and $12\rho_i \times 6\rho_i$. These cases consider the importance of correctly resolving the ETG streamer lengths and the longest wavelength zonal flow modes. Additionally, the inclusion of longer ETG mode wavelengths is considered in the $12\rho_i \times 6\rho_i$ case to verify the findings of Section 4.2.2. The number of radial gridpoints was increased in each simulation to retain the original resolution. The electron heat flux for each case is shown over time in Figure 4.14. One can clearly see that the increase in radial dimension is necessary to correctly resolve the heat flux. The late-stage zonal flows of the $6\rho_i \times 3\rho_i$ case, as shown in Figure 4.4(c), are peaking at the longest mode allowable and the box size must be increased to correctly resolve the longest modes. Allowing for longer wavelength ZF modes leads to stronger regulation of the heat flux as seen in Figure 4.14.

The time evolution of various ETG modes for the $12\rho_i \times 6\rho_i$ case is shown in Figure 4.15(a), and the time evolution of the four strongest ZF modes at the final time is shown in Figure 4.15(b). These results are qualitatively similar to the $24\rho_i \times 3\rho_i$ case shown in Figure 4.11 and Figure 4.12. In this new case, the longest wavelength ETG mode, $k_y\rho_i = 1.06$, grows to the highest level. However, it can be seen in Figure 4.15 that from non-dimensional times 5-10 $t/(R/c_s)$, when the longest ETG mode is dominant, the zonal flows are already in the final, slowly growing stage. This indicates that the strongest ZF modes are largely being affected by the intermediate-scale ETG modes, not the

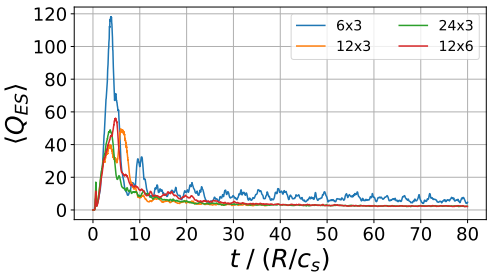

Figure 4.14: Convergence of the electrostatic electron heat flux for the various box size cases compared to the original $6\rho_i \times 3\rho_i$ case.

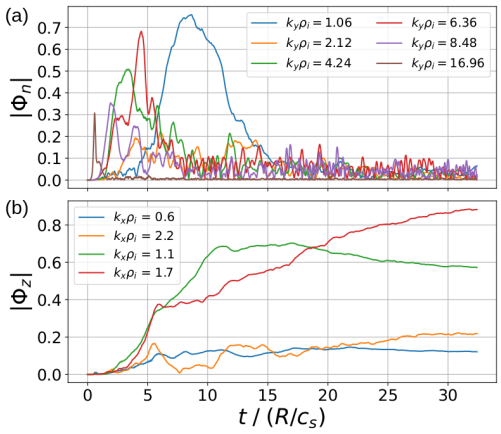

Figure 4.15: (a) ETG and (b) four strongest final ZF mode time traces for the $12\rho_i \times 6\rho_i$, large-y box size. All data is averaged over z.

longest wavelength ETG mode, confirming the results found in Section 4.2.2 which showed little zonal flow generation outside the intermediate-scale range. As increasing L_y from the original size of $3\rho_i$ had no effect on the final quasi-saturated state, the largest L_x case considered, $24\rho_i \times 3\rho_i$, was chosen for the full-spectrum investigation discussed in Section 4.2.3.

4.3 Conclusions

It has been shown here, using the single-mode nonlinear simulations, that the NLSE model [64] accurately describes the zonal flow generation mechanism by intermediate-scale ETG modes and that it provides a theoretical understanding for the slow growth of long-wavelength zonal flows into the long-term quasi-saturated state. As the NLSE model considers only a single ETG mode for a practicable analysis, one cannot say conclusively that the same is true of the full-spectrum nonlinear results. However, in the full-spectrum case the high-k_y ETG modes are quickly saturated by a stronger ZF response as compared to the intermediate-scale ETG modes. The intermediate-scale ETG modes then drive exponential ZF mode growth initially, and slow, algebraic ZF mode growth as they are suppressed in the late stage. This result is in good agreement with the NLSE model for

intermediate-scale ETG-ZF dynamics, as well as various long time, saturated electron-scale [108, 202] and multiscale [61, 218] flux-tube simulations. The final transport levels for the full-spectrum case are in similar ranges found in thorough electron-scale CBC benchmarks which compare well with experimental observations [198]. As the zonal flows are driven at long electron-scale wavelengths, multiscale effects could become important and ETG-driven zonal flows may have an effect on ion-scale turbulence. This effect where intermediate-scale zonal flows contribute to ion-scale turbulence suppression has been reported in large multiscale simulations [61, 218].

Chapter 5

Subgrid ETG Model

This chapter focuses on the primary work of the thesis - a subgrid model for electron-scale turbulent effects in global ion-scale simulations. An introduction is given regarding local multiscale gyrokinetic simulation results which represent the highest fidelity physics model. The theoretical subgrid ETG model is then derived which can account for electron-scale heat transport and possible effects of electron-scale turbulence on the ion scale. Local electron-scale simulations are performed at multiple radial locations to incorporate in global ion-scale simulation. The local and global simulations are described and the effects of including electron-scale transport in global ion-scale simulation are discussed. Topics of consideration for future work are addressed. This chapter is largely compiled from the contents of Ref. [219] where the original work is published.

5.1 Introduction

Gyrokinetic simulations of ion gyroradius scales are currently able to confidently predict ion transport and power spectra in experiment; however, they can often underestimate electron thermal transport [136, 220]. The role of ETG turbulence has been studied in various tokamak scenarios [107, 130, 200, 201, 221] and is particularly important in cases of marginal ion-scale turbulence [111]. Specifically for ITER, alpha-particle and electron cyclotron heating effects are expected to drive meaningful ETG turbulence levels, leading to important multiscale dynamics [61, 222]. To better understand interactions between the disparate scales, local multiscale simulations of core ITG and ETG turbulence have garnered much interest [61, 186, 218, 222–225]. In general, turbulent spectra are distinctly scale-separated, and cross-scale interactions lead to changes in steady-state transport levels which can better predict experimental losses for both species. A recent overview of multiscale

simulation results can be found in Ref. [226].

Refs. [218] and [61] both report evidence of rich-cross scale interations which are highly sensitive to equilibrium profile changes when ITG turbulence is marginal. In Ref. [218] multiscale gyrokinetic simulations of an Alcator C-Mod L-mode scenario are performed with varying ion

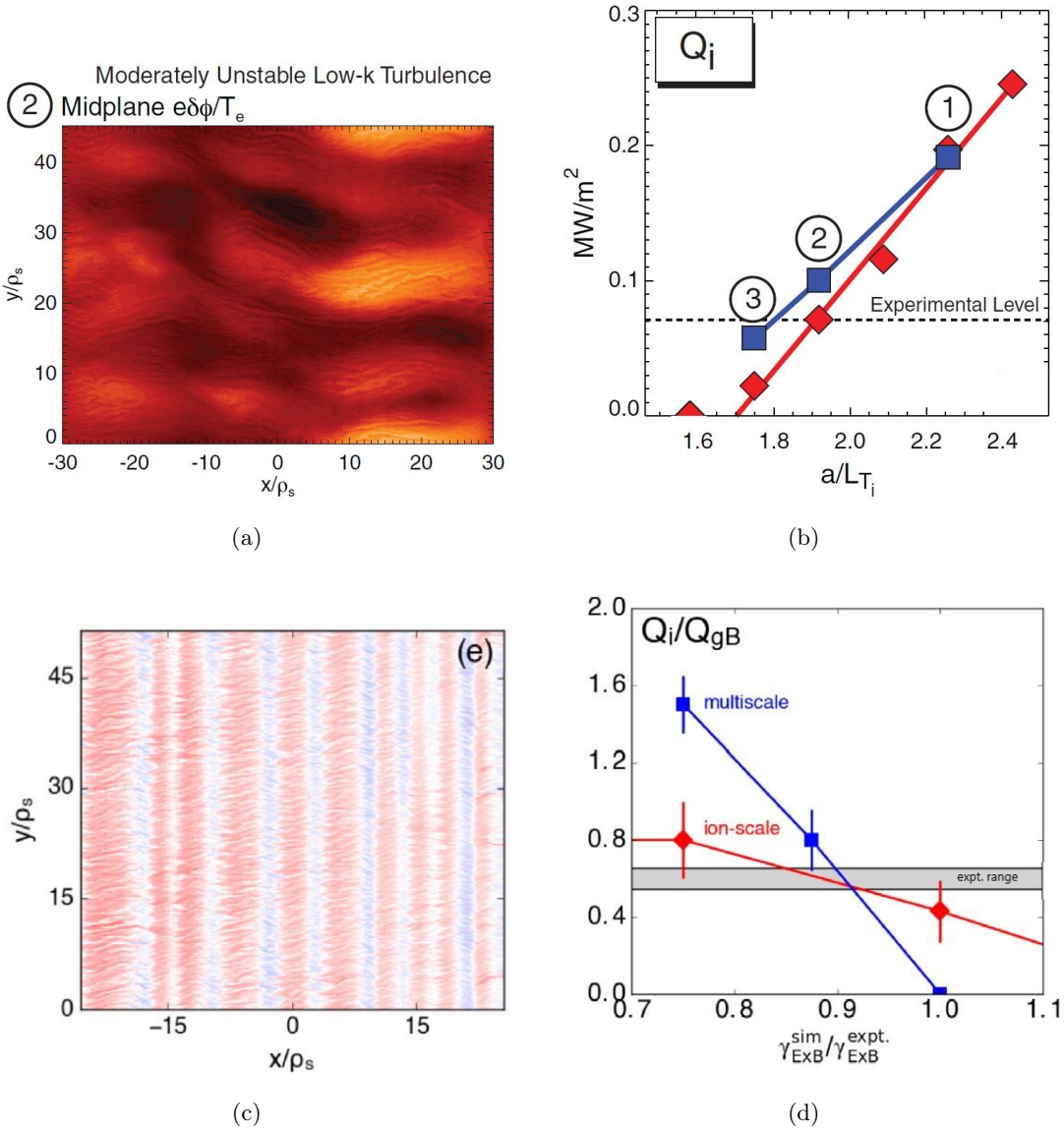

Figure 5.1: (a) Outboard midplane potential showing ETG streamers present for run 2 from (b) comparison of multiscale to ion-scale ion heat fluxes from Ref. [218]. (c) Outboard midplane potential for highest shear flow run showing intermediate-scale ZFs present, and (d) comparison of multiscale to ion-scale ion heat fluxes from Ref. [61]. Note, Fig. (c) was originally Fig. 7(e) in Ref. [61].

temperature gradients. As the ion temperature gradient is reduced, electron-scale streamers become more prominent, resulting in an increase in ion heat flux when compared to ion-scale simulation results. The outboard midplane electrostatic potential of the median run and a comparison of ion heat fluxes between ion-scale and multiscale simulations are shown in Figures 5.1(a) and 5.1(b). Ref. [218] describes the increase in Q_i as due to a lower efficiency of zonal flow shearing in the presence of ETG streamers, whereas local multiscale CBC simulations report a damping of zonal flow amplitudes by ETG streamers [224].

Multiscale gyrokinetic simulations of the DIII-D ITER Baseline Scenario are described in [61], where the background **E**x**B** shear is varied within experimental uncertainty. The lowest value of equilibrium shear flow indicates a similar trend as in Ref. [218], while the largest value reports intermediate-scale zonal flows growing at late times and helping to regulate ITG turbulence. These zonal flows are expected to be driven by electron-scale turbulence, as reported by Refs. [108, 197]. The outboard midplane electrostatic potential for the run with highest shear flow and a comparison of ion heat fluxes between ion-scale and multiscale simulations are shown in Figures 5.1(c) and 5.1(d).

As multiscale simulations require resolving electron gyroradius scales, the sizes of simulation domains become limited. Consequently, reduced modeling of electron-scale turbulence is particularly valuable for whole-device modeling efforts in future burning plasma experiments. Previous work has considered the importance of cross-scale interactions [223, 227, 228], while more recent efforts have led to the development of reduced models for pedestal ETG transport [229] and multiscale quasilinear saturation rules [177]. Additionally, a scale-separated model of coupled gyrokinetic equations [230] has shown that ion-scale turbulence influences electron-scale dynamics through parallel-to-the-field shearing which suppresses the ETG growth rate [231].

The goal of the work presented in this chapter is to account for heat losses due to ETG turbulence in global ion-scale simulations and to probe the effects of ETG turbulence on the ITG background. The remaining sections are outlined as follows. Section 5.2 derives a theoretical model which accounts for electron-scale effects in global ion-scale gyrokinetic simulation. Local ITG and ETG simulations are carried out in GENE to test for a valid scale-separated scenario which is

described in Section 5.3. Section 5.4 then details the global ITG simulation in GEM. This is followed by the results of including a kinetic source term in GEM which accounts for excess electron-scale thermal losses due to ETG turbulence. Section 5.6 concludes with future plans to couple the ETG streamer potential and intermediate-scale zonal flows [61, 108, 197] found in ETG simulations to the ion scale.

5.2 Subgrid ETG Model

The gyrokinetic framework for modeling microturbulence in tokamak plasmas assumes an expansion in the parameter $\epsilon = \rho/a \ll 1$, where ρ is the species gyroradius involved in the generation of instabilities and a is the device minor radius [68, 69, 71]. This in part allows for separating dynamical equations between small-scale fluctuating quantities and background equilibrium quantities. A further subsidiary expansion can be made using the small electron-to-ion mass ratio, $\sqrt{m_e/m_i} \ll 1$, to separate the dynamics of ion-scale (IS) and electron-scale (ES) instabilities, such as ITG and ETG modes [65, 230]. Distinct equations can then be used to investigate the effects of coupling between the two scales. Note that a lowercase 'es' is instead used to refer to electrostatic simulations further on.

The primary assumption of the subgrid model is to take the electron-scale gyrokinetic equation as stand-alone, i.e. unaffected by ion-scale turbulence. Then local ES turbulence is averaged over intermediate scales in time and space perpendicular to the field to include effects of ETG turbulence in global ITG simulations. The amplitude of the ES flux-tube steady-state is varied in accordance with values reported in multiscale simulations involving core ITG and ETG turbulence and the effect of new terms are either discussed further or investigated.

The subgrid model might further be incorporated with the multiscale model of Ref. [230] to perform self-consistent coupled simulations of ITG and ETG turbulence. As the theory in Ref. [230] makes various assumptions about the electron-scale turbulence, the final equations focus on the effects of ITG turbulence on the electron scale. The goal here is to recreate effects of electron-scale turbulence in multiscale simulations by using minimal assumptions and incorporating ES effects

directly from flux-tube simulation. The intermediate-scale averaging procedure offers a reduced approach for including ES turbulent effects, making it practical for use in global ion-scale simulations. The accuracy of the subgrid model in capturing cross-scale interactions can be validated and improved by comparing to local IS simulations that directly include ES turbulence.

In focusing on the combined effects of ITG and ETG turbulence, the subgrid model includes only electrostatic effects. The governing gyrokinetic Vlasov equation used here takes the form

$$\begin{aligned}\frac{\partial \delta f}{\partial t} + \left(v_\parallel \mathbf{b} + \mathbf{v}_D\right) \cdot \nabla \delta f + \frac{1}{B} \langle \delta \mathbf{E} \rangle_\alpha \times \mathbf{b} \cdot \nabla \delta f \\ = -\frac{1}{B} \langle \delta \mathbf{E} \rangle_\alpha \times \mathbf{b} \cdot \nabla f_0 + q(v_\parallel \mathbf{b} + \mathbf{v}_D) \cdot \langle \delta \mathbf{E} \rangle_\alpha \frac{f_0}{T},\end{aligned} \tag{5.1}$$

where $\langle \dots \rangle_\alpha$ represents a gyro-phase angle average. For simplicity, the gyroaverage notation is dropped from now on. Collisions are ignored assuming low collision frequency in the core. Fluctuations of the perturbed distribution function and electrostatic potential are split into IS and ES terms

$$\begin{aligned}\delta f &= \delta f' + \delta f_{\mathrm{ES}}, \\ \delta \mathbf{E} &= \delta \mathbf{E}_{\mathrm{IS}} + \delta \mathbf{E}_{\mathrm{ES}},\end{aligned} \tag{5.2}$$

where $\delta f'$ retains new components that may be generated in the original IS distribution function due to the inclusion of ES **E**x**B** effects. In general this could also include cross-scale energy cascading effects, though this is ignored with the stand-alone ES assumption. An averaging procedure over intermediate mesoscales in time and in space perpendicular to the field, τ_{m} and l_{m}, can then be introduced, where the intermediate values lie between ion and electron scales defined by $a \gg \rho_i \gg \rho_e$ and $\tau \gg a/v_{th,i} \gg a/v_{th,e}$. Here, τ is the transport timescale and v_{th} is the particle thermal velocity. The specific choice of intermediate-scale values is described further in Section 5.3 in reference to the ES flux-tube simulation results.

Mesoscale averaging the components of Equation (5.2) results in retaining only IS fluctuations:

$$\begin{aligned} \langle \delta f' \rangle_{\mathrm{m}} &= \delta f_{\mathrm{IS}}, \quad \langle \delta f_{\mathrm{ES}} \rangle_{\mathrm{m}} = 0, \\ \langle \delta \mathbf{E}_{\mathrm{IS}} \rangle_{\mathrm{m}} &= \delta \mathbf{E}_{\mathrm{IS}}, \quad \langle \delta \mathbf{E}_{\mathrm{ES}} \rangle_{\mathrm{m}} = 0. \end{aligned} \tag{5.3}$$

Here, $\langle \dots \rangle_{\mathrm{m}}$ represents a mesoscale average in space perpendicular to the field and time. It is assumed the mesoscale average of $\delta f'$ recovers the IS distribution function. As the electron scale is stand-alone, the ES dynamics are described by the gyrokinetic equation

$$\begin{aligned} &\frac{\partial \delta f_{\mathrm{ES}}}{\partial t} + \left(v_{\parallel} \mathbf{b} + \mathbf{v}_D + \frac{1}{B} \delta \mathbf{E}_{\mathrm{ES}} \times \mathbf{b} \right) \cdot \nabla \delta f_{\mathrm{ES}} \\ &\qquad = -\frac{1}{B} \delta \mathbf{E}_{\mathrm{ES}} \times \mathbf{b} \cdot \nabla f_0 + q (v_{\parallel} \mathbf{b} + \mathbf{v}_D) \cdot \delta \mathbf{E}_{\mathrm{ES}} \frac{f_0}{T} + S_{\mathrm{ES}}. \end{aligned} \tag{5.4}$$

A source term, S_{ES}, has been explicitly included to ensure a steady-state consistent with the flux-tube approximation. To obtain an equation for the remaining scales, the total fluctuating quantities are substituted into Equation (5.1) and the ES equation subtracted, resulting in

$$\begin{aligned} &\frac{\partial \delta f'}{\partial t} + \left(v_{\parallel} \mathbf{b} + \mathbf{v}_D + \frac{1}{B} \delta \mathbf{E}_{\mathrm{IS}} \times \mathbf{b} \right) \cdot \nabla \delta f' \\ &\qquad + \frac{1}{B} \delta \mathbf{E}_{\mathrm{ES}} \times \mathbf{b} \cdot \nabla \delta f' + \frac{1}{B} \delta \mathbf{E}_{\mathrm{IS}} \times \mathbf{b} \cdot \nabla \delta f_{\mathrm{ES}} + S_{\mathrm{ES}} \\ &\qquad = -\frac{1}{B} \delta \mathbf{E}_{\mathrm{IS}} \times \mathbf{b} \cdot \nabla f_0 + q (v_{\parallel} \mathbf{b} + \mathbf{v}_D) \cdot \delta \mathbf{E}_{\mathrm{IS}} \frac{f_0}{T}. \end{aligned} \tag{5.5}$$

Equation (5.5) is then averaged over the intermediate mesoscales to find the new IS gyrokinetic equation

$$\begin{aligned} &\frac{\partial \delta f_{\mathrm{IS}}}{\partial t} + \left(v_{\parallel} \mathbf{b} + \mathbf{v}_D + \frac{1}{B} \delta \mathbf{E}_{\mathrm{IS}} \times \mathbf{b} \right) \cdot \nabla \delta f_{\mathrm{IS}} \\ &\qquad + \langle \frac{1}{B} \delta \mathbf{E}_{\mathrm{ES}} \times \mathbf{b} \cdot \nabla \delta f' \rangle_{\mathrm{m}} + \langle \frac{1}{B} \delta \mathbf{E}_{\mathrm{IS}} \times \mathbf{b} \cdot \nabla \delta f_{\mathrm{ES}} \rangle_{\mathrm{m}} + \langle S_{\mathrm{ES}} \rangle_{\mathrm{m}} \\ &\qquad = -\frac{1}{B} \delta \mathbf{E}_{\mathrm{IS}} \times \mathbf{b} \cdot \nabla f_0 + q (v_{\parallel} \mathbf{b} + \mathbf{v}_D) \cdot \delta \mathbf{E}_{\mathrm{IS}} \frac{f_0}{T}. \end{aligned} \tag{5.6}$$

The three new terms are grouped together on the middle line of Equation (5.6) for clarity. These new terms represent the averaged effects of electron-scale turbulence in ion-scale simulations. The first term represents the additional guiding-center motion due to the ETG field. The second term is

due to effects of the ITG field on the ETG distribution function, which averages to zero according to Equation (5.3). The final term, S_{ES}, is used to account for electron thermal transport by ES turbulence in IS simulations.

Given local electron-scale simulations, a form for the source term can be found by taking the flux-surface-average of Equation (5.4). Due to the periodic boundary conditions in the flux-tube approximation one finds that the source term must come from the ES **E**x**B** nonlinearity,

$$\langle S_{\mathrm{ES}} - \frac{1}{B}\delta\mathbf{E}_{\mathrm{ES}} \times \mathbf{b} \cdot \nabla \delta f_{\mathrm{ES}} \rangle_{\psi} = 0, \tag{5.7}$$

where $\langle \ldots \rangle_{\psi}$ represents a flux-surface average. Note that the mesoscale average can be used if the turbulence is strongly scale separated, but in principle the linear terms may not average to zero for intermediate-scale modes. As this source is responsible for maintaining the steady-state transport, it can account for excess electron thermal transport from ETG modes. The second non-zero term is recast as a diffusion operator in real space,

$$\langle \frac{1}{B}\delta\mathbf{E}_{\mathrm{ES}} \times \mathbf{b} \cdot \nabla \delta f' \rangle_{\mathrm{m}} \approx \langle D_{\mathrm{ES}} \nabla_{\perp}^2 \delta f' \rangle_{\mathrm{m}} = D_{\mathrm{ES}} \nabla_{\perp}^2 \delta f_{\mathrm{IS}}. \tag{5.8}$$

It is expected that the ES **E**x**B** effects can lead to changes in the IS electron distribution function. This effect can likely be modeled as a diffusion, D_{ES}, acting on the IS distribution function due to the ETG electrostatic potential. Such a model of microturbulence-induced diffusion has previously been studied in the saturation of TAE modes [232].

The following sections address including the ES source term in global ion-scale simulations to capture electron-scale heat transport. Flux-tube ETG simulations are carried out using GENE at different radial locations. A kinetic source term is constructed using local results at the peak temperature gradient location and the source term is added to global IS GEM simulations. The ES source term is varied in accordance with various multiscale simulation results, and the result of adding ES transport to global IS simulation is discussed. Different analytic radial profiles of the

ETG heat flux are then compared to results from local ES simulations at multiple radial locations.

5.3 Local Simulations

Local linear and nonlinear flux-tube simulations of ITG and ETG turbulence were carried out in GENE [62] to test for a simple scenario with suitable scale separation. Circular Cyclone Base Case (CBC) parameters [145] are taken for geometric and computational simplicity. Gyrokinetic ions and electrons are used for simulations at both scales with deuterium chosen as the main ion species and collisions included at both scales. As described in Ref. [145], normalized radial density and temperature profiles and the associated normalized gradients for both species are given by the following equations:

$$A(r)/A(r_0) = \exp\left[-\kappa_A w_A \frac{a}{R}\tanh\left(\frac{r-r_0}{w_A a}\right)\right], \tag{5.9}$$

$$R/L_A = -R\partial_r(\ln A(r)) = \kappa_A \cosh^{-2}\left(\frac{r-r_0}{w_A a}\right), \tag{5.10}$$

for A $\in \{n_0, T_0\}$, $\kappa_A \in \{\kappa_n, \kappa_T\} = \{2.23, 6.96\}$ defining the gradient profile peaks, and $w_A = 0.30$ the gradient profile widths.

The density and temperature profiles and their gradients are shown in Figure 5.2(a) and Figure 5.2(b). The safety factor profile is given by

$$q(r) = 2.52(r/a)^2 - 0.16(r/a) + 0.86, \tag{5.11}$$

with $\hat{s} = \frac{r}{q}\frac{dq}{dr}$ the magnetic shear profile. To retain only the electrostatic instabilities of interest, the plasma beta factor, $\beta = 8\pi n_{0e} T_{0e}/B_0^2$, with B_0 the on-axis magnetic field, is taken to be $\beta = 1e^{-4}$. Multiscale CBC simulations have previously reported important cross-scale interactions [224], and so the simplified circular CBC parameters were chosen to facilitate initial theoretical investigation. While these parameters are idealized, ETG turbulence profiles can in principle be captured for any experimental scenario by using results from multiple flux-tube simulations at different radial locations.

The normalized mode frequencies, $\omega/(c_s/R)$, and growth rates, $\gamma/(c_s/R)$, for the instabilities are calculated using GENE linear electrostatic simulations. Here $c_s = \sqrt{T_e/m_D}$ is the deuteron sound speed. The linear growth rates at $r/a = 0.50$ are shown in Figure 5.2(c) spanning IS and ES scales in $k_y\rho_i$, where k_y is the wavenumber in the binormal direction. Grid convergence values in $z \times v_\parallel \times \mu$ were found by increasing grid resolution until growth rates were constant to three decimal places. Here, z is the field-line-following coordinate, $v_\parallel$ is the particle velocity along a field line, and $\mu = mv_\perp^2/2B$ is the magnetic moment which represents particle velocity perpendicular to a field line. Convergence was checked for the most unstable mode as well as a longer wavelength mode closest to the peak of the nonlinear flux spectra.

The resulting grid resolutions, $z \times v_\parallel \times \mu$, used for linear simulations were $32 \times 48 \times 16$ at the ion scale and $48 \times 48 \times 48$ at the electron scale. For both scales 32 gridpoints are taken in the local radial coordinate x. The IS modes start at $k_y\rho_i = 0.05$ with 40 modes up to $k_y\rho_i = 2.0$ and the ES modes start at $k_y\rho_i = 2.0$ with 32 modes up to $k_y\rho_i = 64.0$. A clear scale separation in both frequency and wavenumber can be seen in Figure 5.2(c). The scale separation is of order $\gamma_{ES}/\gamma_{IS} \sim k_{y,ES}/k_{y,IS} \sim \sqrt{m_D/m_e} \sim 60$, which is expected given the respective IS and ES orderings

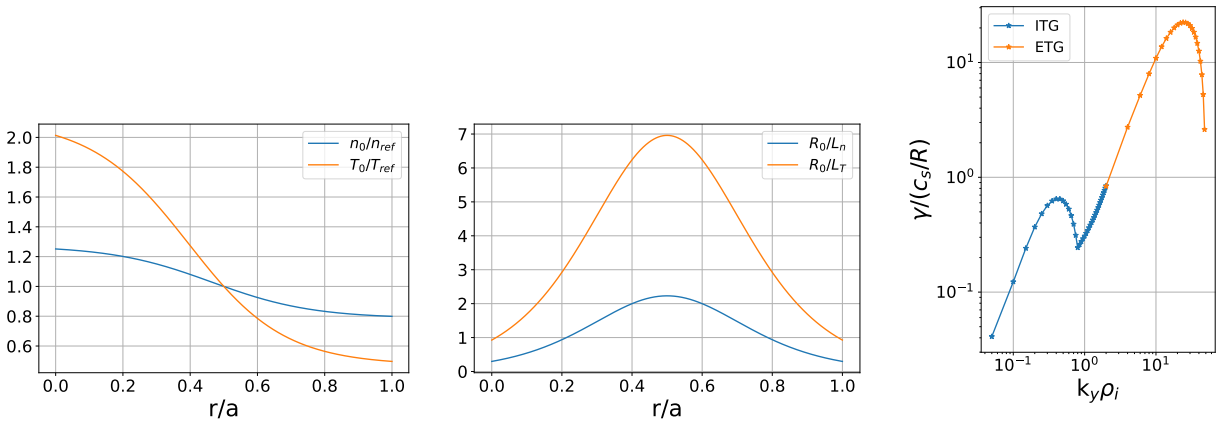

(a) (b) (c)

Figure 5.2: (a) Density and temperature profiles and (b) the respective normalized gradient profiles as functions of r/a defined by Equation (5.9) and Equation (5.10). (c) ITG and ETG growth rates from linear electrostatic GENE simulations at $r/a = 0.50$.

of ρ_i and ρ_e in space perpendicular to the field and $a/v_{th,i}$ and $a/v_{th,e}$ in time. With the equilibrium gradients dropping off outward from the center, growth rates for both scales remained appreciable out to $r/a = 0.35$ and 0.65, while falling to zero near $r/a = 0.20$ and 0.80. Although the linear simulation results might include trapped-electron modes (TEMs), primarily in the range $k_y\rho_i \sim 0.50 - 2.0$, the nonlinear GENE results presented next show little radial heat flux or electrostatic potential in k_y at this intermediate range.

The nonlinear simulations are discussed here in detail for both scales at $r/a = 0.50$. The nonlinear $z \times v_{\|} \times \mu$ grid resolution was reduced to lower values for which growth rates were still converged to within $\pm 1\%$. The new grid resolutions are $16 \times 32 \times 8$ and $32 \times 32 \times 16$ for the IS and ES scales. Nonlinear IS simulations were also tested with an increased resolution of $32 \times 48 \times 16$, while for ES simulations the resolution in each of the three dimensions was increased by a factor of 2

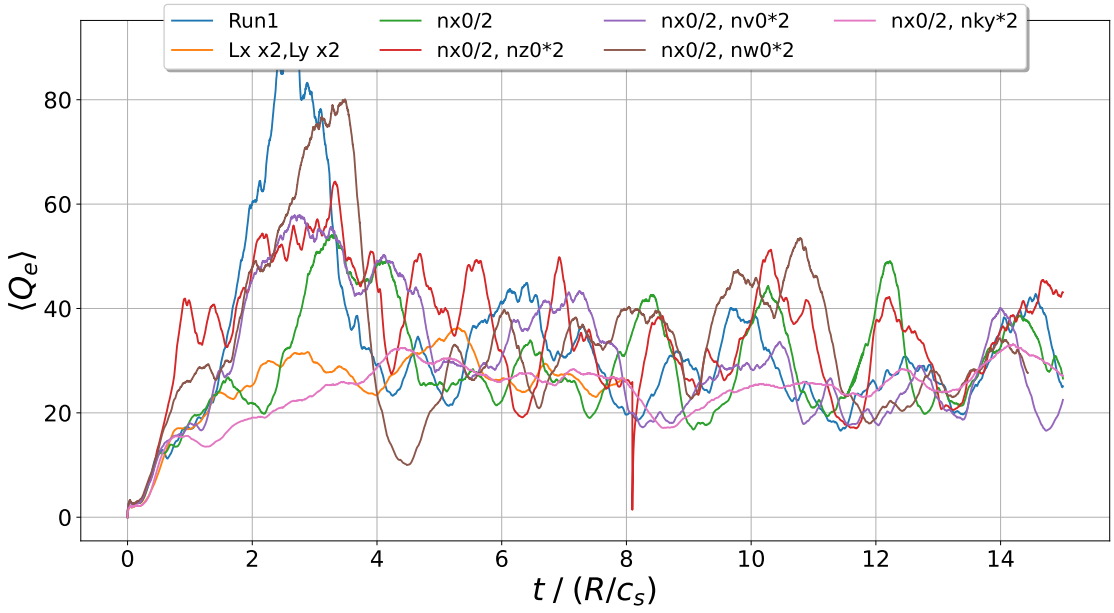

Figure 5.3: Comparison of electron heat fluxes at $r/a = 0.50$ for the many cases considered for convergence. The values of nx0, nz0, nv0, and nw0 are the number of x, z, $v_{\|}$ and μ gridpoints respectively and nky is the number of toroidal modes. All dimensions are in reference to those of Run #1, i.e. the case nx0/2 is the case used for multiple radial locations. The spurious drop in the red line is due to an issue continuing from a checkpoint file.

Table 5.1: Time-averaged heat fluxes for all simulations, in gyroBohm units.

Run	Code	Scale	β	$\gamma_{E'}$	Q_i	Q_e
#1	GENE	ES	$1e^{-4}$	0	0.22	30.78
#2	GENE	IS	$1e^{-4}$	0	171.26	50.16
#3	GENE	ES	$1e^{-2}$	0.2	0.21	29.19
#4	GENE	IS	$1e^{-2}$	0.2	8.82	4.79
#5	GEM	IS (global)	$1e^{-4}$	0	74.94	14.39

respectively to test for convergence. The ITG runs include 32 modes ranging from $k_y\rho_i = 0.0625$ to 2.0, and the ETG runs include 32 modes ranging from $k_y\rho_i = 2.0$ to 64.0. The perpendicular domain sizes, $L_x \times L_y$, are $96\rho_i \times 100\rho_i$ and $360\rho_e \times 190\rho_e$, with the $L_x : L_y$ ratio increased for ETG runs to allow for possible generation of intermediate-scale zonal flows. The radial grid resolutions are $\Delta x = 0.50\rho_i$ and $\Delta x = 0.62\rho_e$ respectively. The perpendicular domain for ETG runs was tested by separately increasing L_x and L_y by a factor of 2 each. For runs at multiple radii, the radial grid resolution was also reduced by a factor of 2 such that $\Delta x = 1.24\rho_e$ to decrease computational cost. The heat fluxes over time for all cases considered to test for convergence are shown in Figure 5.3.

Ion and electron heat fluxes, Q_i and Q_e, are listed in Table 5.1 for all ES and IS nonlinear runs. Heat fluxes are normalized using the gyroBohm value $Q_{gB} = n_e c_s T_e (\rho_D/R)^2$, with ρ_D the deuteron gyroradius. Runs #1 and #2 correspond to ES and IS simulations without background shear flow or electromagnetic effects. Runs #3 (ES) and #4 (IS) include these effects to regulate ITG turbulence [96, 99] in the unstable CBC scenario, providing a comparison to multiscale scenarios in which ITG turbulence is marginal. This results in a 95% reduction in Q_i. By comparison, simulations with only shear flow or finite-beta effects show reductions of approximately 37.5% and 85% respectively. The value of β is derived directly from the equilibrium profiles, and is near the point where the dominant mode transitions from an ITG mode to a KBM mode. The choice of shearing rate, $\gamma_{E'} \approx \gamma_{\mathrm{ITG}}^{\mathrm{max}}/2 = 0.2$, comes from comparing the most unstable ITG growth rate in the electromagnetic case to the maximum shearing rate within experimental uncertainty for the

DIII-D IBS values from Ref. [61]. The heat fluxes are further compared to results from the global ion-scale GEM simulation (run #5) which is discussed further in Section 5.4. The GEM simulation ranges from $r/a = 0.20$ to 0.80, and the heat flux is calculated by averaging over a centered domain spanning from $r/a = 0.35$ to 0.65.

These scenarios provide variable ratios of IS and ES turbulence for comparison with multiscale simulations results. In runs #1 and #5, the ratio of ES to total electron heat transport falls within the approximate range of $1/2 - 2/3$ seen in multiscale scenarios with appreciable ES effects [61, 218]. Finite-beta and shear flow effects are not included directly in GEM as the CBC scenario with electromagnetic effects is often numerically challenging [233]. Instead, ES effects are magnified by a factor of 3 when included in GEM in Section 5.4. This increased factor is used to match the ratio of electron heat flux in runs #3 and #4 when ITG is regulated. The magnified ES scenario represents cases of marginal ITG turbulence in multiscale scenarios, where the ratio of total $Q_e : Q_i$ can range from 1-3 [61, 218, 225].

For Runs $\#1 - 4$, the spatial averages of the heat flux spectra are shown as functions of k_y in Figure 5.4(a). The spatial averages of the electrostatic potential spectra are further shown as functions of k_y in Figure 5.4(b) and k_x in Figure 5.4(c). Electrostatic simulation results are labeled 'es', while the electromagnetic results with shear flow are labeled 'em+$\gamma_{E'}$'. The difference in ITG turbulence levels between both cases is clear. A strong spatial separation of scales exists in k_y for both the heat flux and potential spectra. However, the k_x potential spectrum is continuous, due to the generation of intermediate-scale zonal flows at the electron scale. Such zonal flows have been reported in multiscale simulations with marginal levels of ITG turbulence, where they may further suppress ion-scale fluctuations [61]. Capturing these effects would require breaking scale-separation assumptions and this is briefly mentioned further in Section 5.6.

The choice of mesoscale values in space perpendicular to the field and in time, l_{m} and τ_{m}, is based on the peaks of the nonlinear k_y spectra, rather than peaks of the linear growth rate. For the electrostatic cases, the peaks occur at $k_y\rho_i = 0.25$ and 10.1 for the IS and ES scales, giving length scales of $25\rho_i$ and $0.62\rho_i$. The linear mode frequencies for these wavenumbers are $\omega/(c_s/R)$

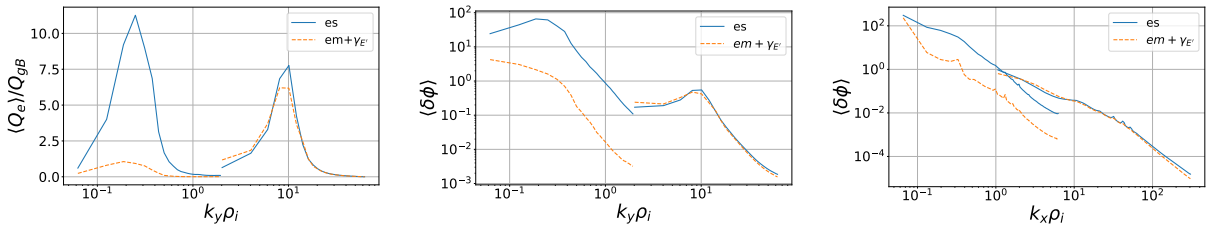

(a) (b) (c)

Figure 5.4: Flux spectra for GENE IS and ES flux-tube scenarios. (a) Electron heat flux and (b) electrostatic potential spectra as functions of k_y, averaged over k_x and z. (c) Electrostatic potential spectra as a function of k_x, averaged over k_y and z. Labels 'es' and 'em+$\gamma_{E'}$' correspond to electrostatic runs and electromagnetic runs with shear flow respectively.

= 0.586 and 17.1, giving time scales of $10.72R/c_s$ and $0.367R/c_s$. The separation of scales is then approximately $40x$ in space and $29x$ in time, compared to the theoretical estimate of $60x$ seen in the linear simulation results. The mesoscale length is taken at $k_y\rho_i = 2.0$, where the linear mode frequency is $\omega/(c_s/R) = 2.8$, giving $l_\mathrm{m} = 3.14\rho_i$ and $\tau_\mathrm{m} = 2.24R/c_s$. This choice of $k_y\rho_i$ then allows for using a perpendicular flux-surface-average in lieu of a true intermediate-scale averaging since this represents the extent of the y-domain. Since only k_y modes contribute to the radial transport, the issue of scale separation in x is ignored for now, and the whole radial domain is averaged over.

Finally, multiple ES simulations were carried out at various radial locations. The global radial electron heat flux profile is shown later in Figure 5.10(b) in comparison to the various global theoretical models considered in Section 5.4. Necessary simulation parameters were updated accordingly using Eqns. 5.9-5.11. The runs used for different radial locations had the radial grid resolution reduced by a factor of 2 to save on computational cost. The new value of Q_e/Q_{gB} at $r/a = 0.50$ for the updated case was 28.24, similar to the original 30.78, as shown in Figure 5.3. Local IS simulations were not performed at multiple radii.

5.4 Global Ion-Scale Simulations

Nonlinear nonlocal electrostatic gyrokinetic simulations are carried out with the δf particle-in-cell code GEM [158, 159]. The grid resolution is $256 \times 128 \times 64$ in the radial, binormal, and parallel

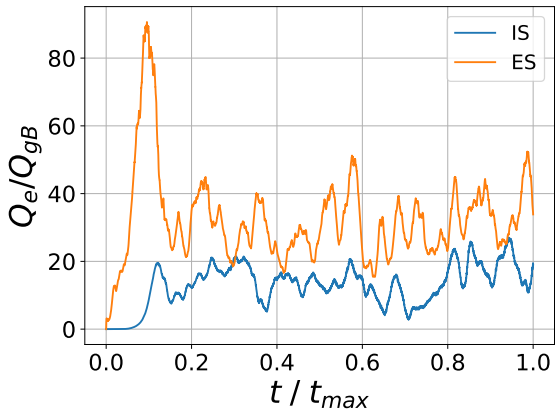

Figure 5.5: Comparison of surface-averaged heat fluxes over time for local GENE ES and global GEM IS cases (Runs #1 and #5). The final times, $t_{\max}$, are $27.50R/c_s$ for the ES run and $147.85R/c_s$ for the IS run.

directions. 16 ions and 32 electrons per cell are used. The time step is $\Omega_p \Delta t = 1$, with Ω_p the proton cyclotron frequency, and the radial domain is $0.20 \leq r/a \leq 0.80$. Drift-kinetic electrons are included using a split-weight scheme [159]. Each particle is given a weight defined by $w = \delta f / f_M$, where f_M is the Maxwellian distribution. Electron weights are evolved in time according to Equation (2.107),

$$\dot{w}_e = -\left[\mathbf{v}_E \cdot \frac{\nabla f_M}{f_M} - \frac{e}{T_{0e}}(\mathbf{v}_G \cdot \nabla \delta\phi) \quad + \frac{e}{T_{0e}}(\partial_t \delta\phi(\mathbf{x}) + \mathbf{v}_G \cdot \nabla \delta\phi|_{\mathbf{x}}) - \frac{S}{f_M}\right] \frac{f_M}{g_0}, \tag{5.12}$$

with g_0 the marker particle distribution, $\mathbf{v}_E$ the **E**x**B** drift, $\mathbf{v}_G$ the guiding-center drift, and $\mathbf{x}$ the particle location. S represents a numerical heat source which maintains the steady-state transport [160]. Figure 5.5 compares the electron heat fluxes over time for the local ES (#1) and global IS (#5) simulations. The heat flux plotted from GEM is averaged over a toroidal annulus extending radially from $r/a = 0.35$ to 0.65.

The changes to GEM discussed here account for excess electron heat transport from the electron scale by including the new source term in Equation (5.6). This term is responsible for radial **E**x**B** transport caused by electron-scale turbulence in ion-scale simulations, and can be broken up

into total divergence and compressible flow terms

$$\begin{aligned}\langle S_{\mathrm{ES}}\rangle_{\mathrm{m}} &= \langle \frac{1}{B}\delta\mathbf{E}_{\mathrm{ES}}\times\mathbf{b}\cdot\nabla\delta f_{\mathrm{ES}}\rangle_{\mathrm{m}} = \langle\nabla\cdot(\mathbf{v}_{E,\mathrm{ES}}\delta f_{\mathrm{ES}}) - \delta f_{\mathrm{ES}}(\nabla\cdot\mathbf{v}_{E,\mathrm{ES}})\rangle_{\mathrm{m}} \\ &= \langle\nabla_r\cdot(\mathbf{v}_{E,\mathrm{ES}}\delta f_{\mathrm{ES}})\rangle_{\mathrm{m}} + \cancel{\langle\nabla_x\cdot(\mathbf{v}_{E,\mathrm{ES}}\delta f_{\mathrm{ES}})\rangle_{\mathrm{m}}} - \langle\delta f_{\mathrm{ES}}(\nabla\cdot\mathbf{v}_{E,\mathrm{ES}})\rangle_{\mathrm{m}} \\ &= \nabla_r\cdot\langle\mathbf{v}_{E,\mathrm{ES}}\delta f_{\mathrm{ES}}\rangle_{\mathrm{m}} - \langle\delta f_{\mathrm{ES}}(\nabla\cdot\mathbf{v}_{E,\mathrm{ES}})\rangle_{\mathrm{m}}.\end{aligned} \tag{5.13}$$

Here, v_E is the **E**x**B** drift velocity which, in the case of electrostatic waves in toroidal geometry, varies as $\nabla\cdot v_E \sim v_E/R$. The global radial divergence is pulled out of the local intermediate-scale spatial average, and, due to the periodic boundary conditions of the flux-tube approximation, the total divergence is zero for ES fluctuations.

A crude assumption can be made by focusing on the effects of ETG heat flux to assume a global radial variation $\nabla_r\cdot Q_e \sim Q_e/L_T$, so that the radial variation of both terms can be compared:

$$\frac{\nabla\cdot\langle(\delta f_{\mathrm{ES}}\mathbf{v}_{E,\mathrm{ES}})\rangle_{\mathrm{m}}}{\langle\delta f_{\mathrm{ES}}\nabla\cdot\mathbf{v}_{E,\mathrm{ES}}\rangle_{\mathrm{m}}} \sim \frac{\langle\delta f_{\mathrm{ES}}\mathbf{v}_{\mathrm{ES}}\rangle_{\mathrm{m}}/L_T}{\langle\delta f_{\mathrm{ES}}\mathbf{v}_{\mathrm{ES}}\rangle_{\mathrm{m}}/R} \sim R/L_T. \tag{5.14}$$

The compressibility term can then be ignored, as R/L_T ranges from 3 to 7 when $r \in [0.2, 0.8]$ for the CBC profiles shown in Figure 5.2(b). However, this assumption is only reasonable when taking the second moment of these terms in velocity space. This allows for focusing on ETG heat transport, but at the loss of compressible effects regarding other moments as the ETG particle and momentum flux are considered negligible. Any possible contribution from the Reynolds stress of ETG turbulence is also lost. Notably, inclusion of the ETG Reynolds stress can result in an effective dissipation of TEM modes in good agreement with multiscale scenarios [234].

Due to the choice of perpendicular spatial mesoscale, l_{m}, discussed in Section 5.3, the perpendicular spatial mesoscale average is replaced with a flux-surface average. The z-average has been retained for simplicity and is defined as

$$\langle\ldots\rangle_z = \frac{\int(\ldots)J(z)dz}{\int J(z)dz}. \tag{5.15}$$

In the general subgrid model formulation, any dependence on z must be preserved as the source can depend on the poloidal angle. The flux-surface average is only employed here to more readily test adding the ES heat transport to GEM. The final ES source then becomes

$$\langle S_{ES}\rangle_{\mathrm{m}} \approx \nabla_r \cdot \langle\langle \mathbf{v}_{E,\mathrm{ES}} \delta f_{\mathrm{ES}}\rangle_{\tau_{\mathrm{m}}}\rangle_{\psi} = \nabla_r \cdot \hat{\Gamma}_{\mathrm{ETG}}(r, v_{\parallel}, \mu). \tag{5.16}$$

In this context, $\hat{\Gamma}$ is used instead of Γ to indicate that it is not a particle flux, but rather a kinetic form that has been both flux-surface-averaged and time-averaged. Hereafter, $\hat{\Gamma}$ will be referred to as the kinetic flux density. It is important to note that the z-averaging process does not commute with velocity-space integration, and the kinetic flux density is further normalized to yield the correct heat flux upon integration with factor $\frac{1}{2}mv^2$. Consequently, the particle flux differs from the exact value. However, because the ion response to ETG turbulence is typically adiabatic, the particle flux is negligible, and the focus remains on the heat flux.

A simple initial form for $\hat{\Gamma}$ can be constructed by using the diffusion coefficient at the peak temperature gradient location. All radial variation is retained in the equilibrium temperature profile to obtain a Fick's law diffusive model

$$\langle S_{ES}\rangle_{\mathrm{m}} = \nabla_r \cdot \hat{\Gamma}_{\mathrm{ETG}}(r, v_{\parallel}, \mu) = \nabla_r \cdot (-\hat{D}^*_{0,\mathrm{ETG}}(v_{\parallel}, \mu)\nabla_r T_{0e}(r)) = -\hat{D}^*_{0,\mathrm{ETG}}(v_{\parallel}, \mu)\nabla_r^2 T_{0e}(r). \tag{5.17}$$

The subscript ETG is chosen here to not conflict with D_{ES} of Equation (5.8), and the temperature gradient is used to recover an appropriate ETG heat flux when the second moment is taken. This pseudo ETG diffusion coefficient, $\hat{D}^*_{0,\mathrm{ETG}}$, is defined by dividing the peak kinetic flux density by the peak temperature gradient and density at $\mathrm{r}_0 = 0.50a$,

$$\hat{D}^*_{0,\mathrm{ETG}} = -\hat{\Gamma}_{0,\mathrm{ETG}}/(n_{0e}\nabla_r T_{0e})|_{r_0}. \tag{5.18}$$

D^* has been used to differentiate from the actual diffusion coefficient. This model then allows for correctly capturing the heat diffusivity when taking the second moment, while maintaining negligible

particle transport. The radial Laplacian is taken in cylindrical coordinates, giving the normalized value

$$-R^2\frac{\nabla_r^2 T_{0e}}{T_{0e}} = -R^2\frac{\frac{1}{r}\partial_r(r\nabla_r T_{0e})}{T_{0e}} = -\left[\kappa_T^2\mathrm{sech}^2(\frac{r-r_0}{w_T a}) + 2\frac{\kappa_T R}{w_T a}\tanh(\frac{r-r_0}{w_T a})\right] \times \mathrm{sech}^2(\frac{r-r_0}{w_T a}) + \frac{R}{r}\frac{R}{L_T}. \tag{5.19}$$

The negative sign is added for consistency with Equation (5.10).

$\hat{\Gamma}_{0,\mathrm{ETG}}(v_\parallel,\mu)$ is shown in Figure 5.6 above, where the mesoscale time average is taken over $t/t_{\max} = 0.458 - 0.540$ in Figure 5.5. This corresponds to the same heat flux listed in Table 5.1 which was averaged over the full nonlinear phase, $t/t_{\max} = 0.182 - 1.0$. The global radial variation is added in accordance with Equation (5.17), and the source term converted to GEM normalizations as described in Section 5.5. The ES source term is then included in GEM according to the updated weight and vorticity equations:

$$\dot{w}_e = \dot{w}_{e,\mathrm{GEM}} - \frac{\langle S_{\mathrm{ES}}\rangle_{\mathrm{m}}}{g_0}, \tag{5.20}$$

$$-n_p(\dot{\delta\phi}) = q\partial_t\langle\delta n_i\rangle_\alpha - e\partial_t\delta n_e, \tag{5.21}$$

where changes to $\partial_t\delta n_e$ in GEM must reflect changes in the density due to the new source in the electron weights.

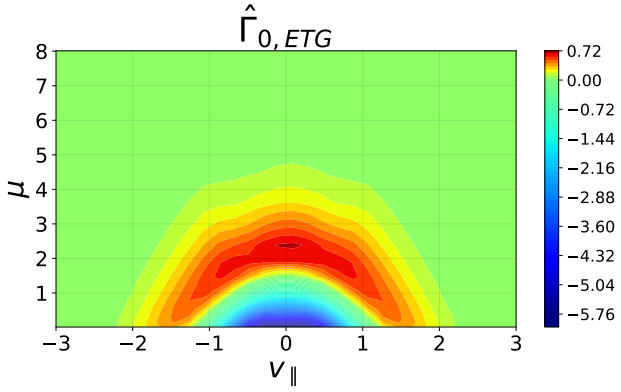

Figure 5.6: Mesoscale and z average of kinetic flux density taken from GENE ES run #1 at $r/a = 0.50$.

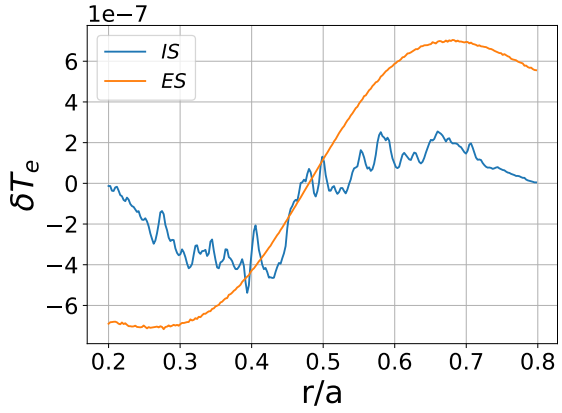

Figure 5.7: Comparison of the electron temperature perturbations generated by ITG (IS) and ETG (ES) turbulence in GEM.

Simple diagnostic equations can be used to understand the effect of the new ES term. By focusing on the change in time of the IS distribution function in Equation (5.6) due only to the ES source term, Equation (5.17), one can take moments to find

$$\begin{aligned} \partial_t \delta n_{\mathrm{IS}} &= D^*_{0,\mathrm{ETG}} \nabla_r^2 T_{0e} \approx 0, \\ \partial_t \delta T_{\mathrm{IS}} &= \frac{2}{3} \frac{1}{n_{0e}} \chi_{0,\mathrm{ETG}} \nabla_r^2 T_{0e}, \end{aligned} \tag{5.22}$$

where $\chi_{0,\mathrm{ETG}} = -Q_{0,\mathrm{ETG}}/(n_{0e}\nabla_r T_{0e})|_{r_0}$ is the ETG heat diffusivity at $r/a = 0.50$. Pressure isotropy has been assumed as there as there is no rotational flow, and the temperature equation is found by linearizing the standard equation of state, $p = nT$, and solving for the change in the pressure perturbation

$$\partial_t \delta p_{\mathrm{IS}} = \cancel{\partial_t (\delta n_{\mathrm{IS}} T_{0e})} + \partial_t (\delta T_{\mathrm{IS}} n_{0e}) = -\int \frac{2}{3} (\frac{1}{2} m v^2) \langle S_{\mathrm{ES}} \rangle_{\mathrm{m}} d^3 v. \tag{5.23}$$

Temperature perturbations are calculated by integrating over particle trajectories in time in GEM. The IS and ES contributions are separated and compared in Figure 5.7. The IS perturbation is calculated by averaging over all time in the standard GEM case (run #5) without any subgrid contribution included. The ES perturbation is calculated by integrating just the $\langle S_{\mathrm{ES}} \rangle_{\mathrm{m}}$ term over

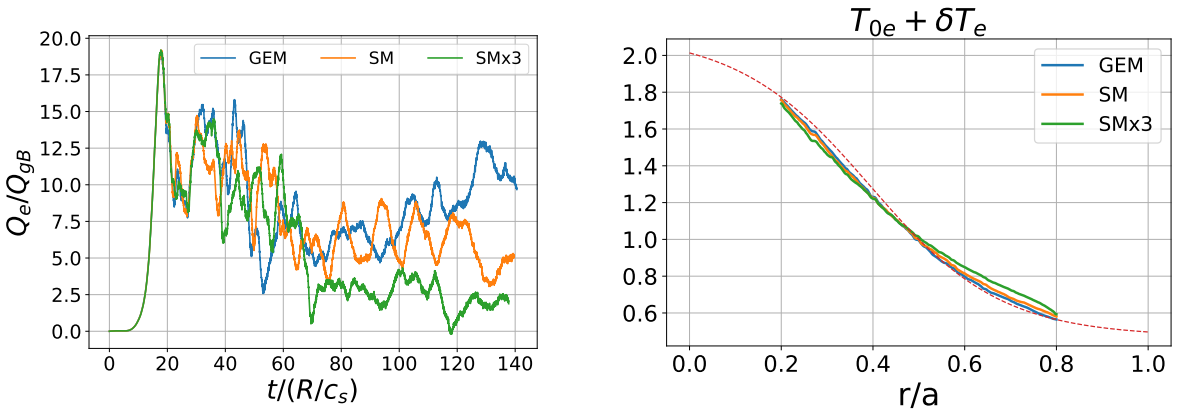

(a) (b)

Figure 5.8: Comparison of (a) electron heat flux evolution averaged over a toroidal annulus from $r/a = 0.35$ to 0.65 and (b) electron temperature profile flattening for three different GEM scenarios at $t = 129.75R/c_s$. 'GEM', 'SM', and 'SMx3' correspond to standard GEM, GEM with subgrid model, and GEM with enhanced (3x factor) subgrid model runs. The dashed red line corresponds to the initial electron temperature profile.

one time step as the subgrid term is constant over time. The effect of these temperature perturbations is to increase T_e when $r/a \gtrsim 0.50$ and decrease T_e when $r/a \lesssim 0.50$, thus flattening the electron temperature profile and reducing the possible ITG transport.

To observe the change in electron heat flux over time, the original heat source in GEM was removed and three simulations were run: one with no subgrid term, one with the subgrid term included, and one with the subgrid term increased in magnitude. As discussed previously in Section 5.3, the increased magnitude (3x) comes from scaling the subgrid term in GEM to match the electron heat flux ratio, $Q_{e,ES} : Q_{e,IS}$, observed in runs #3 and #4. Runs #3 and #4 include electromagnetic and shear flow effects which suppress ion-scale turbulence so that this adjusted ratio in GEM represents multiscale scenarios with marginal ITG turbulence.

Figure 5.8(a) compares the difference in electron heat flux over time for the three scenarios. Heat fluxes are calculated by averaging over a toroidal annulus with radial extent $r/a = 0.35$ to 0.65. Figure 5.8(b) compares the corresponding temperature profile flattening, with the time-averaged perturbations calculated from times $t = 0 - 129.75R/c_s$. As the subgrid contribution is increased,

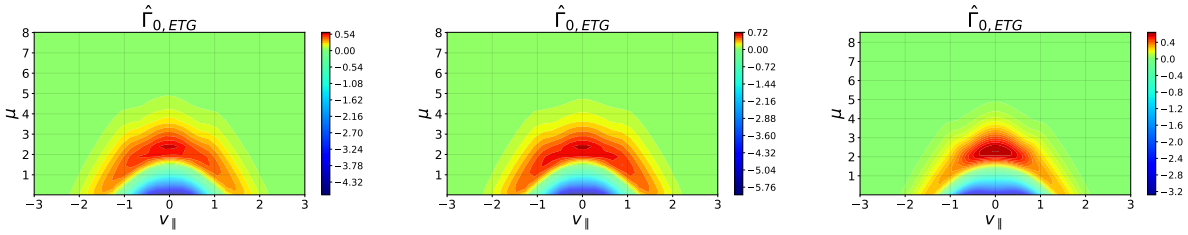

(a) (b) (c)

Figure 5.9: Kinetic flux density averaged in time over (a) the linear phase, $t/t_{\max} = 0.007 - 0.072$, and (b) the nonlinear saturated phase, $t/t_{\max} = 0.182 - 0.982$, of run #1 shown in Figure 5.5. (c) Quasilinear model of kinetic flux density using linear GENE simulations. All plots at $r/a = 0.50$.

the electron temperature profile flattens more quickly and the ITG mode drives less electron thermal transport. Although the source term directly affects the electron distribution function, the ITG turbulence was unaffected and no meaningful differences in the ion particle and heat fluxes or electron particle flux were observed. Furthermore, it must be noted here that the effect of temperature relaxation by ETG transport was reduced by approximately 50% in the presence of ITG turbulence, though currently the specific reason why remains unknown.

Lastly, the validity of the Fick's law diffusive model is discussed. A key limitation of this model is that all radial variation is attributed to the temperature gradient. Since the electron temperature gradient remains non-zero at the ends of the domain, the source term does not vanish. However, as discussed in Section 5.3, the ETG modes are stabilized near the boundaries and there should be no ES heat transport. This issue is evident in Figure 5.7, where the ES temperature perturbation does not fall to zero at the ends of the simulation domain like with the IS perturbation. A more accurate model would incorporate radial variation in the diffusion coefficient which correctly reflects linear properties of the mode. Furthermore, the Fick's law model cannot account for any small but finite particle flux correctly.

To illustrate the possibility for a flux model which can capture linear mode properties, the time average of $\hat{\Gamma}_{0,\mathrm{ETG}}(v_\parallel, \mu)$ from run #1 is shown over both the linear phase and the saturated state of the nonlinear phase in Figure 5.9(a) and Figure 5.9(b). Clearly there is qualitative agreement between

the linear and nonlinear phases, and input from linear simulations at multiple radial locations can be used to account for radial changes in ETG mode properties. Quasilinear estimates for the flux spectra are used to better capture radial changes in ETG transport levels for each k_y mode in linear simulations [169, 170]:

$$\Gamma^{\mathrm{QL}}_{k_y} = A_0 \frac{(\gamma/\langle k_\perp^2 \rangle)^2}{|\phi_{0,k_y}(0)|^2} \Gamma^{\mathrm{lin}}_{k_y}, \qquad Q^{\mathrm{QL}}_{k_y} = A_0 \frac{(\gamma/\langle k_\perp^2 \rangle)^2}{|\phi_{0,k_y}(0)|^2} Q^{\mathrm{lin}}_{k_y}. \tag{5.24}$$

A_0 is a constant of proportionality used to match the nonlinear fluxes and $\Gamma^{\mathrm{lin}}_{k_y}$ and $Q^{\mathrm{lin}}_{k_y}$ are the linear simulation fluxes at the final time step. The electrostatic potential, $\phi_{0,k_y}(0)$, is taken at $k_x = z = 0$, and $\langle k_\perp^2 \rangle$ is the ballooning-mode-averaged perpendicular wavenumber squared. The flux spectrum models defined by Equation (5.24) are the same, and so can be applied to the linear kinetic flux density directly.

The quasilinear kinetic flux density is calculated at $r/a = 0.50$ and shown in Figure 5.9(c) in comparison to the nonlinear results of Figure 5.9(a) and Figure 5.9(b). All parameters excluding A_0 are taken from linear simulations at different radial locations $r/a = 0.20, 0.30, 0.40, 0.50, 0.60, 0.70,$ and 0.80. The parameter A_0 is chosen to match the nonlinear heat flux at $r/a = 0.50$. While this quasilinear model has been validated for ITG and TEM modes, it doesn't capture the ETG flux spectra as accurately. This is illustrated in Figure 5.10(a). However, Figure 5.9(a) - Figure 5.9(c) show it works well as an initial test of feasibility. As in Section 4.2.3, the quasilinear model does not account for any regulation from the secondary instability saturation mechanism. A proper quasilinear model for ETG flux spectra is beyond the scope of this work.

The quasilinear model combines a single nonlinear simulation with multiple linear simulations, enabling a more efficient approach which can help expedite direct coupling of global IS and local ES simulations. Nonlinear simulation results at $r/a = 0.40, 0.50, 0.60,$ and 0.70, as described at the end of Section 5.3, are used to provide the most realistic radial profile of the ETG heat flux. The three different heat flux models discussed are compared directly in Figure 5.10(b). Spline fits are made for the quasilinear and nonlinear models using simulation results at each plotted point. All

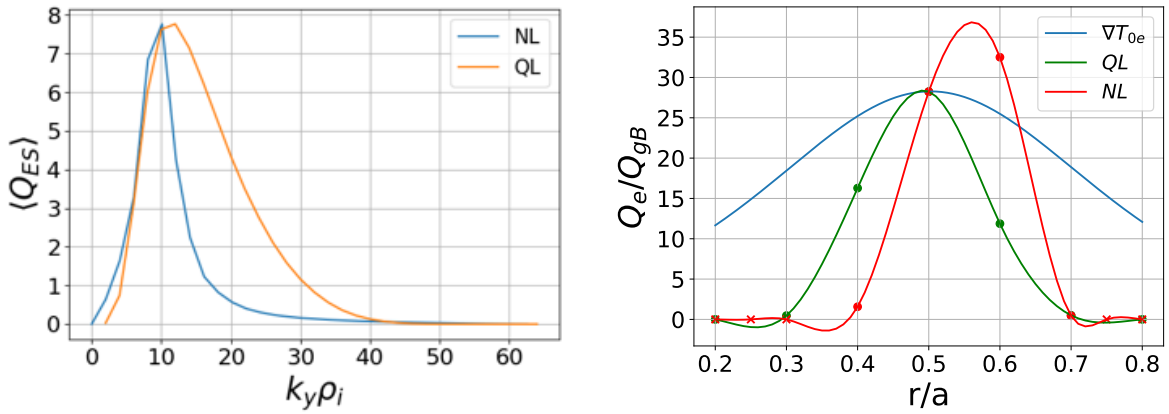

(a) (b)

Figure 5.10: (a) Comparison of quasilinear and nonlinear electron heat flux spectra at $r/a = 0.50$ averaged over k_x and z. (b) Comparison of three radial ETG heat flux models with increasing fidelity. 'QL' and 'NL' stand for quasilinear and nonlinear respectively. A red x corresponds to points assumed to go to zero for nonlinear simulations.

three models coincide at the peak temperature gradient location, $r/a = 0.50$, where one nonlinear simulation result must be used.

These heat flux models correspond to three different levels of fidelity. Clearly the Fick's law ∇T_{0e} model does not fall off to zero like the nonlinear results, while the quasilinear model provides an efficient and more reasonable prediction of the radial variation for the nonlinear ETG heat flux profile. Various fits can then be tested to include the quasilinear or nonlinear source profiles in GEM. While the focus of this work has been on capturing ES electron heat transport, the model constructed from multiple nonlinear results would best account for any fine-scale particle transport as well.

5.5 Normalizations

The normalizations involved in converting GENE output to GEM input are discussed here. Including Equation (5.17) in GEM requires converting the amplitude as well as the velocity-space grid to be consistent at different radii with global variation in temperature. Normalizations are taken from the values described in sections 2.5.1 and 2.5.2. The conversion from normalized units to

SI units for parallel velocity and magnetic moment are defined in each code as

$$v_{\parallel,e}^{\mathrm{SI}} = v_{\parallel,e}^{\mathrm{GN}}\sqrt{\frac{2T_{0e}(r)}{m_e}}, \quad v_{\parallel,e}^{\mathrm{SI}} = v_{\parallel,e}^{\mathrm{GM}}\sqrt{\frac{T_{0e}(r_0)}{m_p}}, \tag{5.25}$$

$$\mu_e^{\mathrm{SI}} = \mu_e^{\mathrm{GN}}\frac{T_{0e}(r)}{B_0}, \quad \mu_e^{\mathrm{SI}} = \mu_e^{\mathrm{GM}}\frac{T_{0e}(r_0)}{B_0}. \tag{5.26}$$

'GN' and 'GM' stand for GENE and GEM respectively. Equation (5.25) and Equation (5.26) are used to convert the normalized velocity-space grid in GENE to SI values at multiple radial locations, and then to GEM normalized units. The velocity-space grid is recalculated for each particle depending on its radial location and particles are interpolated onto the new velocity-space grid to calculate $\hat{\Gamma}_{\mathrm{ETG}}$. Approximately 95% of GEM particles fall into the velocity-space grid at all radial locations, with the remaining particles outside the $v_{\parallel,e}$ domain $\pm 3v_{Te}$ set in GENE, where $v_{Te} = \sqrt{2T_{0e}(r)/m_e}$.

Furthermore, the magnitude of $\hat{\Gamma}_{0,\mathrm{ETG}}$ needs to be converted to GEM normalized units. The quantities v_{Ex} and δf_e are normalized as follows

$$v_{Ex}^{\mathrm{SI}} = \rho^*\sqrt{\frac{T_{0e}(r_0)}{m_D}}v_{Ex}^{\mathrm{GN}}, \quad v_{Ex}^{\mathrm{SI}} = \sqrt{\frac{T_{0e}(r_0)}{m_p}}v_{Ex}^{\mathrm{GM}}, \tag{5.27}$$

$$\begin{aligned} \delta f_e^{\mathrm{SI}} &= \delta f_e^{\mathrm{GN}}\rho^* n_{0e}(r)/v_{Te}^3(r), \\ \delta f_e^{\mathrm{SI}} &= \delta f_e^{\mathrm{GM}} n_{0e}(r_0)/(T_{0e}(r_0)/m_p)^{3/2}, \end{aligned} \tag{5.28}$$

where GENE includes a factor of $\rho^* = \rho_D/R$ scaling for the perturbations $\delta\phi$ and δf. Radial variation in v_{Ex} is ignored to use only the peak turbulence level. While GENE uses the radial basis vector $\mathbf{e}_x = \nabla r$ by default, GEM uses the unit vector $\hat{\mathbf{e}}_x = \nabla_r/|\nabla_r|$ for the radial dot product. For the circular geometry used this makes no difference, however this can be changed in GENE using the 'norm_flux_projection' flag if necessary.

Finally, $L_{\mathrm{ref}}^{\mathrm{GN}} = R$, while $L_{\mathrm{ref}}^{\mathrm{GM}} = \rho_p$, the proton gyroradius, so that the normalized second

derivative, Equation (5.19), must be multiplied by a factor $(\rho_p/R)^2$, giving a total factor

$$\nabla \cdot \hat{\Gamma}^{\mathrm{GM}}_{\mathrm{ETG}} = \frac{n_{0e}(r)}{n_{0e}(r_0)} \left(\frac{2T_{0e}(r)}{T_{0e}(r_0)} \frac{m_p}{m_e} \right)^{-3/2} (\frac{\rho_p}{R})^2 (\frac{\rho_D}{R})^2 (\nabla \cdot \hat{\Gamma}^{\mathrm{GN}}_{\mathrm{ETG}}). \tag{5.29}$$

While this correctly accounts for differences in normalizations between the codes it does not yet give a radially constant $\hat{D}^*_{0,\mathrm{ETG}}$ consistent with Equation (5.17). This is because Equation (5.29) depends radially on $n_{0e}(r)$. The other factor of $T_{0e}^{-3/2}(r)$ is cancelled by Equation (5.25) and Equation (5.26) when integrating over velocity-space. Furthermore, when calculating the heat flux an extra $\frac{1}{2}mv^2$ factor will add another radial dependence on $T_{0e}(r)$. To see this, consider the GENE formula for the normalized heat flux as defined by Equation (2.92)

$$\begin{aligned} \frac{\langle Q_e \rangle_\psi}{Q_{gB}} = -\frac{\hat{n}_{0e}(r)\hat{T}_{0e}(r)}{\int_{-\pi}^{\pi} \hat{J}(r,z)dz} \int_{-\pi}^{\pi} \sum_{\mathbf{k}} \hat{J}(r,z) i\hat{k}_y \delta\hat{\bar{\phi}}(\mathbf{k}) \\ \times \left(\pi \hat{B}_0(r,z) \int d\hat{v}_\parallel d\hat{\mu} \hat{v}^2 \delta \hat{f}_e(\mathbf{k}) \right)^*, \end{aligned} \tag{5.30}$$

which contains radial dependence on $\hat{p}_{0e}(r) = \hat{n}_{0e}(r)\hat{T}_{0e}(r)$. A caret ($\hat{}$) in Equation (5.30) indicates normalized variables.

The extra pressure factor is divided from Equation (5.29) to retrieve an approximately radially-constant $\hat{D}^*_{0,\mathrm{ETG}}$. The source term is integrated on the original GENE velocity-space grid and converted to GEM normalization to compare to direct integration in GEM which sums over particle weights. The results of both integration methods are compared in Figure 5.11(a) using the kinetic flux density of Figure 5.6 and agree well. Note, some radial variation remains in $\hat{D}^*_{0,\mathrm{ETG}}$ due to radial changes in $J(r,z)$ and $B_0(r,z)$ which are used when integrating Equation (5.30). The effect of this is small and simply ignored. This remaining radial variation can be seen in Figure 5.11(b), where the fluxes are calculated by integrating $\hat{\Gamma}_{0,\mathrm{ETG}}$ in Figure 5.6 using CBC equilibrium profiles.

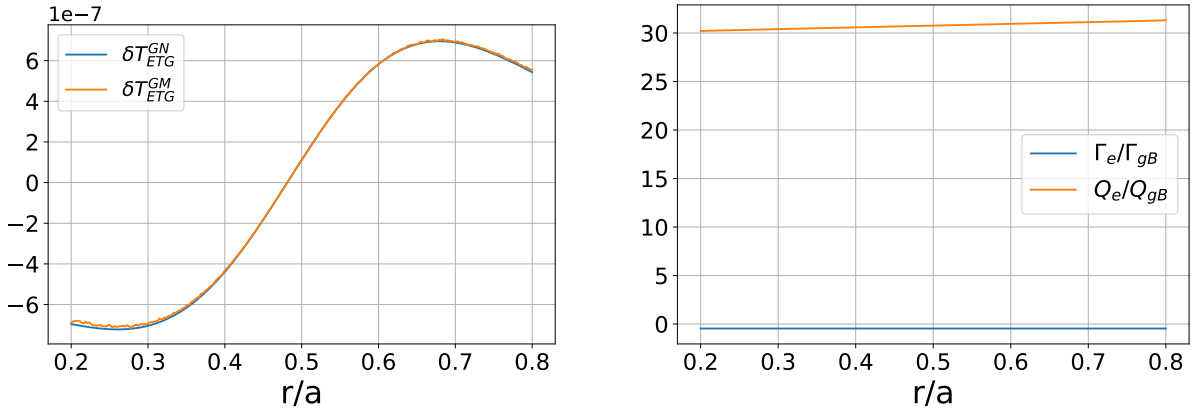

(a) (b)

Figure 5.11: (a) Comparison of source terms when integrating GENE data directly in velocity-space and when integrating by interpolating over particles in GEM. (b) Electron flux profiles when $\hat{\Gamma}_{0,\mathrm{ETG}}$ is integrated assuming only radial changes in geometry $(B(r,z), J(r,z))$.

5.6 Discussion

A subgrid ETG model has been derived here which averages local electron-scale turbulence over intermediate scales in space perpendicular to the field and in time to include in global ion-scale simulation. CBC simulations are carried out which show a clear scale separation in turbulent spectra in k_y. A kinetic form of the electron-scale electron heat flux is taken from local GENE simulation and added into global GEM ITG simulations using a simple Fick's law diffusion model. Multiple ratios of ITG to ETG turbulent heat flux levels are considered, and the effects of increased electron temperature relaxation are described. A more accurate quasilinear heat flux model is constructed and compared against nonlinear ETG heat fluxes at multiple radial locations. Such a quasilinear model allows for the possibility of using a single nonlinear ETG simulation at the peak temperature gradient only, which can help expedite coupling of simulations at both scales.

Future work will consider the effects of the ETG potential on the ion-scale distribution of electrons, as described by Equation (5.8). The diffusion coefficient, D_{ES}, can be found by following the motion of tracer particles in the ETG field of a local ES simulation, and a theoretical model developed to capture radial variation of the diffusion. The ETG streamer potential can also be

added directly to local GEM ion-scale simulations, assuming periodicity on ion scales, and evolved in time to compare to the diffusive model. The effects of intermediate-scale zonal flows as shown in Figure 5.4(c) might also be included as an extra global radial shear parameter. Theoretically this would require breaking the scale separation hypothesis as $\langle \delta f_{\mathrm{ES}} \rangle_{\mathrm{m}} \neq 0$ and $\langle \delta \mathbf{E}_{\mathrm{ES}} \rangle_{\mathrm{m}} \neq 0$ when the spectra become multiscale in k_x. If local ion-scale simulations extend to $k_x \rho_i \sim 2$ the longest wavelength ZFs could be added directly to investigate the effect. The formation of intermediate-scale zonal flows in multiscale simulation is dependent on the level of ITG turbulence [61], and so it would be prudent to first focus on including effects of ion-scale turbulence in electron-scale simulations per Ref. [230].

Many further topics exist for future research directions. These include adding the compressible effects and effects of ETG Reynolds stress which have been ignored here, considering any spectral transfer between scales, and proper coupling of ITG and ETG simulations to capture effects of ion-scale turbulence in electron-scale simulations. Furthermore, it is important to understand when a scale separation hypothesis is valid, as electron transport spectra can broaden to become multiscale in the pedestal [235].

Chapter 6

Conclusions and Outlook

The primary objective of this work is to advance the theoretical understanding of ETG turbulence in core tokamak plasmas through gyrokinetic simulations. After decades of extensive development, gyrokinetic modeling has become an essential tool for studying the nonlinear dynamics of tokamak microturbulence. Numerical simulations have successfully reproduced flux spectra and transport levels associated with ion-scale instabilities in agreement with experimental observations. However, electron thermal transport levels are often underestimated. The ETG mode, which exists at electron gyroradius scales, is a leading candidate to explain these excess electron heat losses. In reactor-relevant plasmas, such as ITER, a combination of ECH and fusion alpha-particle heating is expected to drive significant ETG turbulence in the core. Furthermore, such scenarios can result in complex multiscale interactions when ITG turbulence is suppressed by stabilizing electromagnetic effects and equilibrium shear flow. Additionally, in the edge pedestal region, turbulence is often governed by a combination of ETG and MTM modes, as the strong shear flows characteristic of the edge transport barrier suppress ITG instabilities.

The cross-scale interactions observed in multiscale simulations are highly sensitive to small variations in equilibrium parameters. This makes it challenging to systematically study these dependencies as multiscale gyrokinetic simulations are computationally demanding due to the disparate scales involved. As a result, reduced models of electron-scale turbulence are of particular interest for whole-device modeling efforts of future burning plasmas. Quasilinear theory offers an efficient approach to estimating nonlinear turbulence characteristics by leveraging significantly less

expensive linear simulation results. In Chapter 3, quasilinear theory was introduced, along with its applications in modeling the nonlinear electrostatic potential and flux spectra of drift wave turbulence. Linear GENE simulations were used for quasilinear modeling of ion-scale turbulence in DIII-D shot #162940, with results compared against nonlinear local GENE and global GEM simulations. The quasilinear predictions showed good agreement with flux spectra for all species, including carbon impurities. The analysis was extended to negative triangularity (NT) plasma shaping, a configuration that has gained interest as a promising method for reducing turbulent transport while enabling ELM-free operation. Linear results showed complete TEM stabilization and reduced ITG growth rates, and the corresponding flux spectra agreed well with nonlinear GENE simulation results. Future work might consider extending quasilinear saturation rules to include electromagnetic modes of interest and explore the role of non-diffusive pinch effects, as well as analyze the stabilizing effects of NT on ITG modes.

While these heuristic mixing-length quasilinear models have historically been successful in describing ITG and TEM turbulence, their agreement was found to be less robust for the cases of ETG turbulence considered in both Chapter 4 and Chapter 5. This discrepancy is overall unsurprising, as the regulation of ETG modes has been less extensively studied and has only recently become a more active topic of research. In Chapter 4, nonlinear flux-tube GENE simulations with a single toroidal mode revealed that ETG turbulence is regulated through two distinct mechanisms at long and short wavelengths respectively. At shorter wavelengths, suppression occurs via the generation of secondary Kelvin-Helmholtz type instabilities, consistent with earlier fluid theories of ETG mode regulation. These theories predicted weaker regulation at longer wavelengths, leading to a steady state characterized by radial streamers and high transport levels. However, the single-mode simulations of longer-wavelength ETG modes instead showed an initial exponential growth of zonal flows, followed by slow growth into late times, validating a more recent intermediate-scale gyrokinetic theory which expected lower ETG transport levels. Furthermore, full-spectrum nonlinear ETG simulations were carried out which showed good qualitative agreement with the separate dynamics observed in the single-mode simulations.

Developing a more accurate quasilinear saturation rule for ETG modes would likely require incorporating both saturation mechanisms. As mentioned in Chapter 4, the earlier fluid analyses derived a saturation rule of $\phi \sim \gamma/k_\perp^4$ - notably different from the standard mixing-length estimate - which showed better agreement with the steeper drop off of the ETG potential spectrum at shorter wavelengths. Additionally, further investigation of nonlinear ETG dynamics under varying magnetic shear and in negative triangularity configurations would further provide valuable insights into ETG mode regulation. More thorough understanding of nonlinear ETG turbulence dynamics would prove especially helpful in future efforts to model multiscale effects. Multiscale gyrokinetic simulations have recently garnered much interest, reporting improved agreement with experimental transport levels for both species in core tokamak plasmas when ITG and ETG turbulence coexist. In cases of strong ITG turbulence ETG modes are generally regulated, while cases of marginal ITG turbulence report effects of ETG turbulence at ion scales. Typically, the electron scale is characterized by radially extended streamers which lead to enhancement of ITG transport, though intermediate-scale zonal flows can develop in cases of weak or sub-critical ITG turbulence which help to further regulate ion-scale turbulence.

Chapter 5 details preliminary efforts to couple ETG turbulence effects from local gyrokinetic GENE simulations into global ion-scale GEM simulations. The theoretical subgrid ETG model considers averaging ETG turbulence over intermediate scales in space perpendicular to the field and in time to provide a reduced method of capturing ETG turbulence effects. This approach results in ion-scale equations which incorporate the electron heat transport from ETG turbulence and effects of electron-scale turbulence on the ion scale. Flux-tube ETG Cyclone Base Case simulations were performed at different radial locations and a kinetic form of the flux was added to global ion-scale simulations as a source term. Analytic radial profiles of ETG heat flux were constructed by considering radial variation in the background temperature profile and quasilinear theory to compare against flux-tube results at multiple radial locations. Different ratios of ITG to ETG heat flux levels were considered and the results of capturing ETG heat transport in global ion-scale simulations was discussed.

Initial global GEM simulations incorporated a kinetic flux density profile averaged along the field line to more readily test ETG transport effects. Simulation results showed stronger flattening of the electron temperature profile and a subsequent reduction in electron heat flux driven by ITG turbulence. No substantial change in ITG transport levels was otherwise noticed, indicating minimal effect on ITG dynamics. Interestingly, the temperature flattening by ETG heat transport was found to be reduced by approximately half, a result which needs to be further analyzed and understood. Future work should aim to retain flux variation along the field line and implement the more realistic quasilinear or nonlinear models by interpolating data from multiple radial simulations which would also better account for small but finite ETG particle fluxes. Additionally, any Reynolds stress and compressible **E**x**B** flow contributions were ignored in this work. Any coupling of the ETG streamer potential and intermediate-scale zonal flows to the ion scale must further be addressed. One approach to testing ETG streamer effects on ion-scale transport is to incorporate them directly into local ITG simulations. It is expected that a diffusive model can be used to account for averaged effects in global ion-scale simulations. Meanwhile, capturing the influence of intermediate-scale zonal flow shearing on ITG modes would necessitate breaking scale-separation assumptions. If local ion-scale simulations extend into the intermediate-scale, the strongest ZFs could be directly included to investigate any regulative effect. Moreover, electron transport spectra can broaden to become multiscale in the pedestal, and so it is important to better understand when a scale separation hypothesis is valid.

References

[1] E. Institute, *Statistical Review of World Energy*, (2024) https://www.energyinst.org/statistical-review (Cited on p. 2).

[2] V. Smil, *Energy Transitions: Global and National Perspectives*, 2nd ed. (Praeger, 2016) (Cited on p. 2).

[3] U.S. Energy Information Administration, *Monthly Energy Review October 2024*, (2024) https://www.eia.gov/mer (Cited on p. 3).

[4] U.S. Department of Energy, *The Ultimate Fast Facts Guide to Nuclear Energy*, (2019) https://www.energy.gov/ne/articles/ultimate-fast-facts-guide-nuclear-energy (Cited on p. 3).

[5] J. Ongena and G. V. Oost, "Energy for Future Centuries: Prospects for Fusion Power as a Future Energy Source", Fusion Science and Technology **61**, 3 (2012) (Cited on p. 3).

[6] J. A. Wesson, *Tokamaks* (Clarendon Press, 2008) (Cited on pp. 4, 6–8, 13, 18, 19, 22, 26, 29, 31, 39, 40, 61, 80).

[7] NCSSM, *Binding Energy vs Mass*, (2002) https://www.dlt.ncssm.edu/tiger/chem2.htm#nuclear (Cited on p. 5).

[8] U. of Wisconsin-Madison, *Inertial Electrostatic Confinement Fusion*, (2014) https://iec.neep.wisc.edu/operation.php (Cited on p. 6).

[9] J. D. Lawson, "Some Criteria for a Power Producing Thermonuclear Reactor", Proceedings of the Physical Society. Section B **70**, 6 (1957) (Cited on p. 8).

[10] S. E. Wurzel and S. C. Hsu, "Progress Toward Fusion Energy Breakeven and Gain as Measured Against the Lawson Criterion", Physics of Plasmas **29**, 062103 (2022) (Cited on pp. 9–11).

[11] A. J. Creely, M. J. Greenwald, S. B. Ballinger, D. Brunner, J. Canik, J. Doody, T. Fülöp, D. T. Garnier, R. Granetz, T. K. Gray, and et al., "Overview of the SPARC tokamak", Journal of Plasma Physics **86**, 865860502 (2020) (Cited on pp. 9, 31).

[12] I. P. B. Editors, I. P. E. G. Chairs, Co-Chairs, I. J. C. Team, and P. I. Unit, "Chapter 1: Overview and summary", Nuclear Fusion **39**, 2137 (1999) (Cited on p. 9).

[13] A. B. Zylstra, O. A. Hurricane, D. Callahan, et al., "Burning plasma achieved in inertial fusion", Nature **601**, 542 (2022) (Cited on p. 11).

[14] J. Kaslow, M. Brown, R. Hirsch, et al., "Criteria for practical fusion power systems: Report from the EPRI fusion panel", Journal of Fusion Energy **13**, 181 (1994) (Cited on p. 11).

[15] S. Woodruff, J. K. Baerny, N. Mattor, D. Stoulil, R. Miller, and T. Marston, "Path to Market for Compact Modular Fusion Power Cores", Journal of Fusion Energy **31**, 305 (2012) (Cited on p. 11).

[16] M. C. Handley, D. Slesinski, and S. C. Hsu, "Potential Early Markets for Fusion Energy", Journal of Fusion Energy **40**, 18 (2021) (Cited on p. 11).

[17] D. Maisonnier, "RAMI: The main challenge of fusion nuclear technologies", Fusion Engineering and Design **136**, Special Issue: Proceedings of the 13th International Symposium on Fusion Nuclear Technology (ISFNT-13), 1202 (2018) (Cited on p. 11).

[18] Lawrence Livermore National Laboratory, *Ignition Experiment Advances Stockpile Stewardship Mission*, (2023) https://lasers.llnl.gov/news/ignition-experiment-advances-stockpile-stewardship-mission (Cited on p. 11).

[19] W. Spears and J. Wesson, "Scaling of tokamak reactor costs", Nuclear Fusion **20**, 1525 (1980) (Cited on p. 11).

[20] J. Sheffield, "Physics requirements for an attractive magnetic fusion reactor", Nuclear Fusion **25**, 1733 (1985) (Cited on p. 11).

[21] U.S. Department of Energy, *DoE Explains...Tokamaks*, (2019) https://www.energy.gov/science/doe-explainstokamaks (Cited on p. 12).

[22] H. Zohm, *Magnetohydrodynamic stability of Tokamaks* (Wiley-VCH Verlag GmbH & Company KGaA, 2015) (Cited on pp. 12, 19, 20, 22, 23, 29, 36, 38, 190).

[23] F. F. Chen, *Introduction to plasma physics* (Springer International Publishing, 2016) (Cited on pp. 13, 14, 17–19, 25, 35, 39–41).

[24] D. R. Nicholson, *Introduction to plasma theory* (Krieger Pub. Co, 1992) (Cited on pp. 13, 17, 35, 76).

[25] D. A. Gurnett and A. Bhattacharjee, *Introduction to plasma physics: With space, laboratory and Astrophysical Applications* (Cambridge University Press, 2017) (Cited on pp. 13, 16, 17, 35, 36, 76, 79).

[26] R. J. Goldston and P. H. Rutherford, *Introduction to plasma physics* (CRC Press, 2020) (Cited on pp. 13, 17, 35).

[27] D'haeseleer and Caron, *Flux coordinates and magnetic field structure* (Springer Berlin Heidelberg, 1991) (Cited on p. 19).

[28] R. D. Hazeltine and J. D. Meiss, *Plasma confinement* (Addison-Wesley, 1992) (Cited on p. 19).

[29] EUROfusion, *Geometry of a toroidal magnetic field with a divertor*, (2007) https://euro-fusion.org/wp-content/uploads/2023/12/Focus_on_JET.pdf (Cited on p. 20).

[30] V. D. Shafranov, "Plasma Equilibrium in a Magnetic Field", Rev. Plasma Phys. **2**, 103 (1966) (Cited on p. 21).

[31] F. Troyon, R. Gruber, H. Saurenmann, S. Semenzato, and S. Succi, "MHD-Limits to Plasma Confinement", Plasma Physics and Controlled Fusion **26**, 209 (1984) (Cited on p. 24).

[32] R. L. Miller, M. S. Chu, J. M. Greene, Y. R. Lin-Liu, and R. E. Waltz, "Noncircular, finite aspect ratio, local equilibrium model", Physics of Plasmas **5**, 973 (1998) (Cited on pp. 26, 85).

[33] J. P. Graves, "Toroidal drift precession and wave–particle interaction in shaped tokamaks with finite beta and neoclassical equilibrium effects", Plasma Physics and Controlled Fusion **55**, 074009 (2013) (Cited on p. 26).

[34] F. L. Hinton and R. D. Hazeltine, "Theory of plasma transport in toroidal confinement systems", Rev. Mod. Phys. **48**, 239 (1976) (Cited on pp. 27, 28).

[35] P. Helander and D. J. Sigmar, *Collisional transport in magnetized plasmas* (Cambridge University Press, 2005) (Cited on p. 27).

[36] W. Horton, "Drift waves and transport", Rev. Mod. Phys. **71**, 735 (1999) (Cited on pp. 27, 28, 42, 43, 58, 98, 101, 110, 188, 193).

[37] I. P. E. G. on Confinement, Transport, I. P. E. G. on Confinement Modelling, Database, and I. P. B. Editors, "Chapter 2: Plasma confinement and transport", Nuclear Fusion **39**, 2175 (1999) (Cited on pp. 27, 31, 60, 98).

[38] E. Doyle, W. Houlberg, Y. Kamada, V. Mukhovatov, T. Osborne, A. Polevoi, G. Bateman, J. Connor, J. Cordey, T. Fujita, X. Garbet, T. Hahm, L. Horton, A. Hubbard, F. Imbeaux, F. Jenko, J. Kinsey, Y. Kishimoto, J. Li, T. Luce, Y. Martin, M. Ossipenko, V. Parail, A. Peeters, T. Rhodes, J. Rice, C. Roach, V. Rozhansky, F. Ryter, G. Saibene, R. Sartori, A. Sips, J. Snipes, M. Sugihara, E. Synakowski, H. Takenaga, T. Takizuka, K. Thomsen, M. Wade, H. Wilson, I. T. P. T. Group, I. C. Database, M. T. Group, I. Pedestal, and E. T. Group, "Chapter 2: Plasma confinement and transport", Nuclear Fusion **47**, S18 (2007) (Cited on pp. 27, 28, 55, 60, 98).

[39] M. Yoshida, R. McDermott, C. Angioni, Y. Camenen, J. Citrin, M. Jakubowski, J. Hughes, Y. Idomura, P. Mantica, A. Mariani, S. Mordijck, E. Paul, T. Tala, G. Verdoolaege, A. Zocco, F. Casson, G. Dif-Pradalier, B. Duval, B. Grierson, S. Kaye, P. Manas, M. Maslov, T. Odstrcil, J. Rice, L. Schmitz, F. Sciortino, E. Solano, G. Staebler, M. Valovič, E. Wolfrum, J. Snipes, the Transport, and C. Group, "Transport and confinement physics: Chapter 2 of the special issue: on the path to tokamak burning plasma operation", Nuclear Fusion **65**, 033001 (2025) (Cited on pp. 27, 60).

[40] D. A. Batchelor, M. Beck, A. Becoulet, R. V. Budny, C. S. Chang, P. H. Diamond, J. Q. Dong, G. Y. Fu, A. Fukuyama, T. S. Hahm, D. E. Keyes, Y. Kishimoto, S. Klasky, L. L. Lao, K. Li, Z. Lin, B. Ludaescher, J. Manickam, N. Nakajima, T. Ozeki, N. Podhorszki, W. M. Tang, M. A. Vouk, R. E. Waltz, S. J. Wang, H. R. Wilson, X. Q. Xu, M. Yagi, and F. Zonca, "Simulation of Fusion Plasmas: Current Status and Future Direction", Plasma Science and Technology **9**, 312 (2007) (Cited on pp. 27, 62, 98, 99, 110).

[41] V. A. Soukhanovskii, "A review of radiative detachment studies in tokamak advanced magnetic divertor configurations", Plasma Physics and Controlled Fusion **59**, 064005 (2017) (Cited on p. 29).

[42] F. Ryter, W. Suttrop, B. Brüsehaber, M. Kaufmann, V. Mertens, H. Murmann, A. G. Peeters, J. Stober, J. Schweinzer, H. Zohm, and A. U. Team, "H-mode power threshold and transition in ASDEX Upgrade", Plasma Physics and Controlled Fusion **40**, 725 (1998) (Cited on p. 30).

[43] H. Zohm, "Edge localized modes (ELMs)", Plasma Physics and Controlled Fusion **38**, 105 (1996) (Cited on p. 30).

[44] S. Konishi, M. Enoeda, M. Nakamichi, T. Hoshino, A. Ying, S. Sharafat, and S. Smolentsev, "Functional materials for breeding blankets—status and developments", Nuclear Fusion **57**, 092014 (2017) (Cited on p. 31).

[45] G. Van Oost, A. V. Dedov, and V. P. Budaev, "The Plasma-Facing Materials of Tokamak Thermonuclear Reactors: Requirements, Thermal Stabilization, and Tests (a Review)", Thermal Engineering **68**, 185 (2021) (Cited on p. 31).

[46] M. E. Fenstermacher et al., "DIII-D research advancing the physics basis for optimizing the tokamak approach to fusion energy", Nuclear Fusion **62**, 042024 (2022) (Cited on p. 31).

[47] H. Zohm et al., "Overview of ASDEX upgrade results in view of ITER and DEMO", Nuclear Fusion **64**, 112001 (2024) (Cited on p. 31).

[48] R. L. Boivin, J. L. Luxon, M. E. Austin, N. H. Brooks, K. H. Burrell, E. J. Doyle, M. E. Fenstermacher, D. S. Gray, M. Groth, C.-L. Hsieh, R. J. Jayakumar, C. J. Lasnier, A. W. Leonard, G. R. McKee, R. A. Moyer, T. L. Rhodes, J. C. Rost, D. L. Rudakov, M. J. Schaffer, E. J. Strait, D. M. Thomas, M. Van Zeeland, J. G. Watkins, G. W. Watson and C. P. C. Wong, "DIII-D Diagnostic Systems", Fusion Science and Technology **48**, 834 (2005) (Cited on p. 31).

[49] M. E. Austin, A. Marinoni, M. L. Walker, M. W. Brookman, J. S. deGrassie, A. W. Hyatt, G. R. McKee, C. C. Petty, T. L. Rhodes, S. P. Smith, C. Sung, K. E. Thome, and A. D. Turnbull, "Achievement of Reactor-Relevant Performance in Negative Triangularity Shape in the DIII-D Tokamak", Phys. Rev. Lett. **122**, 115001 (2019) (Cited on pp. 31, 93).

[50] K. E. Thome, M. E. Austin, A. Hyatt, A. Marinoni, A. O. Nelson, C. Paz-Soldan, F. Scotti, W. Boyes, L. Casali, C. Chrystal, S. Ding, X. D. Du, D. Eldon, D. Ernst, R. Hong, G. R. McKee, S. Mordijck, O. Sauter, L. Schmitz, J. L. Barr, M. G. Burke, S. Coda, T. B. Cote, M. E. Fenstermacher, A. Garofalo, F. O. Khabanov, G. J. Kramer, C. J. Lasnier, N. C. Logan, P. Lunia, A. G. McLean, M. Okabayashi, D. Shiraki, S. Stewart, Y. Takemura, D. D. Truong, T. Osborne, M. A. Van Zeeland, B. S. Victor, H. Q. Wang, J. G. Watkins, W. P. Wehner, A. S. Welander, T. M. Wilks, J. Yang, G. Yu, L. Zeng, and the DIII-D Team, "Overview of results from the 2023 DIII-D negative triangularity campaign", Plasma Physics and Controlled Fusion **66**, 105018 (2024) (Cited on pp. 31, 93).

[51] E. Joffrin et al., "Overview of the JET preparation for deuterium-tritium operation with the ITER like-wall", Nuclear Fusion **59**, 112021 (2019) (Cited on p. 31).

[52] C. Maggi, T. Tala, A. Hakola, A. Järvinen, J. Karhunen, A. Kirjasuo, J. Likonen, A. Salmi, and et al., "Overview of T and D–T results in JET with ITER-like wall", English, Nuclear Fusion **64**, 10.1088/1741-4326/ad3e16 (2024) (Cited on p. 31).

[53] J. Huang, X. Gong, A. M. Garofalo, J. Qian, R. Ding, X. J. Zhang, J. L. Chen, M. H. Li, Y. W. Yu, Y. F. Wang, Y. Huang, H. Si, L. Y. Meng, T. Q. Jia, Y. X. Sun, L. Zeng, L. Han, Y. M. Duan, A. Ekedahl, C. T. Holcomb, R. Maingi, E. Z. Li, H. Q. Liu, B. Lyu, Q. L. Ren, Y. W. Sun, L. Wang, L. Q. Xu, D. M. Yao, Q. Q. Yang, Q. Zang, B. Zhang, L. Zhang, X. M. Zhai, G. Z. Zuo, G. Q. Li, P. F. Zi, M. Wang, H. D. Xu, Q. P. Yuan, Y. H. Xie, L. S. Huang, J. Zhang, Y. L. Hu, W. B. Xi, Z. W. Zhou, Z. C. Wang, B. Guo, G. S. Xu, J. S. Hu, K. Lu, Y. T. Song, B. N. Wan, J. Li, and E. team, "Long-pulse high-performance H-mode plasmas achieved on EAST", Physics of Plasmas **30**, 062504 (2023) (Cited on p. 31).

[54] H.-S. Kim, Y. Jeon, H. Han, K. Kim, K. Kim, H. Kim, T. Rhee, J. Kim, J. Kim, D. Seo, E. Bang, H.-J. Ahn, H.-S. Ahn, J. Hong, J. Jeong, J. Kong, J.-G. Kwak, J. Jin, J. Bak, K. Park, K.-D. Lee, M. Joung, S. W. Kwag, S.-H. Hahn, S. Kim, S.-W. Yoon, S. Wang, W. C. Kim, Y.-O. Kim, and K. Teams, "Development of high-performance long-pulse discharge in KSTAR", Nuclear Fusion **64**, 016033 (2023) (Cited on p. 31).

[55] M. Greenwald, "10 - Alcator C-Mod and the high magnetic field approach to fusion", in *Magnetic Fusion Energy*, edited by G. H. Neilson (Woodhead Publishing, 2016), pp. 295–322 (Cited on p. 31).

[56] Exascale Computing Project, *WDMApp*, (2016) https://www.exascaleproject.org/research-project/wdmapp/ (Cited on p. 32).

[57] J. Degrave, F. Felici, J. Buchli, M. Neunert, B. Tracey, F. Carpanese, T. Ewalds, R. Hafner, A. Abdolmaleki, D. de las Casas, C. Donner, L. Fritz, C. Galperti, A. Huber, J. Keeling, M. Tsimpoukelli, J. Kay, A. Merle, J.-M. Moret, S. Noury, F. Pesamosca, D. Pfau, O. Sauter, C. Sommariva, S. Coda, B. Duval, A. Fasoli, P. Kohli, K. Kavukcuoglu, D. Hassabis, and M. Riedmiller, "Magnetic control of tokamak plasmas through deep reinforcement learning", Nature **602**, 414 (2022) (Cited on p. 32).

[58] J. Vega, A. Murari, and S. o. Dormido-Canto, "Disruption prediction with artificial intelligence techniques in tokamak plasmas", Nature Physics **18**, 741 (2022) (Cited on p. 32).

[59] M. Greenwald, U. Shumlak, and D. T. Anderson, "Preface to special issue: Private fusion research: Opportunities and challenges in plasma science", Physics of Plasmas **31**, 090401 (2024) (Cited on p. 32).

[60] N. Howard, C. Holland, A. White, M. Greenwald, and J. Candy, "Multi-scale gyrokinetic simulation of tokamak plasmas: enhanced heat loss due to cross-scale coupling of plasma turbulence", Nuclear Fusion **56**, 014004 (2015) (Cited on pp. 32, 33, 98, 99).

[61] C. Holland, N. Howard, and B. Grierson, "Gyrokinetic predictions of multiscale transport in a DIII-D ITER baseline discharge", Nuclear Fusion **57**, 066043 (2017) (Cited on pp. 32, 33, 98, 99, 104, 124–128, 136, 150).

[62] F. Jenko, W. Dorland, M. Kotschenreuther, and B. N. Rogers, "Electron temperature gradient driven turbulence", Physics of Plasmas **7**, 1904 (2000) (Cited on pp. 33, 58, 62, 98, 99, 103, 109, 115, 121, 132).

[63] W. Dorland, F. Jenko, M. Kotschenreuther, and B. N. Rogers, "Electron Temperature Gradient Turbulence", Phys. Rev. Lett. **85**, 5579 (2000) (Cited on pp. 33, 58, 98, 99, 103, 115, 121).

[64] H. Chen, S. Tirkas, and S. E. Parker, "Excitation of zonal flow by intermediate-scale toroidal electron temperature gradient turbulence", Nuclear Fusion **61**, 066017 (2021) (Cited on pp. 33, 98–100, 104, 106–109, 113, 116, 117, 122, 123).

[65] I. G. Abel, G. G. Plunk, E. Wang, M. Barnes, S. C. Cowley, W. Dorland, and A. A. Schekochihin, "Multiscale gyrokinetics for rotating tokamak plasmas: fluctuations, transport and energy flows", Reports on Progress in Physics **76**, 116201 (2013) (Cited on pp. 35, 45–47, 49, 51, 53, 54, 104, 128, 183).

[66] T. H. Stix, *Waves in plasmas* (American Institute of Physics, 1992) (Cited on p. 39).

[67] E. M. Lifshitz, L. D. Landau, and L. P. Pitaevskij, *Course of theoretical physics. 10, physical kinetics* (Butterworth-Heinemann, 2008) (Cited on p. 43).

[68] E. A. Frieman and L. Chen, "Nonlinear gyrokinetic equations for low frequency electromagnetic waves in general plasma equilibria", The Physics of Fluids **25**, 502 (1982) (Cited on pp. 44, 45, 47, 104, 128).

[69] D. H. E. Dubin, J. A. Krommes, C. Oberman, and W. W. Lee, "Nonlinear gyrokinetic equations", The Physics of Fluids **26**, 3524 (1983) (Cited on pp. 44, 47, 104, 128).

[70] R. G. Littlejohn, "Variational principles of guiding centre motion", Journal of Plasma Physics **29**, 111 (1983) (Cited on pp. 44, 47).

[71] W. W. Lee, "Gyrokinetic approach in particle simulation", The Physics of Fluids **26**, 556 (1983) (Cited on pp. 44, 69, 71, 128).

[72] E. Mazzucato, "Spectrum of Small-Scale Density Fluctuations in Tokamaks", Phys. Rev. Lett. **48**, 1828 (1982) (Cited on p. 44).

[73] A. Wootton, B. Carreras, H. Matsumoto, K. McGuire, W. Peebles, C. Ritz, P. Terry, and S. Zweben, "Fluctuations and anomalous transport in tokamaks", Physics of Fluids B **2**, 10.1063/1.859358 (1990) (Cited on p. 44).

[74] H. Chen, L. Chen, F. Zonca, J. Li, and M. Xu, "Validity of gyrokinetic theory in magnetized plasmas", Communications Physics **7**, 261 (2024) (Cited on p. 44).

[75] G. Kagan and P. J. Catto, "Arbitrary poloidal gyroradius effects in tokamak pedestals and transport barriers", Plasma Physics and Controlled Fusion **50**, 085010 (2008) (Cited on p. 44).

[76] P. J. Catto, F. I. Parra, G. Kagan, and A. N. Simakov, "Limitations, insights and improvements to gyrokinetics", Nuclear Fusion **49**, 095026 (2009) (Cited on p. 44).

[77] P. J. Catto, "Linearized gyro-kinetics", Plasma Physics **20**, 719 (1978) (Cited on pp. 45, 47).

[78] M. A. Beer, "Gyrofluid Models of Turbulent Transport in Tokamaks", PhD thesis (Princeton, 1995) (Cited on pp. 47, 107).

[79] A. J. Brizard and T. S. Hahm, "Foundations of nonlinear gyrokinetic theory", Rev. Mod. Phys. **79**, 421 (2007) (Cited on p. 47).

[80] M. Kotschenreuther, X. Liu, D. Hatch, S. Mahajan, L. Zheng, A. Diallo, R. Groebner, the DIII-D TEAM, J. Hillesheim, C. Maggi, C. Giroud, F. Koechl, V. Parail, S. Saarelma, E. Solano, A. Chankin, and J. Contributors, "Gyrokinetic analysis and simulation of pedestals to identify the culprits for energy losses using 'fingerprints'", Nuclear Fusion **59**, 096001 (2019) (Cited on p. 55).

[81] J. W. Connor, R. J. Hastie, and J. B. Taylor, "Shear, Periodicity, and Plasma Ballooning Modes", Phys. Rev. Lett. **40**, 396 (1978) (Cited on pp. 56, 190).

[82] J. W. Connor, R. J. Hastie, and J. B. Taylor, "High mode number stability of an axisymmetric toroidal plasma", Proceedings of the Royal Society of London. A. Mathematical and Physical Sciences **365**, 1 (1979) (Cited on pp. 56, 190).

[83] L. Chen, M. Chance, and C. Cheng, "Absolute dissipative drift-wave instabilities in tokamaks", Nuclear Fusion **20**, 901 (1980) (Cited on pp. 56, 190).

[84] F. Jenko, D. Told, T. Görler, J. Citrin, A. Bañón Navarro, C. Bourdelle, S. Brunner, G. Conway, T. Dannert, H. Doerk, D. Hatch, J. Haverkort, J. Hobirk, G. Hogeweij, P. Mantica, M. Pueschel, O. Sauter, L. Villard, E. Wolfrum, and the ASDEX Upgrade Team, "Global and local gyrokinetic simulations of high-performance discharges in view of ITER", Nuclear Fusion **53**, 073003 (2013) (Cited on p. 56).

[85] W. L. Zhong, K. J. Zhao, X. L. Zou, and J. Q. Dong, "Recent progress on turbulence and multi-scale interactions in tokamak plasmas", Reviews of Modern Plasma Physics **4**, 11 (2020) (Cited on p. 56).

[86] D. R. Ernst, J. Lang, W. M. Nevins, M. Hoffman, Y. Chen, W. Dorland, and S. Parker, "Role of zonal flows in trapped electron mode turbulence through nonlinear gyrokinetic particle and continuum simulation", Physics of Plasmas **16**, 055906 (2009) (Cited on p. 56).

[87] P. Terry, D. Carmody, H. Doerk, W. Guttenfelder, D. Hatch, C. Hegna, A. Ishizawa, F. Jenko, W. Nevins, I. Predebon, M. Pueschel, J. Sarff, and G. Whelan, "Overview of gyrokinetic studies of finite-beta microturbulence", Nuclear Fusion **55**, 104011 (2015) (Cited on p. 57).

[88] J. Horton Wendell, D.-I. Choi, and W. M. Tang, "Toroidal drift modes driven by ion pressure gradients", The Physics of Fluids **24**, 1077 (1981) (Cited on p. 57).

[89] M. Kotschenreuther, W. Dorland, M. A. Beer, and G. W. Hammett, "Quantitative predictions of tokamak energy confinement from first-principles simulations with kinetic effects", Physics of Plasmas **2**, 2381 (1995) (Cited on p. 57).

[90] A. M. Dimits, G. Bateman, M. A. Beer, B. I. Cohen, W. Dorland, G. W. Hammett, C. Kim, J. E. Kinsey, M. Kotschenreuther, A. H. Kritz, L. L. Lao, J. Mandrekas, W. M. Nevins, S. E. Parker, A. J. Redd, D. E. Shumaker, R. Sydora, and J. Weiland, "Comparisons and physics basis of tokamak transport models and turbulence simulations", Physics of Plasmas **7**, 969 (2000) (Cited on pp. 57, 109).

[91] D. W. Ross and W. Dorland, "Comparing simulation of plasma turbulence with experiment. II. Gyrokinetic simulations", Physics of Plasmas **9**, 5031 (2002) (Cited on p. 57).

[92] R. Waltz, J. Candy, F. Hinton, C. Estrada-Mila, and J. Kinsey, "Advances in comprehensive gyrokinetic simulations of transport in tokamaks", Nuclear Fusion **45**, 741 (2005) (Cited on p. 57).

[93] X. Garbet, Y. Idomura, L. Villard, and T. Watanabe, "Gyrokinetic simulations of turbulent transport", Nuclear Fusion **50**, 043002 (2010) (Cited on pp. 57, 60).

[94] Y. IDOMURA, M. NAKATA, and S. JOLLIET, "Progress of Full-f Gyrokinetic Simulation Toward Reactor Relevant Numerical Experiments", Plasma and Fusion Research **9**, 3503028 (2014) (Cited on p. 57).

[95] T. Happel, T. Görler, P. Hennequin, C. Lechte, M. Bernert, G. D. Conway, S. J. Freethy, C. Honoré, J. R. Pinzón, U. Stroth, and T. A. U. Team, "Comparison of detailed experimental wavenumber spectra with gyrokinetic simulation aided by two-dimensional full-wave simulations", Plasma Physics and Controlled Fusion **59**, 054009 (2017) (Cited on p. 57).

[96] J. Y. Kim, W. Horton, and J. Q. Dong, "Electromagnetic effect on the toroidal ion temperature gradient mode", Physics of Fluids B: Plasma Physics **5**, 4030 (1993) (Cited on pp. 58, 135).

[97] S. C. Cowley, R. M. Kulsrud, and R. Sudan, "Considerations of ion-temperature-gradient-driven turbulence", Physics of Fluids B: Plasma Physics **3**, 2767 (1991) (Cited on p. 58).

[98] D. R. Ernst, B. Coppi, S. D. Scott, M. Porkolab, and T. Group, "Unifying Role of Radial Electric Field Shear in the Confinement Trends of TFTR Supershot Plasmas", Phys. Rev. Lett. **81**, 2454 (1998) (Cited on p. 58).

[99] J. E. Kinsey, R. E. Waltz, and J. Candy, "Nonlinear gyrokinetic turbulence simulations of ExB shear quenching of transport", Physics of Plasmas **12**, 062302 (2005) (Cited on pp. 58, 62, 135).

[100] G. Hammett, *Introduction to Gyrokinetic Theory and Simulations, ITER Summer School 2014*, (2014) https://w3.pppl.gov/~hammett/refs/2014/gk_intro/Hammett_2014_Gyrokinetic_Intro_ITER_Summer_School.pdf (Cited on p. 59).

[101] F. Jenko and W. Dorland, "Prediction of Significant Tokamak Turbulence at Electron Gyroradius Scales", Phys. Rev. Lett. **89**, 225001 (2002) (Cited on pp. 58, 98, 103).

[102] Y. C. Lee, J. Q. Dong, P. N. Guzdar, and C. S. Liu, "Collisionless electron temperature gradient instability", The Physics of Fluids **30**, 1331 (1987) (Cited on pp. 58, 98).

[103] X. Wei, V. Sokolov, and A. K. Sen, "Experimental production and identification of electron temperature gradient modes", Physics of Plasmas **17**, 042108 (2010) (Cited on p. 60).

[104] S. K. Singh, L. M. Awasthi, S. K. Mattoo, P. K. Srivastava, R. Singh, and P. K. Kaw, "Investigations on ETG turbulence in finite beta plasmas of LVPD", Plasma Physics and Controlled Fusion **54**, 124015 (2012) (Cited on p. 60).

[105] E.-j. Kim, C. Holland, and P. H. Diamond, "Collisional Damping of ETG-Mode-Driven Zonal Flows", Phys. Rev. Lett. **91**, 075003 (2003) (Cited on pp. 60, 99, 104, 106, 121).

[106] J. Y. Kim and W. Horton, "Electromagnetic effect on the toroidal electron temperature gradient mode", Physics of Fluids B: Plasma Physics **3**, 3194 (1991) (Cited on p. 60).

[107] Y. Ren, E. Belova, N. Gorelenkov, W. Guttenfelder, S. Kaye, E. Mazzucato, J. Peterson, D. Smith, D. Stutman, K. Tritz, W. Wang, H. Yuh, R. Bell, C. Domier, and B. LeBlanc, "Recent progress in understanding electron thermal transport in NSTX", Nuclear Fusion **57**, 072002 (2017) (Cited on pp. 60, 98, 125).

[108] G. J. Colyer, A. A. Schekochihin, F. I. Parra, C. M. Roach, M. A. Barnes, Y.-c. Ghim, and W. Dorland, "Collisionality scaling of the electron heat flux in ETG turbulence", Plasma Physics and Controlled Fusion **59**, 055002 (2017) (Cited on pp. 60, 98, 99, 104, 108, 118, 124, 127, 128).

[109] W. Guttenfelder, R. Groebner, J. Canik, B. Grierson, E. Belli, and J. Candy, "Testing predictions of electron scale turbulent pedestal transport in two DIII-D ELMy H-modes", Nuclear Fusion **61**, 056005 (2021) (Cited on p. 60).

[110] B. Chapman-Oplopoiou, D. Hatch, A. Field, L. Frassinetti, J. Hillesheim, L. Horvath, C. Maggi, J. Parisi, C. Roach, S. Saarelma, J. Walker, and J. Contributors, "The role of ETG modes in JET-ILW pedestals with varying levels of power and fuelling", Nuclear Fusion **62**, 086028 (2022) (Cited on p. 60).

[111] Y. Ren, W. Guttenfelder, S. M. Kaye, and W. X. Wang, "Transport from electron-scale turbulence in toroidal magnetic confinement devices", Reviews of Modern Plasma Physics **8**, 10.1007/s41614-023-00138-z (2024) (Cited on pp. 60, 98, 125).

[112] B. B. Kadomtsev and 0. P. Pogutse, "PLASMA INSTABILITY DUE TO PARTICLE TRAPPING IN A TOROIDAL GEOMETRY", J. Exptl. Theoret. Phys. **24** (1966) (Cited on p. 60).

[113] J. C. Adam, W. M. Tang, and P. H. Rutherford, "Destabilization of the trapped-electron mode by magnetic curvature drift resonances", The Physics of Fluids **19**, 561 (1976) (Cited on pp. 60, 110).

[114] Y. Xiao and Z. Lin, "Turbulent Transport of Trapped-Electron Modes in Collisionless Plasmas", Phys. Rev. Lett. **103**, 085004 (2009) (Cited on pp. 60, 110).

[115] W. Tang, J. Connor, and R. Hastie, "Kinetic-ballooning-mode theory in general geometry", Nuclear Fusion **20**, 1439 (1980) (Cited on p. 60).

[116] R. D. Hazeltine, D. Dobrott, and T. S. Wang, "Kinetic theory of tearing instability", The Physics of Fluids **18**, 1778 (1975) (Cited on p. 61).

[117] E. Hassan, D. Hatch, M. Halfmoon, M. Curie, M. Kotchenreuther, S. Mahajan, G. Merlo, R. Groebner, A. Nelson, and A. Diallo, "Identifying the microtearing modes in the pedestal of DIII-D H-modes using gyrokinetic simulations", Nuclear Fusion **62**, 026008 (2021) (Cited on pp. 61, 85, 87).

[118] K.-L. Wong, "A review of Alfvén eigenmode observations in toroidal plasmas", Plasma Physics and Controlled Fusion **41**, R1 (1999) (Cited on p. 61).

[119] J. Kim, J. Kang, T. Rhee, J. Jo, H. Han, M. Podestà, J. Lee, S. Lee, J. Bak, M. Choi, R. Nazikian, H. Jhang, J. Ko, M. Joung, Y.-M. Jeon, Y.-S. Na, K. Shinohara, and C. Cheng, "Suppression of toroidal Alfvén eigenmodes by the electron cyclotron current drive in KSTAR plasmas", Nuclear Fusion **62**, 026029 (2022) (Cited on p. 61).

[120] P. H. Diamond, S.-I. Itoh, K. Itoh, and T. S. Hahm, "Zonal flows in plasma—a review", Plasma Physics and Controlled Fusion **47**, R35 (2005) (Cited on pp. 61, 62, 99).

[121] B. B. Kadomtsev, *Plasma turbulence* (Academic Press, 1965) (Cited on pp. 61, 80).

[122] T. H. Dupree, "Nonlinear Theory of Drift-Wave Turbulence and Enhanced Diffusion", The Physics of Fluids **10**, 1049 (1967) (Cited on pp. 61, 80).

[123] P. W. Terry, "Suppression of turbulence and transport by sheared flow", Rev. Mod. Phys. **72**, 109 (2000) (Cited on p. 62).

[124] A. E. White, L. Schmitz, G. R. McKee, C. Holland, W. A. Peebles, T. A. Carter, M. W. Shafer, M. E. Austin, K. H. Burrell, J. Candy, J. C. DeBoo, E. J. Doyle, M. A. Makowski, R. Prater, T. L. Rhodes, G. M. Staebler, G. R. Tynan, R. E. Waltz, and G. Wang, "Measurements of core electron temperature and density fluctuations in DIII-D and comparison to nonlinear gyrokinetic simulationsa)", Physics of Plasmas **15**, 056116 (2008) (Cited on p. 62).

[125] C. Lechte, G. D. Conway, T. Görler, C. Tröster-Schmid, and the ASDEX Upgrade Team, "X mode Doppler reflectometry k-spectral measurements in ASDEX Upgrade: experiments and simulations", Plasma Physics and Controlled Fusion **59**, 075006 (2017) (Cited on p. 62).

[126] A. J. Creely, N. T. Howard, P. Rodriguez-Fernandez, N. Cao, A. E. Hubbard, J. W. Hughes, J. E. Rice, A. E. White, J. Candy, G. M. Staebler, G. D. Conway, S. J. Freethy, and C. Sung, "Validation of nonlinear gyrokinetic simulations of L- and I-mode plasmas on Alcator C-Mod", Physics of Plasmas **24**, 056104 (2017) (Cited on p. 62).

[127] S. J. Freethy, T. Görler, A. J. Creely, G. D. Conway, S. S. Denk, T. Happel, C. Koenen, P. Hennequin, A. E. White, and A. U. Team, "Validation of gyrokinetic simulations with measurements of electron temperature fluctuations and density-temperature phase angles on ASDEX Upgrade", Physics of Plasmas **25**, 055903 (2018) (Cited on p. 62).

[128] R. E. Waltz and E. M. Bass, *Gyrokinetic Simulation of Energetic Particles*, tech. rep., https://doi.org/10.2172/1414579 (General Atomics, San Diego, CA (United States), 2017) (Cited on p. 62).

[129] S. Taimourzadeh, E. Bass, Y. Chen, C. Collins, N. Gorelenkov, A. Könies, Z. Lu, D. Spong, Y. Todo, M. Austin, J. Bao, A. Biancalani, M. Borchardt, A. Bottino, W. Heidbrink, R. Kleiber, Z. Lin, A. Mishchenko, L. Shi, J. Varela, R. Waltz, G. Yu, W. Zhang, and Y. Zhu, "Verification and validation of integrated simulation of energetic particles in fusion plasmas", Nuclear Fusion **59**, 066006 (2019) (Cited on p. 62).

[130] A. D. Gurchenko and E. Z. Gusakov, "Evolution of ETG mode scale turbulence and anomalous electron transport in dynamic tokamak experiments", Plasma Physics and Controlled Fusion **52**, 124035 (2010) (Cited on pp. 62, 125).

[131] A. Casati, T. Gerbaud, P. Hennequin, C. Bourdelle, J. Candy, F. Clairet, X. Garbet, V. Grandgirard, Ö. D. Gürcan, S. Heuraux, G. T. Hoang, C. Honoré, F. Imbeaux, R. Sabot, Y. Sarazin, L. Vermare, and R. E. Waltz, "Turbulence in the TORE SUPRA Tokamak: Measurements and Validation of Nonlinear Simulations", Phys. Rev. Lett. **102**, 165005 (2009) (Cited on p. 62).

[132] A. E. White, W. A. Peebles, T. L. Rhodes, C. H. Holland, G. Wang, L. Schmitz, T. A. Carter, J. C. Hillesheim, E. J. Doyle, L. Zeng, G. R. McKee, G. M. Staebler, R. E. Waltz, J. C. DeBoo, C. C. Petty, and K. H. Burrell, "Measurements of the cross-phase angle between density and electron temperature fluctuations and comparison with gyrokinetic simulationsa)", Physics of Plasmas **17**, 056103 (2010) (Cited on p. 62).

[133] C. Holland, L. Schmitz, T. L. Rhodes, W. A. Peebles, J. C. Hillesheim, G. Wang, L. Zeng, E. J. Doyle, S. P. Smith, R. Prater, K. H. Burrell, J. Candy, R. E. Waltz, J. E. Kinsey, G. M. Staebler, J. C. DeBoo, C. C. Petty, G. R. McKee, Z. Yan, and A. E. White, "Advances in validating gyrokinetic turbulence models against L- and H-mode plasmas a)", Physics of Plasmas **18**, 056113 (2011) (Cited on p. 62).

[134] C. Holland, C. Petty, L. Schmitz, K. Burrell, G. McKee, T. Rhodes, and J. Candy, "Progress in GYRO validation studies of DIII-D H-mode plasmas", Nuclear Fusion **52**, 114007 (2012) (Cited on p. 62).

[135] C. Holland, J. DeBoo, T. Rhodes, L. Schmitz, J. Hillesheim, G. Wang, A. White, M. Austin, E. Doyle, W. Peebles, C. Petty, L. Zeng, and J. Candy, "Testing gyrokinetic simulations of electron turbulence", Nuclear Fusion **52**, 063028 (2012) (Cited on p. 62).

[136] A. E. White, N. T. Howard, M. Greenwald, M. L. Reinke, C. Sung, S. Baek, M. Barnes, J. Candy, A. Dominguez, D. Ernst, C. Gao, A. E. Hubbard, J. W. Hughes, Y. Lin, D. Mikkelsen, F. Parra, M. Porkolab, J. E. Rice, J. Walk, S. J. Wukitch, and A. C.-M. Team, "Multi-channel transport experiments at Alcator C-Mod and comparison with gyrokinetic simulationsa)", Physics of Plasmas **20**, 056106 (2013) (Cited on pp. 62, 125).

[137] T. Görler, A. E. White, D. Told, F. Jenko, C. Holland, and T. L. Rhodes, "A flux-matched gyrokinetic analysis of DIII-D L-mode turbulence", Physics of Plasmas **21**, 122307 (2014) (Cited on p. 62).

[138] A. B. Navarro, T. Happel, T. Görler, F. Jenko, J. Abiteboul, A. Bustos, H. Doerk, D. Told, and A. U. Team, "Gyrokinetic studies of core turbulence features in ASDEX Upgrade H-mode plasmas", Physics of Plasmas **22**, 042513 (2015) (Cited on p. 62).

[139] J. Candy, E. Belli, and R. Bravenec, "A high-accuracy Eulerian gyrokinetic solver for collisional plasmas", Journal of Computational Physics **324**, 73 (2016) (Cited on p. 62).

[140] Y. Chen and S. Parker, "A gyrokinetic ion zero electron inertia fluid electron model for turbulence simulations", Physics of Plasmas **8**, 441 (2001) (Cited on pp. 63, 69).

[141] S.-H. Ku, R. Hager, A. Scheinberg, J. Dominski, A. Sharma, M. Churchill, J. Choi, B. Sturdevant, A. Mollén, G. Wilkie, C.-S. Chang, E. Yoon, M. Adams, J. Seo, S. Koh, E. D'Azevedo, S. Abbott, P. H. Worley, S. Ethier, G. Park, J. Lang, B. MacKie-Mason, K. Germaschewski, E. Suchyta, V. Carey, M. Cole, P. Trivedi, and J. Chowdhury, *XGC*, [Computer Software] https://doi.org/10.11578/dc.20180627.11, 2018 (Cited on p. 63).

[142] V. Grandgirard, Y. Sarazin, X. Garbet, G. Dif-Pradalier, P. Ghendrih, N. Crouseilles, G. Latu, E. Sonnendrücker, N. Besse, and P. Bertrand, "GYSELA, a full-f global gyrokinetic Semi-Lagrangian code for ITG turbulence simulations", AIP Conference Proceedings **871**, 100 (2006) (Cited on p. 63).

[143] R. V. Bravenec, J. Candy, M. Barnes, and C. Holland, "Linear and nonlinear verification of gyrokinetic microstability codes", Physics of Plasmas **18**, 122505 (2011) (Cited on p. 63).

[144] Y. Chen, S. E. Parker, W. Wan, and R. Bravenec, "Benchmarking gyrokinetic simulations in a toroidal flux-tube", Physics of Plasmas **20**, 092511 (2013) (Cited on p. 63).

[145] T. Görler, N. Tronko, W. A. Hornsby, A. Bottino, R. Kleiber, C. Norscini, V. Grandgirard, F. Jenko, and E. Sonnendrücker, "Intercode comparison of gyrokinetic global electromagnetic modes", Physics of Plasmas **23**, 072503 (2016) (Cited on pp. 63, 109–111, 132).

[146] G. Merlo, J. Dominski, A. Bhattacharjee, C. S. Chang, F. Jenko, S. Ku, E. Lanti, and S. Parker, "Cross-verification of the global gyrokinetic codes GENE and XGC", Physics of Plasmas **25**, 062308 (2018) (Cited on p. 63).

[147] E. Hassan, D. R. Hatch, W. Guttenfelder, Y. Chen, and S. Parker, "Gyrokinetic benchmark of the electron temperature-gradient instability in the pedestal region", Physics of Plasmas **28**, 062505 (2021) (Cited on pp. 63, 85).

[148] F. Jenko and The GENE Development Team, *The GENE Code*, `https://genecode.org` (Cited on pp. 64, 109, 111, 112).

[149] F. Merz, "Gyrokinetic Simulation of Multimode Plasma Turbulence", PhD thesis (Universität Münster, 2008) (Cited on pp. 64, 67).

[150] D. Told, "Gyrokinetic Microturbulence in Transport Barries", PhD thesis (Universität Ulm, 2012) (Cited on p. 64).

[151] G. Merlo, "Flux-tube and global grid-based gyrokinetic simulations of plasma microturbulence and comparisons with experimental TCV measurements", PhD thesis (École Polytechnique Fédérale de Lausanne, 2015) (Cited on p. 64).

[152] A. Arakawa, "Computational design for long-term numerical integration of the equations of fluid motion: Two-dimensional incompressible flow. Part I", Journal of Computational Physics **1**, 119 (1966) (Cited on p. 66).

[153] S. A. Orszag, "On the elimination of aliasing in finite-difference schemes by filtering high-wavenumber components", Journal of Atmospheric Sciences **28**, 1074 (1971) (Cited on p. 67).

[154] J. Patterson G. S. and S. A. Orszag, "Spectral Calculations of Isotropic Turbulence: Efficient Removal of Aliasing Interactions", The Physics of Fluids **14**, 2538 (1971) (Cited on p. 67).

[155] P. Crandall, D. Jarema, H. Doerk, Q. Pan, G. Merlo, T. Görler, A. B. Navarro, D. Told, M. Maurer, and F. Jenko, "Multi-species collisions for delta-f gyrokinetic simulations: Implementation and verification with GENE", Computer Physics Communications **255**, 107360 (2020) (Cited on p. 67).

[156] Y. Chen, *GEM User Manual*, `http://www.gemgyrokinetic.org` (Cited on pp. 69, 70).

[157] Y. Chen and S. Parker, "Gyrokinetic turbulence simulations with kinetic electrons", Physics of Plasmas **8**, 2095 (2001) (Cited on pp. 69, 72).

[158] Y. Chen and S. E. Parker, "A delta-f particle method for gyrokinetic simulations with kinetic electrons and electromagnetic perturbations", Journal of Computational Physics **189**, 463 (2003) (Cited on pp. 69, 72, 137).

[159] Y. Chen and S. E. Parker, "Electromagnetic gyrokinetic delta-f particle-in-cell turbulence simulation with realistic equilibrium profiles and geometry", Journal of Computational Physics **220**, 839 (2007) (Cited on pp. 69, 137, 138).

[160] Y. Chen, J. Cheng, and S. E. Parker, "Effects of the heat source on the steady-state transport in gradient-driven global gyrokinetic simulations", Physics of Plasmas **30**, 014502 (2023) (Cited on pp. 69, 74, 138).

[161] Y. Chen, J. Cheng, and S. E. Parker, "Evolution of the marker distribution in gyrokinetic delta-f particle-in-cell simulations", Physics of Plasmas **29**, 073901 (2022) (Cited on pp. 69, 91).

[162] M. Kotschenreuther, "Numerical simulation", Bull. Am. Phys. Soc **33**, 2107 (1988) (Cited on p. 69).

[163] S. E. Parker and W. W. Lee, "A fully nonlinear characteristic method for gyrokinetic simulation", Physics of Fluids B: Plasma Physics **5**, 77 (1993) (Cited on p. 69).

[164] T. S. Hahm, W. W. Lee, and A. Brizard, "Nonlinear gyrokinetic theory for finite-beta plasmas", The Physics of Fluids **31**, 1940 (1988) (Cited on p. 70).

[165] I. Manuilskiy and W. W. Lee, "The split-weight particle simulation scheme for plasmas", Physics of Plasmas **7**, 1381 (2000) (Cited on p. 72).

[166] S. E. Parker, C. S. Haubrich, S. Tirkas, Q. Cai, and Y. Chen, "Comparison of Saturation Rules Used for Gyrokinetic Quasilinear Transport Modeling", Plasma **6**, 611 (2023) (Cited on pp. 76, 81, 83, 85).

[167] C. Haubrich, "Quasilinear Analysis in Positive and Negative Triangularity", Bachelor's Thesis (University of Colorado Boulder, 2024) (Cited on pp. 76, 85).

[168] G. Staebler, J. Kinsey, and R. Waltz, "A theory-based transport model with comprehensive physics", Physics of Plasmas **14**, 055909 (2007) (Cited on pp. 81, 84).

[169] X. Lapillonne, S. Brunner, O. Sauter, L. Villard, E. Fable, T. Görler, F. Jenko, and F. Merz, "Non-linear gyrokinetic simulations of microturbulence in TCV electron internal transport barriers", Plasma Physics and Controlled Fusion **53**, 054011 (2011) (Cited on pp. 81, 82, 84, 120, 145).

[170] E. Fable, C. Angioni, and O. Sauter, "The role of ion and electron electrostatic turbulence in characterizing stationary particle transport in the core of tokamak plasmas", Plasma Phys. Control. Fusion **52**, 015007 (2010) (Cited on pp. 82, 84, 120, 145).

[171] J. E. Kinsey, G. M. Staebler, J. Candy, C. C. Petty, T. L. Rhodes, and R. E. Waltz, "Predictions of the near edge transport shortfall in DIII-D L-mode plasmas using the trapped gyro-Landau-fluid model", Physics of Plasmas **22**, 012507 (2015) (Cited on pp. 82, 84).

[172] S. E. Parker, W. Dorland, R. A. Santoro, M. A. Beer, Q. P. Liu, W. W. Lee, and G. W. Hammett, "Comparisons of gyrofluid and gyrokinetic simulations*", Physics of Plasmas **1**, 1461 (1994) (Cited on pp. 83, 99).

[173] C. Bourdelle, X. Garbet, F. Imbeaux, A. Casati, N. Dubuit, R. Guirlet, and T. Parisot, "A new gyrokinetic quasilinear transport model applied to particle transport in tokamak plasmas", Physics of Plasmas **14**, 112501 (2007) (Cited on pp. 83, 84, 99, 121).

[174] N. Kumar, Y. Camenen, S. Benkadda, C. Bourdelle, A. Loarte, A. Polevoi, F. Widmer, and J. contributors, "Turbulent transport driven by kinetic ballooning modes in the inner core of JET hybrid H-modes", Nuclear Fusion **61**, 036005 (2021) (Cited on p. 83).

[175] T. Dannert and F. Jenko, "Gyrokinetic simulation of collisionless trapped-electron mode turbulence", Physics of Plasmas **12**, 072309 (2005) (Cited on pp. 84, 99, 110, 121).

[176] G. Staebler, J. Kinsey, and R. Waltz, "Gyro-Landau fluid equations for trapped and passing particles", Physics of Plasmas **12**, 102508 (2005) (Cited on p. 84).

[177] G. Staebler, J. Candy, N. T. Howard, and C. Holland, "The role of zonal flows in the saturation of multi-scale gyrokinetic turbulence", Physics of Plasmas **23**, 062518 (2016) (Cited on pp. 84, 127).

[178] J. Kinsey, C. Singer, D. Cox, and G. Bateman, "Systematic comparison of a theory-based transport model with a multi-tokamak profile database", Physica Scripta **52**, 428 (1995) (Cited on p. 84).

[179] G. Bateman, A. Kritz, J. Kinsey, A. Redd, and J. Weiland, "Predicting temperature and density profiles in tokamaks", Physics of Plasmas **5**, 1793 (1998) (Cited on p. 84).

[180] T. Rafiq, A. Kritz, J. Weiland, A. Pankin, and L. Luo, "Physics basis of Multi-Mode anomalous transport module", Physics of Plasmas **20**, 10.1063/1.4794288 (2013) (Cited on p. 84).

[181] J. Weiland, A. Zagorodny, and T. Rafiq, "Theory for transport in magnetized plasmas", Physica Scripta **95**, 105607 (2020) (Cited on p. 84).

[182] C. Bourdelle, J. Citrin, B. Baiocchi, A. Casati, P. Cottier, X. Garbet, F. Imbeaux, et al., "Core turbulent transport in tokamak plasmas: bridging theory and experiment with QuaLiKiz", Plasma Phys. Control. Fusion **58**, 014036 (2016) (Cited on p. 84).

[183] J. Citrin, C. Bourdelle, F. J. Casson, C. Angioni, N. Bonanomi, Y. Camenen, X. Garbet, L. Garzotti, T. Görler, O. Gürcan, F. Koechl, F. Imbeaux, O. Linder, K. van de Plassche, P. Strand, G. Szepesi, and J. Contributors, "Tractable flux-driven temperature, density, and rotation profile evolution with the quasilinear gyrokinetic transport model QuaLiKiz", Plasma Phys. Control. Fusion **59**, 124005 (2017) (Cited on p. 84).

[184] C. Stephens, X. Garbet, J. Citrin, C. Bourdelle, K. van de Plassche, and F. Jenko, "Quasilinear gyrokinetic theory: a derivation of QuaLiKiz", Journal of Plasma Physics **87**, 10.1017/S0022377821000763 (2021) (Cited on p. 84).

[185] C. Angioni, E. Fable, M. Greenwald, M. Maslov, A. Peeters, H. Takenaga, and H. Weisen, "Particle transport in tokamak plasmas, theory and experiment", Plasma Physics and Controlled Fusion **51**, 124017 (2009) (Cited on p. 84).

[186] N. Howard, C. Holland, T. Rhodes, J. Candy, P. Rodriguez-Fernandez, M. Greenwald, A. White, and F. Sciortino, "The role of ion and electron-scale turbulence in setting heat and particle transport in the DIII-D ITER baseline scenario", Physics of Plasmas **28**, 072502 (2021) (Cited on pp. 84, 125).

[187] C. Angioni, R. Bilato, F. Casson, E. Fable, P. Mantica, T. Odstrcil, M. Valisa, ASDEX Upgrade Team, and JET Contributors, "Gyrokinetic study of turbulent convection of heavy impurities in tokamak plasmas at comparable ion and electron heat fluxes", Nuclear Fusion **57**, 022009 (2017) (Cited on p. 84).

[188] A. Loarte, *Required R & D in existing fusion facilities to support the ITER research plan*, tech. rep. ITR-20-008 (ITER Organization, 2020) (Cited on p. 84).

[189] J. Candy and R. Waltz, "An Eulerian gyrokinetic-Maxwell solver", Journal of Computational Physics **186**, 545 (2003) (Cited on p. 84).

[190] M. Curie, J. Larakers, D. Hatch, A. Nelson, A. Diallo, E. Hassan, W. Guttenfelder, M. Halfmoon, M. Kotschenreuther, R. Hazeltine, S. Mahajan, R. Groebner, J. Chen, D.-D. Team, C. P. von Thun, L. Frassinetti, S. Saarelma, C. Giroud, J. Contributors, and M. Tennery, "A survey of pedestal magnetic fluctuations using gyrokinetics and a global reduced model for microtearing stability", Physics of Plasmas **29**, 042503 (2022) (Cited on p. 85).

[191] L. Lao, H. St. John, R. Stambaugh, A. Kellman, and W. Pfeiffer, "Reconstruction of current profile parameters and plasma shapes in tokamaks", Nuclear Fusion **25**, 1611 (1985) (Cited on p. 85).

[192] C. Greenfield, J. DeBoo, T. Osborne, F. Perkins, M. Rosenbluth, and B. D., "Enhanced fusion performance due to plasma shape modification of simulated ITER discharges in DIII-D", Nuclear Fusion **37**, 1215 (1997) (Cited on pp. 87, 109).

[193] A. Marinoni, S. Brunner, Y. Camenen, S. Coda, J. P. Graves, X. Lapillonne, A. Pochelon, O. Sauter, and L. Villard, "The effect of plasma triangularity on turbulent transport: modeling TCV experiments by linear and non-linear gyrokinetic simulations", Plasma Physics and Controlled Fusion **51**, 055016 (2009) (Cited on p. 94).

[194] G. Merlo, S. Brunner, O. Sauter, Y. Camenen, T. Görler, F. Jenko, A. Marinoni, D. Told, and L. Villard, "Investigating profile stiffness and critical gradients in shaped TCV discharges using local gyrokinetic simulations of turbulent transport", Plasma Physics and Controlled Fusion **57**, 054010 (2015) (Cited on p. 94).

[195] G. Merlo, M. Fontana, S. Coda, D. Hatch, S. Janhunen, L. Porte, and F. Jenko, "Turbulent transport in TCV plasmas with positive and negative triangularity", Physics of Plasmas **26**, 102302 (2019) (Cited on p. 94).

[196] J. M. Duff, B. J. Faber, C. C. Hegna, M. J. Pueschel, and P. W. Terry, "Effect of triangularity on ion-temperature-gradient-driven turbulence", Physics of Plasmas **29**, 012303 (2022) (Cited on p. 95).

[197] S. Tirkas, H. Chen, G. Merlo, F. Jenko, and S. Parker, "Zonal flow excitation in electron-scale tokamak turbulence", Nuclear Fusion **63**, 026015 (2023) (Cited on pp. 98, 104, 127, 128).

[198] W. M. Nevins, J. Candy, S. Cowley, T. Dannert, A. Dimits, W. Dorland, C. Estrada-Mila, G. W. Hammett, F. Jenko, M. J. Pueschel, and D. E. Shumaker, "Characterizing electron temperature gradient turbulence via numerical simulation", Physics of Plasmas **13**, 122306 (2006) (Cited on pp. 98, 124).

[199] B. A. Grierson, G. M. Staebler, W. M. Solomon, G. R. McKee, C. Holland, M. Austin, A. Marinoni, L. Schmitz, R. I. Pinsker, and D.-D. Team, "Multi-scale transport in the DIII-D ITER baseline scenario with direct electron heating and projection to ITER", Physics of Plasmas **25**, 022509 (2018) (Cited on p. 98).

[200] F. Ryter, C. Angioni, M. Dunne, R. Fischer, B. Kurzan, A. Lebschy, R. McDermott, W. Suttrop, G. Tardini, E. Viezzer, M. Willensdorfer, and the ASDEX Upgrade Team, "Heat transport driven by the ion temperature gradient and electron temperature gradient instabilities in ASDEX Upgrade H-modes", Nuclear Fusion **59**, 096052 (2019) (Cited on pp. 98, 125).

[201] C. Kiefer, C. Angioni, G. Tardini, N. Bonanomi, B. Geiger, P. Mantica, T. Pütterich, E. Fable, P. Schneider, A. U. Team, E. M. Team, and J. Contributors, "Validation of quasi-linear turbulent transport models against plasmas with dominant electron heating for the prediction of ITER PFPO-1 plasmas", Nuclear Fusion **61**, 066035 (2021) (Cited on pp. 98, 125).

[202] S. E. Parker, J. J. Kohut, Y. Chen, Z. Lin, F. L. Hinton, and W. W. Lee, "Fine-Scale Zonal Flow Suppression of Electron Temperature Gradient Turbulence", AIP Conference Proceedings **871**, 193 (2006) (Cited on pp. 98, 99, 104, 108, 124).

[203] A. Hasegawa and K. Mima, "Stationary Spectrum of Strong Turbulence in Magnetized Nonuniform Plasma", Phys. Rev. Lett. **39**, 205 (1977) (Cited on pp. 99, 100).

[204] A. Hasegawa, C. G. Maclennan, and Y. Kodama, "Nonlinear behavior and turbulence spectra of drift waves and Rossby waves", The Physics of Fluids **22**, 2122 (1979) (Cited on pp. 99, 102).

[205] Z. Lin, L. Chen, and F. Zonca, "Role of nonlinear toroidal coupling in electron temperature gradient turbulence a)", Physics of Plasmas **12**, 056125 (2005) (Cited on pp. 99, 104, 107, 113, 121).

[206] L. Chen, F. Zonca, and Z. Lin, "Nonlinear toroidal mode coupling: a new paradigm for drift wave turbulence in toroidal plasmas", Plasma Physics and Controlled Fusion **47**, B71 (2005) (Cited on pp. 99, 104, 107, 108, 113, 121).

[207] F. Jenko, T. Dannert, and C. Angioni, "Heat and particle transport in a tokamak: advances in nonlinear gyrokinetics", Plasma Physics and Controlled Fusion **47**, B195 (2005) (Cited on pp. 99, 121).

[208] J.-Y. Kim and W. Horton, "Transition from toroidal to slab temperature gradient driven modes", Physics of Fluids B: Plasma Physics **3**, 1167 (1991) (Cited on p. 105).

[209] M. N. Rosenbluth and F. L. Hinton, "Poloidal Flow Driven by Ion-Temperature-Gradient Turbulence in Tokamaks", Phys. Rev. Lett. **80**, 724 (1998) (Cited on p. 106).

[210] P. Ricci, B. N. Rogers, and W. Dorland, "Collisional damping of zonal flows due to finite Larmor radius effects", Physics of Plasmas **17**, 072103 (2010) (Cited on p. 106).

[211] L. Chen, Z. Lin, and R. White, "Excitation of zonal flow by drift waves in toroidal plasmas", Physics of Plasmas **7**, 3129 (2000) (Cited on p. 106).

[212] X. Lapillonne, S. Brunner, T. Dannert, S. Jolliet, A. Marinoni, L. Villard, T. Görler, F. Jenko, and F. Merz, "Clarifications to the limitations of the s-alpha equilibrium model for gyrokinetic computations of turbulence", Physics of Plasmas **16**, 032308 (2009) (Cited on p. 109).

[213] G. Rewoldt, Z. Lin, and Y. Idomura, "Linear comparison of gyrokinetic codes with trapped electrons", Computer Physics Communications **177**, 775 (2007) (Cited on p. 110).

[214] H.-T. Chen and L. Chen, "Effects of radial envelope modulations on the collisionless trapped-electron mode in tokamak plasmas", Plasma Physics and Controlled Fusion **60**, 055011 (2018) (Cited on p. 110).

[215] H. Chen and L. Chen, "On the cascading of collisionless trapped-electron mode turbulence in tokamak plasmas", Nuclear Fusion **59**, 074003 (2019) (Cited on p. 110).

[216] D. Strintzi and F. Jenko, "On the relation between secondary and modulational instabilities", Physics of Plasmas **14**, 042305 (2007) (Cited on p. 115).

[217] H. Chen and L. Chen, "How Zonal Flow Affects Trapped-Electron-Driven Turbulence in Tokamak Plasmas", Phys. Rev. Lett. **128**, 025003 (2022) (Cited on p. 116).

[218] N. T. Howard, C. Holland, A. E. White, M. Greenwald, J. Candy, and A. J. Creely, "Multi-scale gyrokinetic simulations: Comparison with experiment and implications for predicting turbulence and transport", Physics of Plasmas **23**, 056109 (2016) (Cited on pp. 124–127, 136).

[219] S. Tirkas, Y. Chen, and S. Parker, "A subgrid model for electron-scale turbulent transport in global ion-scale gyrokinetic simulations of tokamak plasmas", Physics of Plasmas **32**, 032504 (2025) (Cited on p. 125).

[220] N. Howard, A. White, M. Reinke, M. Greenwald, C. Holland, J. Candy, and J. Walk, "Validation of the gyrokinetic model in ITG and TEM dominated L-mode plasmas", Nuclear Fusion **53**, 123011 (2013) (Cited on p. 125).

[221] I. Chapman, J. Adamek, R. Akers, S. Allan, L. Appel, O. Asunta, M. Barnes, N. B. Ayed, T. Bigelow, W. Boeglin, et al., "Overview of MAST results", Nuclear Fusion **55**, 104008 (2015) (Cited on p. 125).

[222] N. T. Howard, C. Holland, A. E. White, M. Greenwald, P. Rodriguez-Fernandez, J. Candy, and A. J. Creely, "Multi-scale gyrokinetic simulations of an Alcator C-Mod, ELM-y H-mode plasma", Plasma Physics and Controlled Fusion **60**, 014034 (2017) (Cited on p. 125).

[223] F. Jenko, "On the nature of ETG turbulence and cross-scale coupling", J. Plasma Fusion Res. SERIES **6**, 11 (2004) (Cited on pp. 125, 127).

[224] S. Maeyama, Y. Idomura, T.-H. Watanabe, M. Nakata, M. Yagi, N. Miyato, A. Ishizawa, and M. Nunami, "Cross-Scale Interactions between Electron and Ion Scale Turbulence in a Tokamak Plasma", Phys. Rev. Lett. **114**, 255002 (2015) (Cited on pp. 125, 127, 132).

[225] N. Bonanomi, P. Mantica, J. Citrin, T. Goerler, B. Teaca, and J. Contributors, "Impact of electron-scale turbulence and multi-scale interactions in the JET tokamak", Nuclear Fusion **58**, 124003 (2018) (Cited on pp. 125, 136).

[226] S. Maeyama, N. Howard, J. Citrin, T.-H. Watanabe, and T. Tokuzawa, "Overview of multiscale turbulence studies covering ion-to-electron scales in magnetically confined fusion plasma", Nuclear Fusion **64**, 112007 (2024) (Cited on p. 126).

[227] S.-I. Itoh, K. Itoh, M. Yagi, M. Kawasaki, and A. Kitazawa, "Transition in multiple-scale-lengths turbulence in plasmas", Physics of Plasmas **9**, 1947 (2002) (Cited on p. 127).

[228] C. Holland and P. Diamond, "On the dynamics of large-scale structures in electron temperature gradient turbulence", Physics Letters A **344**, 369 (2005) (Cited on p. 127).

[229] D. R. Hatch, C. Michoski, D. Kuang, B. Chapman-Oplopoiou, M. Curie, M. Halfmoon, E. Hassan, M. Kotschenreuther, S. M. Mahajan, G. Merlo, M. J. Pueschel, J. Walker, and C. D. Stephens, "Reduced models for ETG transport in the tokamak pedestal", Physics of Plasmas **29**, 062501 (2022) (Cited on p. 127).

[230] M. R. Hardman, M. Barnes, C. M. Roach, and F. I. Parra, "A scale-separated approach for studying coupled ion and electron scale turbulence", Plasma Physics and Controlled Fusion **61**, 065025 (2019) (Cited on pp. 127, 128, 150).

[231] M. R. Hardman, M. Barnes, and C. M. Roach, "Stabilisation of short-wavelength instabilities by parallel-to-the-field shear in long-wavelength E × B flows", Journal of Plasma Physics **86**, 905860601 (2020) (Cited on p. 127).

[232] J. Lang and G.-Y. Fu, "Nonlinear simulation of toroidal Alfvén eigenmode with microturbulence-induced radial diffusiona)", Physics of Plasmas **18**, 055902 (2011) (Cited on p. 131).

[233] R. E. Waltz, "Nonlinear subcritical magnetohydrodynamic beta limit", Physics of Plasmas **17**, 072501 (2010) (Cited on p. 136).

[234] T.-H. Watanabe, S. Maeyama, and M. Nakata, "Stabilization of trapped electron mode through effective diffusion in electron temperature gradient turbulence", Nuclear Fusion **63**, 054001 (2023) (Cited on p. 139).

[235] E. A. Belli, J. Candy, and I. Sfiligoi, "Spectral transition of multiscale turbulence in the tokamak pedestal", Plasma Physics and Controlled Fusion **65**, 024001 (2022) (Cited on p. 150).

[236] A. S. Richardson, *2019 NRL Plasma Formulary* (Naval Research Laboratory, 2019) (Cited on p. 174).

[237] P. M. Morse and H. Feshbach, *Methods of theoretical physics* (McGraw-Hill, 1953) (Cited on p. 174).

[238] I. S. Gradshteyn and I. M. Ryzhik, *Table of integrals, series, and products*, Seventh, Translated from the Russian, Translation edited and with a preface by Alan Jeffrey and Daniel Zwillinger, With one CD-ROM (Windows, Macintosh and UNIX) (Elsevier/Academic Press, Amsterdam, 2007), pp. xlviii+1171 (Cited on p. 189).

Appendix A

Complex Notation

A.1 Drift Wave Flux

Waves in the plasma can be described as complex oscillations, so that one can assume a Fourier mode decomposition

$$A(x, \boldsymbol{k}, t) = \widetilde{A}_{\boldsymbol{k}} e^{-i\omega t + i\boldsymbol{k}\cdot\boldsymbol{x}}, \tag{A.1}$$

where $\widetilde{A}_{0,\boldsymbol{k}}$ is a complex number that can be generally represented as,

$$\widetilde{A}_{\boldsymbol{k}} = \widetilde{A}_{0,\boldsymbol{k}} e^{i\psi}, \quad \widetilde{A}_{\boldsymbol{k}} \in \mathbb{R}\,. \tag{A.2}$$

In Equation (2.27) one is interested only in the real parts of the transport fluxes. In dealing with complex wave notation, one can choose to use the notation expressed in Equation (2.25) to find

$$\mathbb{R}e\{A\} = \frac{1}{2}(\widetilde{A} + c.c.) = \frac{1}{2}(\widetilde{A} + \widetilde{A}^*) = \frac{1}{2}(\widetilde{A}_{\boldsymbol{k}} e^{-i\omega t + i\boldsymbol{k}\cdot\boldsymbol{x}} + \widetilde{A}^*_{\boldsymbol{k}} e^{i\omega t - i\boldsymbol{k}\cdot\boldsymbol{x}}), \tag{A.3}$$

Dropping the $\boldsymbol{k}$ subscript for simplicity, one finds that the nonlinear term in Equation (2.27) becomes

$$\begin{aligned}
\widetilde{f}(-\nabla_\theta\widetilde{\Phi}) &= \frac{1}{4}(\widetilde{f} + \widetilde{f}^*)(-\nabla_\theta(\widetilde{\Phi} + \widetilde{\Phi}^*)) = ik_\theta \frac{1}{4}(\widetilde{f} + \widetilde{f}^*)(\widetilde{\Phi}^* - \widetilde{\Phi}) \\
&= ik_\theta \frac{1}{4}[(A_0 e^{i\psi} e^{-i\omega t + i\boldsymbol{k}\cdot\boldsymbol{x}} + A_0 e^{-i\psi} e^{i\omega t - i\boldsymbol{k}\cdot\boldsymbol{x}})(B_0 e^{-i\phi} e^{i\omega t - i\boldsymbol{k}\cdot\boldsymbol{x}} - B_0 e^{i\phi} e^{-i\omega t + i\boldsymbol{k}\cdot\boldsymbol{x}})] \\
&= ik_\theta \frac{A_0 B_0}{4}[(e^{i(\psi-\phi)} - e^{-i(\psi-\phi)}) + (e^{i[2(\omega t - \boldsymbol{k}\cdot\boldsymbol{x}) - (\psi+\phi)]} - e^{-i[2(\omega t - \boldsymbol{k}\cdot\boldsymbol{x}) - (\psi+\phi)]})] \\
&= ik_\theta \frac{A_0 B_0}{2}[i\sin(\psi - \phi) + i\sin(2(\omega t - \boldsymbol{k}\cdot\boldsymbol{x}) - (\psi - \phi))]\,,
\end{aligned} \tag{A.4}$$

where $\widetilde{f}$ and $\widetilde{\Phi}$ have been represented using (A.1) and (A.2) as

$$\widetilde{f} = Ae^{i\psi}e^{-i\omega t + i\boldsymbol{k}\cdot\boldsymbol{x}}, \tag{A.5}$$

$$\widetilde{\Phi} = Be^{i\phi}e^{-i\omega t + i\boldsymbol{k}\cdot\boldsymbol{x}}. \tag{A.6}$$

Considering a flux-surface average over θ and ζ as defined in Equation (2.27), one finds that the second sin term in (A.4) will disappear, as

$$\langle \ldots \rangle_x = \frac{1}{2\pi}\int_0^{2\pi} \sin(ax+b)dx = 0, \quad a \in \mathbb{Z}_+, \mathbb{Z}_- \tag{A.7}$$

Here x represents either the poloidal or toroidal angle, θ or ζ, when flux-surface averaging. The integer a would be m or n, the toroidal or poloidal mode numbers. Using Equation (A.7), only the first sin term must be kept in Equation (A.4), namely $[\widetilde{\Phi}^*\widetilde{f} - \widetilde{f^*}\widetilde{\Phi}]$, thus proving Equation (2.27).

Appendix B

Gyrokinetic Theory Derivations

This chapter contains the more involved derivations used in Section 2.3.2. The starting point of the derivation is Equation (2.33), for which real-space and velocity-space derivatives of the guiding-center coordinates - $\mathbf{R}$, ϵ, μ, and α - are needed. Note that $\nabla \mathbf{v} = 0$ and $\nabla_{\mathbf{v}} \mathbf{x} = 0$ as the coordinates $\mathbf{x}$ and $\mathbf{v}$ are independent. All of the various vector and tensor identities used throughout this section can be found in the convenient list at the beginning of the NRL Plasma Formulary ([236]), which in turn are taken from Ref. [237]. The transformation to guiding-center coordinates is handled in Section B.1, followed by ordering the equation term by term in Section B.2, and finally the gyroaverages of various terms are given for the resulting equations in Section B.3.

B.1 Guiding-Center Transformation

The eight guiding-center variable derivatives are given here, though $\nabla \alpha$ and $\nabla_{\mathbf{v}} \alpha$ are most involved and are derived afterwards

$$\nabla \mathbf{R} = \nabla(\mathbf{x} - \boldsymbol{\rho}) = \overleftrightarrow{\mathrm{I}} - \nabla \boldsymbol{\rho}, \tag{B.1}$$

$$\nabla_{\mathbf{v}} \mathbf{R} = \cancel{\nabla_{\mathbf{v}} \mathbf{x}} - \nabla_{\mathbf{v}} \boldsymbol{\rho} = \nabla_{\mathbf{v}} \left(\frac{\mathbf{v} \times \hat{\mathbf{b}}}{\Omega} \right) = \frac{1}{\Omega} \left[\nabla_{\mathbf{v}} \mathbf{v} \times \hat{\mathbf{b}} + \mathbf{v} \times \cancel{\nabla_{\mathbf{v}} \hat{\mathbf{b}}} \right] = \frac{1}{\Omega} [\overleftrightarrow{\mathrm{I}} \times \hat{\mathbf{b}}], \tag{B.2}$$

$$\nabla \epsilon = \nabla \left(\frac{1}{2} m v^2 \right) = \frac{1}{2} m \nabla (\mathbf{v} \cdot \mathbf{v}) = m (\mathbf{v} \cdot \cancel{\nabla \mathbf{v}}) = 0, \tag{B.3}$$

$$\nabla_{\mathbf{v}} \epsilon = \nabla_{\mathbf{v}} \left(\frac{1}{2} m v^2 \right) = \frac{1}{2} m \nabla_{\mathbf{v}} (\mathbf{v} \cdot \mathbf{v}) = m \nabla_{\mathbf{v}} \mathbf{v} \cdot \mathbf{v} = \overleftrightarrow{\mathrm{I}} \cdot \mathbf{v} = \mathbf{v}, \tag{B.4}$$

$$\begin{aligned}\nabla\mu = \nabla(\frac{mv_\perp^2}{2B}) &= \frac{mv_\perp^2}{2}\nabla\frac{1}{B} + \frac{m}{2B}\nabla\mathbf{v}_\perp\cdot\mathbf{v}_\perp \\ &= -\frac{mv_\perp^2}{2B^2}\nabla B + \frac{m\mathbf{v}_\perp}{B}\cdot\nabla\mathbf{v}_\perp = -\frac{\mu}{B}\nabla B + \frac{m\mathbf{v}_\perp}{B}\cdot\nabla(\cancel{\mathbf{v}} - v_\parallel\hat{\mathbf{b}}) \\ &= -\frac{\mu}{B}\nabla B - \frac{m\mathbf{v}_\perp}{B}\cdot(\cancel{\hat{\mathbf{b}}}\nabla v_\parallel + v_\parallel\nabla\hat{\mathbf{b}}) = -\frac{\mu}{B}\nabla B - \frac{mv_\parallel}{B}\mathbf{v}_\perp\cdot\nabla\hat{\mathbf{b}},\end{aligned} \tag{B.5}$$

$$\begin{aligned}\nabla_{\mathbf{v}}\mu = \nabla_{\mathbf{v}}(\frac{mv_\perp^2}{2B}) &= \frac{m}{2B}\nabla_{\mathbf{v}}(\mathbf{v}_\perp\cdot\mathbf{v}_\perp) = \frac{m\mathbf{v}_\perp}{B}\cdot\nabla_{\mathbf{v}}(\mathbf{v} - v_\parallel\hat{\mathbf{b}}) \\ &= \frac{m\mathbf{v}_\perp}{B}\cdot\left[\overleftrightarrow{\mathrm{I}} - \cancel{\hat{\mathbf{b}}}(\nabla_{\mathbf{v}}v_\parallel) - v_\parallel\cancel{\nabla_{\mathbf{v}}\hat{\mathbf{b}}}\right] = \frac{m\mathbf{v}_\perp}{B},\end{aligned} \tag{B.6}$$

$$\nabla\alpha = \frac{v_\parallel}{v_\perp^2}\hat{\mathbf{b}}\cdot(\mathbf{v}_\perp\times\hat{\mathbf{b}}) + \hat{\mathbf{e}}_1\cdot\nabla\hat{\mathbf{e}}_2, \tag{B.7}$$

$$\nabla_{\mathbf{v}}\alpha = -\frac{1}{v_\perp^2}(\hat{\mathbf{b}}\times\mathbf{v}), \tag{B.8}$$

where $\overleftrightarrow{\mathrm{I}}$ is the identity tensor. Note that $\mathbf{A}\cdot\nabla\mathbf{B} \neq (\mathbf{A}\cdot\nabla)\mathbf{B}$ and any directional derivatives will be explicity denoted using parenthesis where necessary throughout this section; this allows for $\mathbf{A}\cdot\nabla\mathbf{B}$ and $\nabla\mathbf{B}\cdot\mathbf{A}$ to be interchangeble, i.e. in index notation they are both $A_i\partial B_i/\partial x_j$.

The value of $\nabla_{\mathbf{v}}\alpha$ can be found by considering the equations

$$\nabla_{\mathbf{v}}(\mathbf{v}\cdot\hat{\mathbf{e}}_1) = \overleftrightarrow{\mathrm{I}}\cdot\hat{\mathbf{e}}_1 + 0 = \hat{\mathbf{e}}_1 = \nabla_{\mathbf{v}}(-v_\perp\sin\alpha) = -\nabla_{\mathbf{v}}(v_\perp)\sin\alpha - v_\perp\cos\alpha\nabla_{\mathbf{v}}\alpha, \tag{B.9}$$

$$\nabla_{\mathbf{v}}(\mathbf{v}\cdot\hat{\mathbf{e}}_2) = \overleftrightarrow{\mathrm{I}}\cdot\hat{\mathbf{e}}_2 + 0 = \hat{\mathbf{e}}_2 = \nabla_{\mathbf{v}}(v_\perp\cos\alpha) = \nabla_{\mathbf{v}}(v_\perp)\cos\alpha - v_\perp\sin\alpha\nabla_{\mathbf{v}}\alpha. \tag{B.10}$$

Equation (B.9) and (B.10) can be combined to find

$$\begin{aligned}\cos\alpha\hat{\mathbf{e}}_1 + \sin\alpha\hat{\mathbf{e}}_2 &= -v_\perp\nabla_{\mathbf{v}}\alpha \\ \Rightarrow \nabla_{\mathbf{v}}\alpha = -\frac{1}{v_\perp}(\cos\alpha\hat{\mathbf{e}}_1 + \sin\alpha\hat{\mathbf{e}}_2) &= -\frac{1}{v_\perp}\frac{\Omega}{v_\perp}\boldsymbol{\rho} = -\frac{1}{v_\perp^2}(\hat{\mathbf{b}}\times\mathbf{v}).\end{aligned} \tag{B.11}$$

The same steps can be taken to find $\nabla\alpha$. This time one has

$$\nabla(\mathbf{v}\cdot\hat{\mathbf{e}}_1) = 0 + \mathbf{v}\cdot\nabla\hat{\mathbf{e}}_1 = \nabla(-v_\perp\sin\alpha) = -\nabla(v_\perp)\sin\alpha - v_\perp\cos\alpha\nabla\alpha, \tag{B.12}$$

$$\nabla(\mathbf{v}\cdot\hat{\mathbf{e}}_2) = 0 + \mathbf{v}\cdot\nabla\hat{\mathbf{e}}_2 = \nabla(v_\perp\cos\alpha) = \nabla(v_\perp)\cos\alpha - v_\perp\sin\alpha\nabla\alpha. \tag{B.13}$$

Again, these two equations can be combined to find

$$\begin{aligned}\mathbf{v}\cdot(\cos\alpha\nabla\hat{\mathbf{e}}_1+\sin\alpha\hat{\mathbf{e}}_2)&=-v_\perp\nabla\alpha\\ \Rightarrow\nabla\alpha&=-\frac{1}{v_\perp}\mathbf{v}\cdot(\cos\alpha\nabla\hat{\mathbf{e}}_1+\sin\alpha\nabla\hat{\mathbf{e}}_2)\end{aligned}\tag{B.14}$$

Equation (B.14) can be simplified by breaking up $\mathbf{v}$ into parallel and perpendicular components. The parallel component is considered here first, for which one finds

$$\begin{aligned}&-\frac{v_\parallel}{v_\perp}\hat{\mathbf{b}}\cdot(\cos\alpha(\nabla\hat{\mathbf{b}}\times\hat{\mathbf{e}}_2+\cancel{\hat{\mathbf{b}}\times\nabla\hat{\mathbf{e}}_2})-\sin\alpha(\nabla\hat{\mathbf{b}}\times\hat{\mathbf{e}}_1+\cancel{\hat{\mathbf{b}}\times\nabla\hat{\mathbf{e}}_1}))\\ &\quad=-\frac{v_\parallel}{v_\perp}\hat{\mathbf{b}}\cdot(\nabla\hat{\mathbf{b}}\times(\cos\alpha\hat{\mathbf{e}}_2-\sin\alpha\hat{\mathbf{e}}_1))\\ &\quad=-\frac{v_\parallel}{v_\perp^2}\hat{\mathbf{b}}\cdot(\nabla\hat{\mathbf{b}}\times\mathbf{v}_\perp)\\ &\quad=\frac{v_\parallel}{v_\perp^2}\hat{\mathbf{b}}\cdot(\mathbf{v}_\perp\times\nabla\hat{\mathbf{b}}).\end{aligned}\tag{B.15}$$

The perpendicular component of Equation (B.14) becomes

$$\begin{aligned}&-(\cos\alpha\hat{\mathbf{e}}_2-\sin\alpha\hat{\mathbf{e}}_1)\cdot\Big[\cos\alpha(\nabla\hat{\mathbf{b}}\times\hat{\mathbf{e}}_2+\hat{\mathbf{b}}\times\nabla\hat{\mathbf{e}}_2)+\sin\alpha(\nabla\hat{\mathbf{e}}_1\times\hat{\mathbf{b}}+\hat{\mathbf{e}}_1\times\nabla\hat{\mathbf{b}})\Big]\\ &=-\Big[\cos^2\alpha\hat{\mathbf{e}}_2\cdot(\hat{\mathbf{b}}\times\nabla\hat{\mathbf{e}}_2)-\sin\alpha\cos\alpha\hat{\mathbf{e}}_1\cdot(\cancel{\nabla\hat{\mathbf{b}}\times\hat{\mathbf{e}}_2}+\hat{\mathbf{b}}\times\nabla\hat{\mathbf{e}}_2)\\ &\quad-\sin^2\alpha\hat{\mathbf{e}}_1\cdot(\nabla\hat{\mathbf{e}}_1\times\hat{\mathbf{b}})+\cos\alpha\sin\alpha\hat{\mathbf{e}}_2\cdot(\nabla\hat{\mathbf{e}}_1\times\hat{\mathbf{b}}+\cancel{\hat{\mathbf{e}}_1\times\nabla\hat{\mathbf{b}}})\Big]\\ &=-\Big[\cos^2\alpha\hat{\mathbf{b}}\cdot(\nabla\hat{\mathbf{e}}_2\times\hat{\mathbf{e}}_2)-\sin^2\alpha\hat{\mathbf{b}}\cdot(\hat{\mathbf{e}}_1\times\nabla\hat{\mathbf{e}}_1)+\sin\alpha\cos\alpha(\hat{\mathbf{b}}\cdot(\hat{\mathbf{e}}_1\times\nabla\hat{\mathbf{e}}_2+\hat{\mathbf{e}}_1\times\nabla\hat{\mathbf{e}}_1))\Big]\\ &=-\Big[\cos^2\alpha\hat{\mathbf{b}}\cdot[(\nabla\hat{\mathbf{e}}_1\times\hat{\mathbf{b}}+\hat{\mathbf{e}}_1\times\nabla\hat{\mathbf{b}})\times\hat{\mathbf{e}}_2]-\sin^2\alpha\hat{\mathbf{b}}\cdot[\hat{\mathbf{e}}_1\times(\nabla\hat{\mathbf{b}}\times\hat{\mathbf{e}}_2+\hat{\mathbf{b}}\times\nabla\hat{\mathbf{e}}_2)]\\ &\quad+\sin\alpha\cos\alpha\hat{\mathbf{b}}\cdot[\hat{\mathbf{e}}_1\times(\nabla\hat{\mathbf{e}}_1\times\hat{\mathbf{b}}+\hat{\mathbf{e}}\times\nabla\hat{\mathbf{b}})+\hat{\mathbf{e}}_2\times(\nabla\hat{\mathbf{b}}\times\hat{\mathbf{e}}_2+\hat{\mathbf{b}}\times\nabla\hat{\mathbf{e}}_2)]\Big]\\ &=-\Big[\cos^2\alpha\hat{\mathbf{b}}\cdot[\hat{\mathbf{b}}(\nabla\hat{\mathbf{e}}_1\cdot\hat{\mathbf{e}}_2)-\cancel{\hat{\mathbf{e}}_2}(\nabla\hat{\mathbf{e}}_1\cdot\hat{\mathbf{b}})+\nabla\hat{\mathbf{b}}\cancel{(\hat{\mathbf{e}}_1\cdot\hat{\mathbf{e}}_2)}-\cancel{\hat{\mathbf{e}}_2}(\hat{\mathbf{e}}_1\cdot\nabla\hat{\mathbf{b}})]\\ &\quad-\sin^2\alpha\hat{\mathbf{b}}\cdot[\nabla\hat{\mathbf{b}}\cancel{(\hat{\mathbf{e}}_1\cdot\hat{\mathbf{e}}_2)}-\cancel{\hat{\mathbf{e}}_2}(\hat{\mathbf{e}}_1\cdot\nabla\hat{\mathbf{b}})+\hat{\mathbf{b}}(\hat{\mathbf{e}}_1\cdot\nabla\hat{\mathbf{e}}_2)-\nabla\hat{\mathbf{e}}_2\cancel{(\hat{\mathbf{e}}_1\cdot\hat{\mathbf{b}})}]\\ &\quad+\sin\alpha\cos\alpha[\nabla\hat{\mathbf{e}}_1\cancel{(\hat{\mathbf{e}}_1\cdot\hat{\mathbf{b}})}-\hat{\mathbf{b}}(\hat{\mathbf{e}}_1\cdot\nabla\hat{\mathbf{e}}_1)+\cancel{\hat{\mathbf{e}}_1}(\hat{\mathbf{e}}_2\cdot\nabla\hat{\mathbf{b}})-\cancel{\nabla\hat{\mathbf{b}}(\hat{\mathbf{e}}_1\cdot\hat{\mathbf{e}}_1)}+\cancel{\nabla\hat{\mathbf{b}}(\hat{\mathbf{e}}_2\hat{\mathbf{e}}_2)}-\cancel{\hat{\mathbf{e}}_2}(\hat{\mathbf{e}}_2\cdot\nabla\hat{\mathbf{b}})\\ &\quad+\hat{\mathbf{b}}(\hat{\mathbf{e}}_2\cdot\nabla\hat{\mathbf{e}}_2)-\nabla\hat{\mathbf{e}}_2\cancel{(\hat{\mathbf{e}}_2\cdot\hat{\mathbf{b}})}]\Big]\\ &=-\cos^2\alpha(\hat{\mathbf{e}}_2\cdot\nabla\hat{\mathbf{e}}_1)+\sin^2\alpha(\hat{\mathbf{e}}_1\cdot\nabla\hat{\mathbf{e}}_2)+\sin\alpha\cos\alpha(\hat{\mathbf{e}}_2\cdot\nabla\hat{\mathbf{e}}_2-\hat{\mathbf{e}}_1\cdot\nabla\hat{\mathbf{e}}_1)\end{aligned}\tag{B.16}$$

The final value in Equation (B.16) can further be simplified by focusing on the unit vector expressions. First, note that the last term goes to zero because the equation

$$\nabla(\hat{\mathbf{e}}_1 \cdot \hat{\mathbf{e}}_1) = \nabla(\hat{\mathbf{e}}_2 \cdot \hat{\mathbf{e}}_2) = \nabla(1) = 0 \tag{B.17}$$

implies the following are true

$$\nabla(\hat{\mathbf{e}}_1 \cdot \hat{\mathbf{e}}_1) = 2\hat{\mathbf{e}}_1 \cdot \nabla\hat{\mathbf{e}}_1 = 0, \tag{B.18}$$

$$\nabla(\hat{\mathbf{e}}_2 \cdot \hat{\mathbf{e}}_2) = 2\hat{\mathbf{e}}_2 \cdot \nabla\hat{\mathbf{e}}_2 = 0. \tag{B.19}$$

Second, one can rewrite the final vector expression for the $\cos^2\alpha$ term in Equation (B.16) as

$$\begin{aligned}
\hat{\mathbf{e}}_2 \cdot \nabla\hat{\mathbf{e}}_1 &= -(\hat{\mathbf{b}} \times \hat{\mathbf{e}}_1) \cdot \nabla\hat{\mathbf{e}}_1 = \hat{\mathbf{e}}_1 \cdot (\nabla\hat{\mathbf{e}}_1 \times \hat{\mathbf{b}}) = -\hat{\mathbf{e}}_1 \cdot ((\nabla\hat{\mathbf{b}} \times \hat{\mathbf{e}}_2 + \hat{\mathbf{b}} \times \nabla\hat{\mathbf{e}}_2) \times \hat{\mathbf{b}}) \\
&= +\hat{\mathbf{e}}_1 \cdot (\hat{\mathbf{b}} \times (\nabla\hat{\mathbf{b}} \times \hat{\mathbf{e}}_2) + \hat{\mathbf{b}} \times (\hat{\mathbf{b}} \times \nabla\hat{\mathbf{e}}_2)) \\
&= +\hat{\mathbf{e}}_1 \cdot (\nabla\hat{\mathbf{b}}\cancel{(\hat{\mathbf{b}} \cdot \hat{\mathbf{e}}_2)} - \cancel{\hat{\mathbf{e}}_2}(\hat{\mathbf{b}} \cdot \nabla\hat{\mathbf{b}}) + \cancel{\hat{\mathbf{b}}}(\hat{\mathbf{b}} \cdot \nabla\hat{\mathbf{e}}_2) - \nabla\hat{\mathbf{e}}_2(\hat{\mathbf{b}} \cdot \hat{\mathbf{b}})) \\
&= -\hat{\mathbf{e}}_1 \cdot \nabla\hat{\mathbf{e}}_2.
\end{aligned} \tag{B.20}$$

Combining Equation (B.18), Equation (B.19), and Equation (B.20), one can rewrite Equation (B.16) as

$$-\frac{1}{v_\perp}\mathbf{v}_\perp \cdot (\cos\alpha\nabla\hat{\mathbf{e}}_1 + \sin\alpha\nabla\hat{\mathbf{e}}_2) = (\sin^2\alpha + \cos^2\alpha)(\hat{\mathbf{e}}_1 \cdot \nabla\hat{\mathbf{e}}_2) = (\hat{\mathbf{e}}_1 \cdot \nabla\hat{\mathbf{e}}_2). \tag{B.21}$$

Finally, combining Equation (B.21) and Equation (B.15) gives

$$\nabla\alpha = \frac{v_\parallel}{v_\perp^2}\hat{\mathbf{b}} \cdot (\hat{\mathbf{v}}_\perp \times \hat{\mathbf{b}}) + \hat{\mathbf{e}}_1 \cdot \nabla\hat{\mathbf{e}}_2. \tag{B.22}$$

Various simplifications were also made to convert Equation (2.50) to Equation (2.51), which are listed here

$$\frac{q}{m\Omega}\delta\mathbf{E} \cdot (\overleftrightarrow{\mathrm{I}} \times \hat{\mathbf{b}}) = \frac{\delta\mathbf{E} \times \hat{\mathbf{b}}}{B} = \mathbf{v}_E, \tag{B.23}$$

$$\frac{q}{m}\mathbf{v} \times \hat{\mathbf{B}} = \Omega(\mathbf{v} \times \hat{\mathbf{b}}) = \Omega(\mathbf{v}_\perp \times \hat{\mathbf{b}}), \tag{B.24}$$

$$\frac{q}{m}\mathbf{v}\times\hat{\mathbf{b}}\cdot(m\mathbf{v})=0 \tag{B.25}$$

$$\frac{m\Omega}{B}(\mathbf{v}_\perp\times\hat{\mathbf{b}})\cdot\mathbf{v}_\perp=0 \tag{B.26}$$

$$-\frac{\Omega}{v_\perp^2}(\mathbf{v}_\perp\times\hat{\mathbf{b}})\cdot(\hat{\mathbf{b}}\times\mathbf{v}_\perp)=\Omega\frac{\cancel{v_\perp^2}}{\cancel{v_\perp^2}}(\hat{\mathbf{v}}_\perp\times\hat{\mathbf{b}})\cdot(\hat{\mathbf{v}}_\perp\times\hat{\mathbf{b}})=\Omega, \tag{B.27}$$

$$\begin{aligned}\cancel{\Omega}(\mathbf{v}_\perp\times\hat{\mathbf{b}})\cdot(\frac{\cancel{1}}{\cancel{\Omega}}\overleftrightarrow{\mathrm{I}}\times\hat{\mathbf{b}})&=(\mathbf{v}_\perp\times\hat{\mathbf{b}})\times\hat{\mathbf{b}}=-\hat{\mathbf{b}}\times(\mathbf{v}_\perp\times\hat{\mathbf{b}})\\&=-[\mathbf{v}_\perp(\hat{\mathbf{b}}\cdot\hat{\mathbf{b}})-\hat{\mathbf{b}}\cancel{(\mathbf{v}_\perp\cdot\hat{\mathbf{b}})}]=-\mathbf{v}_\perp\end{aligned} \tag{B.28}$$

$$\mathbf{v}\cdot\nabla_{\mathbf{R}}f-\mathbf{v}_\perp\cdot\nabla_{\mathbf{R}}f=v_\parallel\hat{\mathbf{b}}\cdot\nabla_{\mathbf{R}}f. \tag{B.29}$$

B.2 Gyrokinetic Ordering

The second step in deriving the gyrokinetic equation involves splitting up the terms into their different orders as defined by Equation (2.35), Equation (2.36), and Equation (2.37). A few more orderings are delineated here which are necessary to complete the derivation. Because the magnitude of the equilibrium magnetic field varies as $1/L$, one necessarily has macroscopic variations for the following quantities

$$\nabla\rho\sim\nabla\hat{\mathbf{b}}\sim\nabla\hat{\mathbf{e}}_1\sim\nabla\hat{\mathbf{e}}_2\sim 1/L. \tag{B.30}$$

The ordering of $\mathbf{v}_E$ must also be clarified and is readily shown to be

$$\frac{v_E}{v_{th}}\sim\frac{\delta E_1}{v_{th}B_0}\sim\epsilon\frac{E_0}{v_{th}B_0}\sim\epsilon. \tag{B.31}$$

It must also be clarified that orderings of dot products between velocity and perturbed fields must be split up between parallel and perpendicular directions due to the ordering of parallel and perpendicular wavelengths. That is

$$\frac{\mathbf{v}_\parallel\cdot\delta\mathbf{E}_1}{\mathbf{v}_\perp\cdot\delta\mathbf{E}_1}\sim\frac{\cancel{v_{th}}}{\cancel{v_{th}}}\frac{k_\parallel}{k_\perp}\frac{\cancel{\delta\phi_1}}{\cancel{\delta\phi_1}}\sim\epsilon. \tag{B.32}$$

Care must also be taken to split up terms regarding dot products of velocity and gradients of δf_1, as in the case of Equation (B.44). Finally, gradient scales with respect to α must be found. These can be calculated by considering expanding into real-space and velocity-space derivatives as follows

$$\begin{aligned}\frac{\partial f}{\partial \alpha} &= \frac{\partial \mathbf{x}}{\partial \alpha}\nabla f + \frac{\partial \mathbf{v}}{\partial \alpha}\nabla_{\mathbf{v}} f = \frac{\partial \boldsymbol{\rho}}{\partial \alpha}\nabla f + \frac{\partial \mathbf{v}}{\partial \alpha}\nabla_{\mathbf{v}} f = \frac{\mathbf{v}_{th}}{\Omega}\nabla f + (\mathbf{v}_\perp \times \hat{\mathbf{b}})\nabla_{\mathbf{v}} f \\ &\sim \rho(\frac{f_0}{L} + k_\perp \delta f_1) + v_{th}(\frac{f_0}{v_{th}} + \frac{\delta f_1}{v_{th}}) + \mathcal{O}(\epsilon^2 f_0) \\ &\sim \epsilon f_0 + \delta f_1 + f_0 + \delta f_1 + \mathcal{O}(\epsilon^2 f_0) \sim f.\end{aligned} \tag{B.33}$$

Note it has been assumed that $\partial f/\partial \mathbf{v} \sim f/v_{th}$, i.e. this is assumed true for all orders in f.

The orders of each term in Equation (2.51) are provided here relative to $(v_{th}/L)f_0$. Because this derivation ignores the highest-order transport equations, only terms of lower order than the transport timescale, as defined by Equation (2.39) and Equation (B.34), are kept here. For this reason most terms depend only on first order fluctuating quantities, except for Equation (B.42) which depends on δf_2. The terms are ordered as follows:

$$\frac{\partial_t f_0}{\frac{v_{th}}{L} f_0} \sim \frac{\epsilon^3 \Omega L}{v_{th}} \sim \frac{\epsilon^3 L}{\rho} \sim \epsilon^2, \tag{B.34}$$

$$\frac{\partial_t \delta f_1}{\frac{v_{th}}{L} f_0} \sim \frac{\omega_* L \epsilon f_0}{v_{th} f_0} \sim \frac{\omega_* \epsilon}{v_{th} \epsilon} \sim \frac{\omega_*}{\Omega} \sim \epsilon, \tag{B.35}$$

$$\frac{\mathbf{v}_\parallel \cdot \nabla_{\mathbf{R}} f_0}{\frac{v_{th}}{L} f_0} \sim \frac{\frac{v_{th}}{L} f_0}{\frac{v_{th}}{L} f_0} \sim 1, \tag{B.36}$$

$$\frac{\mathbf{v}_\parallel \cdot \nabla_{\mathbf{R}} \delta f_1}{\frac{v_{th}}{L} f_0} \sim \frac{v_{th} k_\parallel \epsilon f_0}{\frac{v_{th}}{L} f_0} \sim \epsilon^2 k_\perp \rho \frac{L}{\rho} \sim \epsilon^2 \frac{1}{\epsilon} \sim \epsilon, \tag{B.37}$$

$$\frac{\mathbf{v}_E \cdot \nabla_{\mathbf{R}} f_0}{\frac{v_{th}}{L} f_0} \sim \frac{\epsilon \frac{v_{th}}{L} f_0}{\frac{v_{th}}{L} f_0} \sim \epsilon, \tag{B.38}$$

$$\frac{\mathbf{v}_E \cdot \nabla_{\mathbf{R}} \delta f_1}{\frac{v_{th}}{L} f_0} \sim \frac{\epsilon v_{th} k_\perp \epsilon f_0}{\frac{v_{th}}{L} f_0} \sim \epsilon^2 k_\perp \rho \frac{L}{\rho} \sim \epsilon^2 \frac{1}{\epsilon} \sim \epsilon, \tag{B.39}$$

$$\frac{\Omega \frac{\partial f_0}{\partial \alpha}}{\frac{v_{th}}{L} f_0} \sim \frac{\frac{v_{th}}{\rho} f_0}{\frac{v_{th}}{L} f_0} \sim \frac{L}{\rho} \sim \frac{1}{\epsilon}, \tag{B.40}$$

$$\frac{\Omega\frac{\partial\delta f_1}{\partial\alpha}}{\frac{v_{th}}{L}f_0} \sim \frac{\frac{v_{th}}{\rho}\epsilon f_0}{\frac{v_{th}}{L}f_0} \sim \epsilon\frac{L}{\rho} \sim \frac{\epsilon}{\epsilon} \sim 1, \tag{B.41}$$

$$\frac{\Omega\frac{\partial\delta f_2}{\partial\alpha}}{\frac{v_{th}}{L}f_0} \sim \frac{\frac{v_{th}}{\rho}\epsilon^2 f_0}{\frac{v_{th}}{L}f_0} \sim \epsilon^2\frac{L}{\rho} \sim \frac{\epsilon^2}{\epsilon} \sim \epsilon, \tag{B.42}$$

$$\frac{\mathbf{v}\cdot\nabla\rho\cdot\nabla_R f_0}{\frac{v_{th}}{L}f_0} \sim \frac{v_{th}\frac{\rho}{L}\frac{f_0}{L}}{\frac{v_{th}}{L}f_0} \sim \frac{\rho}{L} \sim \epsilon \tag{B.43}$$

$$\frac{\mathbf{v}_\perp\cdot\nabla\rho\cdot\nabla_R\delta f_1}{\frac{v_{th}}{L}f_0} \sim \frac{v_{th}\frac{\rho}{L}k_\perp\epsilon f_0}{\frac{v_{th}}{L}f_0} \sim \epsilon k_\perp\rho\frac{L}{\rho}\epsilon \sim \epsilon^2\frac{1}{\epsilon} \sim \epsilon, \tag{B.44}$$

$$\frac{\mathbf{v}_\parallel\cdot\nabla\rho\cdot\nabla_R\delta f_1}{\frac{v_{th}}{L}f_0} \sim \frac{v_{th}\frac{\rho}{L}k_\parallel\epsilon f_0}{\frac{v_{th}}{L}f_0} \sim \epsilon^2 k_\perp\rho\frac{L}{\rho}\epsilon \sim \epsilon^3\frac{1}{\epsilon} \sim \epsilon^2, \tag{B.45}$$

$$\frac{\mathbf{v}\cdot\frac{\mu}{B}\nabla B\frac{\partial f_0}{\partial\mu}}{\frac{v_{th}}{L}f_0} \sim \frac{v_{th}\frac{mv_{th}^2}{B^2}\frac{B}{L}\frac{f_0}{mv_{th}^2/B}}{\frac{v_{th}}{L}f_0} \sim \frac{\frac{v_{th}}{L}\frac{B}{B}}{\frac{v_{th}}{L}} \sim 1, \tag{B.46}$$

$$\frac{\mathbf{v}\cdot\frac{\mu}{B}\nabla B\frac{\partial\delta f_1}{\partial\mu}}{\frac{v_{th}}{L}f_0} \sim \frac{v_{th}\frac{mv_{th}^2}{B^2}\frac{B}{L}\frac{\epsilon f_0}{mv_{th}^2/B}}{\frac{v_{th}}{L}f_0} \sim \epsilon\frac{\frac{v_{th}}{L}\frac{B}{B}}{\frac{v_{th}}{L}} \sim \epsilon, \tag{B.47}$$

$$\frac{\mathbf{v}\cdot\frac{mv_\parallel}{B}(\mathbf{v}_\perp\cdot\nabla\hat{\mathbf{b}})\frac{\partial f_0}{\partial\mu}}{\frac{v_{th}}{L}f_0} \sim \frac{v_{th}\frac{mv_{th}}{B}\frac{v_{th}}{L}\frac{f_0}{mv_{th}^2/B}}{\frac{v_{th}}{L}f_0} \sim \frac{\frac{v_{th}}{L}f_0}{\frac{v_{th}}{L}f_0} \sim 1, \tag{B.48}$$

$$\frac{\mathbf{v}\cdot\frac{mv_\parallel}{B}(\mathbf{v}_\perp\cdot\nabla\hat{\mathbf{b}})\frac{\partial\delta f_1}{\partial\mu}}{\frac{v_{th}}{L}f_0} \sim \frac{v_{th}\frac{mv_{th}}{B}\frac{v_{th}}{L}\frac{\epsilon f_0}{mv_{th}^2/B}}{\frac{v_{th}}{L}f_0} \sim \epsilon\frac{\frac{v_{th}}{L}f_0}{\frac{v_{th}}{L}f_0} \sim \epsilon, \tag{B.49}$$

$$\frac{\mathbf{v}\cdot\frac{v_\parallel}{v_\perp^2}(\nabla\hat{\mathbf{b}})\cdot(\mathbf{v}_\perp\cdot\hat{\mathbf{b}})\frac{\partial f_0}{\partial\alpha}}{\frac{v_{th}}{L}f_0} \sim \frac{v_{th}\frac{1}{v_{th}}\frac{1}{L}v_{th}f_0}{\frac{v_{th}}{L}f_0} \sim 1, \tag{B.50}$$

$$\frac{\mathbf{v}\cdot\frac{v_\parallel}{v_\perp^2}(\nabla\hat{\mathbf{b}})\cdot(\mathbf{v}_\perp\cdot\hat{\mathbf{b}})\frac{\partial\delta f_1}{\partial\alpha}}{\frac{v_{th}}{L}f_0} \sim \frac{v_{th}\frac{1}{v_{th}}\frac{1}{L}v_{th}\epsilon f_0}{\frac{v_{th}}{L}f_0} \sim \epsilon, \tag{B.51}$$

$$\frac{\mathbf{v}\cdot(\hat{\mathbf{e}}_1\cdot\nabla\hat{\mathbf{e}}_2)\frac{\partial f_0}{\partial\alpha}}{\frac{v_{th}}{L}f_0} \sim \frac{v_{th}\frac{1}{L}f_0}{\frac{v_{th}}{L}f_0} \sim 1, \tag{B.52}$$

$$\frac{\mathbf{v}\cdot(\hat{\mathbf{e}}_1\cdot\nabla\hat{\mathbf{e}}_2)\frac{\partial\delta f_1}{\partial\alpha}}{\frac{v_{th}}{L}f_0} \sim \frac{v_{th}\frac{1}{L}\epsilon f_0}{\frac{v_{th}}{L}f_0} \sim \epsilon, \tag{B.53}$$

$$\frac{\frac{q}{m}\delta\mathbf{E}_1\cdot(m\mathbf{v}_\perp)\frac{\partial f_0}{\partial\epsilon}}{\frac{v_{th}}{L}f_0} \sim \frac{q\delta E_{1\perp}v_{th}f_0/T}{\frac{v_{th}}{L}f_0} \sim k_\perp L\frac{q\delta\phi_1}{T} \sim \epsilon k_\perp\rho\frac{L}{\rho} \sim \epsilon\frac{1}{\epsilon} \sim 1, \tag{B.54}$$

$$\frac{\frac{q}{m}\delta\mathbf{E}_1\cdot(m\mathbf{v}_\parallel)\frac{\partial f_0}{\partial\epsilon}}{\frac{v_{th}}{L}f_0} \sim \frac{q\delta E_{1\parallel}v_{th}f_0/T}{\frac{v_{th}}{L}f_0} \sim k_\parallel L\frac{q\delta\phi_1}{T} \sim \epsilon^2 k_\perp\rho\frac{L}{\rho} \sim \epsilon^2\frac{1}{\epsilon} \sim \epsilon, \tag{B.55}$$

$$\frac{\frac{q}{m}\delta\mathbf{E}_1\cdot(m\mathbf{v}_\perp)\frac{\partial\delta f_1}{\partial\epsilon}}{\frac{v_{th}}{L}f_0}\sim\frac{q\delta E_{1\perp}v_{th}\epsilon f_0/T}{\frac{v_{th}}{L}f_0}\sim\epsilon k_\perp L\frac{q\delta\phi_1}{T}\sim\epsilon^2k_\perp\rho\frac{L}{\rho}\sim\epsilon^2\frac{1}{\epsilon}\sim\epsilon, \tag{B.56}$$

$$\frac{\frac{q}{m}\delta\mathbf{E}_1\cdot(m\mathbf{v}_\parallel)\frac{\partial\delta f_1}{\partial\epsilon}}{\frac{v_{th}}{L}f_0}\sim\frac{q\delta E_{1\parallel}v_{th}\epsilon f_0/T}{\frac{v_{th}}{L}f_0}\sim\epsilon k_\parallel L\frac{q\delta\phi_1}{T}\sim\epsilon^3k_\perp\rho\frac{L}{\rho}\sim\epsilon^3\frac{1}{\epsilon}\sim\epsilon^2, \tag{B.57}$$

$$\frac{\frac{q}{m}\delta\mathbf{E}_1\cdot\frac{m\mathbf{v}_\perp}{B}\frac{\partial f_0}{\partial\mu}}{\frac{v_{th}}{L}f_0}\sim\frac{q\delta E_{1\perp}\frac{v_{th}}{B}\frac{f_0}{mv_{th}^2/B}}{\frac{v_{th}}{L}f_0}\sim\frac{q\delta\phi_1k_\perp L}{mv_{th}^2}\sim\frac{q\delta\phi_1}{T}k_\perp\rho\frac{L}{\rho}\sim\epsilon\frac{1}{\epsilon}\sim1, \tag{B.58}$$

$$\frac{\frac{q}{m}\delta\mathbf{E}_1\cdot\frac{m\mathbf{v}_\perp}{B}\frac{\partial\delta f_1}{\partial\mu}}{\frac{v_{th}}{L}f_0}\sim\frac{q\delta E_{1\perp}\frac{v_{th}}{B}\frac{\epsilon f_0}{mv_{th}^2/B}}{\frac{v_{th}}{L}f_0}\sim\frac{q\delta\phi_1k_\perp L\epsilon}{mv_{th}^2}\sim\epsilon\frac{q\delta\phi_1}{T}k_\perp\rho\frac{L}{\rho}\sim\epsilon^2\frac{1}{\epsilon}\sim\epsilon, \tag{B.59}$$

$$\frac{\frac{q}{m}\delta\mathbf{E}_1\cdot\frac{1}{v_\perp^2}(\hat{\mathbf{b}}\times\mathbf{v}_\perp)\frac{\partial f_0}{\partial\alpha}}{\frac{v_{th}}{L}f_0}\sim\frac{\frac{q}{m}\delta E_{1\perp}\frac{1}{v_{th}}f_0}{\frac{v_{th}}{L}f_0}\sim\frac{q\delta\phi_1k_\perp L}{v_{th}^2}\sim\frac{q\delta\phi_1}{T}k_\perp\rho\frac{L}{\rho}\sim\epsilon\frac{1}{\epsilon}\sim1, \tag{B.60}$$

$$\frac{\frac{q}{m}\delta\mathbf{E}_1\cdot\frac{1}{v_\perp^2}(\hat{\mathbf{b}}\times\mathbf{v}_\perp)\frac{\partial\delta f_1}{\partial\alpha}}{\frac{v_{th}}{L}f_0}\sim\frac{\frac{q}{m}\delta E_{1\perp}\frac{1}{v_{th}}\epsilon f_0}{\frac{v_{th}}{L}f_0}\sim\epsilon\frac{q\delta\phi_1k_\perp L}{v_{th}^2}\sim\epsilon\frac{q\delta\phi_1}{T}k_\perp\rho\frac{L}{\rho}\sim\epsilon^2\frac{1}{\epsilon}\sim\epsilon. \tag{B.61}$$

The lowest order term, Equation (B.40), is thus $\mathcal{O}(\epsilon^{-1})$. This term alone makes up Equation (2.52). Terms of $\mathcal{O}(1)$ make up Equation (2.53), while terms of $\mathcal{O}(\epsilon)$ make up Equation (2.54).

B.3 Gyroaveraging Terms

Lastly, all the terms in Equation (2.54) and Equation (2.55) must be gyroaveraged to obtain the final gyrokinetic equations. The first term that needs to be gyroaveraged is the $\mathbf{v}\cdot\left[\frac{\mu}{B}\nabla B\frac{\partial f_0}{\partial\mu}+\frac{mv_\parallel}{B}(\mathbf{v}_\perp\cdot\nabla\hat{\mathbf{b}})\right]$ in Equation (2.55). Noting from Equation (2.49) that only parallel velocity components will survive gyroaveraging the first piece and perpendicular velocity components will survive gyroaveraging the second piece, one has

$$\begin{aligned}
\langle\mathbf{v}\cdot(\frac{\mu}{B}\nabla B\frac{\partial f_0}{\partial\mu}+\frac{mv_\parallel}{B}(\mathbf{v}_\perp\cdot\nabla\hat{\mathbf{b}}))\rangle_\alpha&=\frac{\mu}{B}v_\parallel\hat{\mathbf{b}}\cdot\nabla B+\frac{mv_\parallel}{B}\langle\mathbf{v}_\perp\cdot(\mathbf{v}_\perp\cdot\nabla\hat{\mathbf{b}})\rangle_\alpha\\
&=\frac{\mu}{B}v_\parallel\hat{\mathbf{b}}\cdot\nabla B+\frac{mv_\parallel}{2\pi B}\nabla\hat{\mathbf{b}}:\oint_0^{2\pi}d\alpha\mathbf{v}_\perp\mathbf{v}_\perp\\
&=\frac{\mu}{B}v_\parallel\hat{\mathbf{b}}\cdot\nabla B+\frac{mv_\perp^2}{2B}v_\parallel\nabla\hat{\mathbf{b}}:(\overleftrightarrow{\mathrm{I}}-\hat{\mathbf{b}}\hat{\mathbf{b}})\\
&=\frac{\mu}{B}v_\parallel\hat{\mathbf{b}}\cdot\nabla B+\mu v_\parallel(\nabla\cdot\hat{\mathbf{b}})\\
&=\frac{\mu v_\parallel}{B}(\hat{\mathbf{b}}\cdot\nabla B+B\nabla\cdot\hat{\mathbf{b}})=\frac{\mu v_\parallel}{B}\nabla\cdot\mathbf{B}=0.
\end{aligned} \tag{B.62}$$

Note that Equation (B.17) and Equation (B.18) can be used to show the following fact which has been used above

$$\begin{aligned}\nabla\hat{\mathbf{b}} : \hat{\mathbf{b}}\hat{\mathbf{b}} &= \nabla(\hat{\mathbf{e}}_2 \times \hat{\mathbf{e}}_1) : \hat{\mathbf{b}}\hat{\mathbf{b}} = [\nabla\hat{\mathbf{e}}_2 \times \hat{\mathbf{e}}_1 + \hat{\mathbf{e}}_2 \times \nabla\hat{\mathbf{e}}_1] : \hat{\mathbf{b}}\hat{\mathbf{b}} \\ &= [\nabla\hat{\mathbf{e}}_2 \times (\hat{\mathbf{b}} \times \hat{\mathbf{e}}_2) - \nabla\hat{\mathbf{e}}_1 \times (\hat{\mathbf{e}}_1 \times \hat{\mathbf{b}})] : \hat{\mathbf{b}}\hat{\mathbf{b}} \\ &= [\hat{\mathbf{b}}(\nabla\hat{\mathbf{e}}_2 \cdot \hat{\mathbf{e}}_2) - \cancel{\hat{\mathbf{e}}_2}(\nabla\hat{\mathbf{e}}_2 \cdot \hat{\mathbf{b}}) - \cancel{\hat{\mathbf{e}}_1}(\hat{\mathbf{b}} \cdot \nabla\hat{\mathbf{e}}_1) + \hat{\mathbf{b}}(\hat{\mathbf{e}}_1 \cdot \nabla\hat{\mathbf{e}}_1)] : \hat{\mathbf{b}}\hat{\mathbf{b}} \\ &= (\hat{\mathbf{b}} \cdot \hat{\mathbf{b}})(\hat{\mathbf{e}}_1 \cdot \nabla\hat{\mathbf{e}}_1 + \hat{\mathbf{e}}_2 \cdot \nabla\hat{\mathbf{e}}_2) \cdot \hat{\mathbf{b}} = 0.\end{aligned} \tag{B.63}$$

The next term which needs to be gyroaveraged is $-\mathbf{v} \cdot \nabla\boldsymbol{\rho}$ in Equation (2.60). Substituting the definition of $\boldsymbol{\rho}$ gives

$$\begin{aligned}-\langle \mathbf{v} \cdot \nabla\boldsymbol{\rho} \rangle_\alpha &= -\langle \mathbf{v} \cdot \nabla(\frac{\hat{\mathbf{b}} \times \mathbf{v}}{\Omega}) \rangle_\alpha \\ &= -\langle \left[(\hat{\mathbf{b}} \times \mathbf{v})(\mathbf{v} \cdot \nabla(\frac{1}{\Omega})) + \frac{1}{\Omega}\mathbf{v} \cdot (\nabla\hat{\mathbf{b}} \times \mathbf{v}) + \frac{1}{\Omega}\mathbf{v} \cdot (\hat{\mathbf{b}} \times \cancel{\nabla\mathbf{v}}) \right] \rangle_\alpha \\ &= \langle \left[(\hat{\mathbf{b}} \times \mathbf{v})(\frac{m}{qB^2}\mathbf{v} \cdot \nabla B) - \frac{1}{\Omega}\mathbf{v} \cdot (\nabla\hat{\mathbf{b}} \times \mathbf{v}) \right] \rangle_\alpha \\ &= \frac{1}{\Omega}\langle \left[\frac{1}{B}(\mathbf{v} \cdot \nabla B)(\hat{\mathbf{b}} \times \mathbf{v}) - (\mathbf{v} \cdot \nabla\hat{\mathbf{b}}) \times \mathbf{v} \right] \rangle_\alpha.\end{aligned} \tag{B.64}$$

The final terms in Equation (B.64) are split up and solved below. Note that for the first term $\hat{\mathbf{b}} \times \mathbf{v}_\parallel = 0$ so that only perpendicular velocities matter. Gyroaveraging the first term using Equation (2.49) gives

$$\begin{aligned}\frac{1}{B\Omega}\langle (\mathbf{v}_\perp \cdot \nabla B)(\hat{\mathbf{b}} \times \mathbf{v}_\perp) \rangle_\alpha &= \frac{1}{2\pi B\Omega}\oint_0^{2\pi} d\alpha v_{\perp i}\frac{\partial B_j}{\partial x_i}\epsilon_{klm}b_l v_{\perp m} \\ &= \frac{1}{2\pi B\Omega}\frac{\partial B_j}{\partial x_i}\epsilon_{klm}b_l \oint_0^{2\pi} d\alpha v_{\perp i}v_{\perp m} = \frac{v_\perp^2}{2B\Omega}\frac{\partial B_j}{\partial x_i}\epsilon_{klm}b_l(\delta_{im} - b_i\cancel{b_m}) \\ &= \frac{1}{B\Omega}\frac{v_\perp^2}{2}\epsilon_{kli}b_l\frac{\partial B_j}{\partial x_i} = \frac{1}{B\Omega}\frac{v_\perp^2}{2}(\hat{\mathbf{b}} \times \nabla B) = \mathbf{v}_{\nabla B}.\end{aligned} \tag{B.65}$$

For the second term in Equation (B.64), Equation (2.49) shows that only factors combining two parallel and two perpendicular velocities survive the gyroaverage. Focusing on the parallel components

first gives

$$-\langle\frac{1}{\Omega}(\mathbf{v}_\parallel\cdot\nabla\hat{\mathbf{b}})\times\mathbf{v}_\parallel\rangle_\alpha=-\langle\frac{v_\parallel^2}{\Omega}(\hat{\mathbf{b}}\cdot\nabla\hat{\mathbf{b}})\times\hat{\mathbf{b}}\rangle_\alpha=\frac{v_\parallel^2}{\Omega}\hat{\mathbf{b}}\times(\hat{\mathbf{b}}\cdot\nabla\hat{\mathbf{b}})=\mathbf{v}_c, \tag{B.66}$$

which is the curvature drift, Equation (1.28), according to Ref. [65]. Then looking at the perpendicular components gives

$$\begin{aligned}
-\frac{1}{\Omega}\langle(\mathbf{v}_\perp\cdot\nabla\hat{\mathbf{b}})\times\mathbf{v}_\perp\rangle_\alpha&=-\frac{1}{2\pi\Omega}\oint_0^{2\pi}d\alpha\epsilon_{ijk}v_{\perp l}\frac{\partial b_j}{\partial x_l}v_{\perp k}=-\frac{1}{2\pi\Omega}\epsilon_{ijk}\frac{\partial b_j}{\partial x_l}\oint_0^{2\pi}d\alpha v_{\perp l}v_{\perp k}\\
&=-\frac{1}{\Omega}\frac{v_\perp^2}{2}\epsilon_{ijk}\frac{\partial b_j}{\partial x_l}(\delta_{lk}-b_lb_k)=-\frac{1}{\Omega}\frac{v_\perp^2}{2}(\epsilon_{ijl}\frac{\partial b_j}{\partial x_l}-\epsilon_{ijk}\frac{\partial b_j}{\partial x_l}b_lb_k)\\
&=-\frac{1}{\Omega}\frac{v_\perp^2}{2}(-\epsilon_{ilj}\frac{\partial b_j}{\partial x_l}-\epsilon_{ijk}(b_l\frac{\partial b_j}{\partial x_l})b_k)=\frac{1}{\Omega}\frac{v_\perp^2}{2}(\nabla\times\hat{\mathbf{b}}+(\hat{\mathbf{b}}\cdot\nabla\hat{\mathbf{b}})\times\hat{\mathbf{b}})\\
&=\frac{1}{\Omega}\frac{v_\perp^2}{2}(\nabla\times\hat{\mathbf{b}}+\hat{\mathbf{b}}\times(\hat{\mathbf{b}}\times(\nabla\times\hat{\mathbf{b}})))\\
&=\frac{1}{\Omega}\frac{v_\perp^2}{2}(\cancel{\nabla\times\hat{\mathbf{b}}}+\hat{\mathbf{b}}(\hat{\mathbf{b}}\cdot(\nabla\times\hat{\mathbf{b}}))-\cancel{(\nabla\times\hat{\mathbf{b}})}(\hat{\mathbf{b}}\cdot\hat{\mathbf{b}}))\\
&=\frac{1}{\Omega}\frac{v_\perp^2}{2}\hat{\mathbf{b}}(\hat{\mathbf{b}}\cdot(\nabla\times\hat{\mathbf{b}}))=\mathbf{v}_B,
\end{aligned} \tag{B.67}$$

where $\mathbf{v}_B$ is the Baños drift [65], which is in the parallel direction and an order smaller than the parallel streaming velocity.

Combining the results of equations (B.65) - (B.67) gives

$$-\langle\mathbf{v}\cdot\nabla\rho\rangle_\alpha=\mathbf{v}_{\nabla B}+\mathbf{v}_c+\mathbf{v}_B. \tag{B.68}$$

Note that the full term in Equation (2.60) becomes $(\mathbf{v}_{\nabla B}+\mathbf{v}_c+\mathbf{v}_B)\cdot\nabla_{\mathbf{R}}(f_0+\delta h)$. However, $\mathbf{b}\cdot\nabla_{\mathbf{R}}f_0=0$ so the Baños drift does not contribute here. Furthermore, there is also a term $v_\parallel\hat{\mathbf{b}}\cdot\nabla_{\mathbf{R}}\delta h$ in Equation (2.60) which is one order larger than than the Baños drift term so that $\mathbf{v}_B\cdot\nabla_{\mathbf{R}}(f_0+\delta h)\approx 0$ and can be ignored. The final term then becomes

$$-\langle\mathbf{v}\cdot\nabla\rho\rangle_\alpha\cdot\nabla_{\mathbf{R}}(f_0+\delta h)\approx(\mathbf{v}_{\nabla B}+\mathbf{v}_c)\cdot\nabla_{\mathbf{R}}(f_0+\delta h)=\mathbf{v}_d\cdot\nabla_{\mathbf{R}}(f_0+\delta h), \tag{B.69}$$

where the magnetic drifts have been combined into a single term $\mathbf{v}_d$.

The last term which needs to be gyroaveraged is $\partial_t(q\delta\phi_1 f_0/T)$ in Equation (2.60). One can

split up this term into three parts

$$\langle \frac{d}{dt}(\frac{q\delta\phi_1}{T}f_0)\rangle_\alpha = \langle \partial_t(\frac{q\delta\phi_1}{T}f_0) + \mathbf{v}\cdot\nabla(\frac{q\delta\phi_1}{T}f_0) + \frac{q}{m}(\delta\mathbf{E}_1 + \mathbf{v}\times\mathbf{B})\cdot\nabla_\mathbf{v}(\frac{q\delta\phi_1}{T}f_0)\rangle_\alpha, \tag{B.70}$$

and each of these three pieces can be considered separately. The first term in Equation (B.70) gives

$$\langle \partial_t(\frac{q\delta\phi_1}{T}f_0)\rangle_\alpha = \frac{q}{T}f_0\partial_t\langle\delta\phi_1\rangle_\alpha + q\langle\delta\phi_1\rangle_\alpha\partial_t(\frac{f_0}{T}) \approx \frac{q}{T}f_0\partial_t\langle\delta\phi_1\rangle_\alpha. \tag{B.71}$$

The second term in Equation (B.70) is left unchanged for now.

Using the fact from Section 2.3.2 that f_0 is Maxwellian and so doesn't depend on μ or α, and Equations (B.1) to (B.4), the final, third term in Equation (B.70) becomes

$$\langle \frac{q}{m}(\delta\mathbf{E}_1+\mathbf{v}\times\mathbf{B})\cdot\nabla_\mathbf{v}(\frac{q\delta\phi_1}{T}f_0)\rangle_\alpha = \langle \frac{q}{m}(\delta\mathbf{E}_1+\mathbf{v}\times\mathbf{B})\cdot[-\frac{1}{\Omega}(\overleftrightarrow{\mathrm{I}}\times\hat{\mathbf{b}})\cdot\nabla_\mathrm{R}(\frac{q\delta\phi_1}{T}f_0) - \frac{q\delta\phi_1}{T}(m\mathbf{v})\frac{\partial f_0}{\partial\epsilon}]\rangle_\alpha. \tag{B.72}$$

Equation (B.72) can be simplified using relations Equations (B.23) to (B.25) and Equation (B.28) to get

$$\langle \frac{q^2}{m\Omega}(\delta\mathbf{E}_1\times\hat{\mathbf{b}})\cdot\nabla_\mathbf{R}(\frac{\delta\phi_1}{T}f_0)\rangle_\alpha - \langle\mathbf{v}_\perp\cdot\nabla_\mathbf{R}(\frac{q\delta\phi_1}{T}f_0)\rangle_\alpha - \langle\frac{q^2}{T^2}\delta\phi_1 f_0\mathbf{v}\cdot\delta\mathbf{E}_1\rangle_\alpha. \tag{B.73}$$

Breaking up the first term in Equation (B.73) and using **??** one has to lowest order

$$\begin{aligned}
&\langle \frac{q^2\delta\phi_1}{m\Omega}(\delta\mathbf{E}_1\times\hat{\mathbf{b}})\cdot\nabla_\mathbf{R}(\frac{f_0}{T})\rangle_\alpha + \langle\frac{q^2 f_0}{mT\Omega}(\delta\mathbf{E}_1\times\hat{\mathbf{b}})\cdot\nabla_\mathbf{R}(\delta\phi)\rangle_\alpha \\
&\quad\approx \langle \frac{q^2\delta\phi_1}{m\Omega}(\delta\mathbf{E}_1\times\hat{\mathbf{b}})\cdot\nabla_\mathbf{R}(\frac{f_0}{T})\rangle_\alpha + \langle\frac{q^2 f_0}{mT\Omega}(\delta\mathbf{E}_1\times\hat{\mathbf{b}})\cdot\nabla(\delta\phi)\rangle_\alpha \\
&\quad= \langle \frac{q^2\delta\phi_1}{m\Omega}(\delta\mathbf{E}_1\times\hat{\mathbf{b}})\cdot\nabla_\mathbf{R}(\frac{f_0}{T})\rangle_\alpha - \langle\frac{q^2 f_0}{mT\Omega}\cancel{(\delta\mathbf{E}_1\times\hat{\mathbf{b}})\cdot\delta\mathbf{E}_1}\rangle_\alpha \\
&\quad\approx 0,
\end{aligned} \tag{B.74}$$

where the order of the remaining term before gyroaveraging is

$$\frac{\frac{q\delta\phi_1}{T}v_E\frac{f_0}{L}}{\frac{v_{th}}{L}f_0} \sim \epsilon\frac{v_E}{v_{th}} \sim \epsilon^2. \tag{B.75}$$

Looking at the final term in Equation (B.73) one has

$$\begin{aligned}
-\langle\frac{q^2}{T^2}\delta\phi_1 f_0\mathbf{v}\cdot\delta\mathbf{E}_1\rangle_\alpha &= \frac{q^2}{T^2}f_0\langle\delta\phi_1(v_\parallel\hat{\mathbf{b}}+\mathbf{v}_\perp)\cdot\delta\mathbf{E}_1\rangle_\alpha \\
&\approx \frac{q^2}{T^2}f_0\langle\delta\phi_1(\mathbf{v}_\perp\cdot\delta\mathbf{E}_1)\rangle_\alpha \\
&= -\frac{q^2}{T^2}f_0\langle\delta\phi_1\Omega\frac{\partial\delta\phi_1}{\partial\alpha}\rangle_\alpha \\
&= -\frac{q^2}{T^2}f_0\langle\frac{1}{2}\Omega\frac{\partial(\delta\phi_1)^2}{\partial\alpha}\rangle_\alpha = 0,
\end{aligned} \tag{B.76}$$

where the parallel velocity term has been dropped as lower order and Equation (2.46) has been used.

At this point only the second term from Equation (B.73) remains, so it can be substituted into Equation (B.70) along with Equation (B.71) to find

$$\langle\frac{d}{dt}(\frac{q\delta\phi_1}{T}f_0)\rangle_\alpha \approx \frac{q}{T}f_0\partial_t\langle\delta\phi_1\rangle_\alpha + \langle\mathbf{v}\cdot\nabla(\frac{q\delta\phi_1}{T}f_0) - \mathbf{v}_\perp\cdot\nabla_{\mathbf{R}}(\frac{q\delta\phi_1}{T}f_0)\rangle_\alpha. \tag{B.77}$$

Using Equation (2.47), the second term in Equation (B.77) can be broken up as

$$\langle\mathbf{v}\cdot\nabla(\frac{q\delta\phi_1}{T}f_0)\rangle_\alpha = -\frac{q}{T}f_0 v_\parallel\hat{\mathbf{b}}\cdot\langle\delta\mathbf{E}_1\rangle_\alpha - \frac{q}{T}f_0\cancel{\langle\mathbf{v}_\perp\cdot\delta\mathbf{E}_1\rangle_\alpha} + \langle q\delta\phi_1\mathbf{v}\cdot\nabla_{\mathbf{R}}(\frac{f_0}{T})\rangle_\alpha, \tag{B.78}$$

while the third term in Equation (B.77) can be broken up as

$$\begin{aligned}
-\langle\mathbf{v}_\perp\cdot\nabla_{\mathbf{R}}(\frac{q\delta\phi_1}{T}f_0)\rangle_\alpha &= -\langle q\delta\phi_1\mathbf{v}_\perp\cdot\nabla_{\mathbf{R}}(\frac{f_0}{T})\rangle_\alpha - \frac{q}{T}f_0\langle\mathbf{v}_\perp\cdot\nabla_{\mathbf{R}}\delta\phi_1\rangle_\alpha \\
&\approx -\langle q\delta\phi_1\mathbf{v}_\perp\cdot\nabla_{\mathbf{R}}(\frac{f_0}{T})\rangle_\alpha - \frac{q}{T}f_0\cancel{\langle\mathbf{v}_\perp\cdot\nabla\delta\phi_1\rangle_\alpha} \\
&= -\langle q\delta\phi_1\mathbf{v}_\perp\cdot\nabla_{\mathbf{R}}(\frac{f_0}{T})\rangle_\alpha
\end{aligned} \tag{B.79}$$

where Equation (2.47) and **??** have been used. Finally, Equation (B.78) and Equation (B.79) can be substituted into Equation (B.77) and simplified to arrive at

$$\langle\frac{d}{dt}(\frac{q\delta\phi_1}{T}f_0)\rangle_\alpha \approx \frac{q}{T}f_0\partial_t\langle\delta\phi_1\rangle_\alpha - \frac{q}{T}f_0 v_\parallel\hat{\mathbf{b}}\cdot\langle\delta\mathbf{E}_1\rangle_\alpha. \tag{B.80}$$

Appendix C

Derivation of ITG Dispersion Relation

The ITG dispersion relation used in Section 2.4.1 can be derived by combining the gyrokinetic equation, Equation (2.63), with the quasineutrality relation, Equation (2.29). Linearizing the gyrokinetic Vlasov equation and assuming a Fourier representation, Equation (2.25), for δh one finds

$$-i(\omega - k_\parallel v_\parallel - \mathbf{v}_d \cdot \nabla_{\mathbf{R}})\delta h = \frac{eJ_0(k_\perp \rho_i)\delta\phi_1}{T_i} f_0 - J_0(k_\perp \rho_i)(\frac{\nabla_{\mathbf{R}}\delta\phi_1 \times \hat{\mathbf{b}}}{B}) \cdot \nabla_{\mathbf{R}} f_0. \tag{C.1}$$

The gradients and drift terms can be simplified given the large aspect-ratio equations defined by Equations (1.45) to (1.48) and the fact that $\nabla_{\mathbf{R}} \approx \nabla$ (as in the case of $\delta\phi$ in Chapter 2). The magnetic drift is given by

$$\mathbf{v}_d = \frac{v_\parallel^2 + \frac{1}{2}v_\perp^2}{\Omega_j} \frac{\mathbf{B} \times \nabla B}{B^2}. \tag{C.2}$$

Simplifying to lowest order in ϵ one has

$$\begin{aligned}
\frac{\boldsymbol{B} \times \nabla B}{B^2} &= \frac{B_0[(1-\epsilon\cos\theta)\hat{\boldsymbol{e}}_\zeta + \frac{\epsilon}{q}\hat{\boldsymbol{e}}_\theta] \times [(\partial_r \hat{\boldsymbol{e}}_r + \frac{1}{r}\partial_\theta \hat{\boldsymbol{e}}_\theta + \frac{1}{R}\partial_\zeta \hat{\boldsymbol{e}}_\zeta) B_0(1-\epsilon\cos\theta)]}{B_0^2(1-\epsilon\cos\theta)^2} \\
&= \frac{[(1-\epsilon\cos\theta)\hat{\boldsymbol{e}}_\zeta + \frac{\epsilon}{q}\hat{\boldsymbol{e}}_\theta] \times [-\frac{1}{R_0}\cos\theta\hat{\boldsymbol{e}}_r + \frac{r}{rR_0}\sin\theta\hat{\boldsymbol{e}}_\theta]}{(1-\epsilon\cos\theta)^2} \\
&= \frac{1}{(1-\epsilon\cos\theta)^2}[-\frac{(1-\epsilon\cos\theta)\cos\theta}{R_0}(\hat{\boldsymbol{e}}_\zeta \times \hat{\boldsymbol{e}}_r) - \frac{(1-\epsilon\cos\theta)\cos\theta}{R_0}(\hat{\boldsymbol{e}}_\zeta \times \hat{\boldsymbol{e}}_\theta) \\
&\qquad - \frac{\epsilon}{qR_0}\cos\theta(\hat{\boldsymbol{e}}_\theta \times \hat{\boldsymbol{e}}_r)] \\
&\simeq (1+2\epsilon\cos\theta)[-\frac{\cos\theta}{R_0}\hat{\boldsymbol{e}}_\theta - \frac{\sin\theta}{R_0}\hat{\boldsymbol{e}}_r] \simeq -\frac{1}{R_0}(\sin\theta\hat{\boldsymbol{e}}_r + \cos\theta\hat{\boldsymbol{e}}_\theta)\ ,
\end{aligned} \tag{C.3}$$

and the third term in Equation (C.1) becomes

$$\begin{aligned}\boldsymbol{v}_d \cdot \nabla_X \approx \boldsymbol{v}_d \cdot \nabla &= -\frac{v_\parallel^2 + \frac{1}{2}v_\perp^2}{\Omega_j}(\sin\theta\hat{\boldsymbol{e}}_r + \cos\theta\hat{\boldsymbol{e}}_\theta)\cdot(\partial_r\hat{\boldsymbol{e}}_r + \frac{1}{r}\partial_\theta\hat{\boldsymbol{e}}_\theta) \\ &= -\frac{v_\parallel^2 + \frac{1}{2}v_\perp^2}{\Omega_j R_0}(\sin\theta\partial_r + \frac{\cos\theta}{r}\partial_\theta) = -\frac{ik_\theta T_j m_j}{q_j T_j B_0 R_0}(v_\parallel^2 + \frac{1}{2}v_\perp^2)(\frac{k_r}{k_\theta}\cos\theta + \sin\theta) \\ &= -\omega_{dj}(\frac{v_\parallel^2}{v_{th,j}^2} + \frac{1}{2}\frac{v_\perp^2}{v_{th,j}^2})(\cos\theta + \frac{k_r}{k_\theta}\sin\theta) = -\bar{\omega}_{dj},\end{aligned} \tag{C.4}$$

where $\omega_{dj} = \frac{n}{\nabla n}\omega_{*j}$ is the magnetic drift frequency and $v_{th,j} = \sqrt{T_j/m_j}$. From hereon we will assume $k_r = 0$ for simplicity.

The spatial gradient of the Maxwellian distribution can be calculated as

$$\begin{aligned}\nabla f_{M,j} &= \frac{dn}{dr}\frac{d}{dn}f_{M,j} + \frac{dT}{dr}\frac{d}{dT}f_{M,j} = \frac{dn}{dr}e^{-\frac{m_j\epsilon^*}{T_j(r)}} + \frac{dT}{dr}\frac{du}{dT}\frac{d}{du}[n_j\left(\frac{m_j u(T(r))}{2\pi}\right)^{3/2}e^{-m_j\epsilon^* u(T_j(r))}] \\ &= \frac{1}{n}\frac{dn}{dr}f_{M,j} + \frac{dT}{dr}\frac{du}{dT}n_j[\frac{3}{2}\left(\frac{m_j u}{2\pi}\right)^{1/2}\left(\frac{m_j}{2\pi}\right) - m_j\epsilon^*\left(\frac{m_j u}{2\pi}\right)^{3/2}]e^{-m_j\epsilon^* u(T_j(r))} \\ &= \frac{1}{n}\frac{dn}{dr}f_{M,j} + \frac{dT}{dr}\frac{du}{dT}[\frac{3}{2}u^{-1} - m_j\epsilon^*]f_{M,j} = [\frac{1}{n}\frac{dn}{dr} + \frac{dT}{dr}(-\frac{1}{T^2})(\frac{3}{2}u^{-1} - m_j\epsilon^*)]f_{M,j} \\ &= [\frac{1}{n}\frac{dn}{dr} - \frac{1}{T}\frac{dT}{dr}(\frac{3}{2} - \frac{m_j v^2}{2T_j})]f_{M,j} = [\frac{1}{n}\frac{dn}{dr} - \frac{1}{T}\frac{dT}{dr}(\frac{3}{2} - \frac{v^2}{2v_{T,j}^2})]f_{M,j} \\ &= \frac{1}{n}\frac{dn}{dr}[1 + (\frac{1}{2}\left(\frac{v}{v_{T,j}}\right)^2 - \frac{3}{2})\eta_j]f_{M,j},\end{aligned} \tag{C.5}$$

given that $u = T^{-1}$, $du = -T^{-2}dT$, and $\epsilon^* = \epsilon/m_j$. Lastly, the **E**x**B** drift becomes

$$\frac{\nabla\delta\phi_1 \times \hat{\mathbf{b}}}{B} = \frac{i\delta\phi_1}{B}\mathbf{k}\times\hat{\mathbf{b}} = \frac{i\delta\phi_1}{B}(k_r\hat{\boldsymbol{e}}_r + k_\theta\hat{\boldsymbol{e}}_\theta + k_\zeta\hat{\boldsymbol{e}}_\zeta)\times(\frac{\epsilon}{q}\hat{\boldsymbol{e}}_\theta + \hat{\boldsymbol{e}}_\zeta) \approx -\frac{i\delta\phi_1}{B}(k_r\hat{\boldsymbol{e}}_\theta + k_\theta\hat{\boldsymbol{e}}_r), \tag{C.6}$$

so that the last term in Equation (C.1) can be rewritten as

$$\begin{aligned}\frac{q_j}{m_j}\langle\mathbf{v}_E\rangle_\alpha\cdot\nabla_{\mathbf{R}}f_0 &= iJ_0(k_\perp\rho_j)\delta\phi_1\frac{k_\theta m_j}{q_j B}\left[1 + \left(\frac{1}{2}(\frac{v}{v_{th,j}})^2 + \frac{3}{2}\right)\eta_j\right]f_{Mj} \\ &= i\frac{q_j}{T_j}J_0(k_\perp\rho_j)\delta\phi_1\omega_{*j}\left[1 + \left(\frac{1}{2}(\frac{v}{v_{th,j}})^2 + \frac{3}{2}\right)\eta_j\right]f_{Mj} \\ &= i\frac{q_j}{T_j}J_0(k_\perp\rho_j)\delta\phi_1\omega_{*j}^T f_{Mj}.\end{aligned} \tag{C.7}$$

The quantity $\omega_{*j}\left[1+\left(\frac{1}{2}(\frac{v}{v_{th,j}})^2+\frac{3}{2}\right)\eta_j\right]$ has been defined as ω_{*j}^T. Equation (C.4) and Equation (C.7) can be substituted into Equation (C.1) for ions to find

$$\delta h = \frac{q_i}{T_i} J_0(k_\perp \rho_i)\delta\phi_1 \frac{\omega-\omega_{*i}^T}{\omega - k_\parallel v_\parallel - \bar{\omega}_{di}} f_{0i} \tag{C.8}$$

Assuming protons as a main ion species and an adiabatic electron response, the quasineutrality equation becomes

$$e(\frac{e\delta\phi_1}{T_i}+\frac{e\delta\phi_1}{T_e})n_0 = e\int d^3\mathbf{v}\langle\delta h\rangle_\alpha = e\int d^3\mathbf{v} J_0(k_\perp\rho_i)\delta h. \tag{C.9}$$

Equation (C.8) and Equation (C.9) can be combined to find

$$(1+\frac{1}{\tau}) = \frac{2\pi}{n_i}\int_{-\infty}^{\infty}\int_0^\infty v_\perp dv_\perp dv_\parallel f_{0i} J_0^2(k_\perp\rho_i)\frac{\omega-\omega_{*j}^T}{\omega-k_\parallel v_\parallel-\bar{\omega}_{di}}, \tag{C.10}$$

where $\tau = T_e/T_i$. Various simplifications are made here to enable simple integration of the resonant denominator. The interested reader can find proper consideration of the contour integration given analytic continuation described in Ref. [36]. Here we assume a fluid ion response, $k_\parallel v_{th,e} \gg \omega \gg k_\parallel v_{th,i}$, and ignore ion FLR effects, $k_\perp\rho_i \Rightarrow 0$, so that $J_0(k_\perp\rho_i)\to 1$. Additionally it is assumed that the wave frequency is much larger than the magnetic drift frequency $\omega \gg \omega_{di}$. These frequency assumptions allow for Taylor expanding the denominator to find

$$\begin{aligned}
(1+\frac{1}{\tau}) &= \frac{2\pi}{n_i}\int_{-\infty}^{\infty}\int_0^\infty v_\perp dv_\perp dv_\parallel f_{0i}\frac{\omega-\omega_{*j}^T}{\omega}\left[1-(-\frac{k_\parallel v_\parallel-\bar{\omega}_{di})}{\omega}\right] \\
&= \frac{2\pi}{n_i}\int_{-\infty}^{\infty}\int_0^\infty v_\perp dv_\perp dv_\parallel f_{0i}(1-\frac{\omega_{*i}^T}{\omega})\left[1+\frac{\cancel{k_\parallel v_\parallel}}{\omega}+\frac{\bar{\omega}_{di}}{\omega}+\frac{k_\parallel^2 v_\parallel^2}{\omega^2}\right] \\
&= \frac{2\pi}{n_i}\int_{-\infty}^{\infty}\int_0^\infty v_\perp dv_\perp dv_\parallel f_{0i}(1-\frac{\omega_{*i}^T}{\omega}+\frac{\bar{\omega}_{di}}{\omega}+\frac{k_\parallel^2 v_\parallel^2}{\omega^2}-\frac{\omega_{*i}^T\bar{\omega}_{di}}{\omega^2}).
\end{aligned} \tag{C.11}$$

Note the second order parallel term has been retained because odd moment integrals of the parallel Maxwellian distribution will result in 0, and ω_{*i}^T only depends on even powers of $v_\parallel$. The general

formulas for moments of Gaussian integrals are [238]

$$\begin{aligned}
\int_{-\infty}^{\infty} x^{2m} e^{-(x/a)^2} dx &= a^{2m+1}\sqrt{\pi}\frac{(2m-1)!!}{2^m}, \qquad \text{for even n} = 2\text{m}, \\
\int_{0}^{\infty} x^{n} e^{-(x/a)^2} dx &= \frac{\sqrt{\pi}}{2} a^{n+1}\frac{(n-1)!!}{2^{(n+1)/2}}, \qquad \text{for odd n}, \\
\int_{0}^{\infty} x^{n} e^{-(x/a)^2} dx &= \frac{1}{2} a^{n+1}\frac{(n-1)!!}{2^{(n+1)/2}}, \qquad \text{for even n}.
\end{aligned} \tag{C.12}$$

where $(2n-1)!! = (2n-1)(2n-3)(2n-5)\ldots$ is the double factorial. Expanding out everything in Equation (C.11) and integrating using Equation (C.12) gives

$$\begin{aligned}
(1+\frac{1}{\tau}) &= 2\pi\left(\frac{m_i}{2\pi T_i}\right)^{3/2}\int_{-\infty}^{\infty}\int_{0}^{\infty} v_\perp dv_\perp dv_\parallel [1 + \frac{k_\parallel^2 v_\parallel^2}{\omega^2} - \frac{\omega_{*i}}{\omega}(1 + (\frac{v_\parallel^2+v_\perp^2}{2v_{th,i}^2} - \frac{3}{2})\eta_i) \\
&+ \frac{\omega_{dj}\cos\theta}{\omega}(\frac{v_\parallel^2}{v_{th,j}^2} + \frac{v_\perp^2}{2v_{th,j}^2}) - \frac{\omega_{*i}\omega_{dj}\cos\theta}{\omega^2}[(1-\frac{3}{2}\eta_i)(\frac{v_\parallel^2+v_\perp^2}{2v_{th,i}^2}) + \eta_i(\frac{v_\parallel^4}{2v_{th,i}^4} + \frac{3v_\parallel^2 v_\perp^2}{4v_{th,i}^4} + \frac{v_\perp^4}{4v_{th,i}^4})]] \\
&= 1 + [\frac{k_\parallel^2 v_{th,i}^2}{\omega^2} - \frac{\omega_{*i}}{\omega}(1 - \cancel{\frac{3}{2}}\eta_i + (1+\cancel{\frac{1}{2}})\eta_i) + 2\frac{\omega_{di}}{\omega}\cos\theta - 2\omega_{*i}\omega_{di}[1 - \frac{3}{2}\eta_i + 4\eta_i(\frac{5}{8})]] \\
&= 1 - \frac{\omega_{*i}}{\omega} + 2\frac{\omega_{di}}{\omega}\cos\theta + \frac{k_\parallel^2 v_{th,i}^2}{\omega^2} - 2\frac{\omega_{*i}\omega_{di}}{\omega^2}(1+\eta_i)\cos\theta.
\end{aligned} \tag{C.13}$$

The final result here is equal to Equation (2.68). In Section 2.4.1 the dispersion relation is solved to find the ITG growth rate formula, Equation (2.72).

Appendix D

Ballooning Mode Representation

The ballooning mode representation, or ballooning transformation, is a useful mathematical tool which allows for reducing the drift-wave eigenmode equation to one dimension, allowing for a more straightforward solution for the eigenfunction along the field line at a given flux surface [81, 82]. One can best understand the physical meaning behind the ballooning transform by starting from the general eigenmode expression, Equation (2.25), and following the methods of [83]. The notes deriving the ballooning mode transform are reproduced courtesy of Scott Parker and figures are generated from Python simulations written in collaboration with Wes Johnson. A simplification can be made for high-n modes in tokamaks ($n \gg 1$) such as ITG or ETG modes by considering two factors. The first is that ballooning modes are most unstable on rational flux surfaces as $k_{\|} \to 0$ and the stabilizing effect of Landau damping is lost. Secondly, the mode width around a rational surface takes the form of a Gaussian to lowest order, where the width depends on some inverse factor of n and so decreases as the mode number increases [22]. In these cases, Equation (2.25) can be rewritten for a single mode n_0 and a sum of coupled poloidal harmonics due to the nearby resonant surfaces,

$$\phi(r,\theta,\zeta,t) = \sum_{j=-N_\theta}^{+N_\theta} \phi_j(r) e^{-i\omega_{n_0} t - i n_0 \zeta + i(m_0+j)\theta}. \tag{D.1}$$

The dominant poloidal mode here occurs at $m_0 = n_0 q(r_0)$, and the next most important modes are the sidebands at $m = m_0 \pm 1$, ± 2, and so on. The wave notation for n_0 and ω is now dropped for simplicity.

Considering a local approximation with constant magnetic shear one can determine the spacing between mode rational surfaces,

$$m_0 + 1 = n_0(q(r_0) + q'(r - r_0)) \Rightarrow 1 = \Delta r n_0 q' \Rightarrow \Delta r = \frac{1}{n_0 q'} = \frac{r_0}{m_0}\frac{q(r_0)}{r_0 q'} = \frac{1}{k_\theta \hat{s}}. \tag{D.2}$$

The different radial modes can be assumed to have the same shape such that one can make the replacement

$$\phi_j(r) = \phi(\frac{r}{\Delta r} - j). \tag{D.3}$$

In general however, the amplitude of modes varies globally and one must consider a slowly varying envelope function $A_{n_0}(r)$ as well. The new form for the toroidal eigenfunction is then

$$\phi_{n_0,\omega}(r,\theta) = A_{n_0}(r) \sum_{j=-N_\theta}^{+N_\theta} \phi(\frac{r}{\Delta r} - j) e^{i(m_0+j)\theta}. \tag{D.4}$$

The conventional ballooning mode representation is found by Fourier transforming Equation (D.4).

For now the transformation of the radial envelope will be ignored, and one can define the Fourier transform of the radial function

$$\phi(u) = \int_{-\infty}^{\infty} \tilde{\phi}(\eta) e^{i\eta u} d\eta. \tag{D.5}$$

Substituting Equation (D.5) into Equation (D.4) one finds

$$\begin{aligned}
\phi_{n_0,\omega}(r,\theta) &= A_{n_0}(r) \sum_{j=-N_\theta}^{+N_\theta} \int_{-\infty}^{\infty} \tilde{\phi}(\eta) e^{\left(i\eta(\frac{r}{\Delta r} - j)\right)} e^{i(m_0+j)\theta} d\eta \\
&= A_{n_0}(r) \sum_m \int_{-\infty}^{\infty} \tilde{\phi}(\eta) e^{im\theta} e^{-i(m-m_0)\eta} e^{i\eta\frac{r}{\Delta r}} d\eta \\
&= A_{n_0}(r) \sum_m e^{im\theta} \int_{-\infty}^{\infty} \tilde{\phi}(\eta) e^{-i(m - n_0 q(r_0) - \frac{r}{\Delta r})\eta} d\eta \\
&= A_{n_0}(r) \sum_m e^{im\theta} \int_{-\infty}^{\infty} \tilde{\phi}(\eta) e^{-i(m - n_0 q(r))\eta} d\eta.
\end{aligned} \tag{D.6}$$

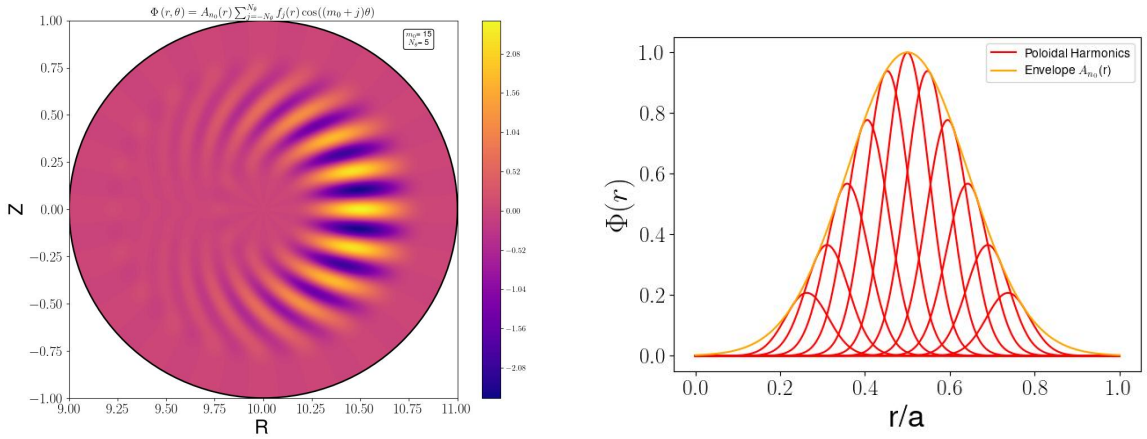

(a) (b)

Figure D.1: (a) Ballooning mode structure in the tokamak cross section given by the radial eigenmodes shown in (b).

Considering the large aspect-ratio approximation and recalling the definition of the parallel wavenumber, Equation (2.26), it is clear from the exponential factor of Equation (D.6) that

$$\eta = q_0 R_0 z, \tag{D.7}$$

for a coordinate z along the field line. Therefore, η is a field-line-following coordinate which spans the domain $(-\infty, \infty)$, and it is evident that the Fourier transform for the local radial eigenmode in the tokamak gives an eigenfunction extending infinitely along a field line.

Furthermore, one can consider transforming the slow radial envelope as well to find the ballooning mode representation defined in Section 4.1.3,

$$\phi_{\mathbf{k}} = \sum_m e^{i(m\theta - n\zeta)} \int\int d\eta d\theta_k e^{i[nq(\eta-\theta_k)-m\eta]} A_{\mathbf{k}} \tilde{\phi}_{\mathbf{k}}. \tag{D.8}$$

The ballooning mode structure is plotted in Figure D.1(a) using Equation (D.4). Gaussian radial modes and a Gaussian envelope are assumed, along with the magnetic field defined by Equation (1.45) and Equation (1.46), and the safety factor profile for the circular CBC case. The radial mode structure is illustrated in Figure D.1(b). The variable θ_k is known as the ballooning or tilting angle,

defined as the poloidal angle at which the mode peaks. One may notice that the mode begins to tilt in the perpendicular plane when moving poloidally from the mode peak at $\theta = 0$.

This effect can be understood more clearly by the standard representation of the ballooning mode transformation [36]

$$\phi(r, \theta, \zeta) = \sum_{p=-\infty}^{\infty} \hat{\phi}(\theta_0, \theta + 2\pi p) e^{-in(\zeta - q(r)(\theta - \theta_0 + 2\pi p))}. \tag{D.9}$$

Here θ is the field-line-following angle and θ_0 gives the ballooning angle, generally assumed to peak at $\theta = 0$. An infinite sum over modes along the field line is required to enforce poloidal periodicity if each mode extends more than $\pm\pi$ along the field. The ballooning mode structure along the field line for the case of Figure D.1(a) is shown in Figure D.2 for comparison to the corresponding radial mode structure in Figure D.1(b). Note the field-line structure is only plotted in the domain $[-\pi, \pi]$ but is periodic over 2π. In this case, the mode is considered "strongly ballooning" and only the $p = 0$ term is necessary to describe it. Assuming $p = 0$ and $\theta_0 = 0$ and calculating the radial wavenumber, $k_r = -i\partial_r$, one finds [36]

$$k_r = nq'\theta = k_\theta \hat{s}\theta, \tag{D.10}$$

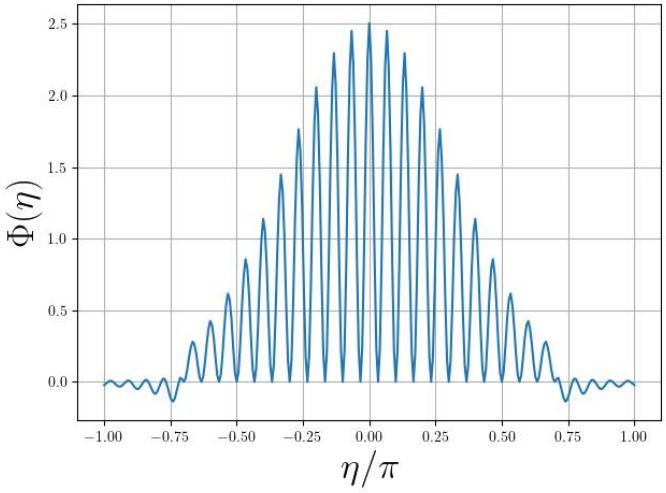

Figure D.2: Real value of the electrostatic potential plotted along the field line for the ballooning mode from Figure D.1(a).

where $k_\theta = nq/r$. That is, increasing k_x components will be located further along the field line in θ, causing the mode to tilt radially along the field line. This is fairly unsurprising given the original treatment, as the Fourier transform of the radial coordinate was related to the field line coordinate.

Appendix E

Hasegawa-Mima Toy Model Derivation

The Hasegawa-Mima equation simulated in Section 4.1.1 is derived here for the case of an ETG mode with adiabatic ions, $k_\parallel \neq 0$, and isothermal electrons ($\delta T_e = 0$). These notes are provided courtesy of Haotian Chen. The continuity and momentum equations for the electrons are

$$\partial_t n_e + \nabla \cdot (n_e \mathbf{v}_e) = 0, \tag{E.1}$$

$$m_e \frac{d\mathbf{v}_e}{dt} = -e(-\nabla\phi + \frac{\mathbf{v}_e \times \mathbf{B}}{c}) - \frac{\nabla(P_e + \delta P_e)}{n_e} = (1+\tau)e\nabla\phi - e\frac{\mathbf{v}_e \times \mathbf{B}}{c} - \frac{\nabla P_e}{n_e}, \tag{E.2}$$

where $\tau = T_e/T_i$. Taking parallel and perpendicular components of Equation (E.2) results in

$$m_e \hat{\mathbf{b}} \cdot \frac{d\mathbf{v}_e}{dt} = (1+\tau)e\nabla_\parallel \delta\phi \quad \Rightarrow \quad \mathbf{v}_\parallel = (1+\tau)\frac{e}{m_e}\partial_t^{-1}\nabla_\parallel \delta\phi, \tag{E.3}$$

and

$$\hat{\mathbf{b}} \times \frac{d\mathbf{v}_e}{dt} = (1+\tau)\frac{e}{m_e}\hat{\mathbf{b}} \times \nabla\delta\phi - \Omega_{ce}\mathbf{v}_{e\perp} - \frac{\hat{\mathbf{b}} \times \nabla P_e}{m_e n_e}. \tag{E.4}$$

Equation (E.4) can be solved perturbatively. To lowest order one finds

$$\mathbf{v}_{e\perp,0} = (1+\tau)\frac{e}{m_e\Omega_{ce}}\hat{\mathbf{b}} \times \nabla\delta\phi - \frac{\hat{\mathbf{b}} \times \nabla P_e}{m_e\Omega_{ce}n_e} = (1+\tau)\mathbf{v}_E + \mathbf{v}_D, \tag{E.5}$$

and the total lowest order drift motion is

$$\mathbf{v}_{e,0} = \mathbf{v}_{\parallel} + (1+\tau)\mathbf{v}_E + \mathbf{v}_D. \tag{E.6}$$

The polarization drift can be found to next order,

$$\mathbf{v}_{e,1} = -\frac{1}{\Omega_{ce}}(\partial_t + \mathbf{v}_{e,0}\cdot\nabla)(\hat{\mathbf{b}}\times\mathbf{v}_{e,0}), \tag{E.7}$$

which can be approximated to second order as

$$\begin{aligned}
\mathbf{v}_{e,1} &\approx -\frac{1+\tau}{\Omega_{ce}}\left[\partial_t + ((1+\tau)\mathbf{v}_E + \mathbf{v}_D)\cdot\nabla\right](\hat{\mathbf{b}}\times\mathbf{v}_E) \\
&= \{\partial_t + \frac{1}{m_e\Omega_{ce}}\left[(1+\tau)e\hat{\mathbf{b}}\times\nabla_\perp\delta\phi - \frac{\hat{\mathbf{b}}\times\nabla P_e}{n_e}\right]\cdot\nabla_\perp\}\frac{e(1+\tau)}{m_e\Omega_{ce}^2}\nabla_\perp\delta\phi \\
&= \frac{e(1+\tau)}{m_e\Omega_{ce}^2}\partial_t\nabla_\perp\delta\phi - \left[\frac{\hat{\mathbf{b}}\times\nabla P_e}{n_e}\cdot\nabla_\perp\right]\frac{e(1+\tau)}{m_e^2\omega_{ce}^3}\nabla_\perp\delta\phi + \frac{e^2(1+\tau)^2}{m_e^2\Omega_{ce}^3}\left[\hat{\mathbf{b}}\times\nabla_\perp\delta\phi\cdot\nabla_\perp\right]\nabla_\perp\delta\phi.
\end{aligned} \tag{E.8}$$

Incompressibility in slab geometry ($\nabla\cdot\mathbf{v}_{e,\perp,0}$) combined with Equation (E.1) yields

$$\partial_t\delta n_e + n_e\nabla\cdot(\mathbf{v}_{\parallel} + \mathbf{v}_{e,1}) + \nabla\delta n_e\cdot\mathbf{v}_D + (1+\tau)\nabla n_e\cdot\mathbf{v}_E = 0, \tag{E.9}$$

where the following orderings have been assumed:

$$\frac{k_\parallel}{k_\perp}\sim\frac{\rho_e}{r_n}\sim\epsilon,\ \frac{\omega}{\Omega_{ce}}\sim\frac{k_\perp\rho_e}{2\tau}\frac{\rho_e}{r_n}\sim\epsilon^{3/2},\ \frac{\delta n_e}{n_e}\sim\epsilon,\ k_\perp^2\rho_e^2\sim\epsilon,\ \tau\sim 1,\ \frac{v_D}{v_E}\sim 1,\ k_\parallel^2 r_n^2\sim\epsilon, \tag{E.10}$$

$$\frac{n_e\nabla\cdot\mathbf{v}_\parallel}{\nabla n_e\cdot\mathbf{v}_E}\sim\frac{4\tau^2k_\parallel^2r_n^2}{k_\perp^2\rho_e^2}\sim 1,\ \frac{n_e\nabla\cdot\mathbf{v}_{e,1}}{\nabla n_e\cdot\mathbf{v}_E}\sim k_\perp\rho_e\frac{r_n}{\rho_e}\frac{\omega}{\Omega_{ce}}\sim\epsilon, \tag{E.11}$$

$$\frac{\nabla\delta n_e\cdot\mathbf{v}_D}{\nabla n_e\cdot\mathbf{v}_E}\sim k_\perp\rho_e\frac{r_n}{\rho_e}\frac{\delta n_e}{n_e}\sim\epsilon^{1/2},\ \frac{\nabla_\parallel\delta n_e\cdot\mathbf{v}_\parallel}{\nabla n_e\cdot\mathbf{v}_E}\sim\frac{\delta n_e}{n_e}k_\parallel r_n\frac{k_\parallel}{k_\perp}\frac{\Omega_{ce}}{\omega}\sim\epsilon^{3/2},\ \frac{\nabla n_e\cdot\mathbf{v}_{e,1}}{\nabla n_e\cdot\mathbf{v}_E}\sim\epsilon^{3/2}. \tag{E.12}$$

Substituting $\delta n_e = \delta n_i$ into Equation (E.9) and retaining terms up to order ϵ gives the HM

equation

$$
\begin{aligned}
&- n_e\partial_t\frac{e\delta\phi}{T_i} + n_e(1+\tau)\frac{e}{m_e}\partial_t^{-1}\nabla_\parallel^2\delta\phi + \frac{en_e(1+\tau)}{m_e\Omega_{ce}^2}\partial_t\nabla_\perp^2\delta\phi \\
&- \frac{e(1+\tau)}{m_e^2\Omega_{ce}^3}\left[\hat{\mathbf{b}}\times\nabla P_e\cdot\nabla_\perp\right]\nabla_\perp^2\delta\phi + \frac{e^2n_e(1+\tau)^2}{m_e^2\Omega_{ce}^3}\left[\hat{\mathbf{b}}\times\nabla_\perp\delta\phi\cdot\nabla_\perp\right]\nabla_\perp^2\delta\phi \\
&+ \nabla_\perp\frac{e\delta\phi}{T_i}\cdot\frac{\hat{\mathbf{b}}\times\nabla P_e}{m_e\Omega_{ce}} + \frac{e(1+\tau)}{m_e\Omega_{ce}}\nabla n_e\cdot\hat{\mathbf{b}}\times\nabla\phi = 0.
\end{aligned}
\tag{E.13}
$$

Lastly, applying electron normalizations,

$$
\frac{e\delta\phi}{T_i} = \Phi,\ \frac{\partial_x n_e}{n_e} = -\frac{1}{r_n},\ \frac{\partial_x T_e}{T_e} = -\frac{1}{r_t},\ \eta_e = \frac{r_n}{r_t},\ \rho_e = \sqrt{\frac{\tau m_e}{m_i}}\rho_i,\ \frac{\mathbf{x}}{\rho_e}\to\mathbf{x},\ \frac{\rho_e}{r_n}\Omega_{ce}t\to t, \tag{E.14}
$$

one finds

$$
\begin{aligned}
&- (1-\frac{1+\tau}{2\tau}\nabla_\perp^2)\partial_t\Phi + \frac{1+\tau}{2\tau}\frac{r_n^2}{\rho_e^2}\partial_t^{-1}\nabla_\parallel^2\Phi + \frac{(1+\tau)(1+\eta_e)}{4\tau}\partial_y\nabla_\perp^2\Phi \\
&+ \frac{(1+\eta_e)}{2\tau}\partial_y\Phi + \frac{(1+\tau)^2}{\tau^2}\frac{r_n}{4\rho_e}\left[\hat{\mathbf{b}}\times\nabla_\perp\Phi\cdot\nabla_\perp\right]\nabla_\perp^2\Phi = 0.
\end{aligned}
\tag{E.15}
$$